INVESTIGATING TOTAL AEROSOL LOAD OF EASTERN MEDITERRANEAN BASIN WITH SENTINEL-5P

SENTINEL-5P İLE DOĞU AKDENİZ HAVZASININ TOPLAM AEROSOL YÜKÜNÜN İNCELENMESİ

DENİZ YURTOĞLU

PROF. DR GÜLEN GÜLLÜ

Supervisor

Submitted to

Graduate School of Science and Engineering of Hacettepe University

as a Partial Fullfillment to the Requirements

for the Award of the Degree of Bachelor's

in Environmental Engineering.

2023

ABSTRACT

INVESTIGATING THE TOTAL AEROSOL LOAD OF THE EASTERN MEDITERRANEAN BASIN WITH SENTINEL-5P

Deniz YURTOĞLU

Master of Science, Department of Environmental Engineering

Supervisor: Prof. Dr. Gülen GÜLLÜ

September 2023, 215 pages

The Eastern Mediterranean Basin has a high aerosol load formed from different sources and is subject to atmospheric transport. This region, which includes the deserts of Africa and the Middle East, is one of the regions that is most affected by climate change.

Aerosols, which are highly present in the Eastern Mediterranean Basin in a form of dust, directly affect the radiative balance of the earth by absorbing and/or scattering the sun rays reaching the atmosphere and indirectly affect the balance by affecting cloud formation by acting as a nucleus. This study aims to investigate the spatial and temporal distribution of aerosols over the Eastern Mediterranean Basin with the daily Absorbing Aerosol Index (AAI) data obtained from the Sentinel-5P satellite, which carries a spectrometer called TROPOMI in order to quantify specific pollutants over the atmosphere. Sentinel-5P is a Low-Earth orbiting satellite that performs atmospheric measurements with high spatiotemporal resolution (5.5 km x 3.5 km). While retrieving the data, The Level-2 Reprocessing UVAI product, which is the aerosol index measured between the wavelength ranges of 340/380, 354/388, and 335/367 nm, was converted to

the Level-3 AAI product by quality standards, that represents aerosols that absorb the incoming solar rays. After retrieving the data, “Not a Number” (NaN) values, which are present due to the orbit's geometry, were removed from the dataset. Then, daily data were visualized by days, months, years, and seasons and the distribution of aerosol load was examined. Time series graphs were created with Mann Kendall trend test, and then the data were decomposed in order to visualize the trends that AAI product includes. As a result of these analyses, it was seen that the Level-3 AAI data were consistent with the meteorological seasons. Except for the cases where NaN is rarely observed due to the geometry of the satellite, and the extreme cases caused by the effect of some dust oscillations, the temporal and spatial changes of the aerosols can be examined in an accurate way with the Sentinel-5P data. It was seen that the AAI value in the Eastern Mediterranean Basin shows a decreasing trend over the four years. In Türkiye, there were no significant trends over the four years. However, when the data is divided into years, for example, an increase trend was observed in 2019 and a decreasing trend was observed in 2020. As North Africa and the Northern Arabian Peninsula are constantly exposed to dust storms, no significant trend has been observed in these two regions.

Additionally, three dust related cases have been investigated, one of which is the forest fires that happened over Türkiye in the summer months of 2021. During the case study analyses, the Sentinel-5P data visuals have been compared with satellite images, such as MODIS and EUMETSAT. The ground-based measurements for temperature, wind speed, and atmospheric pressure have been used to find the causes and drivers of the dust episodes. PM_{10} measurements were obtained from the Continuous Monitoring Center, a ground-based measurement network, and high PM_{10} concentrations have been observed during dust events. As a result of these comparisons, the compatibility of the AAI data of the Sentinel-5P satellite with other satellites has been observed.

Keywords: Absorbing Aerosol, Sentinel-5P, TROPOMI, Remote Sensing, Eastern Mediterranean Basin

ÖZET

SENTINEL-5P İLE DOĞU AKDENİZ HAVZASININ TOPLAM AEROSOL YÜKÜNÜN İNCELENMESİ

Deniz YURTOĞLU

Yüksek Lisans, Çevre Mühendisliği Bölümü

Tez Danışmanı: Prof. Dr. Gülen GÜLLÜ

Eylül 2023, 215 sayfa

Doğu Akdeniz Havzası, farklı kaynaklarda oluşan ve atmosferik taşınıma maruz kalan yüksek bir aerosol yüküne sahiptir. Afrika ve Orta Doğu çöllerini de içerisinde bulunduran bu bölge, dünya üzerinde iklim değişikliğinden en çok etkilenen bölgelerden biridir.

Bu çalışmanın amacı, atmosferdeki belirli kirleticileri ölçmek için TROPOMI adlı bir spektrometre taşıyan Sentinel-5P uydusundan elde edilen günlük Emici Aerosol İndeksi verileri ile Doğu Akdeniz Havzası üzerindeki aerosollerin mekânsal ve zamansal dağılımını araştırmaktır. Sentinel-5P, yüksek uzamsal-zamansal çözünürlükle (5,5 km x 3,5 km) atmosferik ölçümler yapan alçak Dünya yörüngeli bir uydudur. Verileri alırken, Seviye-2 Yeniden İşleme Ultraviyole Aerosol İndeksi (UVAI) ürünü; 340/380, 354/388 ve 335/367 nm dalga boyu aralıkları arasında ölçülen aerosol indeksi, kalite standartları tarafından gelen güneş ışınlarını absorbe eden aerosolleri temsil eden Seviye-3 Emici Aerosol İndeksi (AAI)'ne dönüştürülür. Veriler alındıktan sonra, yörüngenin geometrisi nedeniyle mevcut olan NaN (sayı olmayan) değerleri veri setinden çıkarılmıştır. Ardından, günlük veriler günler, aylar, yıllar ve mevsimlere göre görselleştirilmiş ve emici aerosol yükünün dağılımı incelenmiştir. Mann Kendall testi ile zaman serisi

grafikleri oluşturulmuş ve daha sonra AAI ürününün içerdiği trendleri görselleştirmek amacıyla veriler ayrıştırılmıştır. Bu analizler sonucunda Seviye-3 AAI verilerinin meteorolojik mevsimlerle uyumlu olduğu görülmüştür. Uydunun geometrisi nedeniyle NaN'nin nadiren gözlemlendiği durumlar ve bazı toz salınımlarının etkisinin neden olduğu aşırı durumlar dışında, aerosollerin zamansal ve mekânsal değişimleri Sentinel-5P verileri ile hassas bir şekilde incelenebilmektedir. Analizler sonucu, Doğu Akdeniz Havzasında AAI değerinin 4 yıl içerisinde azalış trendi gösterdiği gözlemlendi. Türkiye'de ise kayda değer bir trend gözlemlenmemiştir. Ancak veri yıllara ayrıldığında, örneğin 2019 yılında artış, 2020 yılında ise azalış trendi gözlemlenmiştir. Kuzey Afrika ve Kuzey Arap Yarımadası'nda sürekli olarak toz fırtınalarına maruz kaldığından dolayı, bu iki bölgede önemli bir trend gözlemlenmemiştir.

Ek olarak, biri 2021 yılı yaz aylarında Türkiye genelinde meydana gelen orman yangınları olmak üzere, tozla ilgili üç vaka incelenmiştir. Bu vakalar için Sentinel-5P veri görselleri MODIS ve EUMETSAT gibi uydu görüntüleri ile karşılaştırılmıştır. Toz olaylarının nedenlerini ve etkenlerini bulmak için sıcaklık, rüzgâr hızı ve atmosferik basınç gibi yer bazlı ölçümler kullanılmıştır. PM_{10} ölçümleri yer tabanlı bir ölçüm ağı olan Sürekli İzleme Merkezi'nden alınmış ve toz olayları sırasında yüksek PM_{10} konsantrasyonları gözlemlenmiştir. Bu karşılaştırmalar sonucunda Sentinel-5P uydusuna ait AAI verisinin diğer uydularla uyumluluğu gözlemlenmiştir.

Anahtar Kelimeler: Emici Aerosol, Sentinel-5P, TROPOMI, Uzaktan Algılama, Doğu Akdeniz Havzası

ACKNOWLEDGMENT

First of all, I would like to thank my thesis supervisor, Prof. Dr. Gülen Güllü. Her intelligence and knowledge brought me from loving this department to completing my master's degree.

I would like to thank Prof. Dr. Merih Aydınalp Köksal for gently guiding me to find my purpose. She was not only a teacher for me, and I am grateful to meet her. I would also want to thank Prof. Dr. Alper Ünal for his generous support and trust. The circumstances that make us unite was not ideal. But without him, I would not push myself to a better way. I would like to thank Dr. Saime Yeşer Aslanoğlu for her support and friendship. It was a pleasure to work with her. Lastly, I am thankful to Reza Rezaei for helping me expand my knowledge.

For the big emotional part, I would like to start with my beloved friend, Firdevs Doğrusever. I would like to thank the Environmental Engineering Department of Hacettepe University, for making our paths cross with her. And I would like to thank both of us, for working so hard to strengthen our relationship, even when it's "veeeery" hard and the life was not helping. To complete our thesis was another challenge in our relationship, and I am so proud of both of us. We got this!

My mother, Hamiyet Güney Yurtoğlu, thank you for existing. Thank you for not giving up. Thank you for making me who I am now. I am so grateful that we are still fighting side by side! Special thanks to my aunt, Filiz Kayadelen, and my grandmother, Fitnet Güney, as well.

My boyfriend, Ahmet Can Tatlıçeşme, thank you for believing in me, loving me, and lifting me up when I fall. I have been writing this thesis since we met. What do you think our life will be like from now on?

My cats, Mimi, and Lady, thank you for your infinite and unrequited love and support. Thank you for keeping my feet on the ground when life is tough.

A very special thanks to my dad, Ayhan Yurtoğlu. For chasing after my mother, for being who he is, for always believing in me, for always loving me, and for always protecting me. Even now, above the skies, he is making sure that my path is clear, and towards nothing but goodness.

TABLE OF CONTENTS

LIST OF FIGURES

LIST OF TABLES

SYMBOLS AND ABBREVIATIONS

Symbols

nm	nanometer
µm	micrometer
km	kilometer
w	Watt
h	hours
MB	Megabytes
(n.d)	No date
GB	Gigabytes
Gbit	Gigabits
Rcalc	Calculated Reflectance
Rmeas	Measured Reflectance
ALER	Real Surface Albedo (If there are no clouds or aerosols present)
.JSON	JavaScript Object Notation
NetCDF	Network Common Data Form
.csv	Comma Separated Values
SO_2	Sulphur dioxides
SO_x	Sulphur oxides
NO_2	Nitrogen dioxides
NO_x	Nitrogen oxides
CO	Carbon monoxide
CO_2	Carbon dioxide
CH_4	Methane
CH_2O	Formaldehyde

NaN	Not a Number
O_3	Ozone

Abbreviations

AAI	Absorbing Aerosol Index
AER_AI	Aerosol_AerosolIndex
AERONET	Aerosol Robotic Network Data
AI	Aerosol Index
ALH	Aerosol Layer Height
AOD	Aerosol Optical Depth
BRDF	Bidirectional Reflectance Function
CALIPSO	Cloud-Aerosol Lidar and Infrared Pathfinder Satellite Observations
CAMS	The Copernicus Atmosphere Monitoring Service
COVID	Corona Virus Disease
EARLINET	European Aerosol Research Lidar Network
EMB	Eastern Mediterranean Basin
Envisat	Environmental Satellite
ESA	European Space Agency
EUMETSAT	The European Organization for the Exploitation of Meteorological Satellites
GCAS	GEO-CAPE Airborne Simulator
Geo-TASO	Geostationary Trace Gas and Aerosol Sensor Optimization
Geo-CAPE	Geostationary Coastal and Air Pollution Events
GEOS-FP	Goddard Earth the Observing System Forward Processing
GMES	Global Monitoring for Environment and Security
GOME	Global Ozone Monitoring Instrument

ICU	Instrument Control Unit
IQR	Interquartile Range
TROPOMI	Tropospheric Monitoring Instrument
L2	Level-2
L3	Level-3
Lat	Latitude
Lon	Longitude
LCM	Lambertian Cloud Model
LSM	Lambertian Scene Model
LEO	Low Earth Orbit
MAX-DOAS	Multi-Axis Differential Optical Absorption Spectroscopy
MERRA-2	The Modern-Era Retrospective Analysis for Research and Applications
MetOP-SG	Meteorological Operational Second Generation
MODIS	Moderate Resolution Imaging Spectroradiometer
MISR	The Multi-angle Imaging Spectroradiometer
NAMEM	National Agency for Meteorology and Environmental Monitoring
NASA	National Aeronautics and Space Administration
NIR	Near-Infrared
NRT	Near-real Time
NSO	Netherlands Space Office
OFF	Offline
OMPS	Ozone Mapping and Profiler Suite
OMI	Ozone Monitoring Instrument
PGN	The Pandonia Network
$PM_{2.5}$	Particulate Matter (Aerodynamic Diameter<2.5 μm)

PM_{10}	Particulate Matter (Aerodynamic Diameter <10 μm)
RPRO	Reprocessing
SAI	Scattering Aerosol Index
SCI	Scattering Index
SCIAMACHY	The Scanning Imaging Absorption Spectrometer for Atmospheric Chartography
SCM	Scattering Cloud Model
Sentinel-5P	Sentinel-5 Precursor
SWIR	Short-wave Infrared
Suomi NPP	Suomi National Polar-orbiting Partnership
STL	Seasonal and Trend decomposition using Loess
TOMS	Total Ozone Mapping Spectrometer
USA	United State of America
UV	Ultraviolet
UVAI	Ultraviolet Aerosol Index
VIIRS DB	Visible Infrared Imaging Radiometer Suite Deep Blue
VIS	Visible
ZSL-DOAS	Zenith-Scattering-Light Differential Optical Absorption Spectroscopy
qa_value	Quality Assurance Value
WHO	World Health Organization

1. INTRODUCTION

Aerosols play a significant role in the atmosphere. Anthropogenic and naturally occurring aerosols affect human health, reduce visibility, and change the radiation balance of the Earth. While it directly affects the radiation balance by scattering or absorbing the sunlight, it also affects the balance indirectly by acting as a nucleus during cloud formation. These liquid or solid substances are suspended in a gas. They vary in size but are usually less than 10 μm. While primary aerosols are released directly into the atmosphere through natural or anthropogenic sources, secondary aerosols are formed as a result of various reactions occurring between primary aerosols. Since the diameters of these suspended particles are small, their horizontal transport in the atmosphere occurs more easily than other substances. Their -constantly changing and heterogeneously dispersed- nature in the atmosphere makes them an important parameter that affects the quality of the atmosphere. Therefore, the change in the concentration and location of aerosols must be carefully observed and studied. Ground-based observations of the atmosphere are not enough for a total deduction of the concentration and location of aerosols; since this method is very expensive, and it is not possible to build in-situ measurement stations in all locations in the world.

In this thesis, in order to examine the aerosols, satellite remote sensing has been used because of its ability to cover the whole world and provide information on the spatial and temporal variation of the pollutants. Remote sensing is the process of detecting and monitoring the physical characteristics of an area by measuring reflected and emitted radiation at a distance. These measurements are typically made by satellites or aircraft. There are two kinds of sensors: passive and active. While passive sensors record the electromagnetic radiation that is reflected or emitted from the surface of the Earth, active sensors create their own electromagnetic energy, which is transmitted from the sensor toward the terrain, interacts with the terrain, and is recorded by the remote sensor's receiver. For this thesis, a satellite that has a passive remote sensor has been used. Sentinel-5 Precursor (Sentinel-5P) is one of the European Space Agency's (ESA) satellites dedicated to monitoring Earth's atmosphere with a high-spatio temporal resolution. It continues the measurements of a series of spectrometers such as Global Ozone Monitoring Experiment (GOME), Scanning Imaging Absorption Spectrometer for Atmospheric Cartography (SCIAMACHY), and Ozone Monitoring Instrument (OMI)

(ESA, n.d.-l). The Sentinel-5P mission aims to extend the data records of these missions and form the link between the Sentinel-4 and Sentinel-5 missions (ESA, n.d.-l). Comparing other spectrometers, with 3.5 km x 5.5 km spatial resolution at nadir (the direction that points a specific location perpendicularly) and 2600 km swath width, Tropospheric Monitoring Instrument (TROPOMI), which is mounted on the Sentinel-5P is better at detecting small-scale sources of pollutants with its increased cloud-free observation (ESA, n.d.-l). The fact that Sentinel-5P is a leading satellite in its field, makes it suitable for this study.

Aerosols can be divided into two in terms of radiative properties: absorbing (smoke, dust, volcanic ash) and scattering (sulfate particles and clouds) aerosols. While absorbing aerosols absorb the incoming solar radiation and have a warming effect, scattering aerosols scatter this radiation and have a cooling effect on the Earth's surface. In the investigation of the load of aerosols over an area, aerosol indexes can be used. In this thesis, AAI data measured in the ultraviolet spectral range, retrieved from TROPOMI, has been used to detect the presence of absorbing aerosols in the atmosphere for the selected study area, which is the Eastern Mediterranean Basin. AAI separates the spectral contrast from the effects of Rayleigh scattering, surface reflection, and cloud scattering at two Ultraviolet (UV) wavelengths (de Graaf et al., 2005a). TROPOMI measures the AAI in three wavelength pairs: 340-380, 354-388 (wavelengths used by OMI), and 335-367 nm, where the diffraction of anthropogenic and natural-origin aerosols is most experienced (ESA, n.d.-g) (Stein Zweers, 2022). Usually, while observing Absorbing Aerosol Index, because inversion calculations are more straightforward and Rayleigh scattering is less critical, measurements are made in the visible and infrared regions (Hecht, 2015) (de Graaf et al., 2005a). However, in the ultraviolet range, land and ocean surface albedos are small compared to the visible and infrared ranges. This situation means that most land and ocean surfaces appear dark, and a high contrast with atmosphere effects is achieved (Kooreman et al., n.d.).

The aim of this thesis is to investigate the aerosol load over the Eastern Mediterranean Basin with the AAI data retrieved from Sentinel-5P – TROPOMI which is an instrument that has high resolution compared to other instruments. The importance and uniqueness of this thesis comes from instrument having a high resolution.

After retrieving the raw data of AAI from TROPOMI, data has been prepared by screening the bad quality data (cloud-covered or NaN-containing). By using cumulative probability, the amount of usable data will be detected. The data has been rearranged by quality standards. With the new dataset, yearly, seasonal, and monthly interpolation has been conducted, and the data have been visualized. The data was analyzed with time series analysis to examine the variation of the total aerosol load according to time and space and determine the hot spots formed in the area. Additionally, with the assistance of the Sentinel-5P AAI data, three cases have been investigated in terms of absorbing aerosol load. These are two extreme dust releases in different times and regions, and the forest fires occurred in the summer seasons of the year 2021 over Türkiye.

The structure of the thesis is decided as follows.

- The “Introduction” part briefly defines the aim and the context which was determined for the study.
- In the “Literature Review” part; aerosols, sources of aerosols, their forming mechanisms, remote sensing methods, Sentinel-5P satellite, TROPOMI spectrometer, aerosol index, and studies related to these topics are explained.
- “Data and Methodology” part gives an explanation of the study area (Eastern Mediterranean Basin, Türkiye, Northern Africa, and Northern Arabian Peninsula), the data which was used (Sentinel-5P, Reprocessed Level-3 Absorbing Aerosol Index product), and the methods (Trend Analysis) which were used in the analysis of the data.
- After explaining and conducting the methodology, detailed results of the analyses have been discussed in the “Results and Discussion” part. Three case studies were analyzed.
- The “Conclusion” part concludes the study, gives the overall results of this study, and suggests recommendations for the further investigations.

2. LITERATURE REVIEW

Air pollution is one of the most significant challenges in our daily lives due to its capability to affect the climate, human health, and vital ecological systems. Therefore, it has been a primary subject of many studies worldwide. Where there be humans, there is air pollution. *Air pollution* is defined as "the contamination of the indoor and outdoor environment by any chemical, physical or biological agent that modifies the natural characteristics of the atmosphere" by the World Health Organization (WHO) (WHO Regional Office for Europe, n.d.).

The main reason behind experiencing air pollution at this level is that improving the daily life of humankind has its consequences. For instance, having a household combustion device to keep the heat up on winter days, using motor vehicles for transportation, and needing industrial facilities are activities everywhere in the everyday life of humankind (WHO Regional Office for Europe, n.d.).

Aerosols play a crucial role in atmospheric science. Therefore, it has been studied worldwide by researchers with various analysis methods and several data retrieval sources, such as ground-based observations and satellite measurements. Analysis of the temporal and spatial distribution of aerosols is an essential field of study due to the effects of aerosols in the atmosphere, such as radiation disturbance and health-related problems.

2.1. Aerosols

The atmosphere contains liquid and solid particles called aerosols (France et al., n.d.). These particles have a direct and indirect effect on the radiative force of the atmosphere. While the direct effect is scattering or absorbing the incoming solar rays, the indirect effect is related to the ability of aerosols to act as a nucleus in cloud formation (Pitari et al., 2001). Aerosols increase the droplet number and ice particle concentrations, causing a decrease in the precipitation efficiency of clouds (Pitari et al., 2001). This situation may directly affect the earth's hydrological cycle (Ramanathan et al., 2002). These solid or liquid particles, suspended in the air, generally have a short atmospheric lifetime. However, aerosols with smaller particle sizes may be transported through the atmosphere for long distances and times. The composition of aerosols is highly fluxional through time and space. Therefore, these particles should be observed, classified, and controlled in order to decrease their significantly negative effect on the atmosphere, as well as on human health and the ecology of the earth.

Aerosols can be classified according to their sources and production mechanism. This classification is not straightforward because not all aerosols are directly emitted into the atmosphere, like primary aerosols. Most of them are formed by the reactions between their precursors in different atmospheric conditions, such as secondary aerosols.

Some of the aerosols may have a wide range of size and refractive index, affecting their atmospheric lifetime and capacity to disturb the radiative balance of the atmosphere. For example, while the oversized particles are quickly deposited on the earth by wet or dry deposition, smaller particles may spend more time in the atmosphere, which may result in their transport to another place far away from their production source (Pitari et al., 2001). This atmospheric transport may be misleading in classifying aerosols by their source. The formation mechanism and the source of the aerosols in the atmosphere must be addressed in order to conduct an accurate statistical analysis of the atmosphere. Here, remote sensing, which will be used in this thesis and explained in the following sections, has been proven helpful in atmospheric research by many researchers worldwide.

Aerosol particle size distribution is an important parameter that can provide valuable information about the behavior and impacts of airborne particles in different environments (Bo et al., 2008; Kim et al., 2015; Vitousek et al., 2004). The size-wise classification of the aerosol particles can be challenging since the size and the composition of the aerosols vary widely in spatiotemporal terms (Fuzzi et al., 2006; Jimenez et al., 2009; Kanakidou et al., 2005; Zhang et al., 2007). Several studies have investigated aerosol particle size distribution in different environments, such as indoor and outdoor air, industrial workplaces, and atmospheric aerosols.

The aerosol's shape is not always defined by standard parameters such as radius, which means that not all aerosol particles have perfect sphere shapes. Some examples can be seen in Figure 1.

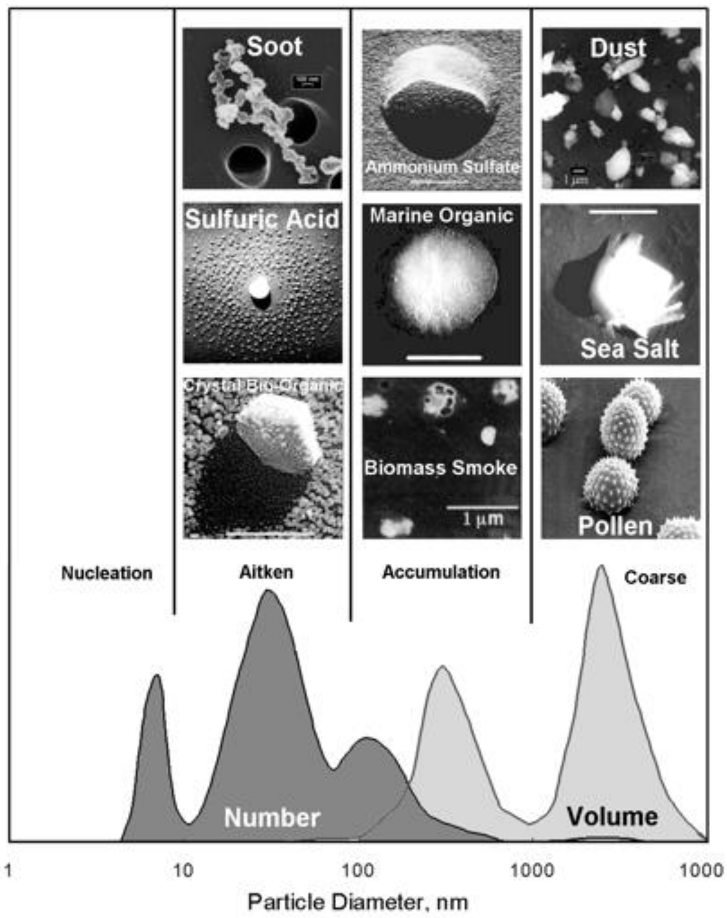

Figure 1. Atmospheric aerosols in a microscope and their particle diameter distributions in nm (Brasseur et al., 2003)

In order to overcome this difficulty and obtain a standard in atmospheric calculations, some mathematical approaches had to be developed. According to Whitby (Whitby, 2007), there are three modes in the distribution of aerosols: nuclei, accumulation, and coarse modes. Nuclei mode is the minor mode where the aerosol particles generally have a diameter between 0.005 and 0.1 µm. Aerosols in this mode are formed by chemical reactions in the atmosphere due to combustion and contain the most significant amount of particles. In accumulation mode, aerosol particles have a diameter range between 0.1 and 2 µm. Generally, the accumulation mode consists of anthropogenic aerosols. Last of all is the coarse mode which is not studied as much as fine particles, which consists of nuclei and accumulation mode. The aerosol particles in coarse mode are bigger than 2 µm in diameter and consist of soil and sea salt particles.

The sources of primary aerosols can be classified as natural and anthropogenic. Soil dust, sea salt, volcanos, and wildfires are the natural sources of primary aerosols. Industrial emissions, burning of fossil fuel, and biomass are anthropogenic sources of primary aerosol emissions. Soil dust can be of both natural and anthropogenic origin. It may be of natural origin because naturally formed deserts have emissions from natural winds. It may be of anthropogenic origin because there may be releases from soil surfaces degraded by humans.

The secondary aerosols such as carbonaceous aerosols (organic and black carbon), organic aerosols, sulfates, nitrates, and ice particles (from volcanic aerosols) are formed as a result of some atmospheric reactions such as oxidation (gas-phase and particle-phase) (Kroll & Seinfeld, 2008), neutralization (T. Wang et al., 2020), accumulation, and ozonolysis (of monoterpenes) (Fayad et al., 2021).The chemical composition of the secondary aerosols depends on the formation mechanism and the composition of the primary aerosol which it was formed from (Myhre, 2013).

2.2. Formation Mechanisms

The formation mechanisms of aerosols are mainly governed by the following processes: Nucleation (gas-to-particle), Condensation (gas-to-liquid), Coagulation (between particles), and Deposition. In the previous section (Aerosols), it was mentioned that secondary aerosols are formed due to atmospheric reactions in the gas phase and particle phase. These reactions occur between primary aerosols, which are directly emitted into the earth's atmosphere. Some of these aerosols act as a precursor in these reactions, resulting in secondary aerosols forming.

Mineral dust, which was investigated in this thesis, is formed from the disintegration and fragmentation of soil particles and rocks. The formation mechanisms are mainly governed with natural geological processes such as wind, erosion, and volcanic activities. As well as natural processes, the anthropogenic activities contribute to the formation of mineral dust by the combustion of fossil fuels, mining, and agricultural activities. Once formed, these particles, which are 2.5 to 10 micrometers in size, can be transported over long distances, inversely proportional to their particle size. The smaller, the further these particles can travel (Engelstaedter & Washington, 2007; Sokolik & Toon, 1996). There are lots of studies that use NO_2, SO_2, CO, and O_3 data as precursors in order to estimate the concentration and composition of the aerosols in the atmosphere.

Spatio-temporal mapping of $PM_{2.5}$ and PM_{10} emissions over China was done with the help of SO_2, NO_2, and O_3 data obtained from Sentinel-5P (Y. Wang et al., 2021), and from the Goddard Earth Observing System-Forward Processing (GEOS-FP) (ground-based measurements) and The Visible Infrared Imaging Radiometer Suite (VIIRS) Aerosol Optical Depth (AOD) Product data. The data is preprocessed and spatially matched with ground-based measurements. The AOD data used for estimating particulate matter in the atmosphere has largely missing values compared to the suggested approach, and this study proves that the effect of these missing values is not negligible and can be covered with satellite data.

During the COVID-19 pandemic, O_3, which is one of the precursors of particulate matter, did not reduce in the atmosphere, unlike the other primary pollutants. For that time, Ozone concentrations obtained from TROPOMI were investigated using the principle of optimal estimation method (Zhao et al., 2021). Ozone production in the atmosphere is controlled by volatile organic compounds in winter, which did not show any concentration difference, causing ozone concentrations to stay the same. On the other hand, the decrease of NO_x concentrations in the atmosphere during COVID-19 weakened the titration of ozone, which increased the ozone concentration.

2.3. Remote Sensing

There are ground-based air-borne, and space-borne measurements of air quality. Air pollution monitoring should be carried out with such reliable data providers. The main disadvantage of ground-based measurements is the impossibility of building in-situ measurement sites for every location on the earth. Satellite-based (space-borne) measurements recompense this disadvantage by having the ability to cover the whole world with various levels of wavelengths in order to detect the spatiotemporal distribution of air pollutants.

Remote sensing is a method of gathering data about the earth at a specific distance without making any interaction (United States Geological Survey, n.d.-b). For instance, a device (a spectrometer) placed on a satellite in an orbital platform, measures the energy reflected from and emitted by the earth (United States Geological Survey, n.d.-b). There are two types of remote sensing: active and passive. While devices with active sensors can produce their energy and are not dependent on external electromagnetic energy, passive sensors need a light/energy source (Rodríguez et al., 1989). Thus, passive sensors cannot detect data when the sun is absent.

The challenge related to remote sensing is the clouds and the surface albedo. Cloud cover in the atmosphere can interrupt the remote sensing device's process of accurately measuring reflected energy. The albedo of a surface is the fragment of the sunlight reflected from the earth's surface (Coakley, 2003) (Copernicus Global Land Service, n.d.) . Thus, the high surface albedo may also interrupt the process of the remote sensing device and may lead to an overestimation in the concentration of the pollutants.

Data retrieved by remote sensing methods have been used by many researchers worldwide since the first satellite devoted to monitoring air pollution was launched.

The history of remote sensing for air quality with satellites can be seen in Table 1.

Table 1. Heritage of remote sensing for investigating air quality

Satellite/Mission/Instrument	**Year**	**Reference**
Total Ozone Mapping Spectrometer (TOMS)	1978	(Hatzianastassiou et al., 2009)
Global Ozone Monitoring Experiment (GOME)	1995	(ESA, n.d.-l)
Moderate Resolution Imaging Spectroradiometer / Multi-angle imaging spectroradiometer (MODIS/MISR)	1999	(United States Geological Survey, n.d.-a)
The Scanning Imaging Absorption Spectrometer for Atmospheric Chartography (SCIAMACHY)	2002	(ESA, n.d.-l)
Ozone Monitoring Instrument (OMI)	2004	(NASA, n.d.-a)
Cloud-Aerosol Lidar and Infrared Pathfinder Satellite Observation (CALIPSO)	2006	(NASA, n.d.-b)
Sentinel-5 Precursor (S5-P)	2017	(ESA, n.d.-k)

In this thesis, the Sentinel-5 Precursor satellite is used for obtaining data products of TROPOMI.

2.4. Sentinel-5P

Sentinel-5P is one of the Copernicus Mission's satellites, the new name for the Global Monitoring for Environment and Security (GMES), the European Commission's Earth Observation Programme, and this program is co-funded by ESA and Netherlands Space Office (NSO) (ESA, n.d.-k). The main objective of Sentinel-5P, which launched on October 2017, is to provide high-quality atmospheric data for air quality, climate monitoring, and forecasting by measurements with higher spatiotemporal resolution compared to other satellites (ESA, n.d.-k) (Shikwambana et al., 2020). Sentinel-5P also aims to fill the data gap between the Envisat satellite, which carries the SCIAMACHY spectrometer, and the MetOp-SG satellite, which carries the Sentinel-5 instrument (ESA, n.d.-d). Sentinel-5P is a low-earth orbit (LEO) satellite that carries TROPOMI. The satellite has planned to operate for seven years with a 2600 km swath width (ESA, n.d.-d) and 824 km of orbit altitude (ESA, n.d.-i). It takes 16 days for the satellite to pass over precisely the same location on Earth (ESA, n.d.-i). The satellite orbits around the earth by an angular distance of 98.7^0, and this orbit is classified as a "high inclination orbit" (ESA, n.d.-i). The satellite has a near-polar orbit, and its surface is illuminated by the sun at the same angle (ESA, n.d.-i).

Sentinel-5P is currently in Phase-E2 (Operations Phase) since April 2018, according to the mission status reports that the Sentinel-5P Team regularly prepares. These reports are available on the official website of the Sentinel-5P satellite (ESA, n.d.-h).

Table 2 shows the properties of the TROPOMI carried on the Sentinel-5P satellite with the information gathered from the official Sentinel-5P documents (Rozemeijer & Van, 2015).

Table 2. Properties of the TROPOMI (ESA, n.d.-k) (Zhao et al., 2021)

Properties	**TROPOMI**
Type	A passive grating imaging spectrometer
Launch Date	13.10.2017
Mean Local Solar Time	13.30 (at Ascending Node)
Configuration	Double channel push broom staring (non-scanning) in nadir viewing
Swath Width	2,600 km
Field of View	Across the track: High
	Along the track: Small
Spatial Sampling	7 (along the track) x 3.5 (across the track) km^2 5.5 (along the track) x 3.5 (across the track) km^2 (ESA, 2019) (13 times better than OMI) (Shikwambana et al., 2020)
Spectral	4 spectrometers, each electronically split in two bands (2 in UV, 2 in VIS, 2 in NIR, 2 in SWIR)
Wavelength Pairs	340-380 nm, 354-388 nm, and 335-367 nm
Radiometric Accuracy (Absolute)	1.6% (SWIR) to 1.9% (UV) of the measured earth spectral reflectance
Overall Mass	204.3 kg (not including 16.7 kg of ICU -Instrument Control Unit- that is integrated on the platform, separated from the instrument)
Dimensions	1.40 x 0.65 x 0.75 m
Design Lifetime	7 years

Average Power Consumption	155 W
Available Products	Level-0, Level-1B, and Level-2
Processing Ways (Data Streams)	Near-Real Time (NRT) → After 3h Offline (OFFL) → Within a few days Reprocessing (RPRO) → Within a few days
Generated Data Volume	139 Gbits per full orbit

In this thesis, Offline and Reprocessing UV Aerosol Index data, a Level-2 product, will be used in the analyses. The data was then converted to Level-3 Absorbing Aerosol Index data.

In table below, the TROPOMI instrument is compared with other similar instruments which measure aerosol values.

Table 3. Comparison between satellite instruments

Satellite/Instrument	**Name of the Aerosol Data**	**Resolution**
Sentinel-5P – TROPOMI	AER_AI	3.5 km x 5.5 km
The EOS-Aura – OMI (Royal Netherlands Meteorological Institute, n.d.)	OMAERUV and OMAERO	13 km x 24 km
The ERS-2 – GOME (ESA, n.d.-e)	AAH	40 km x 40 km 40 km x 320 km
TOMS (ESA, n.d.-m)	AI	50 km x 50 km
MODIS/MISR (NASA, n.d.-d)	AOD	250 m, 500 m, and 1 km
SCIAMACHY (ESA, n.d.-c)	Aerosol	3 km x 132 km
CALIPSO (ESA, n.d.-a)	Stratospheric and Tropospheric Aerosol Data	1 km x 1 km

As can be seen in Table 3, the resolution of TROPOMI instrument carried by the Sentinel-5P satellite is higher compared to the other instruments. Because this instrument was not used in a study conducted for the investigation of aerosol load over the Eastern Mediterranean Basin yet, this study becomes a pioneer in literature.

2.5. Aerosol Index

Aerosol Index is the qualitative measure of the presence of aerosols in a specific part of the atmosphere (de Graaf et al., 2005b). In Sentinel-5P, the name of this product is the Level-2 Ultraviolet Absorbing Index (UVAI). While retrieving the satellite data, there is a conversion from Level-2 UVAI to Level-3 Absorbing Aerosol Index (AAI), based on filtration in order to remove pixels with quality assurance (qa-value) less than 80% (Earth Engine Data Catalog, n.d.). This index shows the presence of absorbing aerosols in the atmosphere. Unlike Aerosol Optical Thickness measurements, the AAI measurement can be conducted in a cloud-covered atmosphere (Earth Engine Data Catalog, n.d.).

Absorbing aerosols primarily originate from sources such as deserts, biomass burning (including black carbon and organic carbon), and volcanoes. The Absorbing Aerosol Index (AAI), a valuable derived parameter, utilizes a spectral contrast method in the near-UV region (where ozone absorption is minimal) to detect the presence of elevated absorbing aerosols in the atmosphere. The Ultraviolet (UV) Absorbing Aerosol Index (AAI) serves as an indicator of atmospheric absorption caused by aerosols (Torres et al., 2007). It distinguishes the spectral contrast at two UV wavelengths due to aerosol absorption from that arising from molecular Rayleigh scattering, surface reflection, and trace gas absorption (de Graaf et al., 2005a; Torres et al., 2007). Ideally, the AAI remains at zero when no absorbing or scattering aerosols are present in the observed scene. Negative AAI values, on the other hand, suggest the presence of scattering aerosols such as sulfate particles and clouds.

The effect of clouds on the Ultraviolet Absorbing Aerosol Index was investigated with the UVAI product of TROPOMI, which is rearranged by quality standards as mentioned before (qa_value>0.8) (Kooreman et al., n.d.). The effects of clouds on the Absorbing Aerosol Index were investigated at large and small scales. Large-scale investigation reveals that AAI can be individuated from some properties called Bidirectional

Reflectance Function (BRDF), such as sunglint and cloud bow at extreme viewing and solar geometries. In this study, three retrieval models are suggested: Lambertian Scene Model (LSM), Lambertian Cloud Model (LCM), and Scattering Cloud Model (SCM). Within these three models, LCM and SCM give higher and more homogeneous aerosol distribution. However, differing from the GOME-2 and OMI, at a small scale, decreases and increases in AAI are observed due to the high spatial resolution of TROPOMI. While investigating the large-scale effects, the Pacific Ocean is chosen for its suitability to get an accurate visualization of AAI.

2.6. Atmospheric Studies via Sentinel-5P

Sentinel-5P satellite, a pioneering new-generation satellite in its field, has been used in many studies to analyze atmospheric pollutants, especially NO_2. Since the presence of NO_x provides suitable conditions for the formation of secondary pollutants, reduces visibility, and negatively affects human health, monitoring and regulating NO_2 is necessary (Ialongo et al., 2021). Nitrogen oxides are observed due to their potential to form ozone and particulate matter. It is essential to know the share of NO_x emissions in the atmosphere.

The satellite has also been frequently used in studies examining the effects of the COVID-19 virus on the components in the atmosphere since it provides high-quality data. While this study was conducted, there were few studies directly related to the investigation of aerosols with Sentinel-5P data.

2.6.1. Studies Conducted for the COVID-19 Pandemic

The COVID-19 Pandemic started worldwide in the first months of 2020. However, authorities announced the first case in their country at different times due to the way and speed of the virus's spread. Since there were many precautions to stop or at least slow the spread of the virus, their way of living has changed for people. One of the many precautions which were very effective was the lockdowns. While some countries have announced that it was banned to stay out for a dedicated period of time (like in Türkiye), in some countries, this was not the case.

Nevertheless, all the people -except the ones who have to, like doctors or cops- were scared to go out and have their regular routines. This fear has served nature well. Most of the emissions which are harmful to the environment have been reduced.

In the following paragraphs, some studies which investigated these -mostly- positive effects of the COVID-19 pandemic on the environment have been explained.

The effects of the implementations conducted during COVID-19 on climate change and the environment of Cairo (the capital of Egypt) have been investigated (Madkour, 2022). Remote sensing data from Sentinel-5P is used with the carbon footprint methodology and GIS techniques. In 2020, it was seen that greenhouse gas emissions have been reduced by 15% compared to the same period in 2019. Also, temporary emission improvements were seen in some pollutants, such as NO_2 (17%), SO_2 (15.6%), and CO (7.7%) over the studied area.

Similarly, in Dublin, TROPOMI data was used in order to analyze the spatiotemporal change in air quality during the lockdown of the COVID-19 pandemic (Kumari et al., 2022). A 28% reduction in NO_2 emissions and a 27.7% improvement in Air Quality Index, which is mainly affected by particulate matter, were seen between 2019 and 2020. Additionally, ozone has reduced during the analysis period since it is produced from NO_2 as a secondary pollutant. Carbon monoxide emissions have slightly increased during the pandemic.

In Ulaanbaatar- Mongolia, a study was conducted about the effects of COVID-19 on NO2, SO2, and particulate matter by combining the ground-based data from National Agency for Meteorology and Environmental Monitoring (NAMEM) and remote sensing data from the Sentinel-5P satellite (Ganbat et al., 2022). Compared to the last five years, it was determined that there was a 45%, 72%, and 59% decrease in NO_2, $PM_{2.5}$, and PM_{10} emission amounts, respectively, compared to the same period. In addition, the days when the national limit was exceeded were examined. It was seen that the days of exceedance had decreased by 55%, 30%, and 14% for NO_2, PM_{10}, and $PM_{2.5}$ emissions, respectively. However, the number of exceedances for SO2 emissions has increased by 58%.

In another study conducted with the Sentinel-5P satellite data (Behera et al., 2021), the effects of lockdown in COVID-19 before, during, and after have been investigated. As can be predicted, it was found that during the lockdown (2020), the NO_2, SO_2, HCHO, and AAI emissions have decreased compared to 2019. However, after the lockdown, in 2021, the mentioned emissions increased quickly. This study proved that the lockdown had a positive effect on air quality.

The reduction of NO_2 in the first month of the Coronavirus pandemic was observed in Türkiye with the data provided by TROPOMI on the Sentinel-5P satellite (Kaplan & Avdan, 2020a). The study consists of statistical analyses that show maximum and mean concentration differences of NO_2 emission concentrations between March-April 2019 and March-April 2020. Since the NO_2 concentrations in the atmosphere are directly related to traffic emissions, as expected, in the first month of the pandemic, when nearly everyone was at home all the time, NO_2 emissions were reduced significantly. With the same NO_2 data obtained from the TROPOMI spectrometer, the relationship between NO_2 concentration and population density was investigated in Türkiye (Kaplan et al., 2019). According to the correlation of population data with the statistical analyses, which were performed with the min, max, mean, and sum values of NO_2 between July 2019-January 2019, 50% of the NO_2 emission concentration can be explained by the population data. The results prove that NO_2 emissions are caused by anthropogenic activities in the study domain.

2.6.2. Studies for the Validation of TROPOMI Data

Validation is a way of controlling the accuracy of the data to be used in the analysis and is an essential task to obtain a logical result. For this purpose, many studies have been and are being conducted for various datasets. In the following paragraphs, studies related to the validation of TROPOMI data are explained.

The spatiotemporal change of; NO_2 and SO_2 from TROPOMI and AOD from MODIS over Türkiye has been investigated from 2019 to 2020, during the first wave of the pandemic (Ghasempour et al., 2021). Results showed a decrease in NO_2 emissions and AOD data. However, SO_2 emissions did not show any change. Additionally, two datasets were validated with data from ground-based stations in Istanbul and Aerosol Robotic Network data (AERONET).

Another validation study for the TROPOMI data was conducted with a comparison between the Aerosol Layer Height data and the ground-based EARLINET lidars, which was established in 2000 (Michailidis et al., 2022) (ACTRIS, n.d.). Similar to this thesis, the study was conducted for the Mediterranean basin from 2018 to 2021. The results showed a high correlation between the TROPOMI data and selected ground-based data. This study revealed that the TROPOMI data can be safely used for air quality analysis.

In a study conducted for some European countries (Douros et al., 2022), in order to validate the NO_2 data obtained by the TROPOMI, the NO_2 data obtained from Copernicus Atmosphere Monitoring Service (CAMS) has been used. It was seen that in summer (15%), the difference between these two data sets is higher than in winter (50%).

The data from TROPOMI has been compared and validated with "Geostationary Trace gas and Aerosol Sensor Optimization (GeoTASO)" and "GEO-CAPE Airborne Simulator (GCAS)" airborne mapping spectrometers and ground-based Pandora spectrometers (Judd et al., 2020). According to the results, the data of the TROPOMI spectrometer is more correlated to airborne measurements than the measurements of the ground-based Pandora spectrometer.

In another study (Verhoelst et al., 2021), NO_2 data retrieved from the Sentinel-5P satellite, TROPOMI spectrometer, was compared with different ground-based data, which are Zenith-Scattered-Light Differential Optical Absorption Spectroscopy (ZSL-DOAS), Multi-Axis Differential Optical Absorption Spectroscopy (MAX-DOAS), and The Pandonia Global Network (PGN) Pandora data. Three types of data (Stratospheric Column, Tropospheric Column, and Total Column) have been validated with co-location and harmonization methods. Results showed that the TROPOMI data is very similar to mentioned ground-based data for the NO_2 pollutant. It was also found that the Near-Real-Time (NRT) measurements of TROPOMI are 0.79% larger than the Offline (OFFL) measurements.

2.6.3. Studies which Analyze the Spatio-Temporal Change of Air Pollutants

Investigating the number of pollutants over time and location significantly contributes to understanding the behaviour of pollutants.

In a study conducted in Poland (Godłowska et al., 2023), Tropospheric Vertical Column data for NO_x of Sentinel-5P satellite is used in order to obtain information about the annual variability of NO_x. The box model is used in order to quantify the amount of NO_x emissions over the area of Poland. The lifetime of NO_x was estimated with over three years of (May 2018-November 2021) data obtained from TROPOMI. It was seen that the amount of NO_x emissions was higher in winter and lower in the summer seasons. Additionally, the detection of NO_x in winter seasons was more complex than in other seasons due to inaccuracies.

In 2022, the results of forest fires, which happened in the Mediterranean part of Türkiye between July 2021 and August 2021, were investigated using the Sentinel-2 and Sentinel-5P data (Yilmaz et al., 2023a). With the help of Sentinel-2 data, burn severity maps were produced. Post-fire CO emission investigation was conducted with Sentinel-5P data. For the analyses, wind data from the MERRA-2 model created by NASA and the CO data from monitoring stations of The Turkish Ministry of Environment, Urbanization, and Climate Change were used. The information gathered from the Sentinel-2 satellite has been analyzed with a normalized burned ratio index, calculated with NIR (near-infrared) and SWIR (short-wave infrared) wavelength ranges. In addition, the vegetation index affected by the forest fire was also examined, and it was seen that this value naturally decreased after the fire. Also, this study has proven the importance of using remote sensing techniques in air quality investigations.

In order to investigate the relationship between NO_2 and CO mean atmospheric column of the Republic of North Makedonia and geographical and demographical data, statistical and geospatial analyses were conducted with Sentinel-5P data (Kaplan & Avdan, 2020b). It was seen that a positive correlation between NO_2 emission concentration and population data and a negative correlation between altitude and CO emission concentration exists.

Evaluation of NO_x and CH_4, which emerged during gas combustion and oil production in Russia, was done using the Sentinel-5P data (Ialongo et al., 2021). Annual NO_x emissions were retrieved, and these observations were modelled with an exponentially modified Gaussian model. CH_4 anomaly was found in the data with the cross-sectional flux method. The results showed that satellite-based observations for air quality are necessary because of the underestimation made by the emission inventories.

The highest and lowest emissions were found on cold weekdays and warm weekends in the study conducted to determine the share of NO_x emissions in Paris (Lorente et al., 2019). These findings provide information on the spatiotemporal distribution of NOx emissions.

Spatial distribution and seasonality changes of NO_2, SO_2, and CO under the influence of local anthropogenic emissions were investigated with Sentinel-5P data for NO_2, SO_2, and CO between 2018-2020 (Savenets, 2021). The result of the analyses showed that there were air quality differences in winter when coal is used for heating purposes and in the spring season when the open burning process is continued.

2.7. Aerosol Studies in Eastern Mediterranean via Remote Sensing

Eastern Mediterranean Basin is located in an area which makes it a crossroad for air masses, and it is mainly affected by mineral dust and many anthropogenic emissions. Mineral dust emissions may be sourced from deserts around this basin, such as African, Arabian, and Asian (Papachristopoulou et al., 2022). More than 50% of the global dust emissions are from the Saharan Desert. The Mediterranean Sea constantly releases marine aerosol emissions due to sea spray evaporation caused by the bursting of bubbles and wave production by the wind (Monahan et al., 1983). Burning of biomass and atmospheric transport of anthropogenically produced emissions are some of the aerosol sources in the Mediterranean basin (Georgoulias et al., 2016). These aerosol loads from several sources resulted in a sensitive area combined with cloud-free conditions and high-solar radiation intensity, especially in summertime (Lelieveld, Berresheim, Borrmann, Crutzen, & Dentener, 2002).

In the following paragraphs, some studies related to the aerosol load of the atmosphere of the eastern Mediterranean basin are explained.

The climatic importance of aerosols in the Eastern Mediterranean Region was examined by collecting aerosol samples with filter papers throughout 2003 and analyzing the data with the help of satellite observations (Kubilay & Koçak, 2009). Chromatography and spectrometer devices evaluated temporal and spatial variations of water-soluble aerosol ion concentrations and aerosol optical measurements. This study uses a moderate

Resolution Imaging Spectroradiometer (MODIS) sensor on Terra and Aqua satellites. As a result, it was concluded that the effects of aerosols are present in climate, air quality, and hydrological cycles. It was seen that the seasonal changes in the water-soluble ion concentrations in the collected samples are associated with precipitation. While the concentrations of aerosols fall to their minimum values in winter with precipitation, in summer, the absence of precipitation causes these species to accumulate in the atmosphere and create a high load of aerosols. In addition, as a result of these studies, it was emphasized that the aerosol concentrations in the Mediterranean atmosphere should be monitored with uninterrupted measurement programs, such as remote sensing methods, since these species in this atmosphere show significant changes over time and space.

A study conducted in Spain (Querol et al., 2009) aimed to determine the main factors affecting the chemical and physical compositions of aerosols in the regional background across the Mediterranean region. It was found that; there is increasing convection of dust from the western Mediterranean basin to the east Mediterranean basin, a change in the tending of aerosols to absorb moisture from the air due to the presence of nitrate and sulfate compounds, and a profusion of hygroscopic aerosols during low cloud formation periods.

In another study conducted in Greece (Gkikas et al., 2016), an algorithm for identifying and characterizing different aerosol types in the greater Mediterranean region, including areas like the Black Sea, the Atlantic off Iberia, and northwest Africa have been introduced. The algorithm identifies five intense aerosol episodes: biomass burning/urban-industrial (BU), desert dust (DD), dust/sea-salt (DSS), mixed (MX), and undetermined (UN). It utilizes various aerosol properties like aerosol optical depth (AOD), Ångström exponent (a), fine fraction (FF), effective radius (reff), and Aerosol Index (AI). During the study period (2000-2007), DD episodes are the most common, occurring predominantly in the western and central Mediterranean and off northern African coasts, with 7 strong and 4 extreme episodes on average per year. DD episodes contribute significantly to strong aerosol episodes (40%) and dominate extreme episodes (71.5%). The occurrence of strong episodes varies by location, such as BU near southern European coasts, MX off the Spanish Mediterranean coast, and DSS in the western and central Mediterranean. Extreme episodes, excluding DD, exhibit more scattered spatial patterns. These episodes can have high AOD values, reaching up to 1.6 (strong) or 5 (extreme). While most episodes last just one day, some extreme DD episodes persist for up to four days. Mediterranean aerosol episodes are more frequent in spring and summer, with rare occurrences in winter, and exhibit year-to-year variability in frequency. The study validates the algorithm's results using 5-day back trajectories. Mixed (MX) and dust/sea-salt (DSS) episodes often co-occur with desert dust (DD) episodes, with their intensity patterns resembling those of strong DD episodes, underscoring the importance of desert dust in Mediterranean aerosol intensity.

A study (Papadimas et al., 2008) has investigated the temporal changes in aerosol optical properties across the broader Mediterranean region, with a particular focus on AOD, a measure of aerosol concentration. This research utilizes data collected by the MODIS onboard Terra and Aqua satellites, covering the period from 2000 to 2006. The analysis reveals a significant year-to-year variation in AOD within the studied area. Specifically, the average visible AOD, both over land and ocean, decreased by 20% from 2000 to 2006, and this decline is statistically significant according to the Man-Kendall test. However, this AOD decrease is not uniform across the entire Mediterranean basin; it is mainly observed in the western regions of the Iberian, Italian, and Balkan peninsulas, as well as along the coastal areas, and in the southern Anatolian peninsula. Seasonal analysis for summer (June to September) and winter (November to March) shows different trends in both AOD and precipitation. Summer AOD decreased by 14%, possibly due to reduced emissions of anthropogenic pollution. In contrast, winter AOD increased by 19%, primarily attributed to reduced precipitation, which is associated with a rising North Atlantic Oscillation (NAO) index. The decreasing trend in MODIS AOD is consistent with similar trends observed at AERONET stations across the study area and ground based PM10 measurements at selected stations.

In a study conducted in Türkiye (Tutsak, 2018), a 15-year climatology of aerosol optical and physical properties has been made in the atmosphere over the Eastern Mediterranean Basin. This study has analyzed the long-term aerosol optical and microphysical properties in the Eastern Mediterranean from 2000 to 2014. It also examined concentrations of sulfate, ammonium, nitrate, and their precursor gases in 2015. Airflow patterns from Eastern and Western Europe decreased by about 0.2% per year, while airflow from North Africa and Turkey increased. Aerosol optical thickness (AOT) decreased from 2000 to

2014, indicating finer particles dominated. AOT and α (spectral dependence) showed significant day-to-day variations, with lower values in rainy winters and higher values in dry summers due to gas-to-particle conversion. Aerosols from North Africa and the Middle East had distinct characteristics. Three classes of aerosols based on hygroscopicity were identified: non-hygroscopic, moderately hygroscopic, and hygroscopic. Imaginary refractive index, single scattering albedo, and absorption angstrom exponent varied for different aerosol types (dust, mixed, pollution). Overall, sulfate and ammonium were prevalent in $PM_{2.5}$, with decreasing trends observed for sulfate, nitrate, and their precursor gases in the Eastern Mediterranean.

2.8.Aerosol Studies Conducted with Satellite Data other than Sentinel-5P

Studies related to aerosols are conducted with the help of satellites such as MODIS, CALIPSO, and SCIAMACHY. In the following paragraphs, some examples of this kind of study are given.

Remote sensing-based climatology was created for SO2, NO2, aerosol and desert dust in Türkiye with MODIS and CALIPSO (Aslanoğlu et al., 2022). Two types of climatology were prepared. 13 years of trace-gas climatology exhibited some hotspots and statistically significant trends over Türkiye, which may lead to an excess in emissions over world averages. Besides, on winter days when the weather is naturally stagnant, the emissions show an increasing trend. As a result of 9-years of desert dust climatology, it was seen that the dust concentration in the Eastern Mediterranean atmosphere shows an increasing trend from west to east. Similar to trace-gas studies, the concentrations of aerosols are the highest in the summer months. Atmospheric transportation that Türkiye is exposed to due to its geographical location and direct contact with the Middle East region makes the Eastern part of the country more sensitive to particulate matter pollution.

Other than MODIS and CALIPSO, The SCIAMACHY was used for the investigation of aerosols (Penning De Vries et al., 2009). Differing from the previously mentioned studies, the Absorbing Aerosol Index (AAI) data product from SCIAMACHY was used to detect the Scattering Index (SCI) in Southeast USA and Southeast Asia. SCI is a valuable tool when detecting the aerosols that scatter lights, especially where the surface is too dark. Seasonally averaged SCI visualizations show high values in summer in the studied area due to the high production of sulfate and secondary aerosols.

In a study conducted by Peshev et al. (2022), the impact of foreign aerosols interacting with locally generated aerosols on climate, ecology, and health have been investigated (Z. Peshev et al., 2022). The research focuses on lidar observations conducted over Sofia city during Saharan dust events. It involves two types of measurements: vertical lidar sounding and quasi-horizontal lidar scanning for near-surface aerosol mapping. The study analyzes the temporal evolution of aerosol density and derives average profiles of backscattering coefficients at two lidar wavelengths. It also calculates the Ångström exponent to determine aerosol properties and altitude distribution. The research utilizes a combination of CALIPSO satellite lidar and sun-photometer data for vertical profiling and maps near-surface aerosols over a large urban area. The results highlight the effectiveness of an integrated approach involving lidar, radiometer, satellite data, and modeling for ecological monitoring of atmospheric aerosol pollution.

A study (Varga et al., 2021), provided a thorough analysis of Saharan dust storms reaching Iceland, encompassing their observation methods, synoptic patterns, and transportation routes. Over a 12-year period, the research identifies fifteen Saharan dust events, occurring at an average rate of approximately 1.25 events per year. The identification process incorporates the use of data from NASA's Terra satellite, backward trajectory modeling facilitated by the HYSPLIT model, and numerical forecasts from NASA's MERRA-2 and the Barcelona Supercomputing Center. It was found that, these dust episodes were linked to unique meridional atmospheric flow patterns driven by meandering jets. Strong winds transported large Saharan quartz particles (> 100 µm) to Iceland, confirming the atmospheric routes for Saharan dust to reach the Arctic. The study also revealed new northward meridional long-range transport of giant dust particles from the Sahara, including their deposition in Iceland, aligning with previous model predictions.

A paper (Yukhymchuk et al., 2022) focuses on the impact of climate change in regions that experience accelerated and intensified effects, known as "hot spots." One such hot spot is Cyprus, particularly Nicosia in the Mediterranean. The study analyzes significant changes in atmospheric aerosol characteristics during the year 2019 and an extreme event on April 25, 2019 (which is also investigated in the Case Study part of this thesis). The research investigates various aerosol properties, including aerosol optical thickness (AOT), and Ångström exponent, etc. To conduct this analysis, the study utilizes ground-based lidar data, sun-photometer observations from the AERONET Nicosia station, satellite data from the MODIS, and air movement back trajectories calculated using the Hybrid Single Particle Lagrangian Integrated Trajectory Model (HYSPLIT). The findings indicate that from April 23 to April 25, 2019, Nicosia experienced substantial aerosol pollution, with the AOT value exceeding 1.0 at a wavelength of 440 nm on April 25. Examination of optical and microphysical properties suggests that the pollution primarily consisted of Saharan dust and, to a lesser extent, urban aerosols. This conclusion is supported by HYSPLIT backward trajectories, which trace the origin of air masses containing dust particles from North Africa and Eastern Europe, as well as MODIS images.

In another study (Althaf et al., 2022), which is conducted in India, addresses the identification of dust emission hotspots, a critical factor in improving the forecasting of dust events using climate and air quality models. The analysis focuses on data derived from the OMI covering India from 2005 to 2018. Spatial autocorrelation techniques are applied for various seasons to conduct hotspot analysis of the AAI. The findings reveal substantial spatial and temporal variability in AAI observations. During the pre-monsoon season, hotspots are prevalent, extending from the Thar Desert to West Bengal, crossing the Indo Gangetic Plain (IGP) with varying intensities. Back trajectory analysis indicates the transportation of dust particles from arid western Indian deserts to the IGP during this period. Furthermore, the study conducts trend analysis of AAI in selected Indian cities during the pre-monsoon season using the Mann–Kendall test. The results highlight significant upward trends (0.02 yr-1) in AAI at Patna and downward trends (-0.01 yr-1) at Hyderabad. In contrast, other cities exhibit stable or minimal trends. The study also establishes a strong correlation between MERRA-2 Dust aerosol optical thickness and AAI, revealing decreasing trends at Nagpur (0.0005 yr-1) and increasing trends at Jaisalmer (0.004 yr-1). Additionally, a negative correlation between rainfall and AAI suggests that AAI decreases with higher levels of precipitation.

In Table 4, the summary of the studies conducted with Sentinel-5P data have been given.

Table 4. Summary of the literature review related to Sentinel-5P

Author	Year	Study Area	Topic
Lorente et al.	2019	Paris	Investigation of spatiotemporal distribution of NOx emissions
Kaplan et al.	2019	Türkiye	Investigation of the relationship between NO2 concentration and population density
Khoury et al. (El Khoury et al., 2019)	2019	Lebanon	Investigating the relationship between tropospheric NO2 and AOT over Lebanon using TROPOMI data
Kaplan & Avdan	2020	Republic of North Makedonia	Investigation of the relationship between NO2 and CO mean atmospheric column
Kaplan & Avdan	2020	Türkiye	Effects of COVID-19 on NO2
Judd et al.	2020	New York City and Long Island Sound	Comparison and validation of TROPOMI data with airborne mapping spectrometers and ground-based Pandora spectrometers
Roman-Gonzalez et al. (Roman-Gonzalez & Vargas-Cuentas, 2020)	2020	Peru	Investigating the variation of aerosol pollution in Peru during COVID-19 quarantine
Li et al.(Li et al., 2020)	2020	France, Germany, Italy, Spain	Investigating the importance of aerosols in determining the fatality of COVID-19
Behera et al.	2021	India	Effects of COVID-19 on NO2, SO2, HCHO, and AAI
Ghasempour et al.	2021	Türkiye	Investigation of the spatiotemporal change of NO2 and SO2 from TROPOMI and AOD from MODIS
Verhoelst et al.	2021	Global study	Comparison of NO2 data with different ground-based data

Ialongo et al.	2021	Russia	Evaluation of NOx and CH4 sourced from gas combustion and oil production
Savenets	2021	Ukraine	Investigation of spatial and seasonal distributions of NO2, SO2, and CO under the influence of local anthropogenic emissions
Behera et al. (Behera et al., 2022)	2021	India	Investigation of the improvement in air quality influenced by the COVID-19 slowdown using TROPOMI data
Prakash et al. (Prakash et al., 2021)	2021	India	Investigating the environmental effects of COVID-19 in India with TROPOMI data
Shikwambana et al. (Shikwambana et al., 2021)	2021	South Africa	Investigating the temporal changes in anthropogenic emissions during COVID-19 in South Africa
Shikwambana et al. (Shikwambana, 2021)	2021	Southern Africa	Observing the emissions of toxic gases and aerosols over the Southern Africa during 2019
Madkour	2022	Cairo (Egypt)	Effects of COVID-19 on NO2, SO2, and CO
Kumari et al.	2022	Dublin	Effects of COVID-19 on NO2 and air quality
Ganbat et al.	2022	Ulaanbaatar-Mongolia	Effects of COVID-19 on NO2, SO2, PM10, and PM2.5
Michailidis et al.	2022	Mediterranean Basin	Validation of ALH data of TROPOMI with ground based EARLINET lidars
Douros et al.	2022	Europe	Validation of NO2 data of TROPOMI with NO2 data of CAMS
Maurya et al. (Maurya et al., 2022)	2022	India	Spatio-temporal mapping of atmospherşic pollutants using TROPOMI data

Mazlan et al. (Mazlan et al., 2023)	2022	Malaysia	Investigating the effects of COVID-19 restriction on the emissions over Malaysia
Ouerghi et al. (Ouerghi et al., 2022)	2022	-	Detecting the methane plumes with time series of Sentinel-5P images
Morozova et al. (Morozova et al., 2022)	2022	Russia	Assessment of air quality of the largest cities of Russia with TROPOMI
Ganbat et al. (Ganbat et al., 2022)	2022	Mongolia	Assessment of the effects of COVID-19 in Mongolia by TROPOMI data
Taloor et al. (Taloor et al., 2022)	2022	India	Analysis of the air quality in India by geospatial technology during COVID-19
Mohite et al. (Mohite et al., 2022)	2022	India	A case study investigating the impact of lockdown on air quality with Sentinel-5P satellite
Godłowska et al.	2023	Poland	Investigation of the annual variability of Tropospheric Vertical Column data for NOx
Yilmaz et al.	2023	Türkiye	Investigation of the forest fires happened in Türkiye between July 2021 and August 2021
Halder et al. (Halder et al., 2023)	2023	India	Exploration of air pollutants by machine learning-based methods in country-level by using Sentinel-5P
Michailidis et al. (Michailidis et al., 2023)	2023	Mediterranean Region	Validation of ALH data from TROPOMI using EARLINET lidars
Nguyen et al. (Nguyen et al., 2023)	2023	Africa	Estimating the burned area per unit from the biomass burning using Sentinel-5P CO data

Garane et al. (Garane et al., 2023)	2023	Global study	Validation of the total column water vapor data from Sentinel-5P with AERONET measurements

3. DATA AND METHODOLOGY

In this section, the methodology that was used in the study will be explained with a detailed explanation of the study area, the data to be used, and the methods used to analyze the data. The flowchart of the methodology has been given in Figure 2.

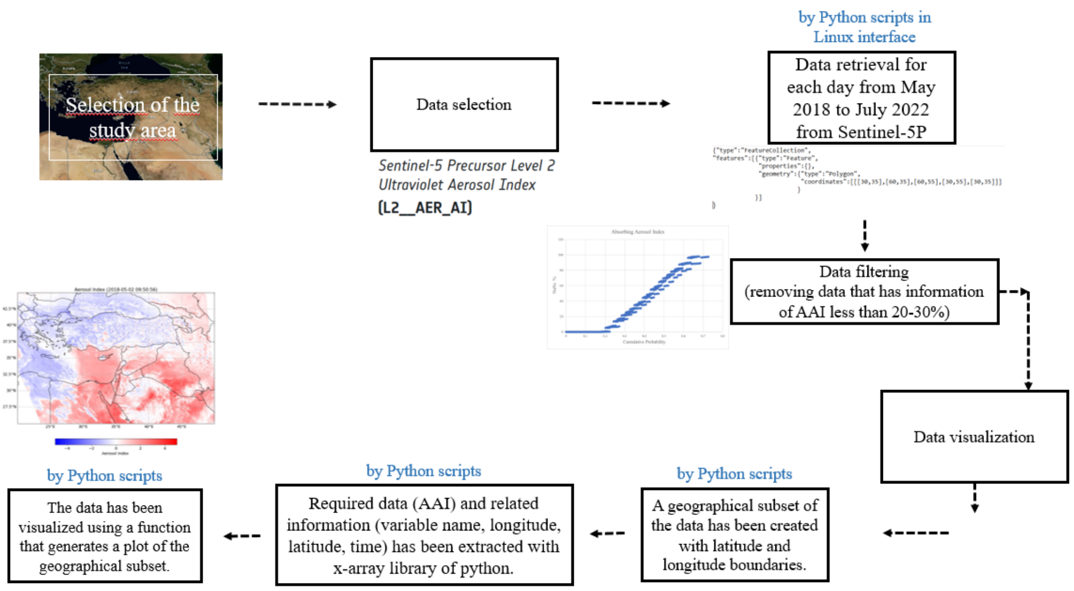

Figure 2. The flowchart of the methodology

First of all, the study area has been selected as Eastern Mediterranean Basin. After the selection of the study area, the data to be used in order to investigate the distribution of aerosols, has been selected. The data has been filtered by selecting a limit for Not a Number (NaN) values in the dataset. The data has been visualized periodically; daily, monthly, seasonal, and annually. Finally, the data has been analyzed by time series and Mann-Kendall test.

3.1. Study Area

The study domain is chosen as the Eastern Mediterranean Basin. The area consists of the countries around the Levantine Sea, which is the Eastern part of the Mediterranean Sea. These countries are Türkiye, Cyprus, the Greek Islands, Lebanon, Syria, Palestine, Israel, Jordan, and Egypt. The selected domain also includes the Northern Arabian Peninsula and Northern Africa. In Figure 3, a visual of the study area was created with the help of the worldwide interface of NASA (NASA, n.d.-e).

Eastern Mediterranean Basin is located in an area that makes it a crossroad for air masses, and it is mainly affected by mineral dust and many anthropogenic emissions. Mineral dust emissions may be sourced from deserts around this basin, such as African, Arabian, and Asian (Papachristopoulou et al., 2022). More than 50% of the global dust emissions are released from the Saharan Desert (Papachristopoulou et al., 2022). The Mediterranean Sea constantly releases marine aerosol emissions due to sea spray evaporation caused by the bursting of bubbles and wave production by the wind (Monahan et al., 1983). Burning of biomass and atmospheric transport of anthropogenically produced emissions are some of the aerosol sources in the Mediterranean basin (Georgoulias et al., 2016). These aerosol loads from several sources resulted in a sensitive area combined with cloud-free conditions and high-solar radiation intensity, especially in summertime (Lelieveld, Berresheim, Borrmann, Crutzen, Dentener, et al., 2002).

Figure 3. Eastern Mediterranean Basin (NASA, n.d.-e)

The area has high loads of aerosols sourced from the deserts of Africa and the Middle East, making it the most affected and vulnerable area in the world by climate change (Querol et al., 2009).

In this study, in addition to the Eastern Mediterranean Basin, the absorbing aerosol load of Türkiye, the Northern Arabian Peninsula, and Northern Africa were investigated separately. The aim of this approach is to observe the effects of aerosol load from the Southern part of the study domain on Türkiye.

Türkiye is a country located partly in Asia, partly in Europe, and in the Mediterranean region, with a unique geographic position, which makes it vulnerable to air pollution from various sources. The country is bordered by the Black Sea to the north, the Aegean Sea to the west, and the Mediterranean Sea to the south. It also shares borders with several countries, such as Syria, Iraq, and Iran, as shown in Figure 3. The aerosol load over Türkiye is influenced by natural sources, such as desert dust and sea salt and anthropogenic sources, such as urban pollution (Agacayak et al., 2015). In addition, desert dust from natural dust sources can be polluted in Türkiye by anthropogenic pollutants released into the atmosphere from anthropogenic sources (Aslanoğlu et al., 2022).

Northern Africa is bounded by the Red Sea in the East, the Atlantic Ocean in the West, and the Mediterranean Sea in the North. This area includes countries such as Egypt, Libya, Morocco, Tunisia, and the world's largest hot desert, the Sahara Desert. As can be seen in Figure 3, the area selected for this study includes only some parts of Egypt and Libya. Although the climate of the whole African continent is changing in the interior and coastal areas, and it mainly varies due to seasons, the most significant aerosol source of this region is desert dust (National Intelligence Council, 2009). The area is hot and very dry. Hot and dry winds with dust storms carry dust particles to the coastal regions, and during the wet seasons, these aerosols may be washed out from the atmosphere (Nations, 2000).

The Arabian Peninsula is located in the Southwest part of the Asia continent. The area is surrounded by the Red Sea on the West, the Persian Gulf on the northeast, the Arabian Sea and the Gulf of Aden on the south. This area includes some countries such as Saudi Arabia, Yemen, Oman, the United Arab Emirates, Qatar, Bahrain, and significant deserts. As can be seen in Figure 3, the area selected for this study (The Northern Arabian Peninsula) includes Syria, Lebanon, Jordan, Iraq, Kuwait, and Northern parts of Saudi Arabia. The main property of this area is its arid semiarid nature, which assists frequently occurring sandstorms to produce fine particles and aerosols. Aerosols, which are released to the atmosphere by the sandstorms occurring mainly in the cold months, are essential in this area due to their ability to alter the earth's radiation balance (Farahat, 2016).

Since both The Northern Arabian Peninsula and Northern Africa cover large areas of the earth, and these both contain the world's largest deserts, the aerosol load in These areas must be carefully investigated.

The specific coordinates for the mentioned study domains were determined in Table 5.

Table 5. Details of the study area

Area	Coordinates [(Lat_{min}, Lat_{max}), (Lon_{min}, Lon_{max})]
The Eastern Mediterranean Basin (Domain 1)	[(25, 45), (20, 50)]
Türkiye (Domain 2)	[(36, 42), (25, 45)]
The Northern Africa (Domain 3)	[(25, 35), (20, 35)]
The Northern Arabian Peninsula (Domain 4)	[(25, 35), (35, 50)]

These domains can be seen in Figure 4.

Figure 4. Study domains

Domain 1 covers the whole area selected for the Eastern Mediterranean Basin. Domain 2 represents the exact location of Türkiye, and Domain 3 and Domain 4 are the southern domains, Northern Africa, and Northern Arabian Peninsula, respectively.

These domains will be analyzed separately and then compared to each other. The results will be in the “Results and Discussion” part of the thesis.

3.2. Data

In this thesis, the data to be used is the Ultraviolet Aerosol Index (UVAI) product of the Sentinel-5P satellite. This satellite carries a spectrometer called Tropospheric Monitoring Instrument (TROPOMI). TROPOMI measures species such as O_3, SO_2, NO_2, CH_2O, CO, cloud, and aerosol distribution at a range of wavelengths which are 340-380 nm, 354-388 nm, and since 2022, 335-367 nm (Stein Zweers, 2022). Within these various types of observation data, the Level-2 Reprocessing Aerosol Index ("S5P_RPRO_L2__AER_AI") data of Sentinel-5P is used in this thesis. While retrieving the satellite data, the Level-3 Absorbing Aerosol Index (AAI), which gives information about the presence of absorbing aerosols such as black carbon and dust, is automatically produced from the Level-2 AER_AI product.

The Absorbing Aerosol Index, which reflects the presence of absorbing aerosols such as dust, is obtained when the residual value between modelled and observed reflectance is positive and is unitless (Apituley et al., 2021). The negative residual value, the Scattering Aerosol Index (SAI), indicates the presence of scattering aerosols such as sulfate, nitrate, and sea salt (Penner, 2022). The reason for using the mentioned wavelengths (340-380 nm and 354-388 nm) is to continue the measurements of the Ozone Monitoring Device (OMI) and GOME-2, which use the same wavelengths in their measurements. The wavelength pairs used by satellites can be seen in Table 6.

Table 6. Satellite Instruments and Their Wavelength Pairs, directly taken from the official documents of Sentinel-5P (Stein Zweers, 2022)

Instrument / Platform	Wavelength Pair (nm)	Years of Available Data
TOMS / Nimbus-7	340 / 380	1978 – 1993
GOME / ERS-2	340 / 380	1995 – 2003
TOMS / Earth Probe	331 / 360	2002 – 2012
SCIAMACHY / Envisat	340 / 380	2002 – 2012
OMI / Aura	354 / 388	2004 – present
GOME-2 / MetOp	340 / 380	2007 – present
OMPS / Suomi NPP	336 / 377	2012 – present
TROPOMI / S5-P	340 / 380; 354 / 388	2018 – present
TROPOMI / S5-P	335 / 367	2022 – present

The calculation of the Aerosol Index depends on the differences in the Rayleigh scattering according to the changes in the wavelength where the absorption of ozone is relatively small. The advantage of TROPOMI is that it can calculate the Absorbing Aerosol Index value when even the clouds are present in the atmosphere. However, the effect of the sun glint on the measurements of UVAI needs to be more accurate in the analyses. So, to ensure that situation while processing this data, qa_values above 0.8 should be removed from the dataset (Stein Zweers, 2022).

In the equations below, the simplest version of the equations, which are used to calculate the aerosol index, are given.

The general expression of the aerosol index (Stein Zweers, 2022) is shown in Equation 1.

$$AI = 100\,.\log_{10}\left(\frac{Rmeas(\lambda_2)Rcalc(\lambda_1, ALER(\lambda_1))}{Rmeas(\lambda_1)Rcalc(\lambda_2, ALER(\lambda_2))}\right) \qquad \text{Equation 1}$$

Where;

AI: Aerosol Index

R_{meas}: Measured reflectance

R_{calc}: Calculated reflectance

A_{LER}: The actual surface albedo (if there are no clouds or aerosol present)

λ_1, λ_2: Two wavelengths measured at two different wavelengths

In Equation 2 and Equation 3, two assumptions made are explained. The first assumption (Equation 2) is that the surface albedos are equal (Stein Zweers, 2022). The second one (Equation 3) represents the setting of the reference wavelength, which is the longer one (Stein Zweers, 2022).

$$ALER\ (\lambda_1) = ALER\ (\lambda_2) \qquad \text{Equation 2}$$

$$Rmeas(\lambda_2) = Rcalc(\lambda_2, ALER(\lambda_2)) \qquad \text{Equation 3}$$

After these assumptions, the general expression of the aerosol index equation (Equation 1) can be rewritten as in Equation 4.

$$AI = 100\,.\log_{10}\left(\frac{Rcalc(\lambda_1, ALER(\lambda_2))}{Rmeas(\lambda_1)}\right) \qquad \text{Equation 4}$$

The explained calculation is used when assuming equal surface albedo for the two wavelengths, λ_1 and λ_2.

Sentinel-5P satellite has three types of data processing; Offline (OFFL), Reprocessing (RPRO), and Near Real Time (NRT) (ESA, n.d.-b). Since the retrospective data (2018-2022) is analyzed in this thesis, the Offline (OFFL) data is suitable for the analyses. However, the satellite data was updated, and the processing quality was upgraded in July 2021 (ESA, n.d.-j). The updated Offline (OFFL) data is now available under the category of Reprocessing (RPRO) data. The content of the updated Reprocessing data consists of the following changes: The cloud properties which are affected by the snow and ice conditions were improved, the surface temperature parameter was added to all data products, and for the AAI product, a degradation correction in the irradiance is included (ESA, n.d.-j). After these improvements, in a study in which the improved NO2 satellite data was compared with the old version, the data was found to be more similar to data from the OMI instrument of the Aura satellite (Behera et al., 2021).

In order to observe the difference between the two versions, datasets have been compared, and the results can be seen in the below figures (Figure 5 and Figure 6).

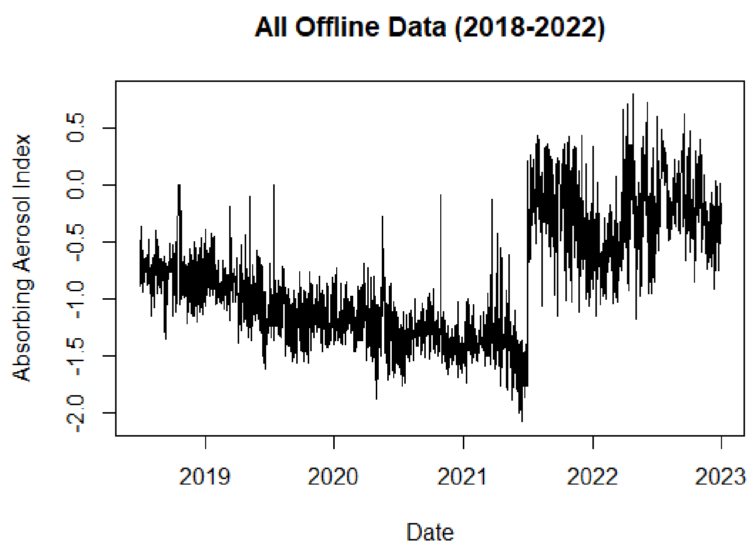

Figure 5. Time series representation of the offline AAI data of Sentinel-5P (2018-2022)

Figure 5 shows an abnormal increase in the Absorbing Aerosol Index value occurred in the middle of 2021. The version update causes this increase.

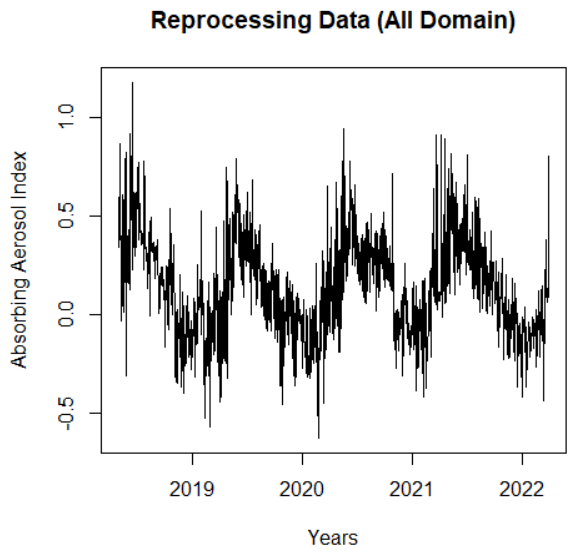

Figure 6.Time series representation of the reprocessing AAI data of Sentinel-5P (2018-2022)

In Figure 6, using Reprocessing data, the range of data has changed from [-2,0.5] to [-1,1], and the graph seems more logical. These time series graphs were created with a script written in R language.

Figure 7 shows the decomposition of the Offline data from 2018 to 2022 for all the selected study areas. It can be seen that the seasons are not observed, and there is no trend to be determined.

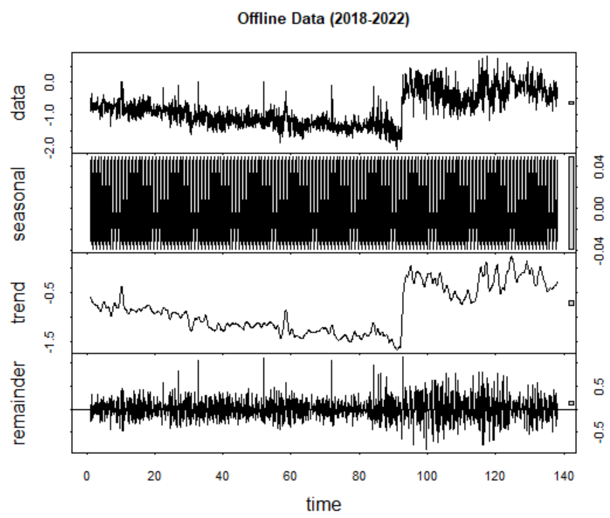

Figure 7. Decomposition of the offline AAI data of Sentinel-5P (2018-2022)

In Figure 8, the trends can be seen clearly with the updated Reprocessing data.

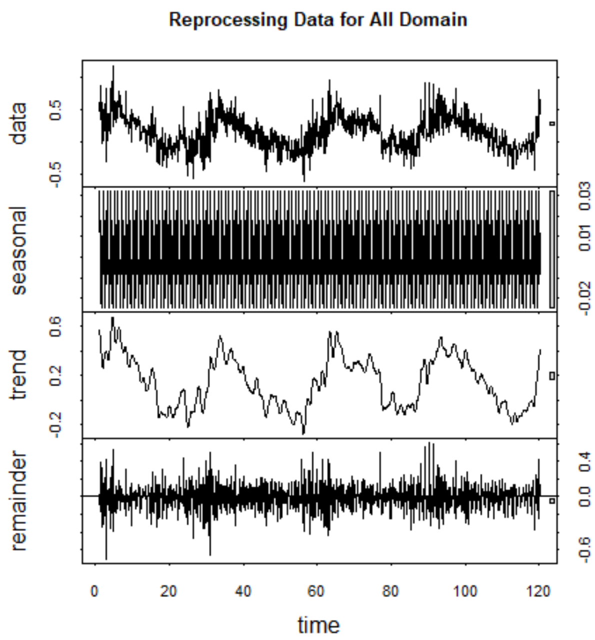

Figure 8. Decomposition of the reprocessing AAI data of Sentinel-5P (2018-2022)

3.2.1. Data Retrieval

The Sentinel-5P data is available as an open source in the URL: “https://scihub.copernicus.eu/”. Four years of data (from 30/04/2018 to 01/08/2022) is obtained with the help of scripts (Omrani, n.d.) that are prepared with the Python programming language. Linux (Ubuntu), an open-source Unix-like operating system, is used to obtain the necessary data. The script needs a file in Python language (“.py”) to execute, the name of the product (AER_AI), a domain (which should be created and presented in the form of a “. JSON” file), and a time interval for the data to be downloaded. With the help of the mentioned script, Level-2 (L2) data of Ultraviolet Aerosol Index (AER_AI) for the requested day and domain is downloaded, and right after, this data is automatically processed and converted to Level-3 (L3) data of Absorbing Aerosol Index (AAI). This conversation makes it possible to extract the pixels with a qa_value below 75%. The result of this extraction is obtaining cloud-free and nominal L3 data.

From Level 2-Ultraviolet Aerosol Index to Level-3 Absorbing Aerosol Index conversion is automatically being made by special Python libraries. The most important amongst them is the “harp” library. Harp library is frequently used to read, process, and inter-compare satellite data as well as model and ground-based data (ESA, n.d.-f). It helps to re-grid the data so that it can be compared to another dataset with another type of gridding (ESA, n.d.-n).

A file in JSON (JavaScript Object Notation) format has been generated for the domain selection. The overall study domain which will be retrieved can be seen in Figure 3.

An appropriate JSON file that was created so that the coordinates cover the whole area can be seen in Figure 9.

```
{"type":"FeatureCollection",
"features":[{"type":"Feature",
             "properties":{},
             "geometry":{"type":"Polygon",
                         "coordinates":[[[30,35],[60,35],[60,55],[30,55],[30,35]]]
                        }
            }]
}
```

Figure 9. Screenshot of the JSON file

The data is prepared in Network Common Data Form (netCDF) format by TROPOMI, a file format that can store array-oriented multidimensional data, for example, dimensions, variables, and attributes (National Snow and Ice Data Center, n.d.). For example, in this study, such data will explain the spatial and temporal variation of the absorption aerosol index variable.

Each S5P Reprocessing Level-2 data occupies approximately 130 MB per data. There are 3 to 5 data are available for each day. Immediately after this data is received, S5P Reprocessing Level-3 data is generated, occupying approximately 280 MB per data. For L3, two netCDF files are available per day that do not contain 100% NaN for this area. One of these data is chosen according to the graph (Figure 10) explained in the “Data Selection” part of this section.

3.2.2. Data Analysis

In the explanations below, all analyses performed for domains after data retrieval are explained step-by-step.

- **Data Filtering**

Firstly, the data were analyzed according to their NaN values. A Python script calculates the NaN percent, maximum, mean, minimum, median, standard deviation, 0.5-0.75-0.90-0.99-0.999th percentiles, and their cumulative probability distribution was prepared. When the script is run, these calculations are made and saved into a file in Comma-Separated Value (.csv) format. The data in this CSV file was converted to an Excel format, and a graph was prepared to visualize cumulative probability distribution as in Figure 10.

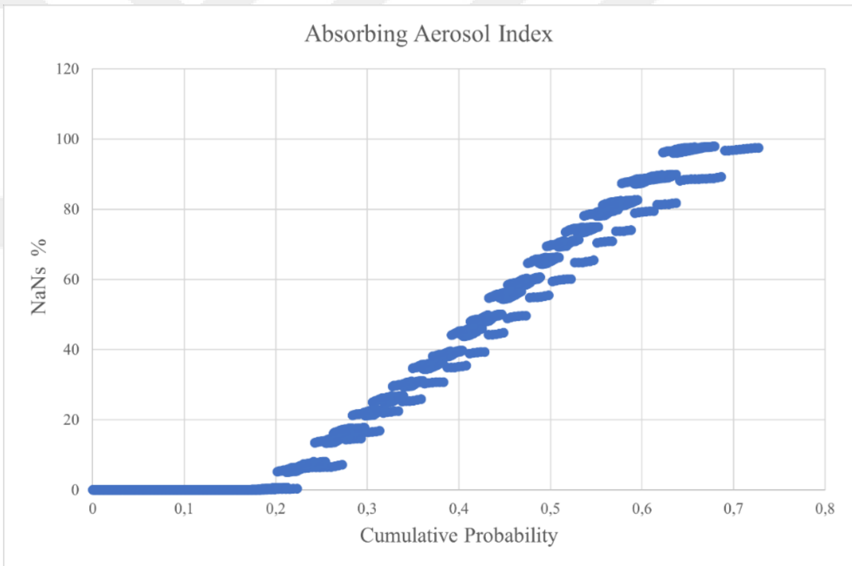

Figure 10. Cumulative probability distribution of the whole data

Figure 10 shows the cumulative probability distribution of the whole data from 2018 to 2022. Since the graph was prepared before the NaN separation, there is repeating data in the dataset, which does not reflect reality. This graph shows that 55-60% of the data, which contains a maximum of 20-30% NaN, is suitable for the analyses. The reason for selecting a range rather than a specific value is that if a specific value of 20% NaN value is selected, there will not be a daily dataset because some critical part of the dataset contains NaN values between 20-30%.

The Sentinel-5P satellite overlaps in approximately the exact location four times a day. Half of these overlap contains 100% NaN values in the selected location for this study. According to the determined NaN value, the data is separated into two as; accepted (equal and/or below 20-30% NaN) and rejected (higher than 20-30% NaN) data. Then it was categorized by years, months, and seasons. After the classification of data and filtering of the NaN values, the mean of the daily data has been used in creating time series graphs.

It is worth mentioning that this script also has a modifiable coordinates section. The explained process is repeated for other domains, which is explained in Table 5.

- **Data Visualization**

The L3-AAI data were visualized with a script created with Python programming language. Due to the geometry of the satellite orbit, some of the data had 100% NaN (Not a Number) values. With another script created with Python programming language, the NaN percentages in the whole data are calculated, and data with is separated into two as accepted and rejected data. 100% of NaN values were extracted from the data to be used in the analyses. After the extraction, the script for the visualization has been modified. The colour scale has been chosen to accurately reflect the difference between absorbing and scattering aerosols in the selected domain. The minimum and maximum number on the visualization legend has been selected with respect to the maximum and minimum values observed within the selected area. Coordinates are set in the script to be changed as desired. Thus, any region within the study area, such as Türkiye or the Northern Africa region, can be visualized. In the time series analysis part, when extreme values were observed, these images help to see what happened on that specific day, month, year, or season.

The data contains four years of AAI information. Over these four years, some periods have been determined to analyze the changes in Absorbing Aerosol Index over time. These are monthly, annual, and seasonal periods. Data were grouped by month for seasonal analysis, and new monthly netCDF files were created. For example, the netCDF file of January contains the data of all January months from 2019 to 2022. This process is repeated for all months, and one single image (Figure 20) was created from these netCDF files for all the months which are in the studied period.

Since the whole study area is coincided in Northern Hemisphere, in normal conditions, it is expected to observe low values in winter months, close to low values in autumn months, close to high values in spring, and high values in summer months. As expected, the images of the Sentinel-5P satellite data reflect normal conditions for meteorological seasons in Northern Hemisphere for AAI data.

Therefore, the meteorological seasons and the corresponding months can be seen in Table 7.

Table 7. Meteorological seasons applied in the analyses for Northern Hemisphere (National Centers for Environmental Information, n.d.)

Seasons	**Months**
Winter	1 December-28 or 29 February
Spring	1 March-31 May
Summer	1 June-31 August
Autumn	1 September-30 November

After the season determination, all the seasons have been visualized as in "Results and Discussion". The data was visualized in different periods: monthly, annually, seasonally, and daily. This process is repeated for all months, seasons, and years between 2018 and 2022.

- **Trend Decomposition and Time Series Analysis**

Time series analyses visualize a dataset mainly using time as an independent variable (Educba, n.d.). This kind of analysis allows for making future predictions about the data, which is the subject of the analysis (Tableau, n.d.). In order to understand the trends of this time series dataset, data must be decomposed to its trends, seasonality, and remainders (Hyndman & Athanasopoulos, n.d.). Since the dataset used in this study consists of data obtained at approximately the same time with regular periods, the time series analysis and decomposition were helpful in understanding and interpreting the data.

For the purpose of analyzing trends in annual data collected from satellite retrievals, the Mann-Kendall test is employed. This test is utilized due to the fact that environmental data often deviate from a normal distribution. Given this characteristic, the Mann-Kendall nonparametric approach, which involves a monotonic regression analysis, becomes suitable for application. The analysis involves comparing discrepancies between posterior and prior data. This technique yields pairs equal to $n(n-1)/2$. Notably, missing values don't present obstacles and are permissible. The test operates under the assumption of data independence, as well as the consistency of data distribution whether in its initial units or after transformation. This adaptability allows for the test's application in various scenarios. The test statistic, represented by the sum of integers denoted as S, is computed as in Equation 5.

$$S = \sum_{i=1}^{n+1} \sum_{j=i+1}^{n} (y_j - y_i)$$

Equation 5

Where;

n: Total observation count

S: Slope

$y_{j,}$: Prior data

y_i: Posterior data

In this context, where j represents posterior data and i represents prior data, the calculated value of S falls within the range of (-1) to (+1). A small absolute value of S implies the absence of a discernible trend. A positive S value nearing (+1) indicates the detection of an increasing trend, whereas a negative S value approaching (-1) suggests the identification of a decreasing trend. The computation of the test statistic Tau (T) is achieved through the formula in Equation 6.

$$\mathrm{T} = \frac{S}{\frac{n(n-1)}{2}}$$

Equation 6

Where;

n: Total number of observations

S: Test statistics

T: Correlation coefficient (Tau statistics)

The correlation coefficient T shares a comparable range with the S parameter, spanning from (-1) to (+1). The null hypothesis, which implies the absence of a trend, is refuted when the absolute values of both S and T deviate from zero. The Sen slope estimator, which determines the rate of trend alteration, can be computed according to the subsequent formula (Helsel et al., 2020) in Equation 7.

$$Q = median(\frac{y_j - y_i}{x_j - x_i})$$

Equation 7

Where;

Q: Sen’s slope estimator

y_j, y_i, x_j, x_i: Calculated slope values

For each combination of i and j where i < j, the Sen's slope estimator is determined by taking the median of all previously computed slope values (S) for these data pairs. Additionally, Z-scores are computed using the variances of each S value, and this process is outlined as in equations below.

$$S > 0 \rightarrow Z = \frac{S-1}{\sqrt{Var(S)}}$$

Equation 8

$$S = 0 \rightarrow Z = 0$$

Equation 9

$$S < 0 \rightarrow Z = \frac{S+1}{\sqrt{Var(S)}}$$

Equation 10

Where;

Z: Standard Z-score

S: Slope

The final decision is reached by considering Z-scores, the Q value, and statistical significance within the 95% confidence interval.

After conducting the time series analysis, the data is analyzed with Seasonal-Trend Decomposition using Loess (STL). This method decomposes time series data into seasonal, trend, and irregular components using locally estimated scatterplot smoothing (loess) (Robert B Cleveland et al., 1990).

The decomposition was obtained with a script written in R language. In this script, the "stl" package was used. The seasonal sub-series is smoothed using the loess method to identify the seasonal component. If "periodic" is set for an argument, the mentioned smoothing is substituted by the mean. The remaining values are smoothed after removing the seasonal values to determine the trend. The seasonal component's overall level is eliminated and transferred to the trend component. This method is repeated multiple times. The residual component is the difference between the seasonal plus, trend fit and the original data (DataCamp, n.d.). These steps collectively transform the original time-series data into its constituent parts: seasonal cycle, trend-cycle, and residuals, as illustrated in below.

$$Yt = St + Tt + Rt$$

Equation 11

Where;

Y_t: Time-series data

S_t: Seasonal cycle

T_t: Trend cycle

R_t: Residuals

The summary of the analyses is explained below.

- After the decomposition of the data, statistical summary tables, which include maximum, mean, minimum, median, standard deviation, 0.5-0.75-0.90-0.99-0.999th percentiles, and their cumulative probability distribution information of the daily data.
- Boxplots, which give visual information about the statistics of the dataset and present the outliers of data, was prepared for months, seasons, and years.
- The dataset is arranged for the time series analyses. Monthly, annual, and seasonal graphs which reflect the time-wise change in the Absorbing Aerosol Index have been prepared.
- Four years of data were compared annually, and changes have been observed.

- Same months and same seasons for different years have been compared.
- Overall changes in the Absorbing Aerosol Index from 2018 to 2022 have been calculated in percentages and interpreted.
- Specific cases related to absorbing aerosols were investigated with the help of the Sentinel-5P AAI data.

The results of all these analyses are presented in the following section, “RESULTS AND DISCUSSION”.

4. RESULTS AND DISCUSSION

The result and discussion section of the study represents the research findings, including the spatial and temporal variability of the aerosol index in specified regions over time. In the first part of this section, the findings for the Eastern Mediterranean Basin is explained. This region is investigated monthly and seasonally with data visualization, boxplots, and time-series. Similarly, a smaller domain, Türkiye is investigated monthly and seasonally with data visualization, boxplots, and time-series. These spatial and temporal variability of AAI in these regions are observed. For the investigation of the southern domains, which are explained in the third part of this section, data visualization, boxplots, and time series are used as well. In the investigation of all domains, the data is decomposed to its seasonal, trend, and remainder components.

Before getting in detail about these regions, the summary statistics of four years of Sentinel-5P L3-AAI data for all domains are represented in Table 8. The summary statistics are composed of the mean, standard deviation, maximum, minimum, and median values of the entire dataset.

Table 8. Summary statistics of four years of Sentinel-5P L3-AAI data

Domain	Season*	Mean ± STD	Maximum	Minimum	Median
EMB	Winter (DJF)	-0.08629 ± 0.14598	0.52871	-0.62862	-0,08298
	Spring (MAM)	0.25864 ± 0.28698	1.02823	-0.45237	0,22697
	Summer (JJA)	0.35507 ± 0.17094	1.18098	-0.02235	0,34073
	Autumn (SON)	0.08826 ± 0.17812	0.71550	-0.45574	0,09002
Türkiye	Winter (DJF)	-0.43161 ± 0.23205	0.23761	-0.89736	-0,44621
	Spring (MAM)	-0.26613 ± 0.38681	1.05347	-1.13479	-0,28586
	Summer (JJA)	-0.16789 ± 0.29796	0.52111	-1.07956	-0,17385
	Autumn (SON)	-0.15793 ± 0.32292	1.24865	-0.96003	-0,11851
NA	Winter (DJF)	0.09965 ± 0.18994	0.89773	-0.36979	0,00000
	Spring (MAM)	0.35619 ± 0.49748	1.91926	0.00000	0,00000
	Summer (JJA)	0.37885 ± 0.49713	2.07013	0.00000	0,00000
	Autumn (SON)	0.18510 ±0.30771	2.01061	-0.29634	0,00000
NAP	Winter (DJF)	0.07053 ± 0.21359	0.88614	-0.61822	0,00000
	Spring (MAM)	0.36425 ± 0.49805	1.74593	-0.29078	0,00000
	Summer (JJA)	0.39686 ± 0.51060	1.55671	0.00000	0,00000
	Autumn (SON)	0.17483 ± 0.29912	0.90468	-0.52897	0,00000

*DJF (December-January-February), MAM (March-April-May), JJA (June, July, August), SON (September-October-November)

As can be seen in Table 8, the mean value of the AAI for all domains shows different patterns in winter, spring, summer, and autumn seasons. For the winter season, the mean value of AAI is very close to zero, in Eastern Mediterranean Basin. This means that, in winter, the absorbing aerosols in EMB are low, and there are scattering aerosols observed. However, in Türkiye, the mean value of AAI is negative for the whole study domain, in fact, lower than in EMB as expected. Compared to EMB domain, Türkiye does not contain deserts that may contribute to increase of absorbing aerosols. Similar to EMB, for the southern domains (Northern Arabian Peninsula and Northern Africa), the mean value of AAI is higher than in Türkiye. The reason is that most of the hot desserts are located in these two regions. The continuous dust release increases the absorbing aerosols, even in winter season. The same pattern applies for other seasons (spring, summer, and autumn) as well: The mean AAI value sorted from highest to lowest is Northern Arabian Peninsula, Northern Africa, Eastern Mediterranean Basin, and Türkiye, respectively. The reason behind, Türkiye having the lowest mean value of AAI among these domains is that this country does not have a single climate pattern due to its geographical conditions. The hot and cold days are happening at their extreme in Türkiye. So, the average representative reflects lower absorbing aerosols compared to whole EMB. Additionally, the reason for median values to be zero for the Northern Africa and the Northern Arabian Peninsula is that, while extracting the data for these domains, it was seen that there are lots of NaN values.

Table 8 shows the qualitative variability of the AAI value over these regions. However, in order to have a logical point of view about the variation of the AAI data, the location and time period, meaning where and when the change in the AAI happens, should be precisely known. Therefore, separation of the study area according to their own characteristics and visualizing the data with a preset script suitable for the distinction of AAI, is very useful. In the following sections, the AAI data obtained from Sentinel-5P satellite is examined through the maps, boxplots, and statistical summaries created for all domains.

4.1.Eastern Mediterranean Basin (EMB)

The Eastern Mediterranean Basin is a region that has experienced significant increases in aerosol load in recent years (Öztürk et al., 2012). Factors contributing to the increase in aerosol load in the region include desertification, increased urbanization and industrialization, and the use of biomass for energy (Andreae & Crutzen, 1997). This has resulted in degraded air quality, reduced visibility, and negative impacts on agriculture and water resources.

In this study, the period was selected as four years between May of 2018 and July of 2022. For these years, the daily Level-3 Absorbing Aerosol Index data obtained for Eastern Mediterranean Basin from the Sentinel-5P satellite was visualized as in Figure 11. The range of AAI value in the legend has been arranged according to the minimum and maximum values observed during the studied time period, which is between -0.6 and 1.

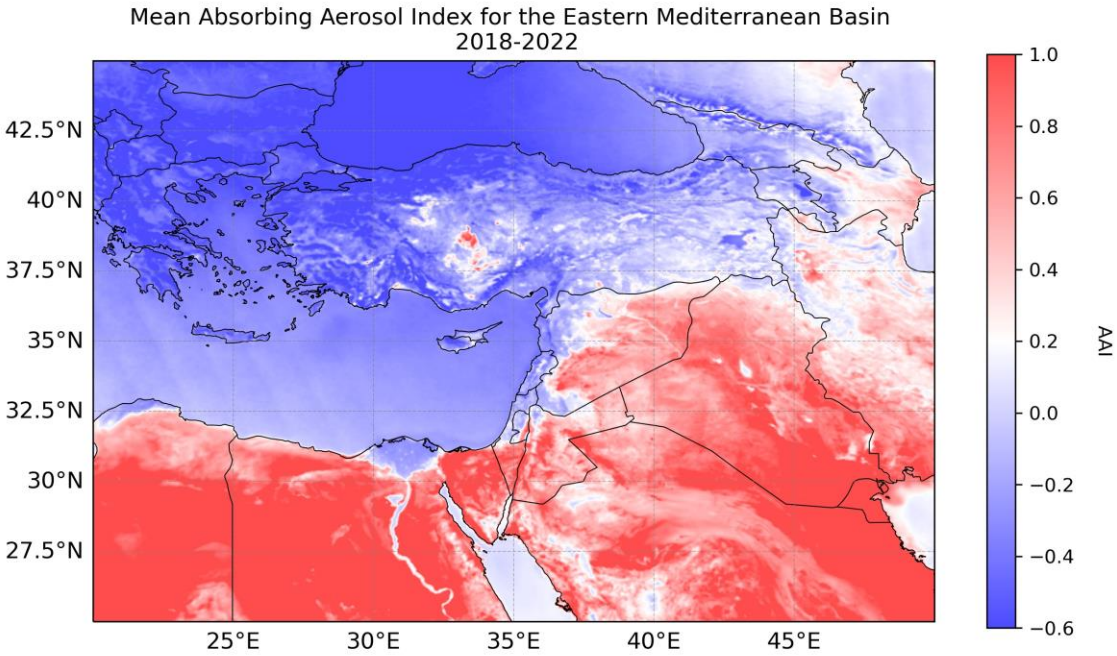

Figure 11. Mean AAI distribution between 2018 and 2022 for Eastern Mediterranean Basin

In this figure, it was seen that over the four years, the southern part of the selected region has a high load of Absorbing Aerosol Index due to the deserts that it contains. In Türkiye, Lake Tuz itself and its surroundings also have a high Absorbing Aerosol Index intensity. The remaining parts of the country are more likely to have scattering aerosols in their atmosphere, except for the south-east. After creating this visual, it was seen that the separation of the study area was logical since all the divided areas have their own specific climatic oscillations.

Table 9 shows the statistical summary of the Absorbing Aerosol Index for the years 2018, 2019, 2020, 2021, and 2022 for the Eastern Mediterranean Basin. This summary includes information of minimum, maximum, median, mean, and standard deviation of the dataset.

Table 9. Statistical summary tables for the Eastern Mediterranean Basin for all study years

Years*	Minimum	Median	Mean	Maximum	Standard Deviation
2018	-0.39955	0.243341	0.227779	1.180982	0.279542
2019	-0.57204	0.074001	0.108978	0.792733	0.237614
2020	-0.62862	0.147036	0.146077	0.946992	0.259902
2021	-0.41778	0.151576	0.171996	0.914141	0.24706
2022	-0.43937	0.089569	0.175259	1.028225	0.327533

*For years 2018 and 2022, the Reprocessing data was not available for the whole year during the conduction of this study. For 2018, the data is available from May to the end of December; and for 2022, the data was available from January to the end of July.

By looking at Table 9, it can be said that the mean value for Absorbing Aerosol Index for the Eastern Mediterranean Basin decreased by 23.05% over the four years. However, increases and decreases have been observed during these four years. Similarly, decreases have been observed for minimum, maximum, and median values by 9.96%, 12.93%, and 63.19%, respectively. However, the standard deviation of the dataset has increased by 17.16% over the four years, which indicates an increase in the variability of the dataset. This shows that the extreme days which are different than the normal conditions occur often in the study area and the time period. Since the study area contains large deserts, the extreme conditions may be created by the dust releases sourced from these deserts. The overall decrease in the mean AAI value may be caused by the increase of the usage of clean energy instead of using fossil fuels. Burning of fossil fuels leads to an increase in the AAI values due to the release of some compounds such as Sulphur, organics, and black carbon, which are absorbing aerosols (IPCC, 2007). According to some studies (CREA, 2021) (Ritchie et al., 2022), the use of fossil fuel has started to decline starting from the years 2000 due to switching renewable energy to increase air quality and at the year 2020 due to the Covid-19 pandemic (CREA, 2023). The decrease in the use of fossil fuels leads to a parallel decrease in the release of compounds such as NO_2, PM, and O_3 (CREA, 2021). The type of fossil fuels which have decreased are oil, gas, and coal (Ritchie et al., 2022). When the annual statistical summary on Table 9 is considered, the low AAI in 2020 compared to the following years can be seen. The decrease in the mean value of AAI in 2020 may be related to the decrease in the usage of oil as a fossil fuel source in that year. Additionally, in year 2020, there was a temperature anomaly has been observed as can be seen in Figure 12 (Statista, n.d.) (NASA, n.d.-c).

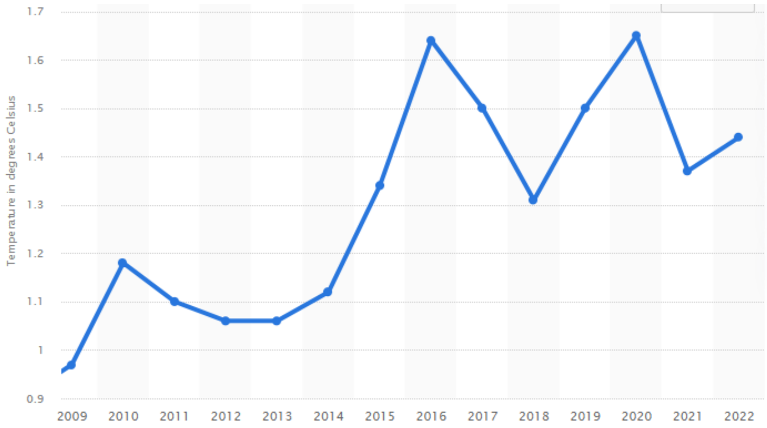

Figure 12. Annual anomalies in global land surface temperature from 2009 to 2022 (Statista, n.d.)

The statistical summary results may not reflect logical situation about all the locations on the study area. As mentioned before, in the "Study Area" part of the "Data and Methodology" section of this thesis, the study area consists of three different regions that have three different climatic behaviors. These are Türkiye, Northern parts of Africa, and Northern parts of Arabian Peninsula. To put the variation of absorbing aerosols in a logical framework, the mentioned regions will be investigated separately in the following parts of this section.

Figure 13 represents the annual boxplots for Absorbing Aerosol Index data of the Eastern Mediterranean Basin from 2018 to 2022.

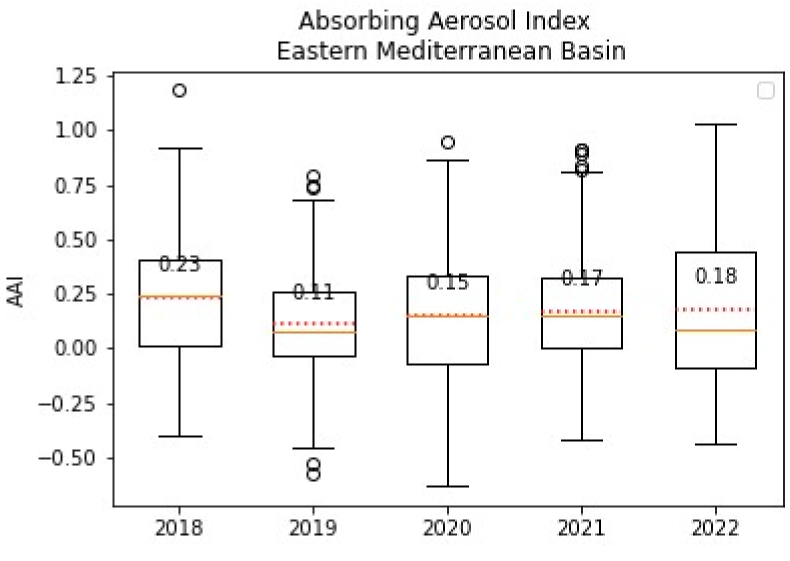

Figure 13. Annual boxplots of AAI for the Eastern Mediterranean Basin (from 2018 to 2022)

Boxplots are used in order to display the data in a standardized way. The box shows the Interquartile Range (IQR), limited by the 25th quartile below and the 75th quartile above the box. The straight line within the box represents the median value, the dashed line shows the mean value, and the length of the box shows how much the data varies. Whiskers are the minimum and maximum values of the dataset. Lastly, the dots around the whiskers are the outlier values appearing in the dataset.

In Figure 13, it can be seen that the amount of outliers is small except for year 2021. The values of outliers are similar to each other. The high amount of outliers in 2021 can be explained by the big forest fires started in and spread from Manavgat Province, in Türkiye. These Eastern Mediterranean Basin has been influenced by these fires. All the outliers for years 2018, 2020, and 2021 are bigger than the mean of the dataset, different than 2019 which has data smaller than mean values. There are no outliers in year 2022. The mean value is greater than median value in year 2019, 2021, and 2022, which indicates a positively skewness in the dataset. The box is smallest in 2019, and biggest in 2022. This means that the dataset of 2022 varies the most, and on the contrary, the dataset varies the less in 2019 over the four years. In Table 9, it was seen that the standard deviation of these two years was the smallest (2019) and the greatest (2022). These two statistical indicators are compatible with each other.

In Figure 14, the temporal variation of the Absorbing Aerosol Index can be seen clearly. The dates on the x-axis start in the May of 2018 and end in the July of 2022. With this information, the seasons can be specified in the graph. The variation of AAI is compatible with meteorological seasons.

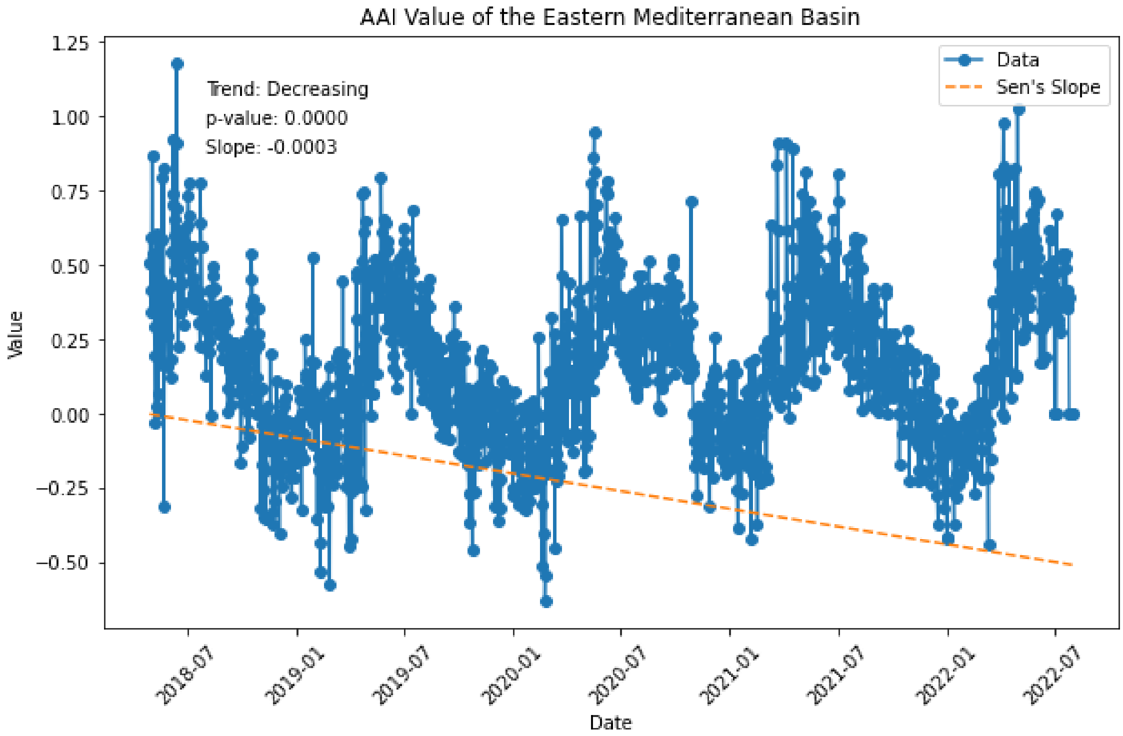

Figure 14. Daily Mean Absorbing Aerosol Index Value for the Eastern Mediterranean Basin (2018-2022)

The trend of the whole AAI data from May 2018 to July 2022 in the Eastern Mediterranean Basin is decreasing trend with a slope of -0.003, as showed in Figure 14. As mentioned before, the reason for the decrease may be caused by the decrease in the use of fossil fuels. Additionally, the policy and mitigation strategies in order to increase air quality may affect the creation of anthropogenic absorbing aerosols.

According to a study conducted by Urdiales Flores et al. (Urdiales-Flores et al., 2023), in the Mediterranean Basin, there are two additional factors that affect the fast increase in the temperature. One is the decrease in aerosols, and the other is a decrease in soil moisture near the surface of the Earth. These two factors, along with the human-made greenhouse gases, are causing the warming to speed up in this specific region. The decreasing trend of the AAI value observed in Figure 14, which was obtained from the Sentinel-5P satellite, supports this hypothesis.

As can be seen in the graph in Figure 14, there are outliers in the dataset, meaning there have been extreme days (negatively and positively) during the four years. These may be dust releases which are intense than normal, or fires happened in the Mediterranean coast which occur often. In section 4.4 of this thesis, which is the Case Studies part, some of these extreme episodes are examined in detail.

In Figure 15, the data is decomposed into its components: seasonal, trend, and remainders.

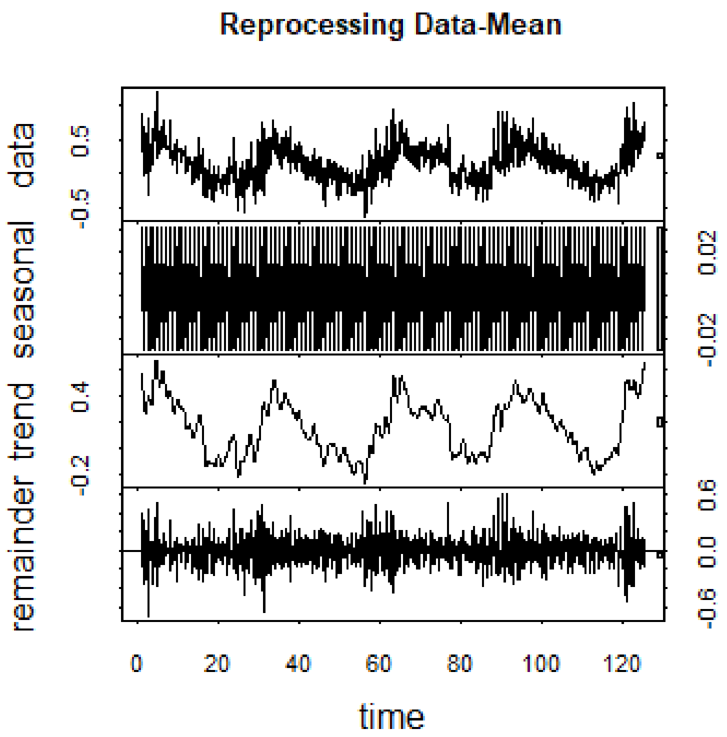

Figure 15. Decomposition of the mean AAI of EMB for the years between 2018-2022

In Figure 15, the trends in the data can be seen clearly. In a specific period, the absorbing aerosol index data decreases, and after the decrease, the absorbing aerosol index data increases. In this case, the decreases coincided with cold seasons, and the increases coincided with warm seasons, as in Table 7. However, the ups and downs are not steady and does not have the same slope, meaning there are unusual changes in absorbing aerosol values observed. All the outliers can be seen in the "remainder" part of Figure 15.

In Figure 16, the seasonal trends observed in the Eastern Mediterranean Basin for the four years can be seen. In the figure below, the seasons have been lined up from winter to autumn, respectively.

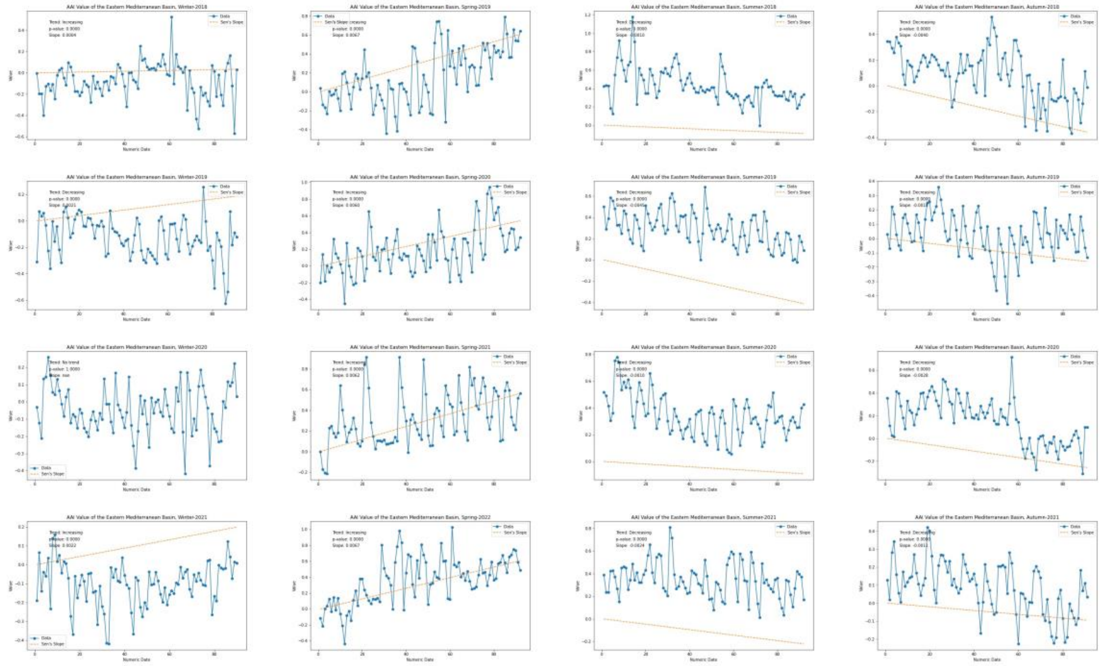

Figure 16. Seasonal trends of AAI in the Eastern Mediterranean Basin

In this figure, the seasonal trends are clearly seen. In summer and spring seasons of the Eastern Mediterranean Basin (first and second column), Absorbing Aerosol Index value shows an increasing trend. On the contrary, in winter and autumn season, AAI value shows a decreasing trend over the four years. These graphs can be viewed separately in the Appendix part of this thesis.

In Figure 17, the representation of the whole data for the EMB can be seen as separated by years. In general, all the studied years showed similar variations. The AAI data increases in the warmer seasons and decreases in the colder seasons of the year. The decrease in AAI during cold seasons can be caused by the increase in scattering aerosols and cloud formation.

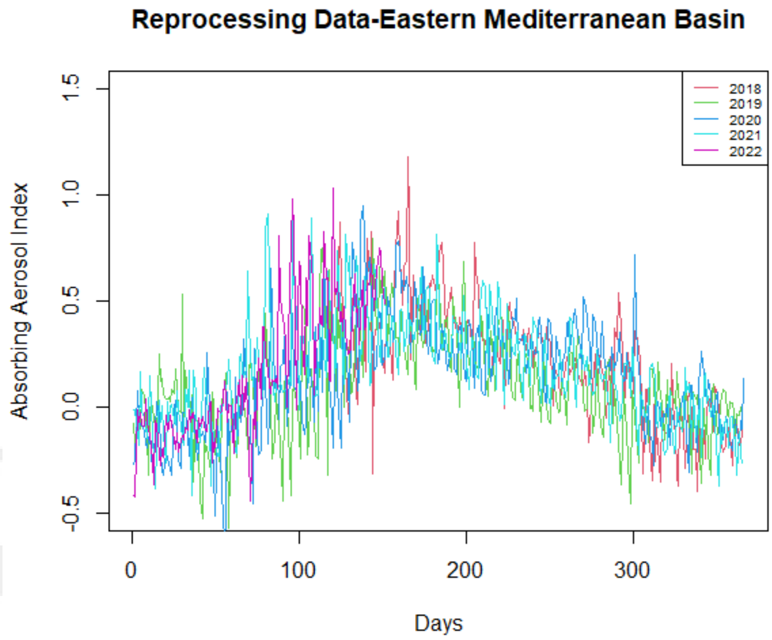

Figure 17. Annual comparison of reprocessing AAI data, EMB

In Figure 17, by looking at the graph, it was seen that the AAI data for all four years represent similar patterns for the Eastern Mediterranean Basin. If the data is analyzed in more detail annually, the outliers can be distinguished clearly. For instance, a peak value is observed for 4 May 2018. When the daily visuals of the Sentinel-5P data and NASA's Earth Observing System Data and Information System (EOSDIS) were checked, it was seen that a dust outbreak was present in the area between 3 and 7 May 2018, especially in the southern parts. Similarly, on 27 October 2018, a peak value was observed, which is very unusual in the four years, as seen in Figure 17. After looking at the visuals of the satellite data, a dust episode is seen. Another dust episode is observed between 5 and 7 April 2022. After this episode, an unusual decrease in the AAI value on 8 April 2022, which can be observed in the graph in Figure 14. In general, AAI values in 2019 were lower than in other years. Conversely, AAI values in 2022 seem higher. This situation can be interpreted as a representation of the effects of climate change on the atmosphere.

For the Eastern Mediterranean Basin, the graph in Figure 17 has been split annually to create time series graphs, and to compare the AAI value year by year. However, due to the lack of the Reprocessing data in years 2018 and 2022, such comparison for a full year was only valid for the years 2019, 2020, and 2021. The remaining years can be used in the seasonal analysis. For example, since the Reprocessing AAI data was available for the months after May for year 2018, this dataset can be used in the summer and autumn seasons. On the other hand, the Reprocessing AAI data was available for until July for the year 2022, which means the dataset of 2022 can be used in the analysis of spring season.

In Figure 18, the time series graphs, which were created with AAI data in the Eastern Mediterranean Basin for 2018 (upper graph) and 2022 (bottom graph) can be seen. These two years are shown together since there are missing data (due to availability) in both of these years. The blue straight line with points represents the data, and the orange dotted line is the Sen's slope.

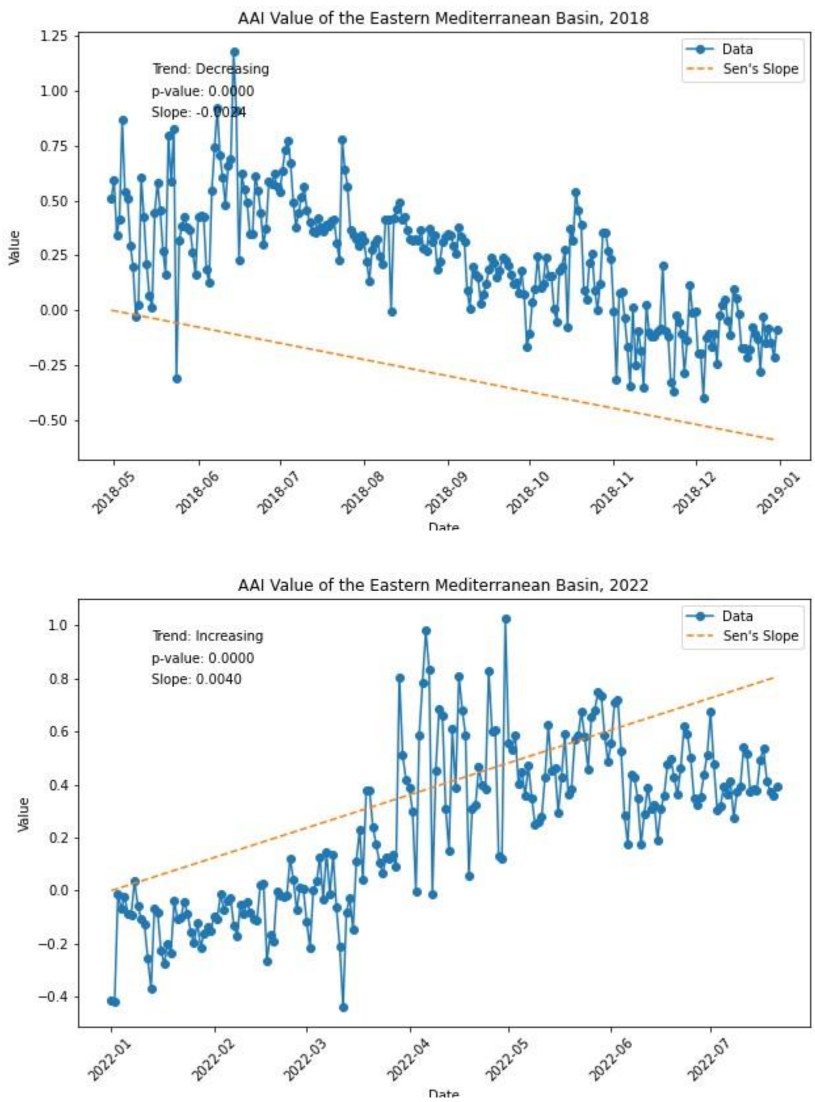

Figure 18. Daily Mean Absorbing Aerosol Index Value for the Eastern Mediterranean Basin, 2018 and 2022

For the year 2018, the mean AAI data for the Eastern Mediterranean (which was available from May to December), shows a decreasing trend as can be seen in Figure 18. According to the results of the North American Multi-Model Ensemble (NMME), as of March 2018, the upper ocean temperature anomalies have shifted from La Niña, which is the cooling phase, to El Niño, which is the warm phase (Becker, 2018). However, even if the Pacific Ocean gets warm, the atmosphere does not. The reason behind this is the Madden-Julian Oscillation (MJO), a fluctuation that moves towards the eastward parts of the equator that occurs monthly in tropical weather (J, n.d.). This oscillation was active in the last months of 2018, changing the wind patterns and cloud formations. Therefore, the decrease in the absorbing aerosol value in 2018 may be caused by this oscillation, even though El Niño is dominant at that time.

For the year 2022, the mean AAI data, which was available from January to July, shows an increasing trend with a positive slope as can be seen in the equation in Figure 18. The reason for this featured increasing trend compared to the other years (as in Figure 19) is that, as mentioned before, the AAI data for the year 2022 was only available until July. This data represents the trends in warmer months, excluding the whole autumn and partially winter seasons, which shows normally decreasing trends in the AAI data due to the dominance of scattering aerosols.

The difference between the trends of these two datasets are due to the part of availability of the data for Reprocessing Level-3 Absorbing Aerosol Index as explained before.

In Figure 19, time series graphs of the mean AAI data for the Eastern Mediterranean Basin can be seen for the years 2019 (upper), 2020 (middle), and 2021 (bottom). This kind of representation will make it possible to compare annual results.

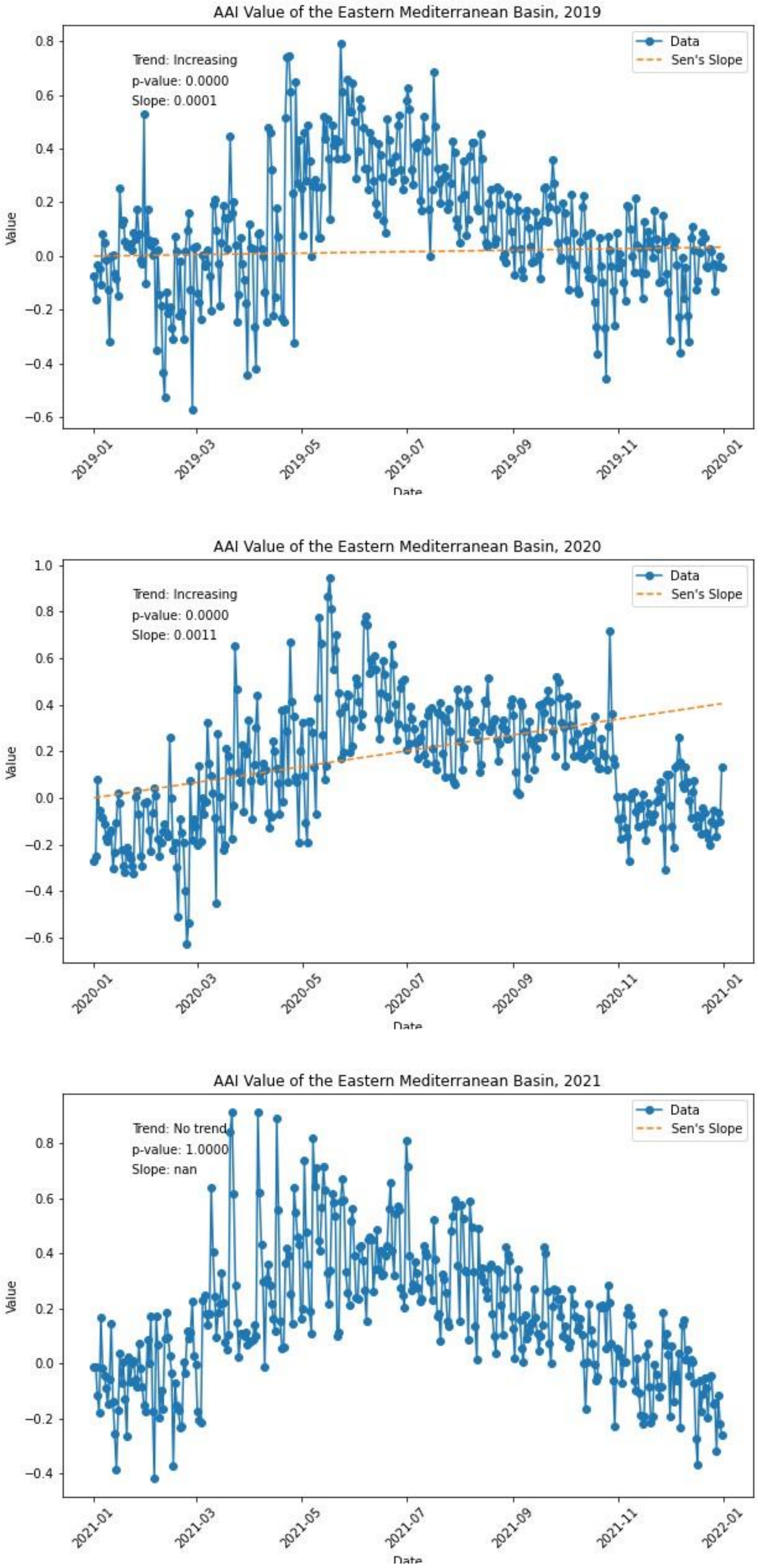

Figure 19. Daily Mean Absorbing Aerosol Index Value for the Eastern Mediterranean Basin, 2019, 2020, and 2021

The time series graph for the mean AAI data for 2019 (upper), shows an increasing trend with a positive slope on the graph in Figure 19. During 2019, the sea surface temperatures were high above the average (natural condition), yet not enough to declare that it is an El Niño phase when combined with the atmospheric temperature, as was in the last months of 2018. According to a report released by NOAA (National Oceanic and Atmospheric Administration), 2019 was the second-warmest year since 1880, with an average temperature of 0.95^{0}C higher than the average of 20th century (Liberto, 2020). This may be caused by the high absorbing aerosol values observed in 2019. The absorbing aerosols tend to absorb incoming solar rays, which can affect the temperature of the atmosphere.

The mean AAI value for 2020 (middle) reflects an increasing trend with a slope of 0.0011, as seen in the equation shown in Figure 19. Compared to the years 2018 and 2019, a high absorbing aerosol content is present in year 2020, except in the winter season which is dominated by high scattering aerosol content. At the beginning of January 2020, the threshold for the El Niño conditions was passed. However, right after January, the conditions approached neutral conditions. After May, the conditions switched from neutral to La Niña as the difference from the average temperature became negative. The La Niña effect may be created due to the decrease in the absorbing aerosol content in the atmosphere in year 2020. As mentioned before, at the start of Section 4.1 of this thesis, the fossil fuel consumption in that year was found to be lower compared to the other years which were investigated. A slight decrease of AAI compared to year 2018 (Table 9) may be caused by the decrease in usage of fossil fuels in that year.

The mean AAI data for the Eastern Mediterranean Basin in 2021 (bottom), shows no trend, as seen in Figure 19. The extreme days, when there are higher AAI values observed, are more frequently occurring in year 2021 compared to other years. For example, the mean AAI value in March 2021 is higher than the average of 0.08 which is the average of four years of AAI data of month March as can be seen in Table 10. This situation may be the reason of not observing any trend for the dataset of year 2021. The mean AAI value in the winter season is also higher than the average values in the winter months.

In the following section, the distribution of the mean Reprocessing Level-3 Absorbing Aerosol Index value over the Eastern Mediterranean Basin is investigated on a monthly and seasonal basis.

4.1.1. Monthly and Seasonal Investigation for EMB

In this section, in order to see the change in the Absorbing Aerosol Index over time in the Eastern Mediterranean Basin, the results of the monthly and seasonal investigation for all the studied years have been explained.

Figure 20 shows the images representing the distribution of the mean Absorbing Aerosol Index over the Eastern Mediterranean Basin for every month between 2018 and 2022. The AAI values have been averaged for every month in order to observe seasonal normal for the investigated area.

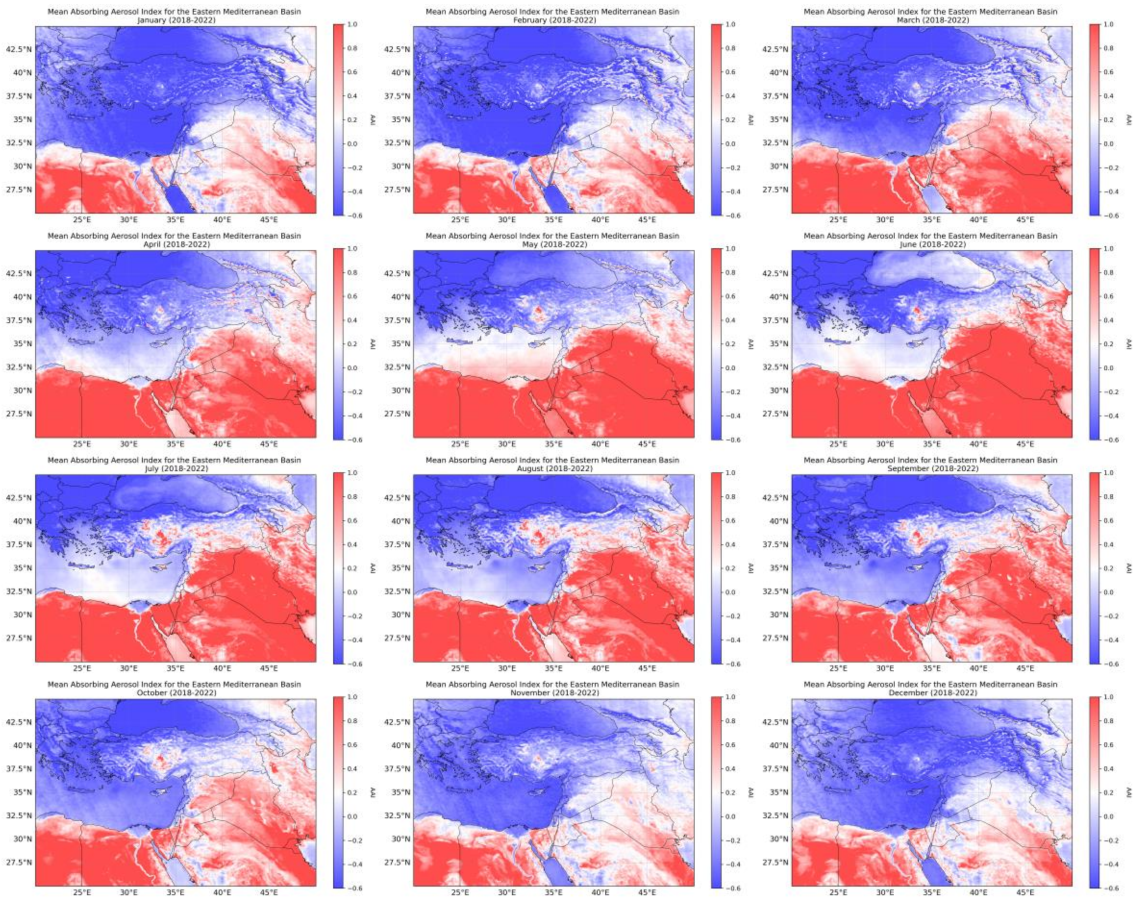

Figure 20. Monthly mean distributions of the AAI on Eastern Mediterranean Basin from 2018 to 2022

The Eastern Mediterranean Basin is mainly affected by the dust episodes sourced by the Saharan Desert. These dust episodes are driven by the Sharav cyclones, which are generated by the thermal difference in the Atlantic air (cold) and North African air (warm) (Nastos, 2012). In warm months, the thermal lows over the desert can create dust erosion, and these dust particles can be transported for long distances (Nastos, 2012). In cold periods, when the precipitation is high, the aerosol load in the atmosphere settles down to the earth's surface. The effect of the Sahara Desert on the aerosol load in the Eastern Mediterranean Basin is maximum in spring and minimum in winter (Nastos, 2012).

In Figure 20, it was seen that the data is matching with the seasonal meteorological movements of the Eastern Mediterranean Basin atmosphere. For example, in the late spring and summer seasons, which are May-July-June-August, the mean value of the Absorbing Aerosol Index increases compared to the other seasons, meaning the absorbing aerosols are dominant over most of the area. During the late autumn and winter seasons, the mean value of the Absorbing Aerosol Index decreases, which is explained by the settling of absorbing aerosols by precipitation and the increase in the scattering aerosols.

For December-January-February (winter season), a low Absorbing Aerosol Index and high scattering aerosol presence were expected. The low AAI value may be caused by the increase in scattering aerosols such as sulfates or nitrate (Penner, 2022), and the cloud formation plays a critical role. This situation is valid for regions other than Northern Africa and the Northern Arabian Peninsula. For these regions, a constant release of desert dust increases the mean value of the Absorbing Aerosol Index. Northern parts of Egypt experience different atmospheric conditions than the rest of Northern Africa. The reason for this situation is that this area is entirely covered by forests. The high rainfall received by this forest area reduces the absorbing aerosol load in that area. There are some blank areas in the Northern Arabian Peninsula, especially in December, where neither absorbing nor scattering aerosols are present.

From March-April-May, the spring season is experienced in most regions in the selected domains. The scattering aerosol ascendancy over Türkiye continues. At the same time, absorbing aerosols over Lake Tuz and South of Türkiye is high. The absorbing aerosol load in and from Northern Africa and the Northern Arabian Peninsula continues.

As the weather gets warmer during the summer (June-July-August), the abundance of the absorbing aerosols increases. This cause-effect relationship works in reverse: as the absorbing aerosols increase, the atmosphere gets warmer due to their ability to absorb the incoming solar rays. The Mediterranean Sea is experiencing the effects of absorbing aerosol transport from the Africa and Arabian Peninsula to the Anatolian Region. From May-June-July-August, the Red Sea is wholly covered with absorbing aerosols.

In September-October-November (autumn season), the absorbing aerosol load over the southern parts of the study domain started to decrease. Central Anatolia and southeast parts of Türkiye still experience the effects of absorbing aerosols. However, the blank areas, where no scattering or absorbing aerosols are present, increased this month.

In Figure 21, the seasonal distribution of the absorbing aerosols can be seen.

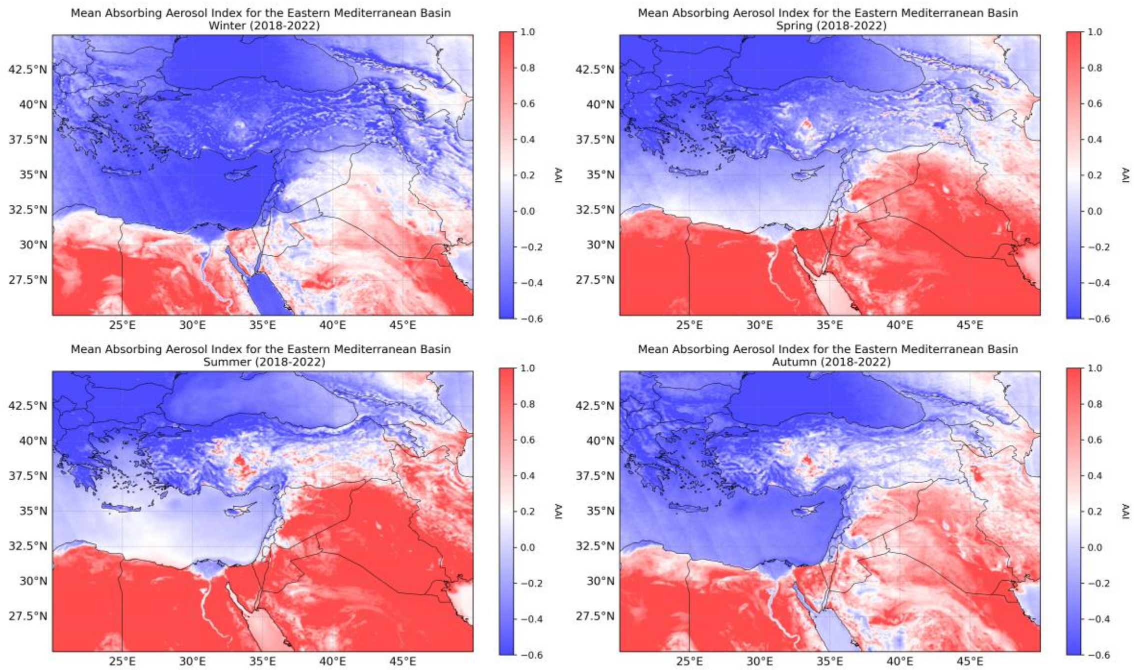

Figure 21. Seasonal mean of the AAI from 2018 to 2022, EMB

In spring, absorbing aerosols accumulate in places with many deserts. Northern Egypt is not affected by the absorbing or scattering of aerosols. However, the Red Sea is covered with absorbing aerosols. In the summer, the absorbing aerosol index increased in Lake Tuz, the eastern parts of Türkiye, and Lake Urmia. Scattering aerosols were taking over the atmosphere of northern Egypt during this season. In autumn, the absorbing aerosols started to diminish from the atmosphere of the eastern Türkiye, the Red Sea, and the Northern Arabian Peninsula. Winter is the one season where the scattering aerosols are the most dominant over the Eastern Mediterranean Basin. The absorbing aerosols are only present where the deserts are present.

Table 10 shows the statistical summary of the Absorbing Aerosol Index for every month for all the years (2018, 2019, 2020, 2021, and 2022) for Eastern Mediterranean Basin. This table is prepared by converting the netCDF data to csv data, then using a specific script prepared for the obtaining the statistical summaries for four years of daily data. The script calculates the statistical summaries of AAI for every grid in the data.

Table 10. Monthly statistical summary of the Absorbing Aerosol Index for the Eastern Mediterranean Basin

Months	Minimum	Median	Mean	Maximum	Standard Deviation
January	-0.4201	-0.0845	-0.0909	0.5287	0.1410
February	-0.6286	-0.0875	-0.0962	0.2583	0.1721
March	-0.4524	0.0941	0.0887	0.9118	0.2368
April	-0.4189	0.2376	0.2686	1.0282	0.3012
May	-0.3110	0.4234	0.4073	0.9470	0.2262
June	0.0854	0.4278	0.4356	1.1810	0.1679
July	0.0000	0.3614	0.3617	0.8104	0.1563
August	-0.0224	0.2910	0.2747	0.5890	0.1325
September	-0.1643	0.1783	0.1868	0.5212	0.1378
October	-0.4557	0.1301	0.1195	0.7155	0.1795
November	-0.3704	-0.0418	-0.0426	0.2143	0.1281
December	-0.3996	-0.0651	-0.0727	0.2603	0.1234

As seen in Table 10, the Absorbing Aerosol Index's mean, maximum, minimum, and median values increase in warmer months and decrease in colder months. The increase in the dataset's standard deviation indicates that the data's dispersion is high in the spring months, which are March, April, and May, the dispersion of the Absorbing Aerosol Index data increases.

Figure 22 represents the monthly boxplots for Absorbing Aerosol Index data of the Eastern Mediterranean Basin from May 2018 to July 2022. The use of boxplots was explained under the Figure 13.

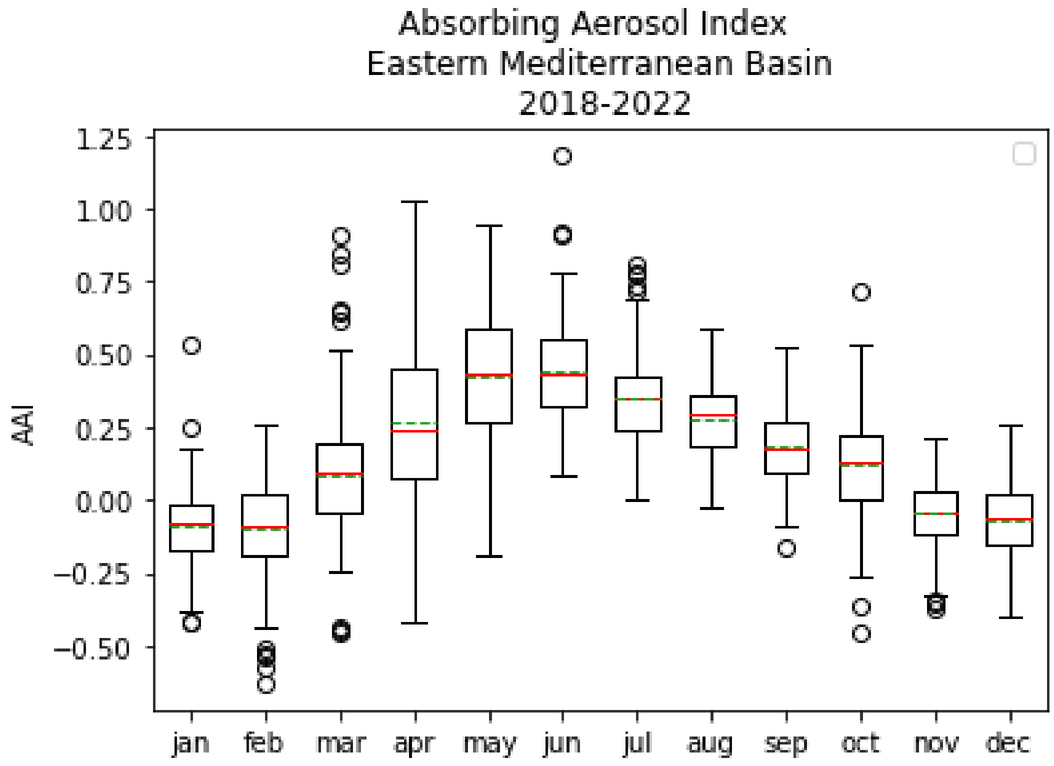

Figure 22. Monthly boxplots of AAI for the Eastern Mediterranean Basin (from 2018 to 2022)

The graph in Figure 22 visualizes the statistics of the four years of Absorbing Aerosol Index data for the Eastern Mediterranean Basin. In general, the data variability was found to be small. However, the dataset varies more in some months, such as April and May. While there are more outliers in months like January, February, and July, there were no outliers in April, May, August, and December. The reason for observing this many outliers is that the investigated area consists of different climates. The mean value exceeds the median in April, June, and September. This means that the distribution of the dataset is positively skewed for these months. For the remaining months, the mean value is closer or smaller than the median value, which means that the distribution of the dataset is negatively skewed.

4.2.Türkiye

The Absorbing Aerosol Index data obtained from the Sentinel-5P satellite for the domain that surrounds Türkiye shows that for four years of data, it was seen that the absorbing aerosol load accumulates in several spots, as in Figure 23. These spots are Lake Tuz and its surroundings, some parts of the Mediterranean region, and the eastern parts of the country. Since Figure 23 represents four years of data, other extreme minimum and maximum values seem smoother.

The following visuals for Türkiye have been prepared for the coordinates between 25-45^{0}E and 36-42^{0}N. The dataset is extracted for the same location. The range of AAI value in the legend has been arranged according to the minimum and maximum values observed during the studied time period, which is between -0.6 and 1.

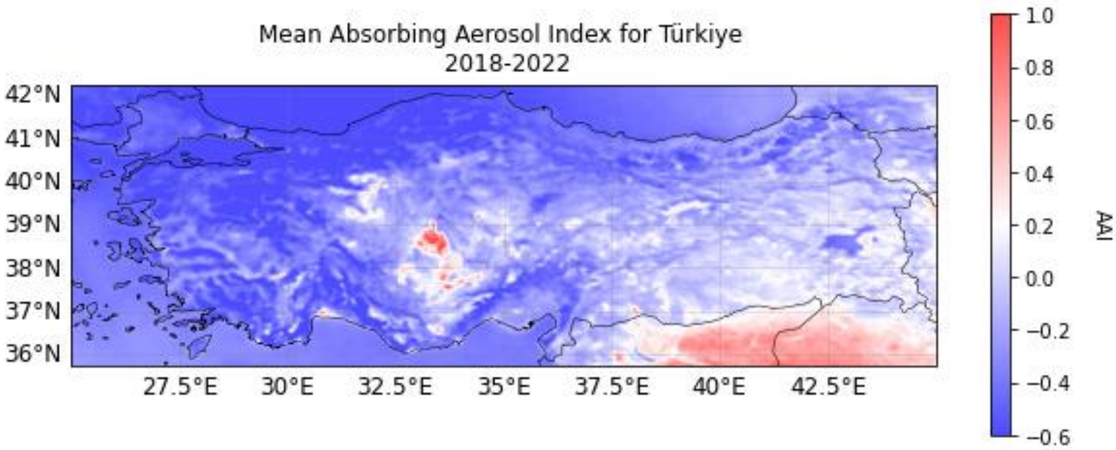

Figure 23. Mean AAI data of Türkiye from 2018 to 2022

In this figure, it was seen that Lake Tuz itself and its surroundings seem to have an Absorbing Aerosol Index intensity over the four years. Lake Tuz is located in the center of Türkiye, and it is the second largest Lake that occupies an area of 1,665 km^2 (Huseyinca & Küpeli, 2021). It contains hypersaline water with a salt content of 32.4% (The Ministry of Environment Urbanization and Climate Change, n.d.-c). At the end of summer season, approximately half of the lake area experiences evaporation. When the hygroscopic property of water, which is the capacity of water to absorb humidity from the atmosphere, is combined with the salt content, the absorbing aerosols over the lake increases (Kilic & Kilic, 2010). Also, the NaCl content (halite) which is very high in this lake, creates absorbing aerosol load when the lake evaporates in spring and summer (Bilgilioğlu et al., 2021) (Huseyinca & Küpeli, 2021). In a study conducted by Huseyinca & Küpeli et al., a sampling and an analysis was done with the sediments of the lake. It was found that the color of the sediments, which are composed of halite, polyhalite, magnesite, calcite, and quartz, was in white-grey-brow. The high Absorbing Aerosol Index value over the atmosphere of Lake Tuz can be explained by the color of the lake sediment content. In another study conducted by Karslıoğlu et al. (Karslıoğlu et al., 2022), it was found that the Aerosol Optical Depth (AOD) values were very high compared to other regions of Türkiye. It was explained by the low Normalized Difference Vegetation Index (NDVI), which is an index that reveals the density of vegetation in any area, and the high content of salt in the lake itself. Low value of this index indicates that whether the area is urban or there is a water content in the area.

In contrast to Lake Tuz, Lake Van hosts some scattering aerosols, its surroundings either absorbing aerosols or no aerosols at all. Lake Van is the biggest soda lake of Türkiye with an area of 3,522 km^2 (Reimer et al., 2009). Soda lakes are highly loaded with sodium and carbonate (Schagerl, 2016). The evaporation of this content is causing the high values of scattering aerosols over the lake, due to its color which is white.

Table 11 shows the statistical summary of the Absorbing Aerosol Index for the years 2018, 2019, 2020, 2021, and 2022 for Türkiye. This summary includes minimum, maximum, median, mean, and standard deviation.

Table 11. Statistical summary tables for Türkiye for all study years

Years*	Minimum	Median	Mean	Maximum	Standard Deviation
2018	-0.64167	-0.13289	-0.11225	0.437559	0.234473
2019	-1.07956	-0.30485	-0.29561	0.623952	0.318387
2020	-1.13479	-0.21973	-0.22571	1.248648	0.356721
2021	-0.93252	-0.2428	-0.24153	1.010567	0.3266
2022	-1.00069	-0.3641	-0.31479	0.608386	0.331968

*For years 2018 and 2022, the Reprocessing data was not available for the whole year during the conduction of this study. For 2018, the data is available from May to the end of December; and for 2022, the data was available from January to the end of July.

By looking at Table 11, it can be said that the mean value for Absorbing Aerosol Index for Türkiye has decreased by 180.43% over the four years. Similarly, decreases have been observed for minimum and median values by 55.95% and 173.98%, respectively. However, the maximum value and the standard deviation of the dataset have increased by 39.04% and 41.58%, respectively, over the four years, which indicates an increase in the variability of the dataset.

Figure 24 represents the annual boxplots for Absorbing Aerosol Index data of Türkiye from May 2018 to July 2022. The use of boxplots was explained under the Figure 13.

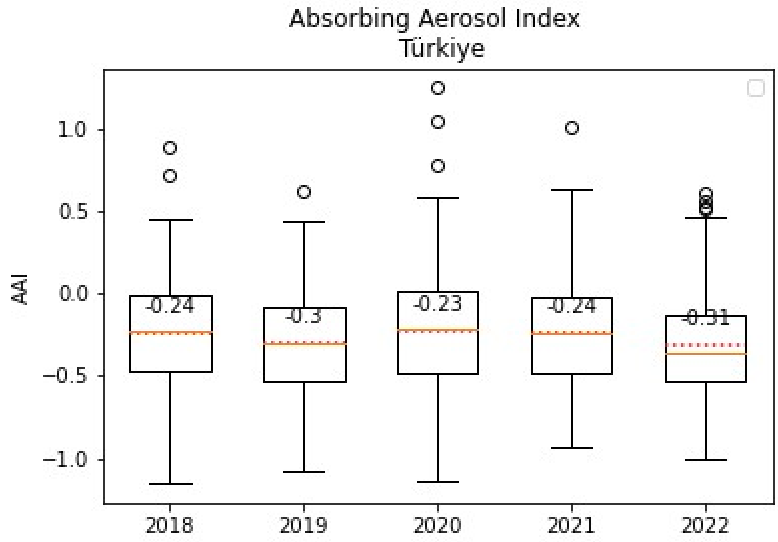

Figure 24. Annual boxplots of AAI for Türkiye (from 2018 to 2022)

In Figure 24, it can be seen that only the dataset of year 2022 is positively skewed, because the mean value exceeds the median value. All the outliers for all years are bigger than the mean of the dataset. Other than year 2022, which has outliers close to maximum value of the dataset, the outliers are higher than the maximum value of the dataset. Compared to the annual boxplot of the data from Eastern Mediterranean Basin (Figure 13), the datasets of all the years show similar patterns to each other.

In Figure 25 shows the mean Absorbing Aerosol Index of Türkiye for four years of data. Compared to Figure 14, which is the time series graph for the Eastern Mediterranean Basin, the seasons cannot be observed clearly in the time series graph of Türkiye. According to the Mann Kendall test, there were no significant trends have been observed.

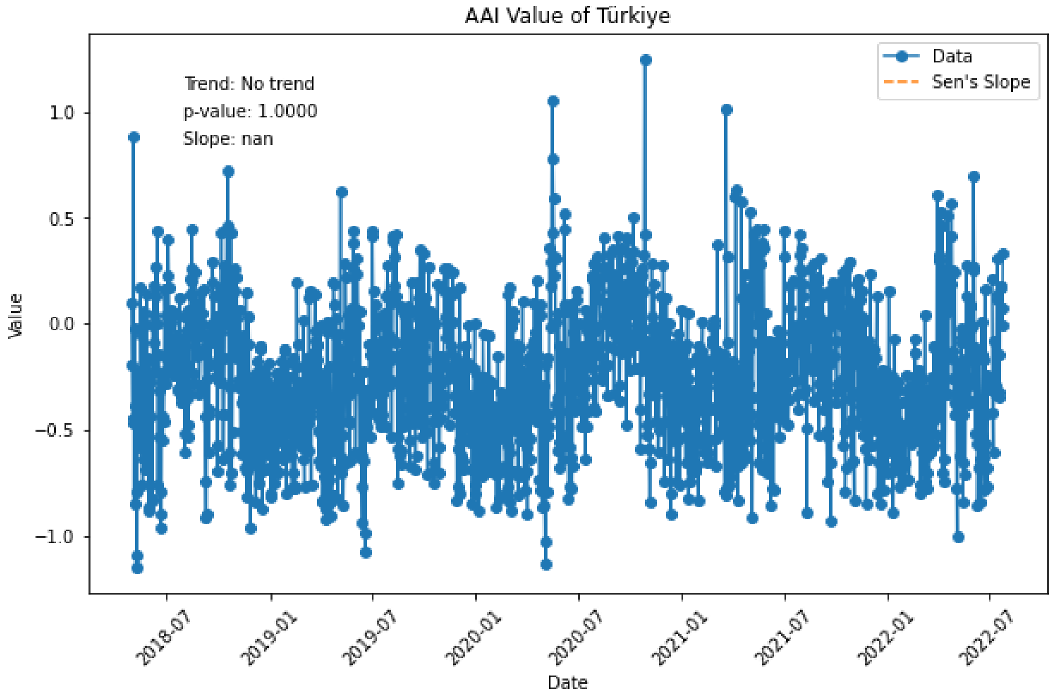

Figure 25. Daily Mean Absorbing Aerosol Index Value for Türkiye (2018-2022)

The reason of not observing any trends over Türkiye may be explained by the high standard deviation in the dataset compared to the Eastern Mediterranean Basin. This means that there are lots of extreme days in the studied time period. However, as can be seen in Figure 26, when the dataset is divided by seasons, trends that are specific to each season have been observed. In the figure below, the seasons have been lined up from winter to autumn, respectively.

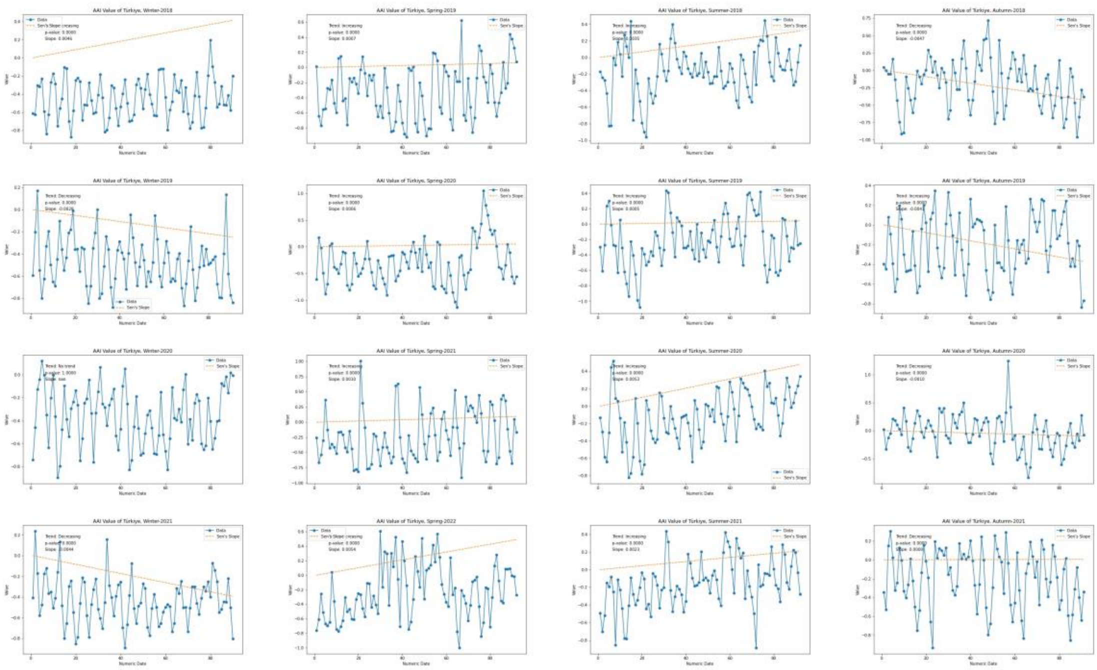

Figure 26. Seasonal trends of AAI in Türkiye

In the second and third column of the figure, it was seen that in spring and summer seasons of Türkiye, the general tendency is an increasing trend. In the fourth column of the figure, which is autumn season, the general tendency is a decreasing trend. In winter, a significant trend was not observed for all the four years. Each trend is different for every year. These graphs can be viewed separately in the Appendix part of this thesis.

In Figure 27, the absorbing aerosol index data of Türkiye is decomposed into its components: seasonal, trend, and remainders. When looking at the trends, the increases and decreases can be seen. However, a pattern in these trends cannot be observed clearly.

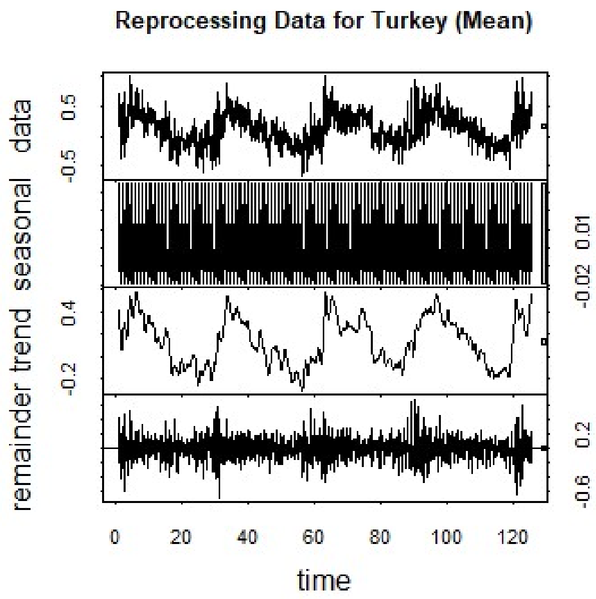

Figure 27. Decomposition of the mean AAI of Türkiye for the years between 2018-2022

In order to differentiate the annual trends, the following graphs were created, which shows the temporal variation of the AAI for Türkiye. However, the same situation in the EMB is valid for Türkiye as well. Due to the lack of the Reprocessing data in years 2018 and 2022, such comparison for a full year was only valid for the years 2019, 2020, and 2021. The remaining years can be used in the seasonal analysis.

In Figure 28, the time series graphs, which were created with AAI data for 2018 (upper graph) and 2022 (bottom graph) can be seen.

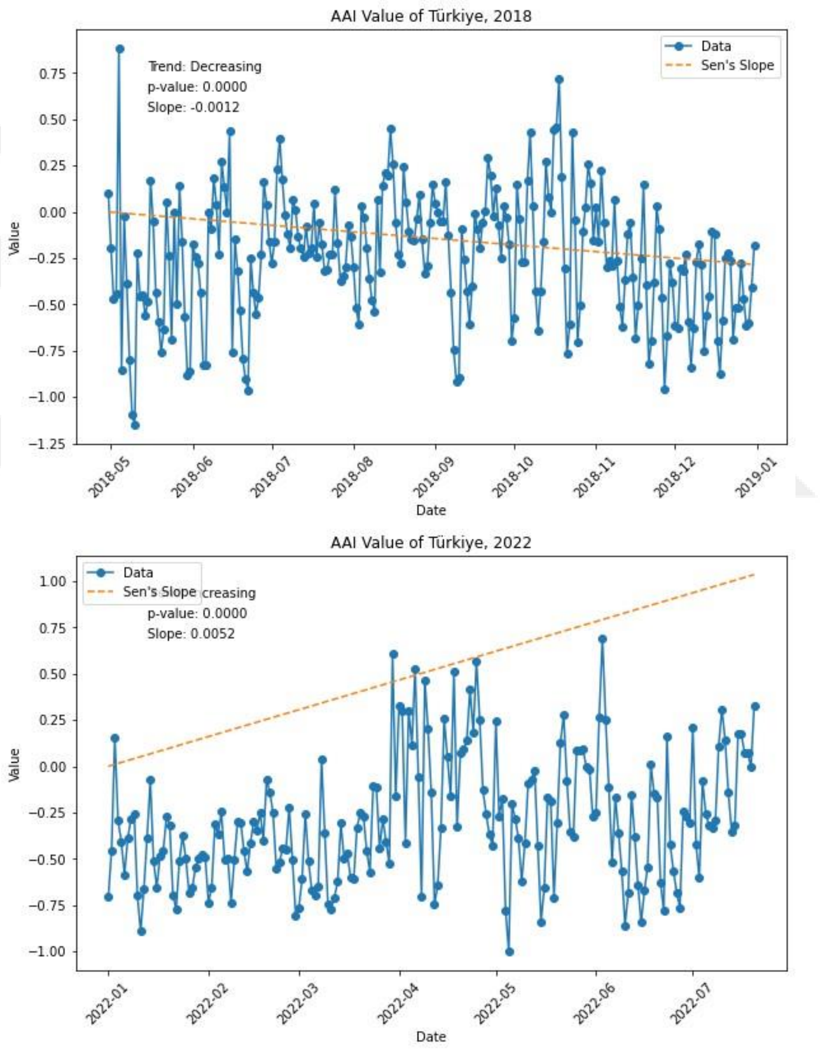

Figure 28. Daily Mean Absorbing Aerosol Index Value for Türkiye in 2018 and 2022

It was seen that from spring to winter, there is a decreasing trend in AAI in the year 2018 (upper). According to the meteorological seasons for the Northern Hemisphere, the spring season, where the AAI value increases to its maximum, ends in May in Türkiye. Followed by the summer, autumn, and winter months, respectively, the AAI value decreases with a negative slope. Other than some extreme days in terms of high AAI values observed, which may be caused by the dust releases from Saharan Desert, there were no abnormal situation.

The mean AAI data for Türkiye in 2022 (bottom), is available from January to July, as in EMB, and shows an increasing trend with a positive slope, as seen in the equation in Figure 28. This data on the graph represents the trends in warmer months, excluding autumn and winter, where there are decreasing trends in the AAI data. In year 2022, La Niña conditions were present as can be seen in Figure 29 (National Institute of Water and Atmospheric Research, n.d.; NOAA, n.d.; Null, 2023). La Niña may be triggered by the increasing absorbing aerosol content in the atmosphere.

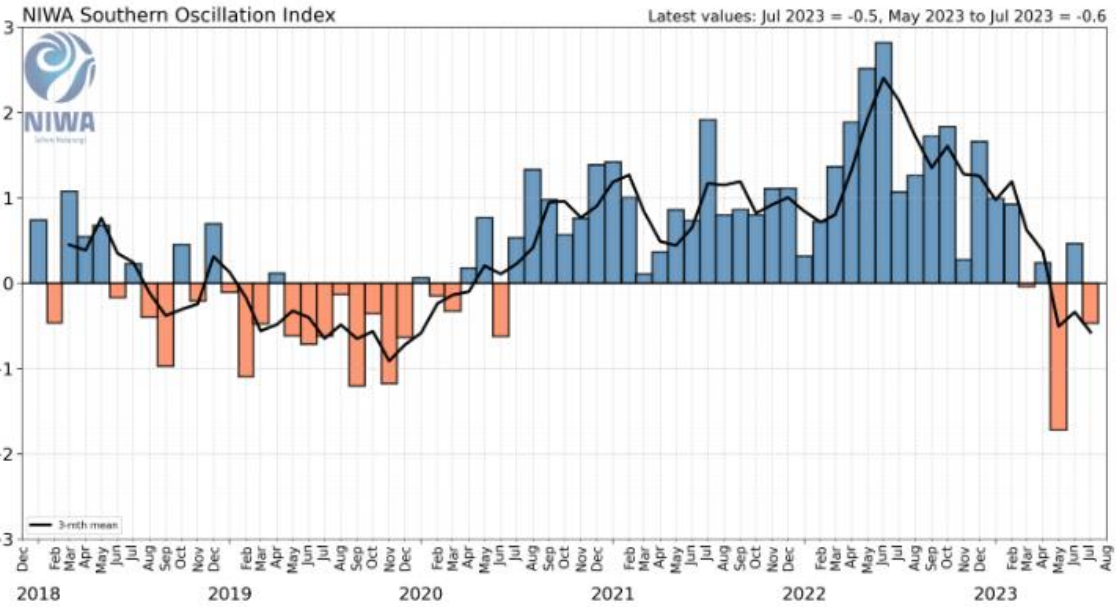

Figure 29. El Niño and La Niña conditions over the years (National Institute of Water and Atmospheric Research, n.d.)

In Figure 29, below -1.0 correspond to El Niño conditions while values above 1.0 correspond to La Niña conditions. Values between -0.5 and -1.0 lean toward El Niño, while values between 0.5 and 1.0 lean toward La Niña. Values between -0.5 and 0.5 are considered neutral.

The El Niño and La Niña Indexes are also given in Figure 30 by differently combined seasons.

ENSO Type	Season	JJA	JAS	ASO	SON	OND	NDJ	DJF	JFM	FMA	MAM	AMJ	MJJ
SL	**2010-2011**	**-1.0**	**-1.4**	**-1.6**	**-1.7**	**-1.7**	**-1.6**	**-1.4**	**-1.1**	**-0.8**	**-0.6**	**-0.5**	-0.4
ML	**2011-2012**	**-0.5**	**-0.7**	**-0.9**	**-1.1**	**-1.1**	**-1.0**	**-0.8**	**-0.6**	**-0.5**	-0.4	-0.2	0.1
	2012-2013	0.3	0.3	0.3	0.2	0.0	-0.2	-0.4	-0.3	-0.2	-0.2	-0.3	-0.3
	2013-2014	-0.4	-0.4	-0.3	-0.2	-0.2	-0.3	-0.4	-0.4	-0.2	0.1	0.3	0.2
WE	**2014-2015**	0.1	0.0	0.2	0.4	**0.6**	**0.7**	**0.6**	**0.6**	**0.6**	**0.8**	**1.0**	**1.2**
VSE	**2015-2016**	**1.5**	**1.9**	**2.2**	**2.4**	**2.6**	**2.6**	**2.5**	**2.1**	**1.6**	**0.9**	0.4	-0.1
WL	**2016-2017**	-0.4	**-0.5**	**-0.6**	**-0.7**	**-0.7**	**-0.6**	-0.3	-0.2	0.1	0.2	0.3	0.3
WL	**2017-2018**	0.1	-0.1	-0.4	**-0.7**	**-0.8**	**-1.0**	**-0.9**	**-0.9**	**-0.7**	**-0.5**	-0.2	0.0
WE	**2018-2019**	0.1	0.2	0.5	**0.8**	**0.9**	**0.8**	**0.8**	**0.7**	**0.7**	**0.7**	**0.5**	**0.5**
	2019-2020	0.3	0.1	0.2	0.4	0.5	0.6	0.5	0.5	0.4	0.2	-0.1	-0.3
ML	**2020-2021**	-0.4	**-0.6**	**-0.9**	**-1.2**	**-1.3**	**-1.2**	**-1.1**	**-0.9**	**-0.8**	**-0.7**	**-0.5**	-0.4
ML	**2021-2022**	-0.4	**-0.5**	**-0.7**	**-0.8**	**-1.0**	**-1.0**	**-1.0**	**-0.9**	**-1.0**	**-1.1**	**-1.0**	**-0.9**
WL	**2022-2023**	**-0.8**	**-0.9**	**-1.0**	**-1.0**	**-0.9**	**-0.8**	**-0.7**	-0.4	-0.2	0.1	0.5	0.8

Figure 30. El Niño and La Niña Indexes (Null, 2023)

It can be seen that in year 2022, the general condition over the world was Weak La Niña. The index range for the "weak" is given as between 0.5 and 0.9.

In Table 12, the ENSO index values, and monthly combined mean Sentinel-5P AAI values are given. The empty cells in 2018 and 2022 coincides to the months which the reprocessing data from Sentinel-5P was not available for the analysis, during the conduction of this study.

Table 12. The ENSO Index values with monthly Sentinel-5P AAI values

Seasons	2018-ENSO	2018-S5P	2019-ENSO	2019-S5P	2020-ENSO	2020-S5P	2021-ENSO	2021-S5P	2022-ENSO	2022-S5P
DJF	-	-	0,7	-0,48	0,5	-0,37	-1	-0,43	-1	-0,45
JFM	-	-	0,7	-0,40	0,5	-0,47	-0,9	-0,37	-0,9	-0,44
FMA	-	-	0,7	-0,38	0,4	-0,43	-0,8	-0,30	-1	-0,28
MAM	-	-	0,7	-0,31	0,2	-0,30	-0,7	-0,22	-1,1	-0,23
AMJ	-	-	0,5	-0,34	-0,1	-0,26	-0,5	-0,22	-1	-0,20
MJJ	0	-0,27	0,5	-0,24	-0,3	-0,19	-0,4	-0,16	-0,9	-0,24
JJA	0,1	-0,17	0,3	-0,22	-0,4	-0,12	-0,4	-0,16	-0,8	-0,24
JAS	0,2	-0,14	0,1	-0,17	-0,6	-0,03	-0,5	-0,11	-	-
ASO	0,5	-0,12	0,2	-0,22	-0,9	0,05	-0,7	-0,13	-	-

SON	0,8	-0,19	0,3	-0,21	-1,2	-0,03	-0,8	-0,20	-	-
OND	0,9	-0,28	0,5	-0,27	-1,3	-0,16	-1	-0,27	-	-
NDJ	0,8	-0,42	0,5	-0,35	-1,2	-0,33	-1	-0,38	-	-

The correlation between these ENSO Index and Sentinel-5P AAI datasets is examined. Correlation graphs for each year in Türkiye is given in Figure 31.

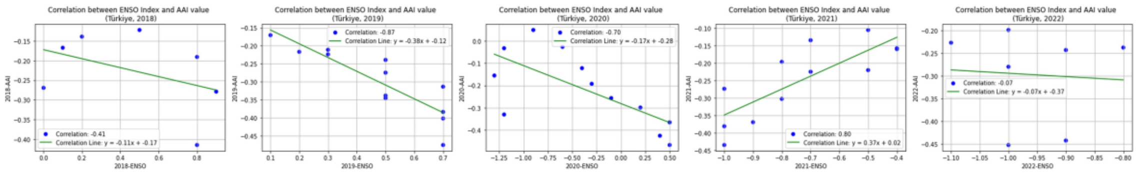

Figure 31. Correlation graphs for each year in Türkiye

The correlation coefficients of each year were given in Table 13.

Table 13. Correlation coefficients of two datasets (ENSO vs. S5P)

Year	2018	2019	2020	2021	2022
Correlation Coefficient	-0,41383	-0,86828	-0,69762	0,80432	-0,06781

As can be seen in Table 13, the correlation coefficients in all the studied years are negative, except for the year 2021. In years 2018, 2019, 2020, and 2022, there is a negative correlation between the ENSO Index and Sentinel-5P AAI value. It means that as the ENSO Index gets higher, which indicates La Niña conditions, the Absorbing Aerosol Index gets lower. However, this is not a straightforward kind of comparison. In 2022, the value of the correlation coefficient is very high, compared to the other negatively correlated years. It may mean that, if the reprocessing AAI dataset for year 2022 was available, the positive correlation may be observed for year 2022 as well.

In Figure 32, time series graphs of the mean AAI data for the Eastern Mediterranean Basin can be seen for the years 2019 (upper), 2020 (middle), and 2021 (bottom). This kind of representation will make it possible that an annual comparison can be made.

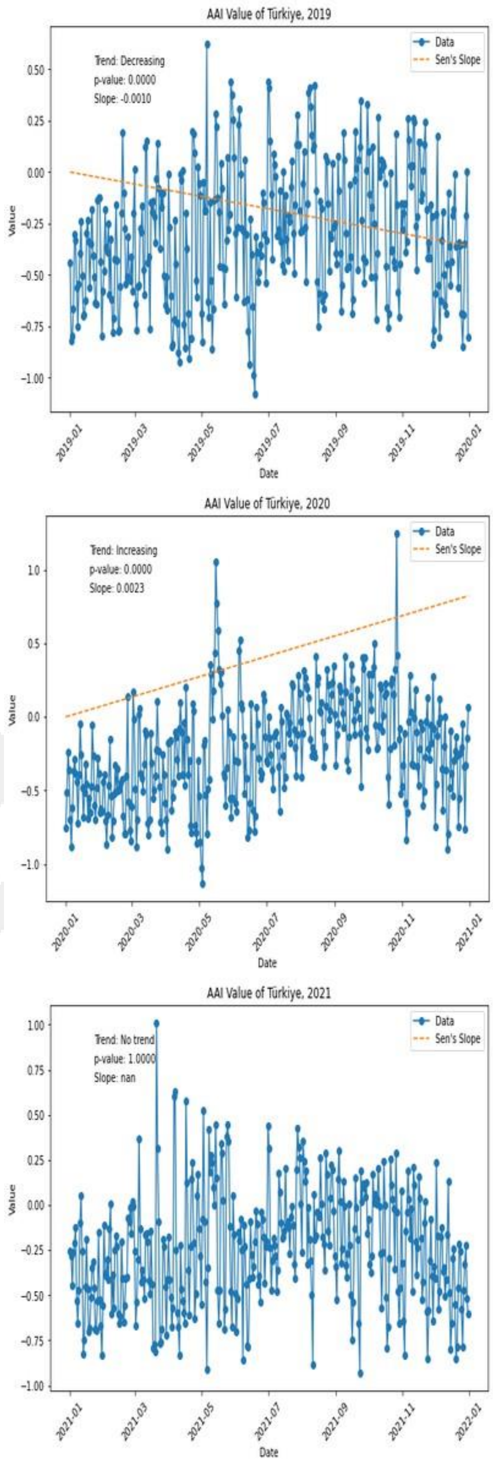

Figure 32. Daily Mean Absorbing Aerosol Index Value for Türkiye in 2019, 2020, and 2021

The mean AAI value for 2019 (upper), shows an increasing trend with a positive slope. However, the seasons cannot be differentiated in the graphs for Türkiye, as in the graphs for the Eastern Mediterranean Basin. There are slight increases and decreases in the mean AAI value. However, other than the extreme days, which may be triggered by dust releases, there are no sharp changes in the trend of the time series for 2019.

In the mean AAI value for 2020 (middle), the same stable situation is valid as in 2019. However, on October 27th, there has been an intense dust episode. This dust episode caused that sharp increase in the graph. In the late May, there has been another dust release, effecting the atmosphere of Türkiye. Other than the extreme days, the mean AAI value is higher in the warm months, and lower in the cold months, which was expected. The graph in Figure 32 reflects an increasing trend with a positive slope, as can be seen in the equation.

The mean AAI value for 2021 in Türkiye again shows an increasing trend with a positive slope, as seen in Figure 32. However, there are more extreme days in cold months this year. The atmosphere reflects La Niña conditions for the whole year. In this year, a huge forest fires were happening in the summer months, which is investigated in this study, in Section 4.4.2. The reflections of this fires were not clearly captured in the time series graphs of Türkiye. It may be caused by the fact that the fires were on the coastal lines of the country. The retrieval of the data from Sentinel-5P product for the Türkiye domain was conducted strictly by the coordinates of the country. During that time, the wind may blow the absorbing aerosols caused by the fires to another location. That is why the outputs of the fire cannot be specified in the time series graph.

4.2.1. Monthly and Seasonal Investigation for Türkiye

In this section, in order to see the change in the absorbing aerosol index over time in Türkiye, the results of the monthly and seasonal investigation for all the studied years have been explained.

In Figure 33, visuals representing the distribution of the mean Absorbing Aerosol Index over the Türkiye are shown for every month.

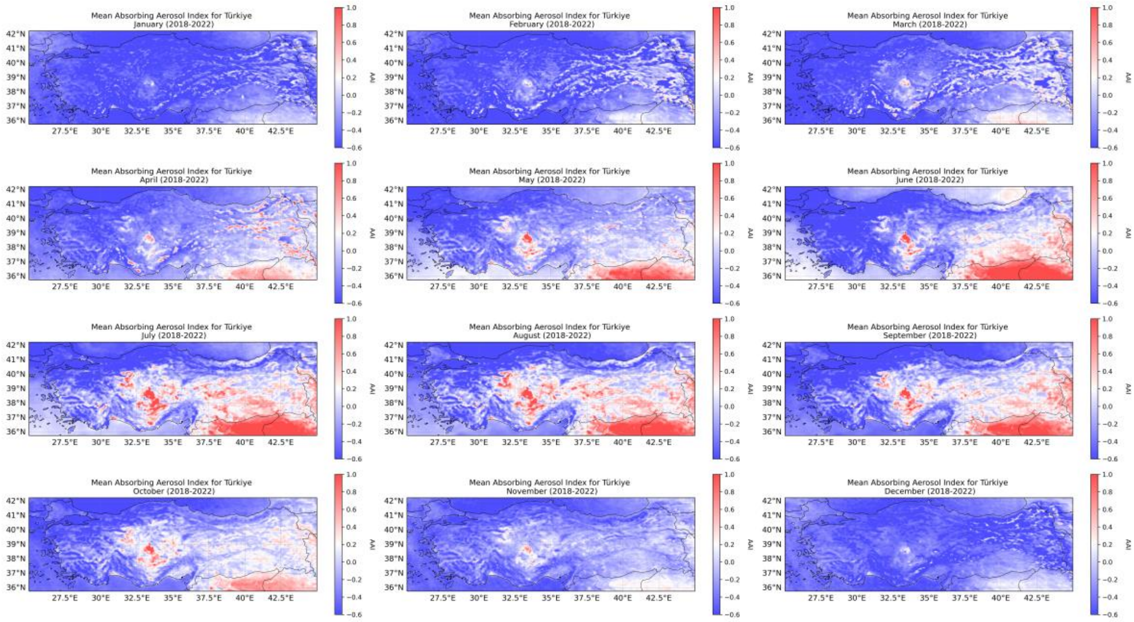

Figure 33. Monthly mean of the AAI on Türkiye from 2018 to 2022

Desert dust transported from the Sahara Desert is affecting the surrounding environments. Türkiye is one of the surrounding countries which is affected. As can be seen in Figure 33, which is a collective monthly visual of four years of data, absorbing aerosols is the most dominant in July, August, and September.

Among four years of AAI data for December-January-February (winter season), scattering aerosols dominate Türkiye. Lake Van experiences high amounts of scattering aerosols in its atmosphere, due to its high content of soda, as was explained in the beginning of Section 4.2.

In March-April-May, absorbing aerosols over the Mediterranean region, Lake Tuz, southern parts, and eastern parts of Türkiye are affected by absorbing aerosols; Lake Van is experiencing a load of scattering aerosol load in March, differing from April and May. In May, the Mediterranean region and the Mediterranean Sea are affected by dust release, most likely from North Africa.

In June-July-May, Lake Tuz and its surroundings which extends to almost Central Anatolia, are covered with absorbing aerosols. The east of Türkiye is under either a slight effect of absorbing aerosols or no aerosols at all.

At the start of the autumn season, September and October, the effects of absorbing aerosols are still present. In the last month of autumn (November), the load of aerosols shifted from absorbing to scattering aerosols which caused a cooling in the atmosphere. As the winter season gets closer, even Lake Tuz loses its absorbing aerosol load.

In Figure 34, the seasonal distribution of the AAI value for Türkiye domain can be seen.

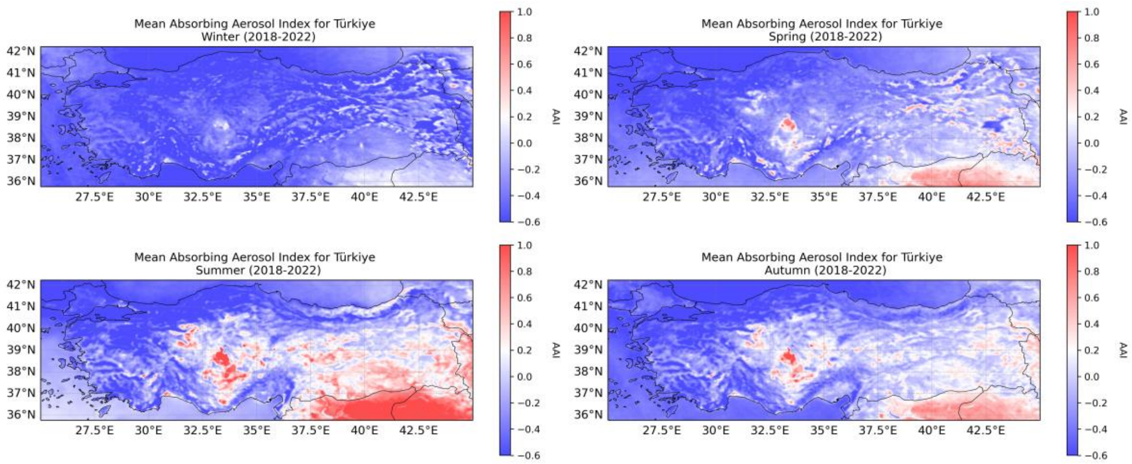

Figure 34. Seasonal mean of the AAI on Türkiye from 2018 to 2022

In winter, there are no signs of absorbing aerosols over Türkiye. It may be due to daily fluctuations; however, the area is experiencing a load of scattering aerosols, especially Lake Van and east Türkiye and in spring, absorbing aerosols accumulated in Lake Tuz and slightly over the mountains of the east region. In the summer, the absorbing aerosol index increased over Lake Tuz, its surroundings, and the eastern parts of Türkiye. Scattering aerosols were present over the atmosphere of northern and western parts of Türkiye during this season. In autumn, as the weather gets colder the absorbing aerosols started to diminish from the atmosphere of eastern Türkiye (Urdiales-Flores et al., 2023).

Table 14 shows the statistical summary of the Absorbing Aerosol Index for every month for all the years (2018, 2019, 2020, 2021, and 2022) for Türkiye.

Table 14. Monthly statistical summary of the Absorbing Aerosol Index for Türkiye

Months	Minimum	Median	Mean	Maximum	Standard Deviation
January	-0.8919	-0.4772	-0.4674	0.1564	0.2121
February	-0.8665	-0.4276	-0.4273	0.1944	0.2262

March	-0.8853	-0.4122	-0.3663	1.0106	0.3106
April	-0.9215	-0.2543	-0.2546	0.6305	0.3993
May	-1.1515	-0.2042	-0.2236	1.0535	0.4299
June	-1.0796	-0.3047	-0.3207	0.6937	0.3328
July	-0.6417	-0.1329	-0.1123	0.4376	0.2345
August	-0.8866	-0.0579	-0.0757	0.4476	0.2806
September	-0.9325	-0.0712	-0.1385	0.4114	0.3081
October	-0.7938	-0.0531	-0.1058	1.2486	0.3548
November	-0.9600	-0.2162	-0.2312	0.2849	0.2906
December	-0.8974	-0.3639	-0.3997	0.2376	0.2524

As seen in Table 14, the mean and median values of the Absorbing Aerosol Index increase in warmer months and decreases in colder months. There is no specific change in the minimum and maximum values. The increase in the dataset's standard deviation indicates that the data's dispersion is high. This is valid for the spring and autumn transition periods between the summer and winter.

Figure 35 represents the monthly boxplots for absorbing aerosol data of Türkiye from May 2018 to July 2022. The use of boxplots was explained under the Figure 13.

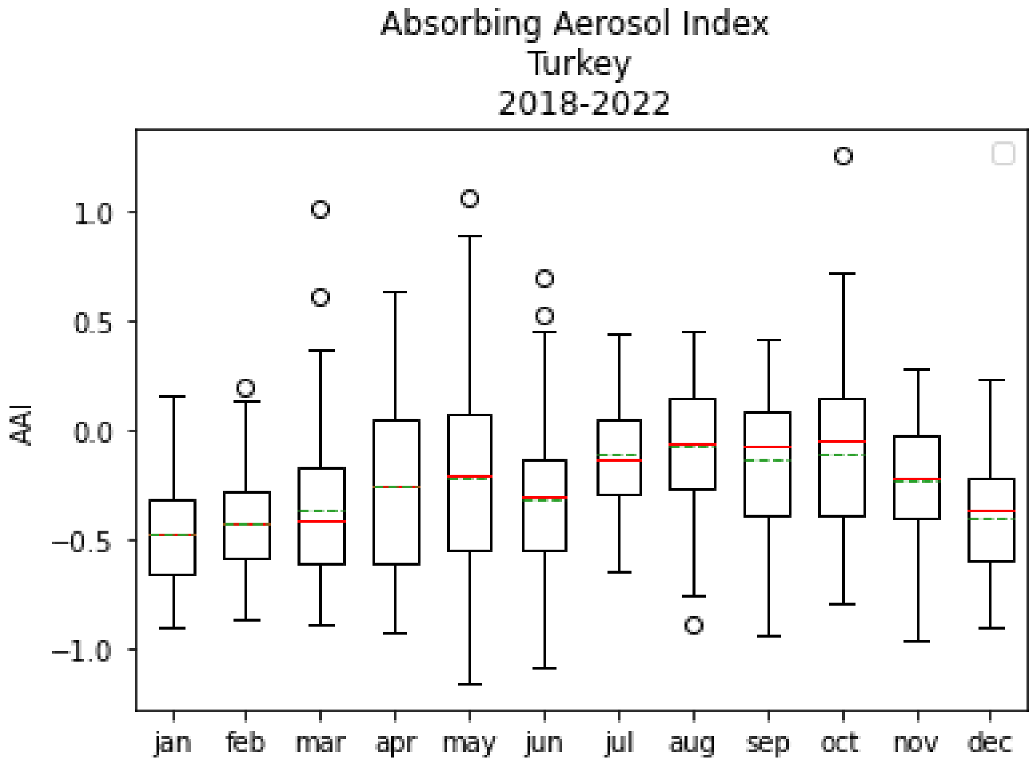

Figure 35. Monthly boxplots of AAI for Türkiye (from 2018 to 2022)

The graph in Figure 35 visualizes the statistics of the four years of Absorbing Aerosol Index data for Türkiye. In general, the data variability was found to be small. However, the dataset varies more in some months, such as April and May. While there are more outliers in months like March and June, there were no outliers in January, April, July, September, November, and December. The mean value is greater than the median value in March and July. This means that the distribution of the dataset is positively skewed for these months.

4.3. Southern Domains (Domain 3 and Domain 4)

Four domains were selected for the study, as explained in the "Data and Methodology" section of the thesis. These are Eastern Mediterranean Basin, Türkiye, and southern domains. The southern domains for the study area are the "Northern Africa" and the "Northern Arabian Peninsula". In this part of the Results and Discussion section, the absorbing aerosol load over these areas are investigated.

4.3.1. The Northern Africa (Domain 3)

In this section, the AAI data for the Northern Africa between 2018 and 2022 are investigated.

In Figure 36, four years of data from Northern Africa can be seen. The following visuals for Northern Africa have been prepared for the coordinates between 20-36^{0}E and 25-35^{0}N. The dataset is extracted for the same location. The range of AAI value in the legend has been arranged according to the minimum and maximum values observed during the studied time period, which is between -0.6 and 1. The Saharan Desert is located in this region, the largest hot desert in the world. This desert affects many regions through its dust releases since it covers an area of 9,200,000 km^2. Therefore, there are lots of studies which investigate the effects of dust releases from the Saharan Desert. The natural conditions of this area has been explained in the "Data and Methodology" section of this thesis. Dust releases are driven mainly by Sharav cyclones, and it is explained in the "Monthly and Seasonal Investigation for EMB" part of the "Results and Discussion" section.

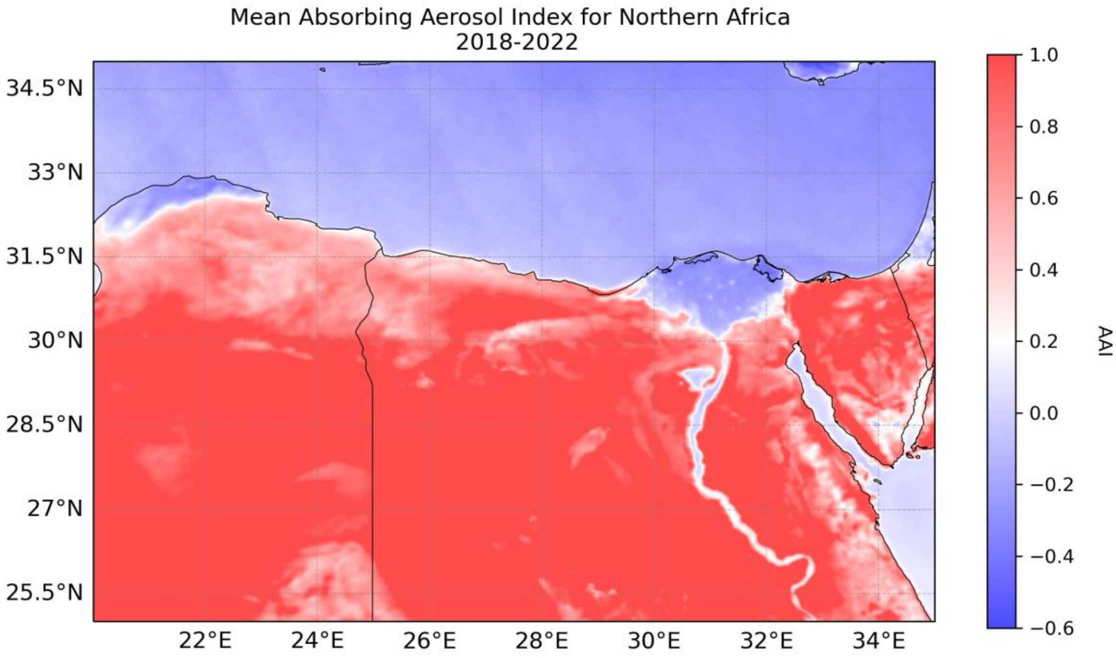

Figure 36. Mean AAI data from May 2018 to April 2022 for Northern Africa

Looking at the Figure 36, which is skimmed from the daily variations, it can be said that the region is generally under the effect of absorbing aerosols (dust) released from the Saharan Desert. However, the aerosol load over The Nile and its riverbed, which are scattering aerosols in this case, is strictly differentiated from the region. For the Northern Africa, it can be said that the inland and coastal areas are experiencing different conditions from each other. The coastal areas, which mostly open to the Mediterranean Sea, are experiencing Mediterranean climate. This climate is famous by the mild and wet winter seasons, and warm and dry summer seasons. Some part of the investigated area, which is occupied by The Nile, is similar to coastal areas.

A statistical summary table for the Northern Africa domain, which includes information about the minimum, median, mean, maximum, and the standard deviation values for years 2018, 2019, 2020, 2021, and 2022, can be seen in Table 15.

At first glance, the high mean value of AAI stands out compared to ones in Türkiye and the Eastern Mediterranean Basin. This situation, although the value is very high, was not unexpected since this area has the greatest deserts in the world. The maximum and the minimum values are representing the reality of this situation. Similarly, the mean standard deviation value is higher than both in the whole Eastern Mediterranean Basin and in Türkiye. This was also expected due to the unexpected dust releases occurring in the area.

Table 15. Statistical summary of the AAI values of all the studied years for the Northern Africa domain

Years*	Minimum	Median	Mean	Maximum	Standard Deviation
2018	-0.11236	0.784996	0.751761	1.738375	0.457123
2019	-0.20797	0.606816	0.638464	2.070134	0.380002
2020	-0.25235	0.712199	0.641863	2.010613	0.414671
2021	-0.36979	0.714007	0.687601	1.919255	0.44342
2022	-0.21539	0.760859	0.631362	1.598172	0.421692

*For years 2018 and 2022, the Reprocessing data was not available for the whole year during the conduction of this study. For 2018, the data is available from May to the end of December; and for 2022, the data was available from January to the end of July.

When this table is investigated in itself, it was seen that, until 2021, the mean AAI value is decreased for this domain. However, in 2021, an increase has been observed before the decrease in 2022. In 2019, the standard deviation of the dataset decreased, meaning that the variation of the data in the dataset has linearly decreased. This value increased again in 2022, indicating a variability between data, yet the value is still under the value in 2018. The same situation is valid for the median value. The standard deviation is correlated with the changes in the minimums and maximums. As these values decrease and increase, the variability (standard deviation) increases in the dataset.

Figure 37 represents the annual boxplots for Absorbing Aerosol Index data of Northern Africa from May 2018 to July 2022. The use of boxplots was explained under the Figure 13.

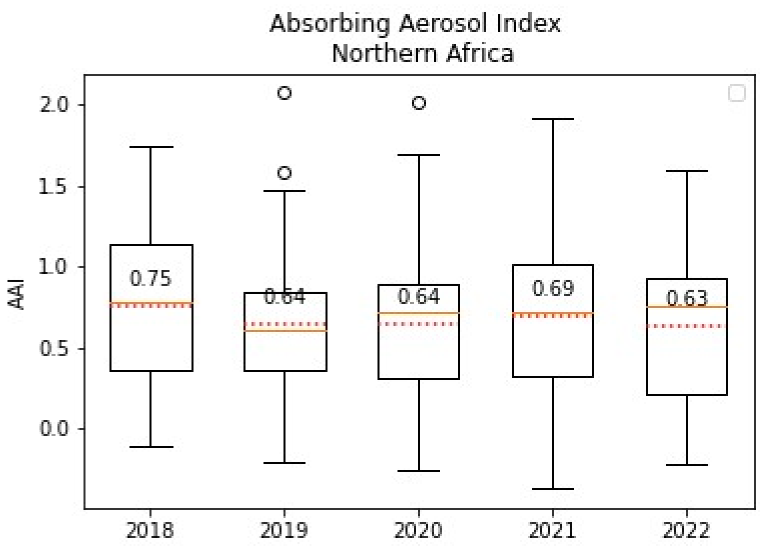

Figure 37. Annual boxplots of AAI for Northern Africa (from 2018 to 2022)

In the boxplot in Figure 37, it can be seen that the outliers are very low in amount, compared to the other domains that investigated so far (The EMB and Türkiye). In 2020 and 2022, the mean values are smaller than median which indicates the negatively skewness of the dataset. The highest mean value belongs to year 2018, due to the missing Reprocessing data in that year. As was explained in the methodology part of this thesis, in year 2018, the reprocessing data was only available from May to December. The Absorbing Aerosol Index value is generally smaller in colder months such as January and February, which is absent in the dataset of 2018. The warmer months available in 2018, that contains higher amounts of AAI value, increase the mean value of the dataset.

The time series representation of four years of AAI data for Northern Africa can be seen in Figure 38. The NaN values, which are present in the dataset, are taken as zero in order to observe the variations time wise.

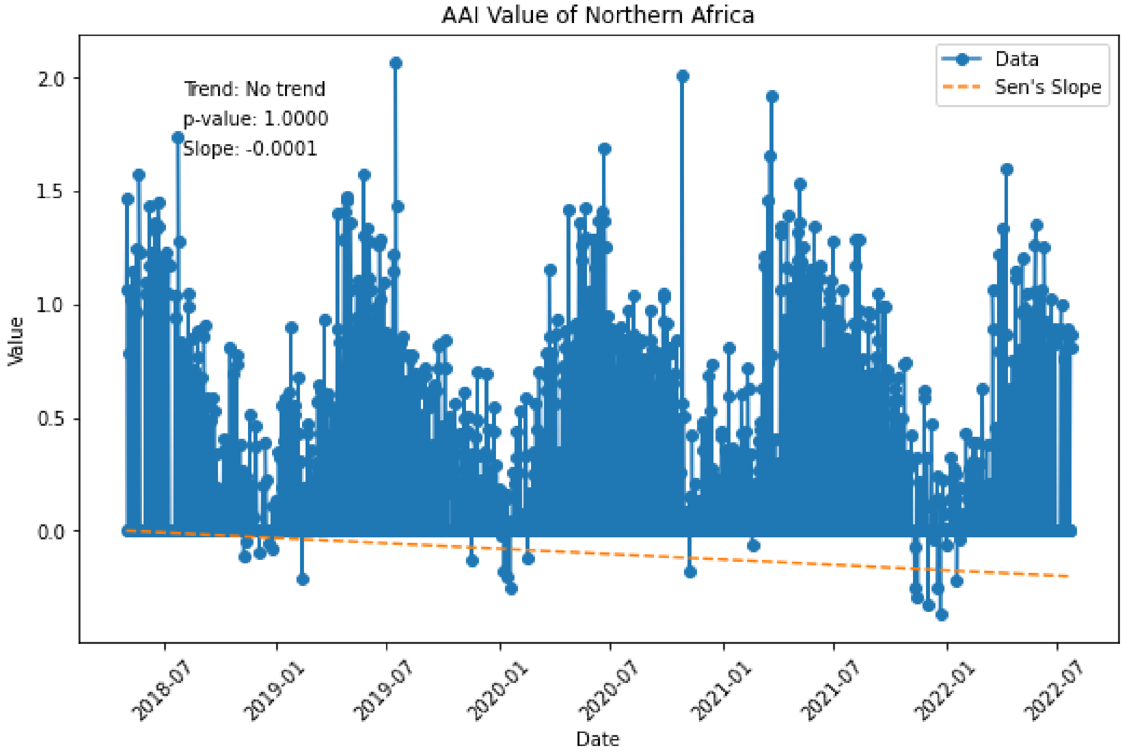

Figure 38. Time series of the mean AAI of Northern Africa for the years between 2018-2022

In Figure 38, it can be seen that the variations in the data are compatible with the meteorological seasons, as explained in Table 7. In all years, outliers are spotted in the cold and warm seasons. These outliers are presented in the “remainder” part of Figure 39, which is the data decomposition. There is a decreasing trend with a slope of -0.0001 observed over the area according to the Sen’s slope. However, the results of Mann-

Kendall test indicate that there are no significant trends over Northern Africa during the studied time period. This can be explained by the NaN values which are highly present in the dataset. Since the absence of data is not regular, a trend cannot be observed.

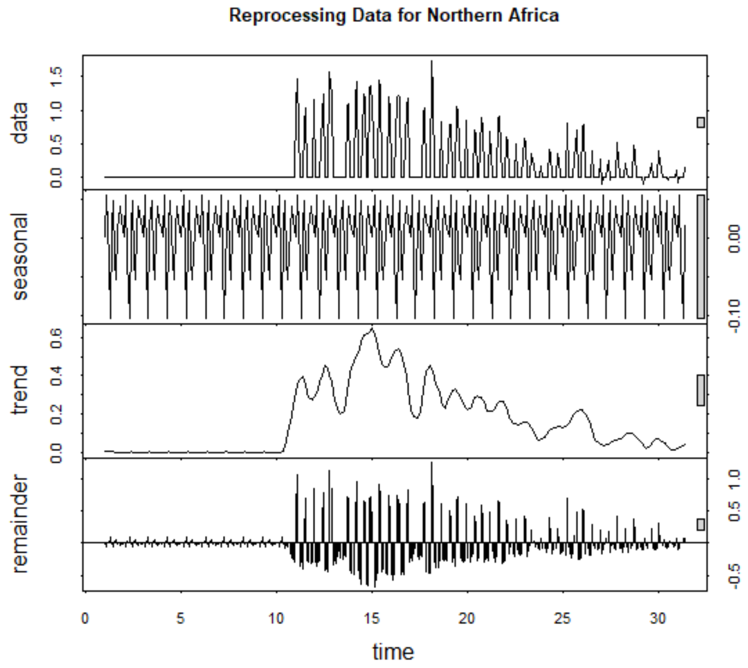

Figure 39. Decomposition of the mean AAI of Northern Africa for the years between 2018-2022

In Figure 39, the trend part of the decomposed dataset does not reflect a regular variation in seasons compared to datasets of the Eastern Mediterranean Basin and Türkiye. This can be caused by that there are no specific trends in this region (as stated by the Sen's slope) due to its deserts, which constantly release dust under the effects of constantly changing atmospheric circulations. However, as can be seen in Figure 41, when the dataset is divided by seasons, trends that are specific to each season have been observed. In the figure below, the seasons have been lined up from winter to autumn, respectively.

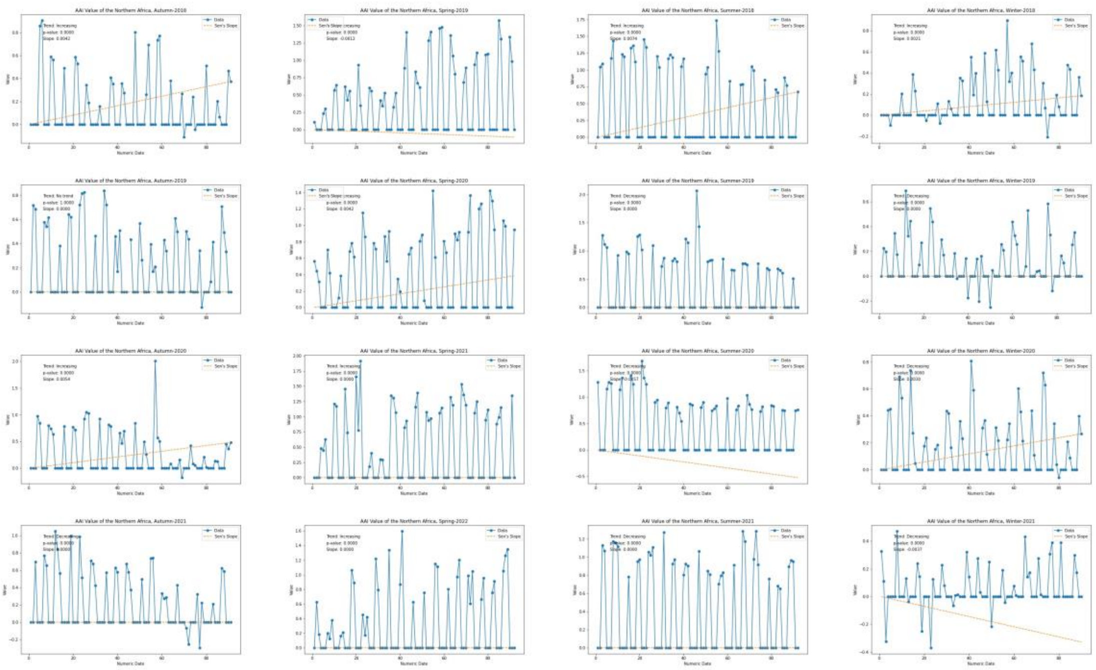

Figure 40. Seasonal trends of AAI in Northern Africa

In the second and third column of the figure, it was seen that in spring and summer seasons of the Northern Africa, the general tendency is an increasing trend. In the fourth column of the figure, which is autumn season, the general tendency is a decreasing trend. These graphs can be viewed separately in the Appendix part of this thesis.

In Figure 41, data visuals representing the monthly distribution of the mean AAI over Northern Africa are shown from January to December.

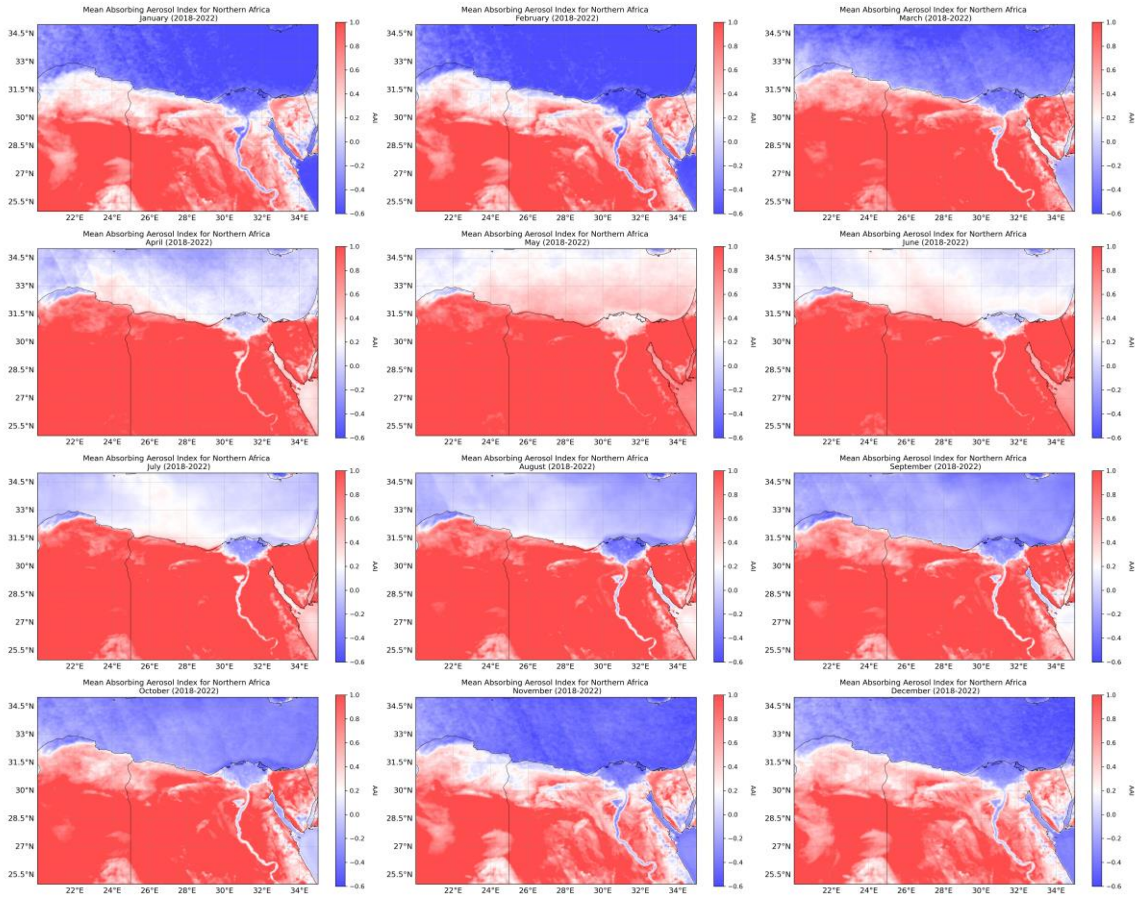

Figure 41. Monthly mean of the AAI on Northern Africa from 2018 to 2022

In this region, apart from the absolute dominance of absorbing aerosols from March to July, the African Easterly Waves are dominant from March to October, which are effective in this region, as can be seen in Figure 41. These waves are the combination of baroclinic (caused by midlatitude storms) and barotropic (caused by excessive horizontal winds) instability of African Jet, which is a region in the lower atmosphere of West Africa where the seasonal wind speed is maximum. The wind blows easterly (Arnault & Roux, 2011) (American Meteorological Society, n.d.).

Aerosol variations which affect the meteorological seasons in Northern Africa are coherent with the introduced meteorological seasons for the Northern Hemisphere, explained in Table 7.

Figure 42 represents the monthly boxplots for Absorbing Aerosol Index data of Northern Africa from May 2018 to July 2022. The use of boxplots was explained under the Figure 13.

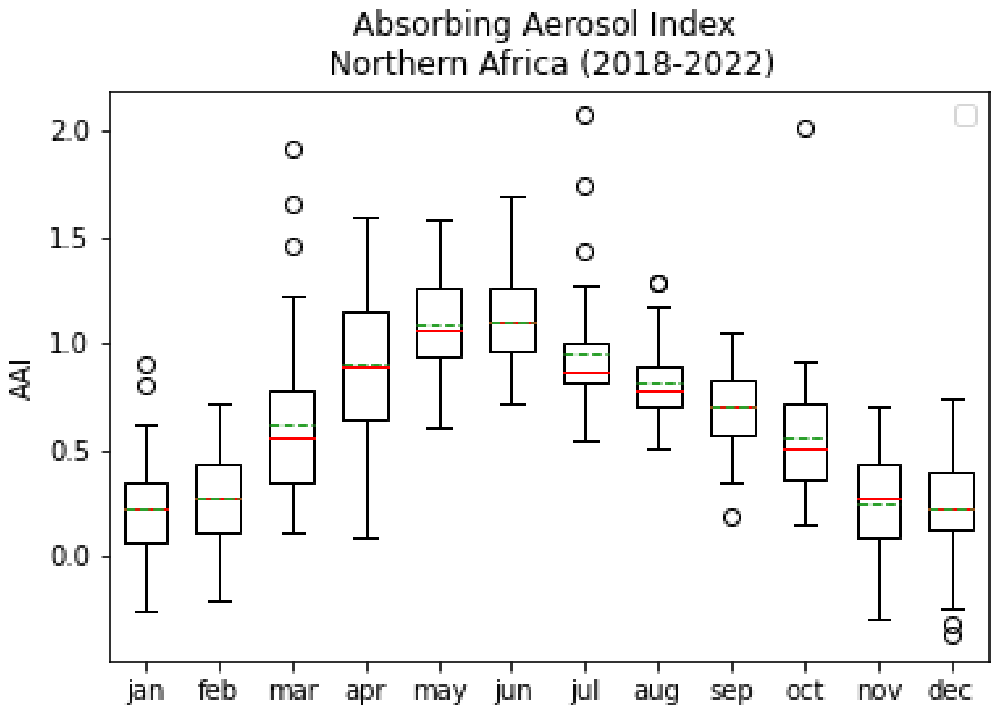

Figure 42. Monthly boxplots of AAI for Northern Africa (from 2018 to 2022)

The graph in Figure 42 visualizes the statistics of the four years of Absorbing Aerosol Index data for Northern Africa. In general, the data variability was minor except in March and April. While there are more outliers in months like March and July, there were no outliers in February, April, May, June, and November. The mean value exceeds the median in March, April, May, July, August, and October. This means that the distribution of the dataset is positively skewed for these months.

Figure 43 shows the seasonal mean values in Northern Africa for AAI from 2018 to 2022.

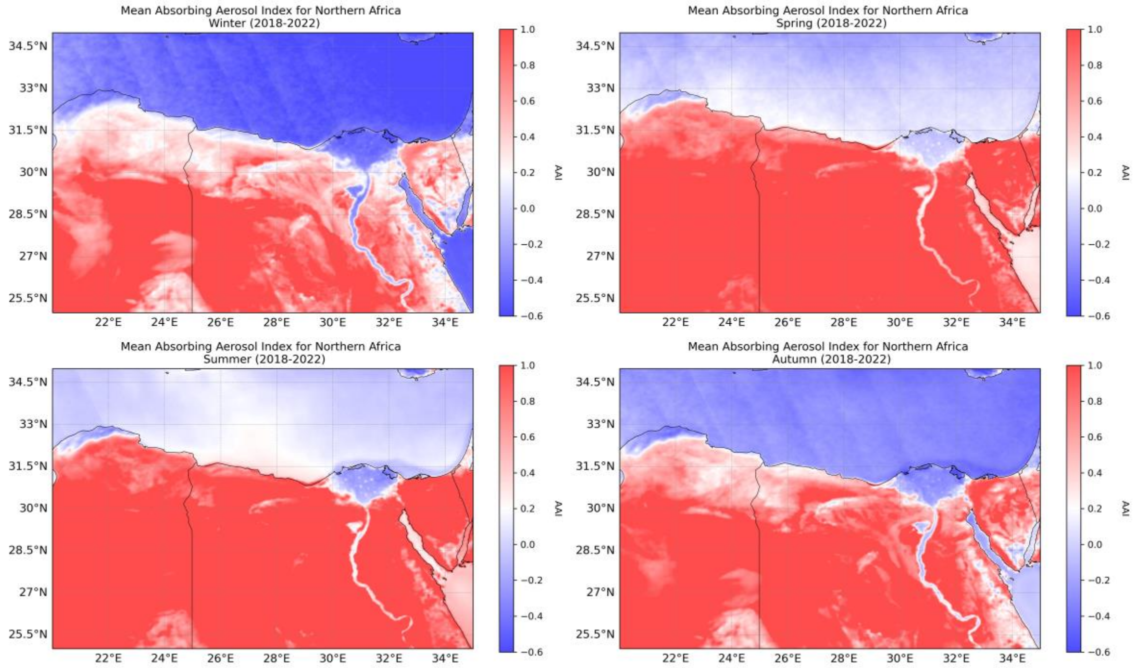

Figure 43. Seasonal mean of the AAI on Northern Africa from 2018 to 2022

The Sentinel-5P AAI data was found to comply with meteorological seasons for Northern Africa. As expected, the absorbing aerosol load is higher in the spring and summer seasons and lower in the autumn and winter seasons. Although there are variations annually, the data was in similar patterns for all the seasons.

4.3.2. The Northern Arabian Peninsula (Domain 4)

In this section, the AAI data for the Northern Arabian Peninsula between 2018 and 2022 are investigated.

In Figure 44, the image of the four years of AAI data from the Northern Arabian Peninsula can be seen. The following visuals for Northern Arabian Peninsula have been prepared for the coordinates between 35-50^{0}E and 25-35^{0}N. The dataset is extracted for the same location. The range of AAI value in the legend has been arranged according to the minimum and maximum values observed during the studied time period, which is between -0.6 and 1. The Arabian Peninsula is mainly covered by deserts. One of which is The Nefud Desert, which is located in the northern parts. The conditions of this region has been explained in the “Literature Review” section.

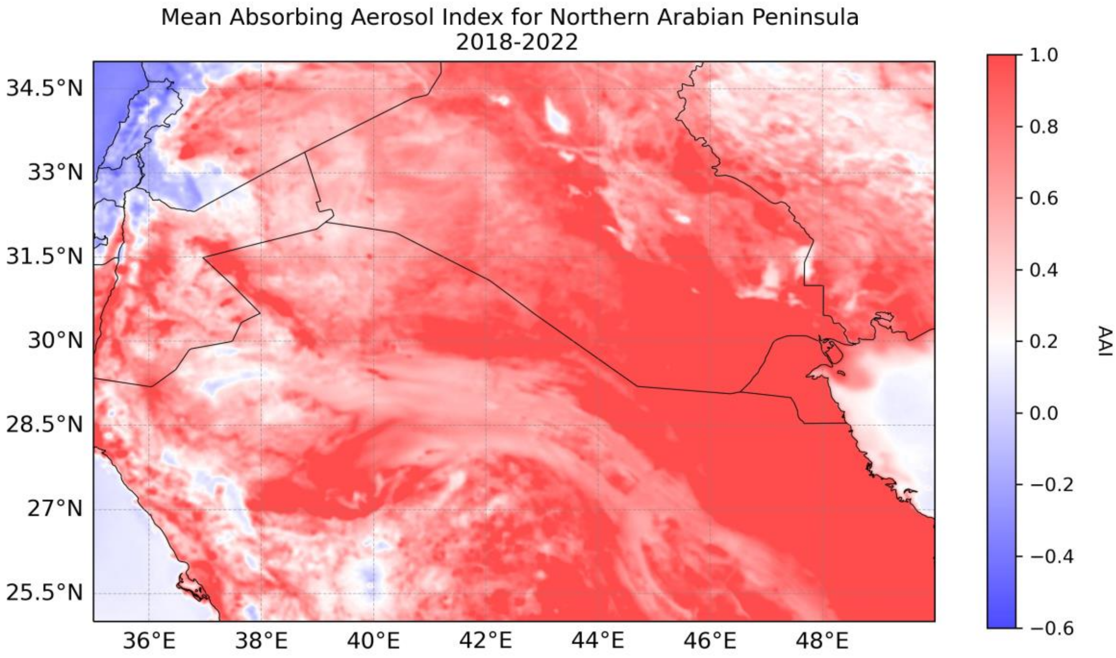

Figure 44. Mean AAI data from May 2018 to April 2022 for Northern Arabian Peninsula

Looking at Figure 44, which is skimmed from the daily variations, the region is generally under the effect of absorbing aerosols (dust), mainly in its southeast regions. However, the absorbing aerosol load over the Red Sea (southwest corner of the area) and the Persian Gulf is lower than in other parts of the region. The effects of the wind on dust storms can be seen over the middle parts of the map, which coincides to the northern parts of Saudi Arabia.

The minimum, median, mean, maximum, and standard deviation values for years 2018, 2019, 2020, 2021, and 2022 in the Northern Arabian Peninsula can be seen in Table 10.

Table 16. Statistical summary of the AAI values of all the studied years for the Northern Arabian Peninsula domain

Years	Minimum	Median	Mean	Maximum	Standard Deviation
2018	-0.52897	0.682271	0.640031	1.585476	0.522791
2019	-0.55599	0.501188	0.502044	1.366819	0.418422
2020	-0.61822	0.646073	0.577583	1.397705	0.424902
2021	-0.52327	0.741173	0.650858	1.579672	0.438977
2022	-0.58318	0.912491	0.827726	1.745928	0.537655

*For years 2018 and 2022, the Reprocessing data was not available for the whole year during the conduction of this study. For 2018, the data is available from May to the end of December; and for 2022, the data was available from January to the end of July.

Until 2019, the mean AAI value decreased for the Northern Arabian Peninsula. However, in 2020, an increase has been observed until 2022. In 2019, the standard deviation of the dataset decreased, meaning that the variation in the dataset has linearly decreased. This value started to increase again in 2022, indicating variability in the dataset. The same situation is valid for the median value.

Figure 45 represents the annual boxplots for Absorbing Aerosol Index data of Northern Arabian Peninsula from May 2018 to July 2022. The use of boxplots was explained under the Figure 13.

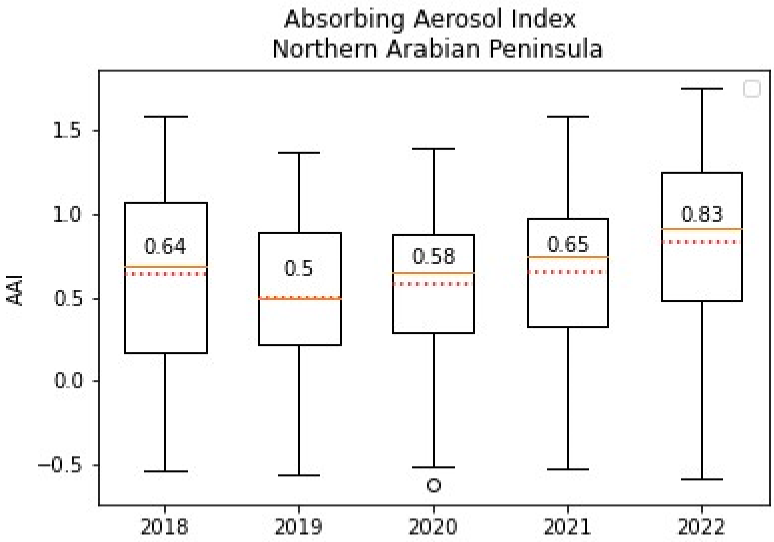

Figure 45. Annual boxplots of AAI for Northern Arabian Peninsula (from 2018 to 2022)

In Figure 45, it can be seen that there are no outliers, except for one outlier in year 2020. It means that there was no unexpected event in Northern Arabian Peninsula over the studied years. The mean values are seeming similar to each other, except for year 2022, which has missing data. As was explained in the methodology part of this thesis, in year 2022, the reprocessing data was only available from January to July. The Absorbing Aerosol Index value is generally smaller in colder months such as October, November, and December, which is absent in the dataset of 2022. The warmer months available in 2022 (spring and summer months), that contains higher amounts of AAI value, increase the mean value of the dataset.

The time series representation of four years of AAI data for the Northern Arabian Peninsula can be seen in Figure 46. The NaN values, which are present in the dataset, are taken as zero in order to observe the variations time wise.

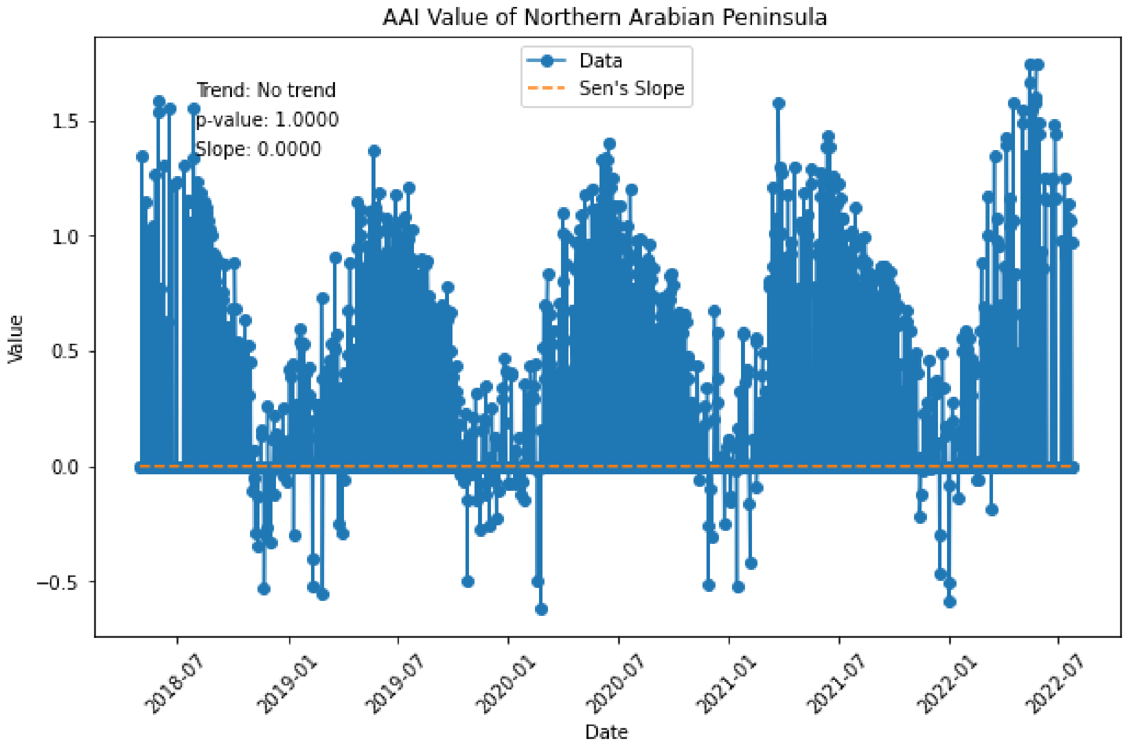

Figure 46. Time series of the mean AAI of Northern Arabian Peninsula for the years between 2018-2022

In Figure 46, it can be seen that the variations in the data are compatible with the meteorological seasons of the Northern Hemisphere, as explained in Table 7. In all years, outliers are spotted in the cold and warm seasons. These outliers are presented in the "remainder" part of Figure 47, which is the data decomposition. The results of Mann Kendall test and Sen's Slope, there are no significant trends observed in the Northern Arabian Peninsula, during the studied time period. This can be explained by the NaN values which are highly present in the dataset, as was in the Northern Africa. Since the absence of data is not regular, a trend cannot be observed.

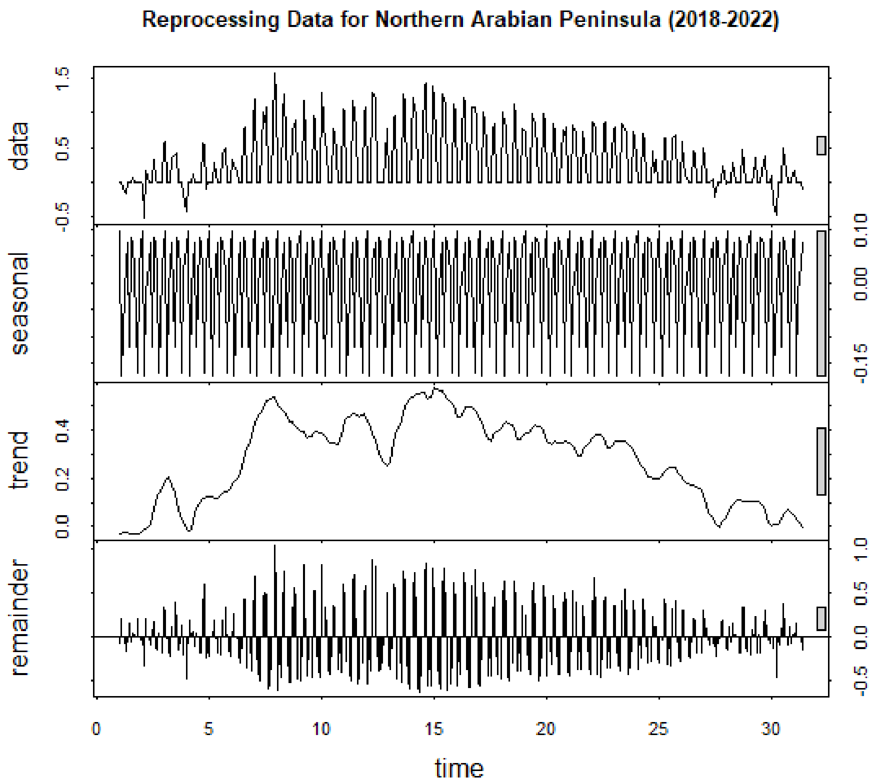

Figure 47. Decomposition of the mean AAI of Northern Arabian Peninsula for the years between 2018-2022

In Figure 47, trend part of the decomposed dataset is similar to those in Figure 39, and not reflecting a regular variation in terms of seasons, compared to datasets of Eastern Mediterranean Basin and Türkiye. This can be caused by there are no specific trends in this region due to its deserts which are constantly releasing dust under the effects of constantly changing atmospheric circulations. However, as can be seen in Figure 48, when the dataset is divided by seasons, trends that are specific to each season have been observed. In the figure below, the seasons have been lined up from winter to autumn, respectively.

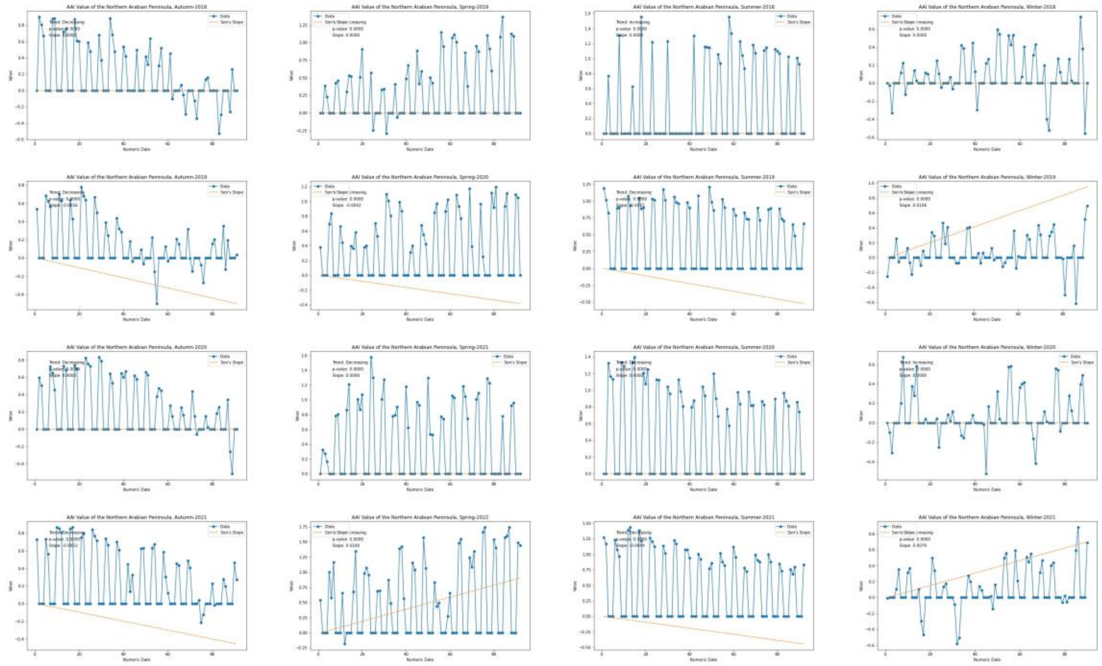

Figure 48. Seasonal trends of AAI in Northern Arabian Peninsula

In the second and third column of the figure, it was seen that in spring and summer seasons of the Northern Arabian Peninsula, the general tendency is a decreasing trend. In the fourth column of the figure, which is autumn season, the general tendency is an increasing trend. Despite the effort, Mann Kendall test did not find any significant trend in some seasons of some years, such as autumn season of year 2018. These graphs can be viewed separately in the Appendix part of this thesis.

Figure 49 shows data visuals representing the distribution of the mean AAI over the Northern Arabian Peninsula every month from January to December.

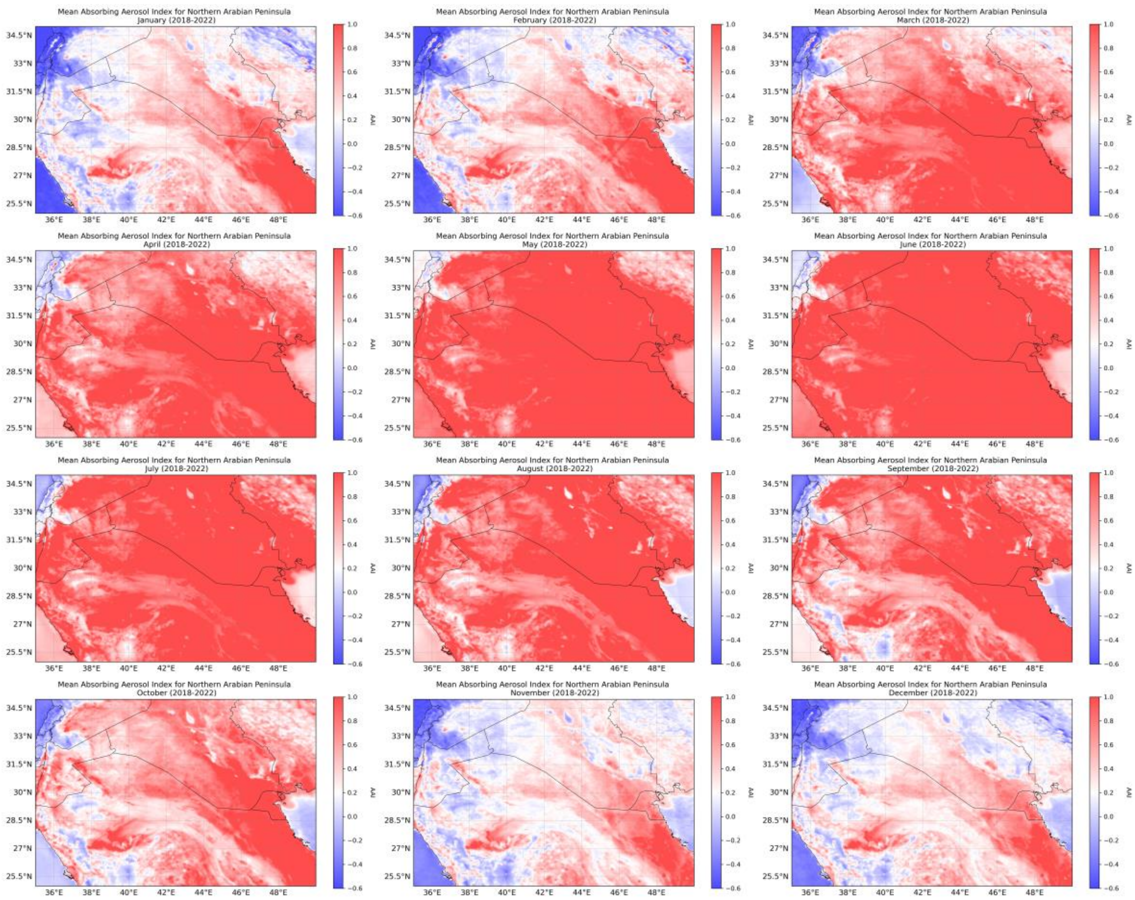

Figure 49. Monthly mean of the AAI on Northern Arabian Peninsula from 2018 to 2022

In this region, the absorbing aerosol load is dominant from March to September, as seen in Figure 49. However, there are high annual variations present in this region. This is because the aerosols over this region are influenced by warm El Niño-Southern Oscillation (ENSO), contributing to higher variability in aerosols (Kumar et al., 2018).

Figure 45 represents the monthly boxplots for Absorbing Aerosol Index data of Northern Arabian Peninsula from May 2018 to July 2022. The use of boxplots was explained under the Figure 13.

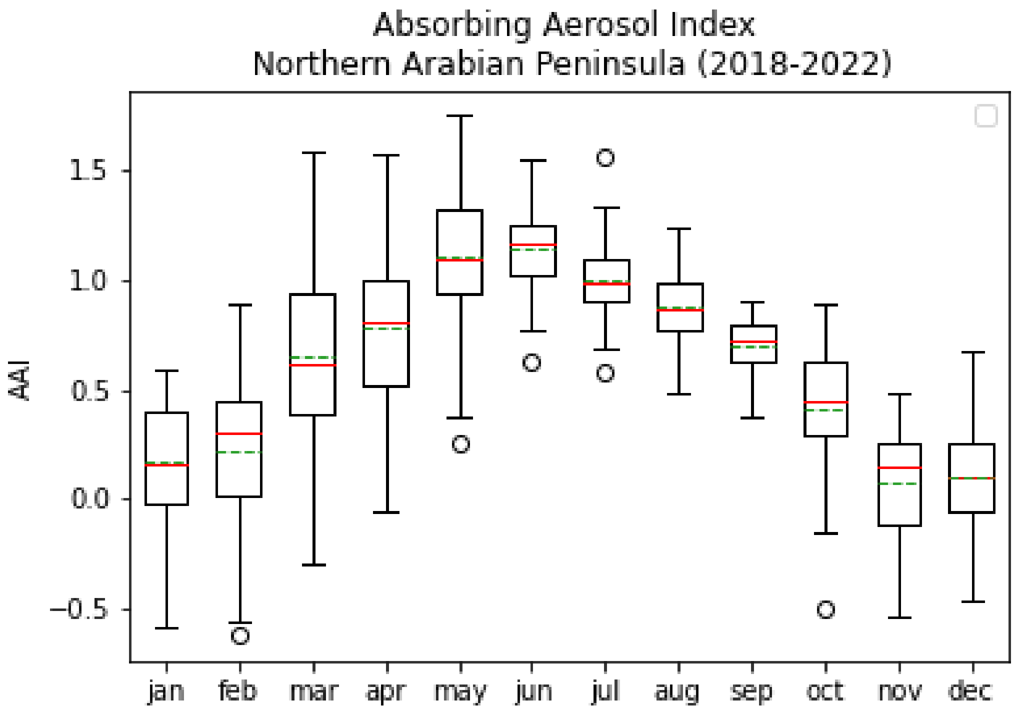

Figure 50. Monthly boxplots of AAI for Northern Arabian Peninsula (from 2018 to 2022)

In general, the data variability was minor except in March and April. There are no outliers in months like January, March, April, August, September, November, and December. Compared with the other domains investigated, this dataset has very few outliers. The mean value is greater than the median value in March. This means that the distribution of the dataset is positively skewed for March. For the remaining months, the distribution is negatively skewed.

Figure 51 shows the seasonal mean values in Northern Arabian Peninsula for AAI from 2018 to 2022.

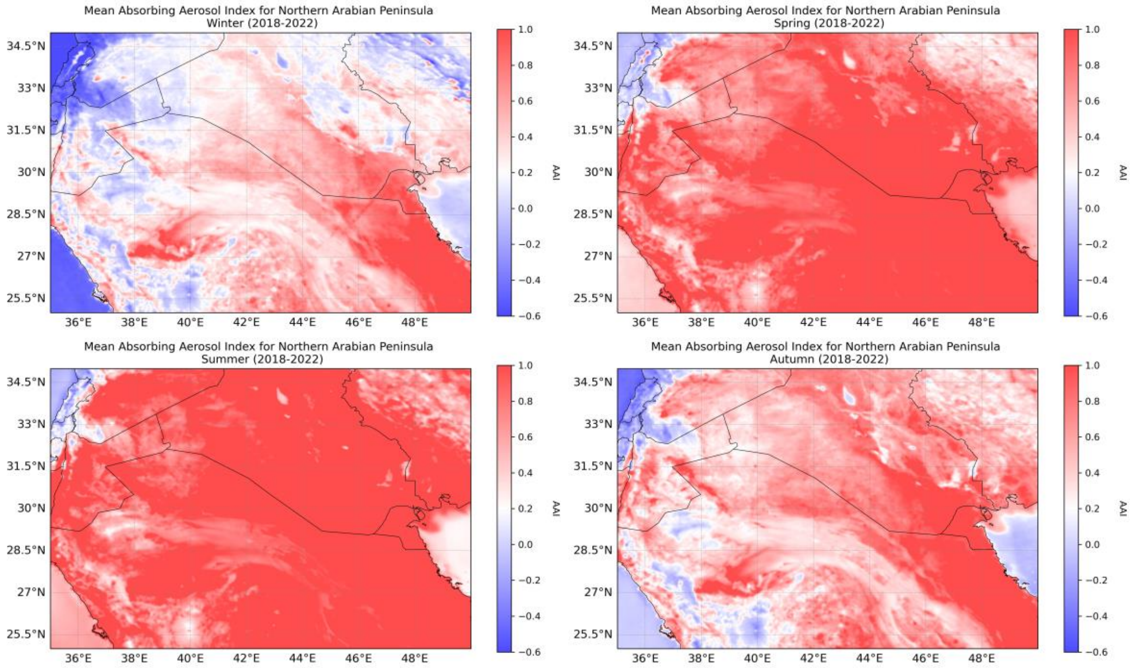

Figure 51. Seasonal mean of the AAI on Northern Arabian Peninsula from 2018 to 2022

The Sentinel-5P AAI data was also found to comply with meteorological seasons for the Northern Arabian Peninsula. As expected, the absorbing aerosol load is higher in the spring and summer seasons and lower in the autumn and winter seasons. Although there are variations annually, the data was in similar patterns for all the seasons.

4.4. Case Studies

In this part of the “RESULTS AND DISCUSSION” section, three cases related to aerosols were investigated. The first is a dust release from Algeria between 23 and 26 April 2019. The second one is the forest fires in the southeast regions of Türkiye in the summer of 2021. The last case is another dust release affecting the Northern Arabian Peninsula in 2022.

4.4.1. Dust Episode Between 23 and 26 April 2019

Between 23 and 26 April 2019, a dust episode was observed over the Eastern Mediterranean Basin. This episode mainly affected the western part of Türkiye. In a study conducted in Türkiye, this episode’s source and effects were investigated with the help of a MODIS spectrometer on the Aqua satellite and NMMB/BSC-Dust model (Oğuz & Pekin, 2019). It was seen that, on 19 April 2019, strong winds that can create dust activity were present over Algeria. The Low-Pressure Centers forming over the country have provided a suitable condition for mixing dust in the atmosphere. This thesis clearly observed this dust episode over the Eastern Mediterranean Basin with the Absorbing Aerosol Index data retrieved from the Sentinel-5P satellite. On these days, between 23 and 26 April, the TROPOMI was overpassing the related area between 09:00 and 10:00 Coordinated Universal Time (UTC).

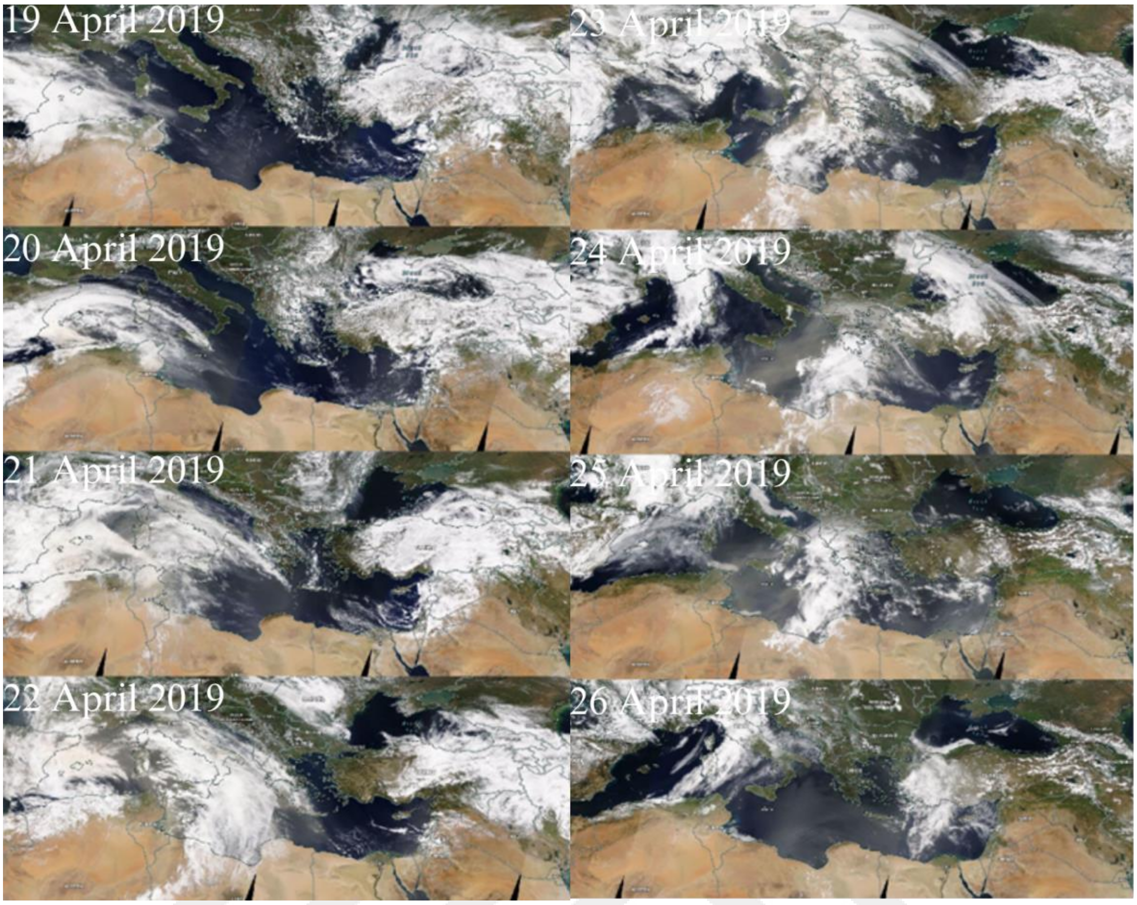

Figure 52. Dust Episode over the Eastern Mediterranean Basin between 23 and 26 April 2019, MODIS (true-color image)

In the left side of Figure 52, obtained from MODIS, the dust release from Algeria can be seen from 19 April to 22 April 2019. Between 23 and 26 April, the right side of the figure, the effect of this release on the west side of Türkiye can be seen clearly, especially in Denizli province.

In Figure 53, the Multi Model Dust Optical Depth forecast from Barcelona Dust Regional Center for the 26th of April 2019 is shown. The intensity of the dust episode moving towards the west side of Türkiye can be observed clearly.

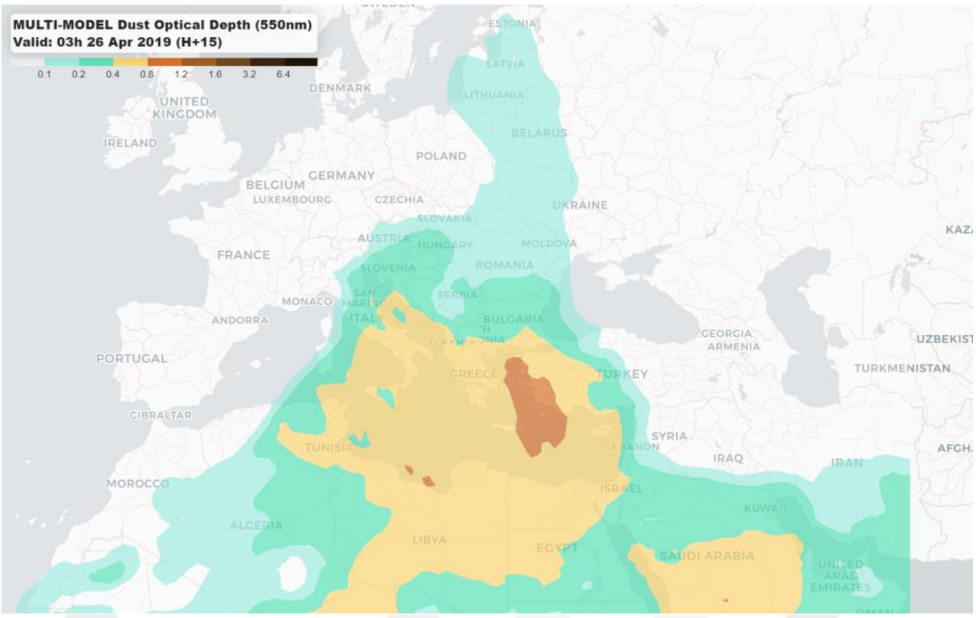

Figure 53. Barcelona Dust Regional Center Multi Model Dust Optical Depth Forecast for 26th of April 2019 (Barcelona Dust Regional Center, n.d.)

The wind speed, temperature, and atmospheric pressure data of Denizli Province has been obtained from NOAA Integrated Surface Database and Airport Weather Stations, and these can be seen in the figures below.

The temperature pattern of Denizli Province in 2019, measured from the Denizli Çardak Airport has been demonstrated in Figure 54.

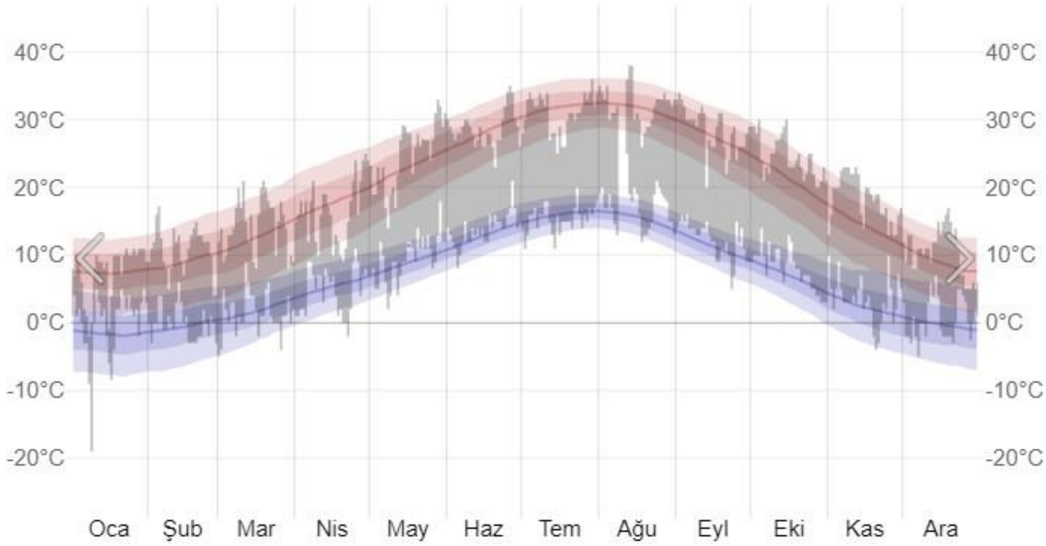

Figure 54. Temperature data from Denizli Çardak Airport in 2021 (Weather Spark, n.d.-a)

The gray lines are the reported temperature range of the day. Red and blue marks indicate the last 24-hour high and lows, respectively. Daily average highs (light red line) and lows (light blue line) from 25 to 75 percentiles of temperatures were placed over the percentile range of 10 to 90. Between 23 and 26 April, the temperature was slightly above the average value measured in the same spot. Additionally, the wind speed on the same spot during the same time period, was reflecting one of the high values in 2019, which can be seen in Figure 55.

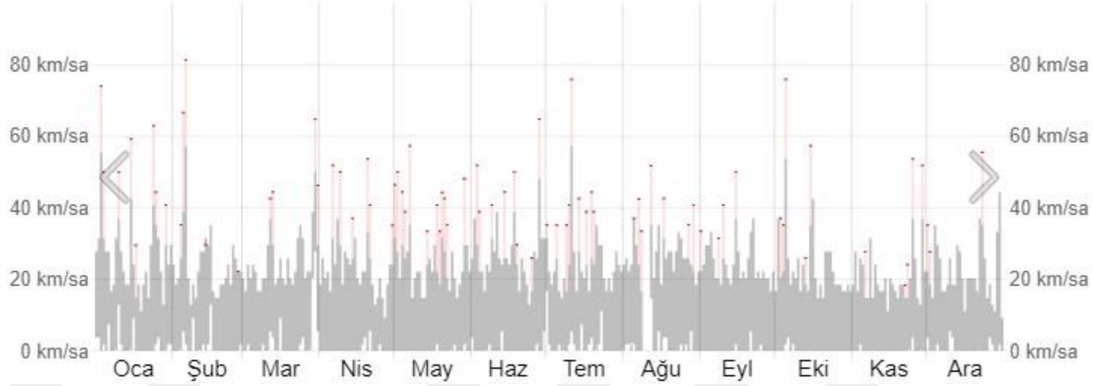

Figure 55. The wind speed measurements from Denizli Çardak Airport in 2019 (Weather Spark, n.d.-a)

The magnitude of the wind speed may have helped the dust release from Algeria to reach the western side of Türkiye. The reason why the wind speed is high on the days where the dust episode occurred, can be explained by the atmospheric pressure. As can be seen in Figure 56, the atmospheric pressure measured in Denizli Çardak Airport was very high, compared to the rest of the year 2019.

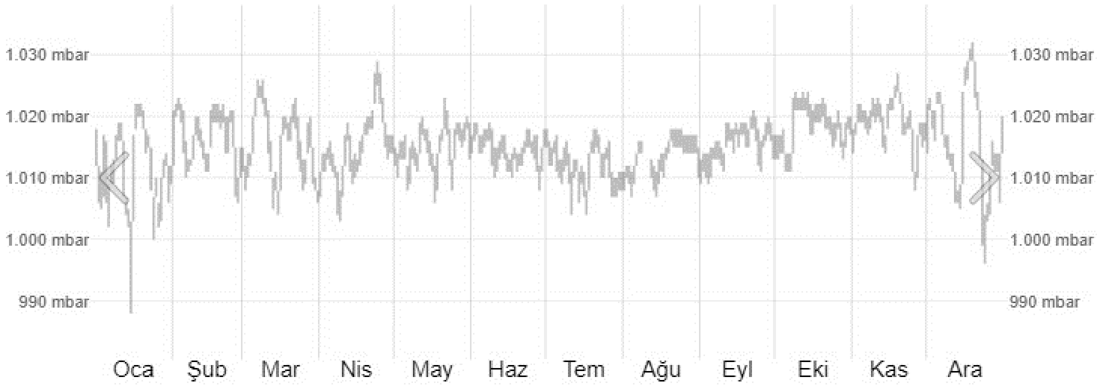

Figure 56. The atmospheric pressure measurements from Denizli Çardak Airport in 2019 (Weather Spark, n.d.-a)

The gray lines on the graph indicates the atmospheric pressure range on that specific day. It can be said that, besides the atmospheric pressure was very high, it did not show any significant change during the day. It remained high.

In Figure 57, the PM10 data obtained from the Continuous Monitoring Center created by the Ministry of Environment, Urbanization, and Climate Change, can be seen.

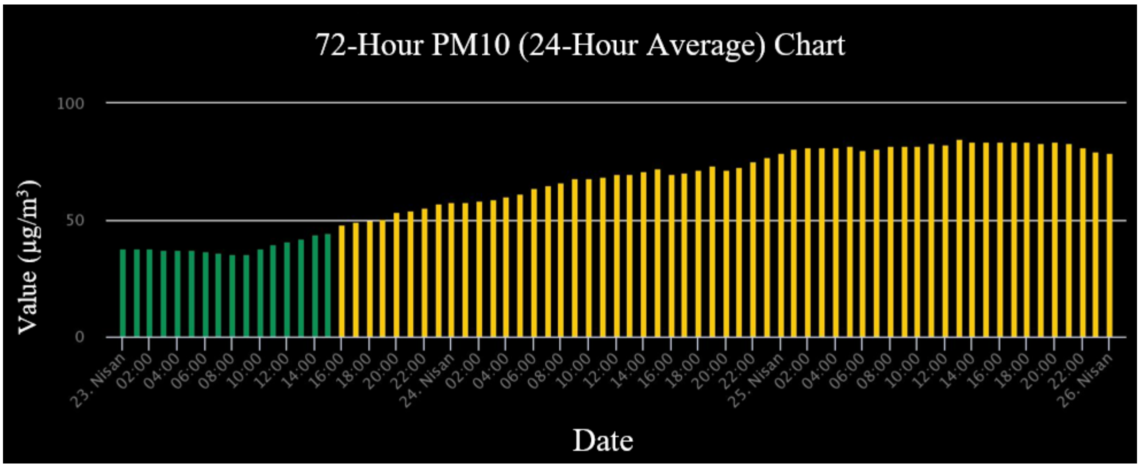

Figure 57. The PM10 data from the Continuous Monitoring Center between 23 and 26 April (The Ministry of Environment Urbanization and Climate Change, n.d.-b)

The graph in Figure 57 shows that the ground measurements captured the dust episode between 23 and 26 April. The PM10 value for these days was higher than the threshold value of 50 µg/m3, determined by the Ministry of Environment, Urbanization, and Climate Change (The Ministry of Environment Urbanization and Climate Change, n.d.-a).

Peshev et al., investigated the effects of this dust episode on Sofia, Bulgaria, which is located within the boundaries of the study area (Zahari Peshev et al., 2022).

In Figure 58, the effects of the dust released from Algeria on the west side of Türkiye between 23 and 26 April are represented with the AAI data of TROPOMI.

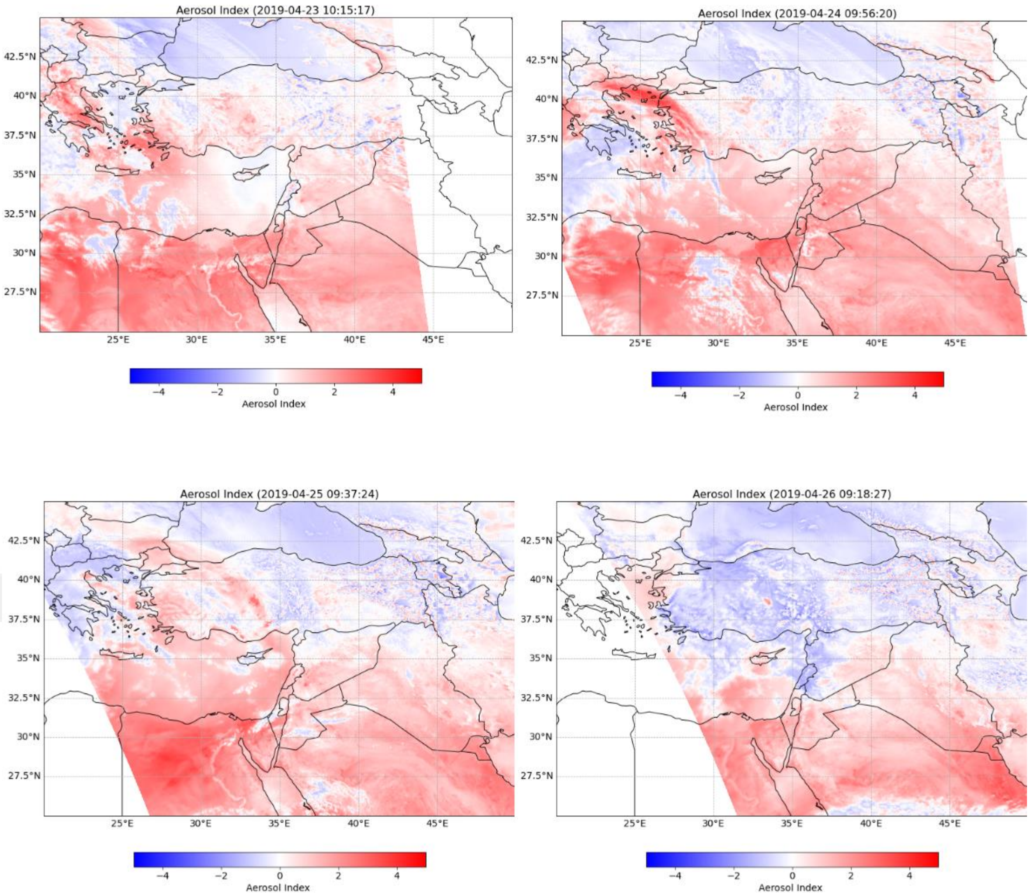

Figure 58. Dust Episode over the Eastern Mediterranean Basin between 23 and 26 April 2019, TROPOMI

The dust released from Algeria reached the atmosphere of the west side of Türkiye on 23 April 2019, followed by its spread to the southwest and central regions of Türkiye on 24 and 25 April, respectively. On 26 April 2019, the effects of the dust released from Algeria seemed to be disappearing from the atmosphere of Türkiye. This dust release affected not only Türkiye but most of the Mediterranean Sea and Northern Africa as it has been well documented by Peshev et al. (2022), Yukhymchuk et al. (2022), and Varga et al. (2021).

4.4.2. Forest Fires Between 28 July and 9 August 2021

Most of the forests located in the Mediterranean climate zone are at risk of forest fires. In 2021, significant forest fires happened in Türkiye during the summer season. These fires were started in Manavgat and Gundogmus districts of Antalya Province, and damaged over 47,824 ha of the area, 59% of the total damage in the first two days (Kavzoğlu et al., 2021). The damage in Muğla was 12,283 ha in Bodrum and 10,234 ha in Marmaris. This disaster was marked as the biggest forest fire in the history of Türkiye (Tuygun et al., 2023). All the mentioned regions (Antalya and Muğla Provinces) are under the influence of Mediterranean climate, which is hot and dry in summers and warm and rainy in winter seasons (Yilmaz et al., 2023b).

In Figure 59, the start of the fires can be seen with Aqua/MODIS data on the left and Sentinel-5P data on the right of the figure. The TROPOMI has overpassed the burned area between 09:00 and 10:30 UTC.

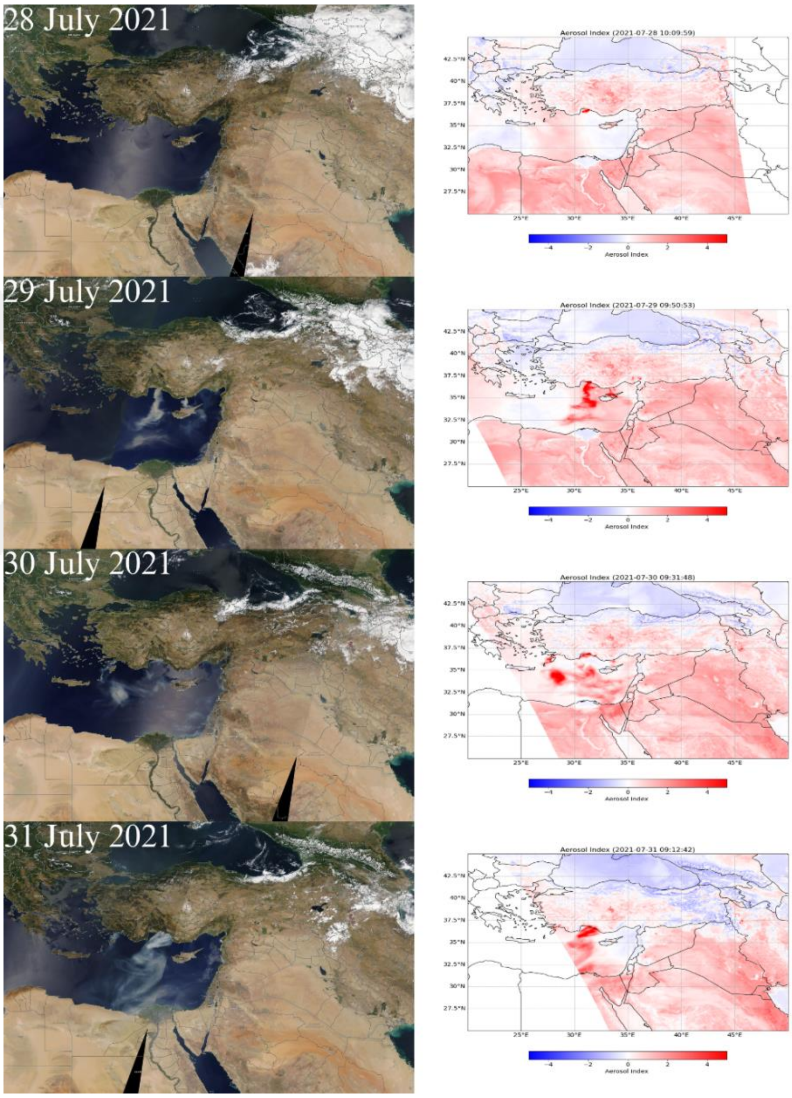

Figure 59. Satellite images of the forest fires in Türkiye, July: Aqua/MODIS (true-color image) on left and Sentinel-5P/TROPOMI on right

In Figure 59, on 28 July 2021, the high absorbing aerosol load can be seen in Manavgat with the data obtained from the Sentinel-5P satellite. At the same time, MODIS data retrieved a dust load sourcing from the same area. On 29 July 2021, the presence of the fires cannot be unseen. This situation continues until approximately 10 August 2021, as shown in Figure 60.

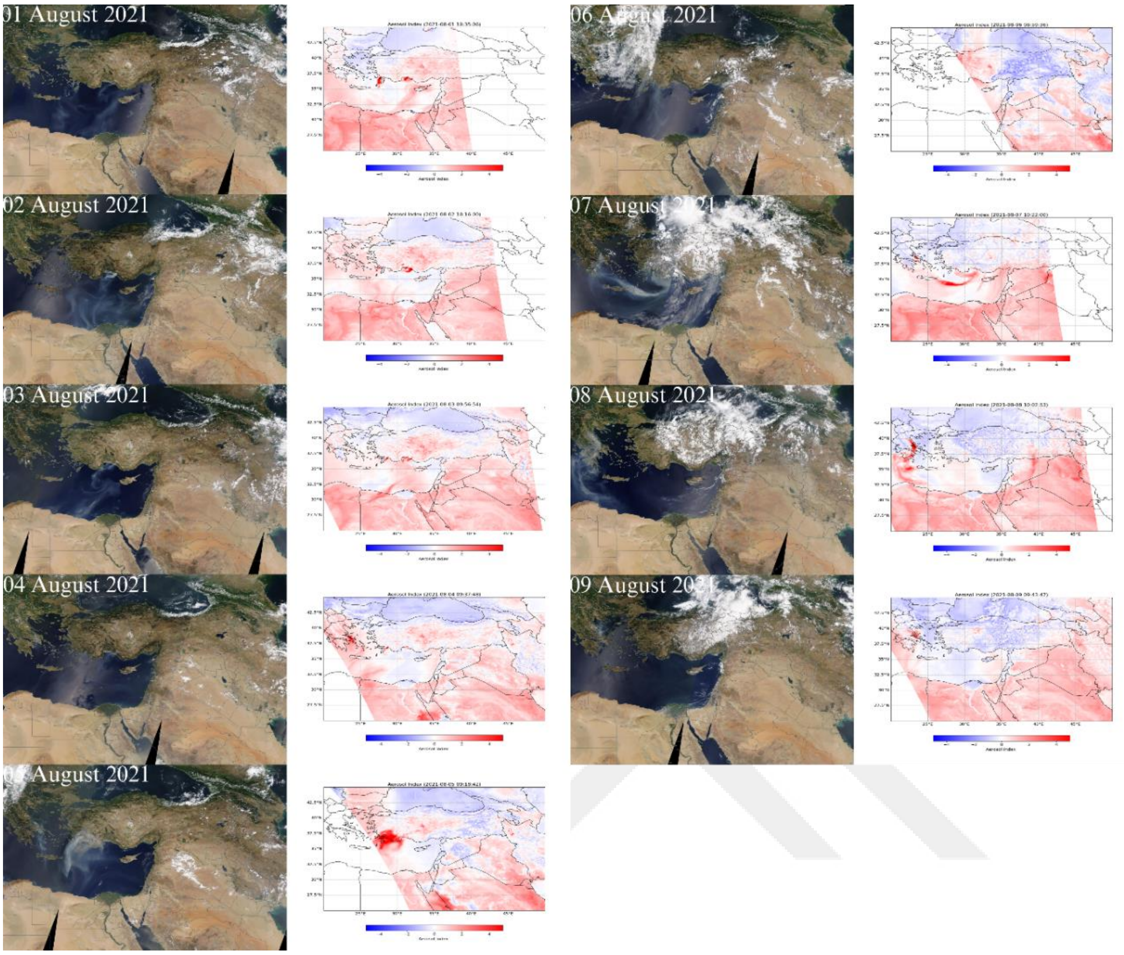

Figure 60. Satellite images (MODIS with true color image and TROPOMI) of the forest fires in Türkiye, August

The similarity between these two columns of data visuals is incontrovertible, which indicates compatibility between the absorbing aerosol load and the intensity and course of fires. The absorbing aerosol load during these fires over the affected area are observed to be 2-3 times higher than the average absorbing aerosol load in these areas. These AAI values are extreme values expected as a result of that great fires. In addition to affecting the regions where they occur, these aerosols were also very effective in the Aegean Sea and the Mediterranean Sea due to the strong winds blowing from the north-west during the fires, as can be seen in Figure 59 and Figure 60.

In Figure 61, the speed of the wind over Manavgat in 2021 can be seen. The gray lines indicate the daily average wind speed, and the red lines indicate the maximum speed of that specific day. This wind speed data and temperature data below, are a combination of weather data from NOAA Integrated Surface Database and Airport Weather Stations.

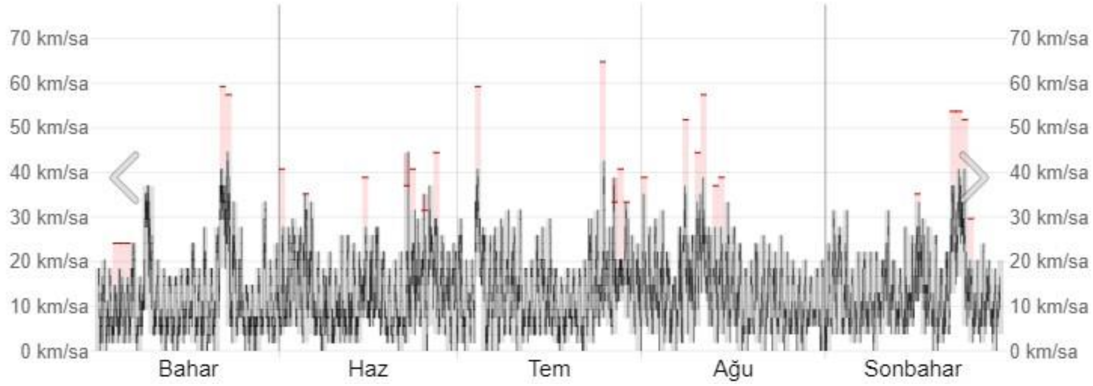

Figure 61. Wind speed in measured in Manavgat in 2021 (Weather Spark, n.d.-b)

The maximum wind speed, which was measured in the late July, when the fires have started, was also the maximum wind speed of year 2021. The high wind speed measures continued until the middle of August, which are the dates when the fires have been taken under control. This wind pattern may be one of the reasons why the fires cannot be contained. Another reason may be the extremely hot weather which is shown in the Figure 62.

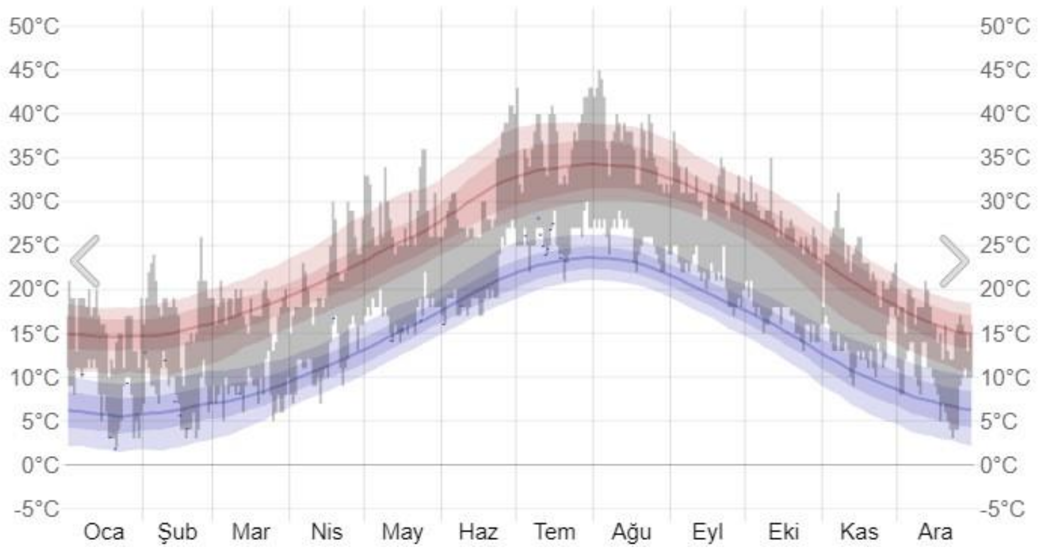

Figure 62. The temperature pattern of the Manavgat in 2021 (Weather Spark, n.d.-b)

The gray lines are the reported temperature range of the day. Red and blue marks indicate the last 24-hour high and lows, respectively. Daily average highs (light red line) and lows (light blue line) from 25 to 75 percentiles of temperatures were placed over the percentile range of 10 to 90. The last days of July and the start of August were the hottest days of Manavgat in 2021, as can be seen Figure 62. When the high wind speed and temperature combined, the fires were become hard to maintain quickly. It can be said that, all the necessary conditions for a fire to occur have met.

As a result of these fires, since a lot of organic structures have been burned, the particulate matter concentration in the atmosphere has been increased drastically. In Figure 63, there is a graph that shows the PM10 measurements between 28 July and 1 August with a 24-hour average.

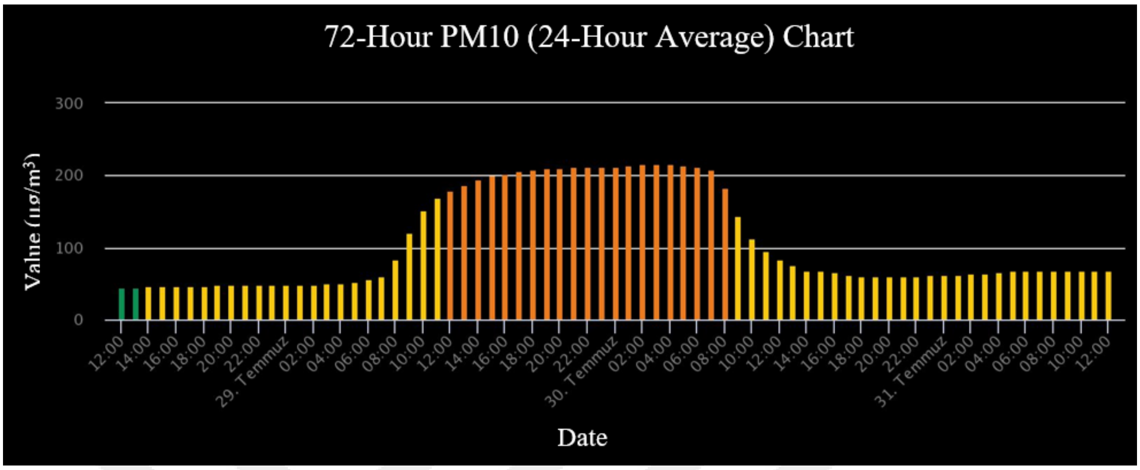

Figure 63. The PM10 data from the Continuous Monitoring Center for the Forest Fires in 2021 (The Ministry of Environment Urbanization and Climate Change, n.d.-b)

The measuring device is located in the Manavgat in Antalya province, where the fires have started. The PM10 value for these days was significantly higher than the threshold value of 50 $\mu g/m^3$, determined by the Ministry of Environment, Urbanization, and Climate Change (The Ministry of Environment Urbanization and Climate Change, n.d.-a).

According to a study which investigates these forest fire (Tariq et al., 2023), fires had a severe impact on air quality, leading to increased AOD and various pollutants, with different regions experiencing varying levels of pollution. Muğla and Antalya were among the most affected areas. The period of most intense fire activity took place from August 4th to August 8th. Another study which investigates the increasing frequency and severity of forest fires in the Mediterranean regions of Türkiye and Greece in recent decades (Bilgiç et al., 2023), found that the largest burned areas were observed in the western Mediterranean regions of Türkiye and Central Greece, covering approximately 50,000 hectares. In Türkiye, most of the damage was sourced from these forest fires.

4.4.3. Dust Episodes on 16 and 23 May 2022

In 2022, two unexpected dust storms were observed on the southeast side of the Eastern Mediterranean Basin in May. A study analyzed the reason for these unexpected dust episodes (Francis et al., 2023). As a result, a new trigger for dust events has been found over the Eastern Mediterranean Basin, a combination of atmospheric rivers and cold drops. While cold drops (cut-off low) are closed cyclonic vortexes that differ from the mainstream (Gaál & Ihász, 2014), atmospheric rivers are long and narrow regions in the atmosphere that allows the transport of water vapor from the tropic regions to another location (National Oceanic and Atmospheric Administration, n.d.). According to this study, dust episodes on 16 and 23 May 2022 were triggered when these atmospheric rivers and cold drops were combined with the diurnal heating in the atmosphere. As a result, convection occurred over the mountains of Türkiye, which triggered the dust episode to be created towards the southern Arabian Peninsula. These dust episodes are observed with data obtained from the MODIS spectroradiometer and the TROPOMI spectrometer, as in Figure 64 and Figure 66.

In Figure 64, the driving force for the dust episode, the wind coming from Northern Africa, can be seen clearly. Even if the geometry of the Sentinel-5P satellite for this day does not cover the whole study area, the area related to the dust episode is captured. The Sentinel-5P satellite was overpassing the area of interest between 08:54 and 10:23 UTC on 16 May and 22 May, respectively.

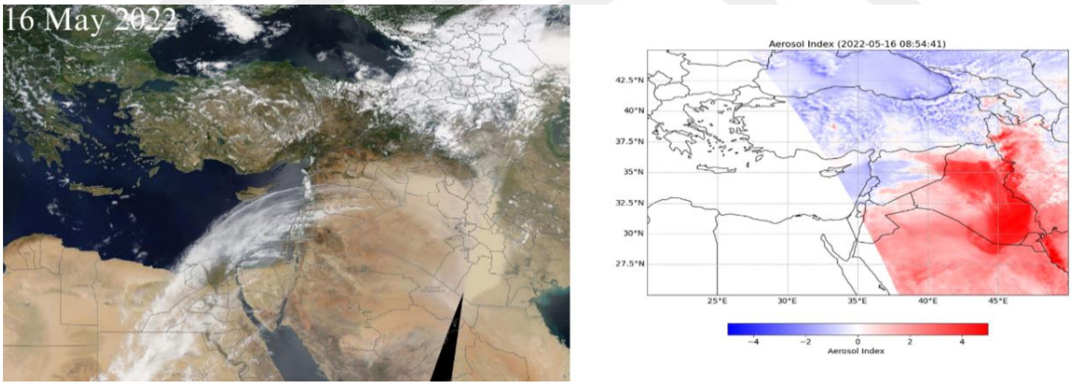

Figure 64. The dust episode observed over the Eastern Mediterranean Basin on 16 May 2022

In Figure 65, The European Organization for the Exploitation of Meteorological Satellites (EUMETSAT), which is an organization that contributes to the systems for meteorological observations, Dust RGB data for May 16 can be seen.

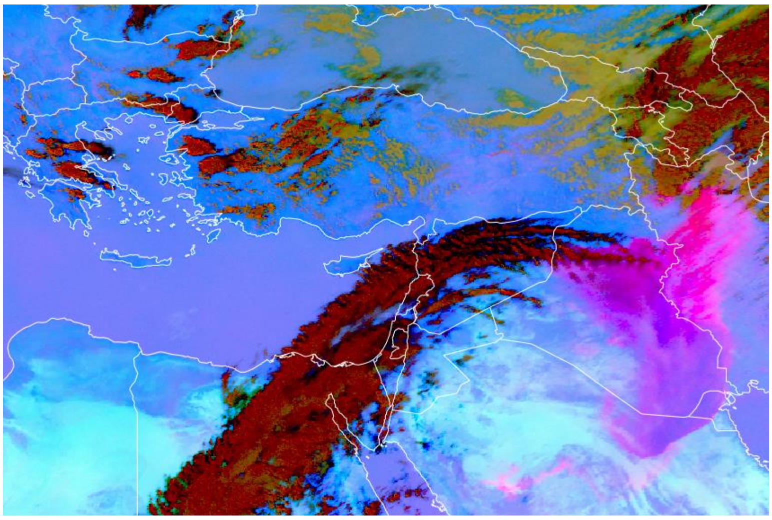

Figure 65. EUMETSAT Dust RGB data for the 16th of May 2022 (EUMETSAT, n.d.)

This Dust RGB data is used to observe the evolution of dust events. In this map, the pink and magenta colors represent the dust. The red color represents the clouds. It can be seen that the Sentinel-5P data is compatible with the EUMETSAT and MODIS.

On the left side, the satellite visuals from MODIS can be seen. On the right side, the daily visual representations of the data retrieved by TROPOMI can be seen. The heavy load of absorbing aerosols in northern Iraq can be differentiated more easily with the help of the TROPOMI data.

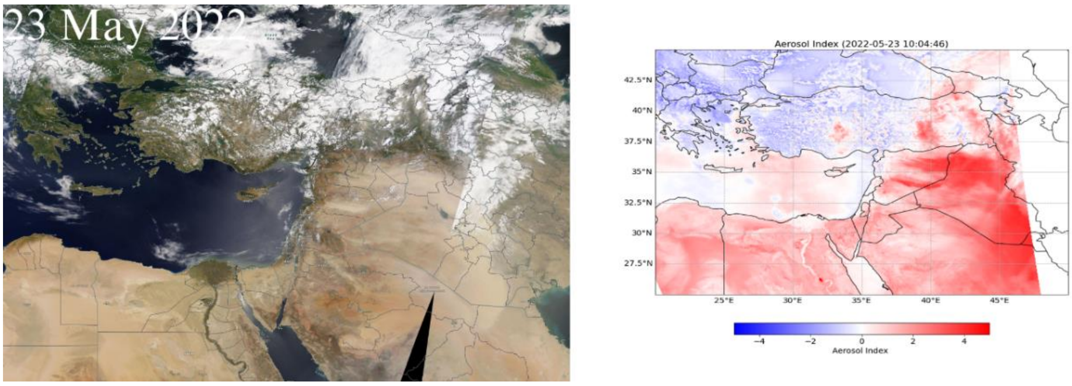

Figure 66. The dust episode observed over the Eastern Mediterranean Basin on 23 May 2022

In Figure 67, the dust episode in the Northern Arabian Peninsula on 23rd May can be seen with the EUMETSAT Dust RGB product.

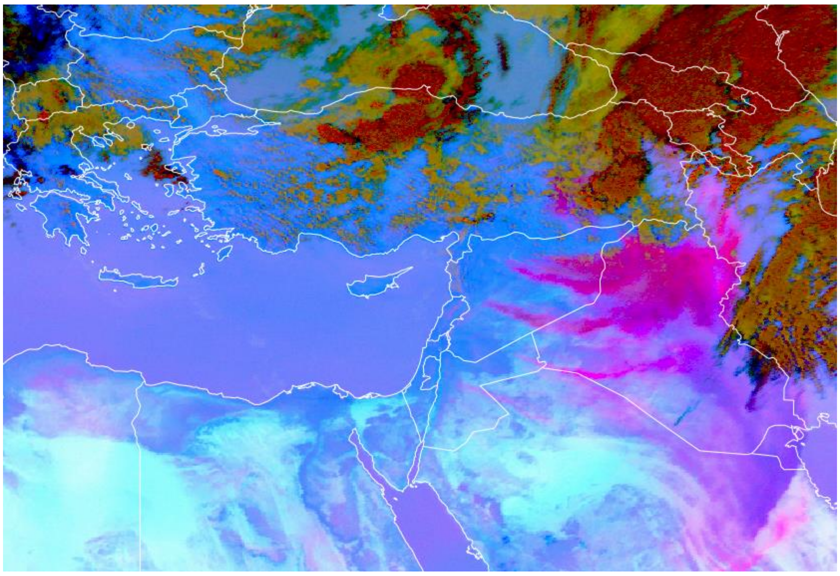

Figure 67. EUMETSAT Dust RGB data for the 23th of May 2022 (EUMETSAT, n.d.)

Both dust episodes are sourced from the dust released from Syria one day before the event. The synoptic scale of the atmosphere between 14 and 24 May 2022 was investigated, and it was found that a cut-off low was observed over the Eastern Mediterranean Basin on 14 May, which was then seen over the Türkiye on 15 and 16 May (Francis et al., 2023).

In Figure 68, the Multi Model Dust Optical Depth forecast from Barcelona Dust Regional Center for the 23th of May 2022 is shown. The intensity of the dust episode moving towards the Northern Arabian Peninsula can be observed clearly.

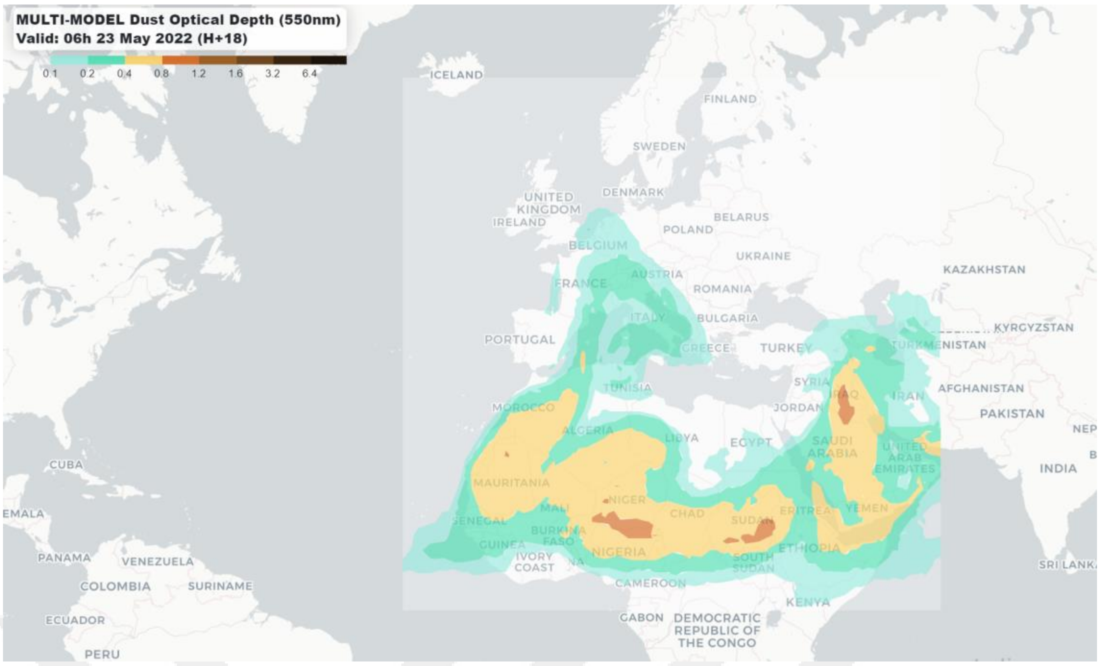

Figure 68. Barcelona Dust Regional Center Multi Model Dust Optical Depth Forecast for 23th of May 2022 (Barcelona Dust Regional Center, n.d.)

Figure 69 shows the temperature, wind speed, and climatologic anomalies measured from an airport (ORSU) in Iraq between 10 and 31 May 2022.

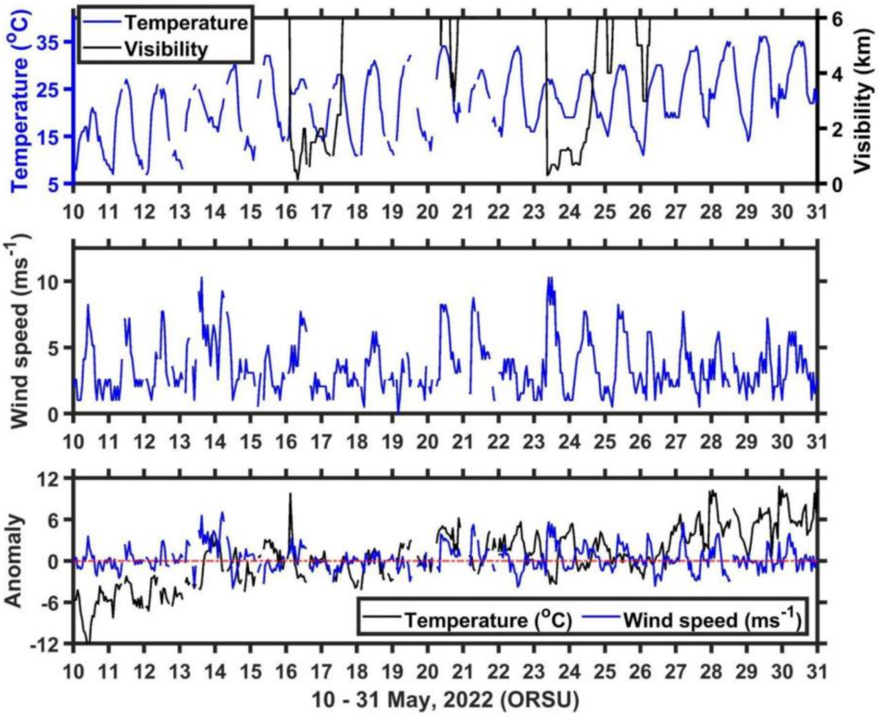

Figure 69. The atmospheric conditions that caused dust episode on 16 and 23 May 2022 (Francis et al., 2023)

In the "Anomaly" part of Figure 69 (bottom graph), on 16th May, the temperature seems abnormal compared to other days. Additionally, the visibility was very low, around 150

m. This may be caused by the absorbing aerosol load resulting from the dust episode near Iraq. On 23rd May, the visibility was 350 m higher than on 616th May. Wind speed reached an extreme value on that day.

5. CONCLUSION

Aerosols are one of the most critical parameters directly affecting the atmosphere's quality and the earth's radiative balance. For this reason, their investigation is crucial. In this study, the absorbing aerosol load over the Eastern Mediterranean Basin was examined with the help of the Level-3 Absorbing Aerosol Index data (produced from the Level-2 Ultraviolet Aerosol Index), obtained from the Sentinel-5P satellite. The satellite carries a spectrometer called TROPOMI, which processes the data in three ways: Near-Real Time, Offline, and Reprocessing (the one used in this study). After retrieving the data, the bad-quality data was screened from the dataset. The study domain was separated into four sections: Eastern Mediterranean Basin, Türkiye, Northern Arabian Peninsula, and Northern Africa. The study period was chosen from the beginning of May 2018 to the end of July 2022. This selection was made based on the availability of the Reprocessing Data generated by the satellite. During the conduction of this study, there were no Reprocessing Data available before and after the selected dates. The selection of the reprocessing data enabled working with improved data using some parameters such as cloud cover (ESA, n.d.-d). After retrieving four years of data, the data was separated into two as accepted and rejected according to the NaN values present in the dataset, the threshold for the separation was between 20-30%. In the analyses, the accepted part of the data was used. This dataset was separated by month, season, and year and used in time series analyses. Box plots were created in order to observe the outliers in the dataset. The outliers have pointed out the extraordinary values of AAI. The analyses were mainly conducted with scripts written in Python and R programming languages.

Additionally, some dust episodes, which are 23-26 April 2019, 16 and 23 May 2022, and the forest fires in Türkiye (28 July-09 August 2021) are observed with Sentinel-5P data. The reason for this dust episodes to occur have been investigated, and the Sentinel-5P data have been compared with other satellite data such as MODIS and EUMETSAT.

The summary of the outcomes of this study can be summarized as below.

- By looking at the statistical analyses for all the study domains and sub-regions, it can be concluded that the absorbing aerosol load shows a decreasing trend with a slope of -0.0003 in the atmosphere of the Eastern Mediterranean Basin. This decrease is directly affecting global warming and inevitably disrupting the climate and the radiation balance of the earth.

- After the investigation of the Eastern Mediterranean Basin as a whole, dividing the study area into its sub-regions was found to be beneficial since these are the regions that show very different profiles in terms of aerosol load in the selected study area. Most of the studied regions comply with meteorological seasons according to their standard conditions. For instance, the absorbing aerosol load in the studied southern regions were higher than in the rest of the area. However, the absorbing aerosol variation in these areas has normal seasonal variations in itself.
- While the Eastern Mediterranean Basin reflect a decreasing trend in terms of AAI, Türkiye, Northern Africa, and Northern Arabian Peninsula does not show any significant trend when investigated annually, from 2018 to 2022. Therefore, a seasonal trend analysis has been conducted for all the sub domains, and it was seen that every season has its own trend.
- Daily visualizations of the data were used to analyze specific cases related to absorbing aerosols, mostly dust. The cause and effect of these specific cases can be seen and understood with the Sentinel-5P data visuals and other satellite observations.
- Apart from the daily visualizations of the data, which were very helpful in daily observations and in the determination of hot spots, the periodic visualizations (monthly, seasonal, and annual) revealed the seasonal movements and expected conditions in the studied areas. For example, owing to the periodic visuals, the high load of Absorbing Aerosol Index has been clearly observed above the Lake Tuz, due to its high salt content. On the contrary, it was seen that Lake Van, which is the largest soda lake of Türkiye, is constantly releasing scattering aerosols.
- With the help of visualizations of the data, case study conduction was made possible. Three case studies were selected. For these case studies, parameters such as temperature, wind speed, and atmospheric pressure, that may cause the dust episodes to occur have been investigated. It was seen that for all the three cases, suitable conditions for a dust episode to occur have been met.
- Case studies showed a compliance with ground-based measurements of PM_{10} concentration obtained from Continuous Monitoring Center. During the dust episodes, the PM_{10} concentrations measured within the area increases.

For the future studies, it is suggested that the Sentinel-5P data is validated with ground-based measurements by a detailed investigation. The dataset obtained from the netCDF files should be improved with a high programming skill. There are validation studies present at the moment. However, the study period, study area, and the product of the satellite, which was used in this study, are unique for now.

6. REFERENCES

ACTRIS. (n.d.). *EARLINET*. Retrieved February 2, 2023, from https://www.earlinet.org/index.php?id=earlinet_homepage

Agacayak, T., Kindap, T., Unal, A., Pozzoli, L., Mallet, M., & Solmon, F. (2015). A case study for Saharan dust transport over Turkey via RegCM4.1 model. *Atmospheric Research*, *153*, 392–403. https://doi.org/10.1016/j.atmosres.2014.09.012

Althaf, P., Kannemadugu, H. B. S., & Kumar, K. R. (2022). Hotspot analysis and long-term trends of absorbing aerosol index from dust emissions measured by the Ozone Monitoring Instrument at different urban locations in India during 2005–2018. *Atmospheric Environment*, *272*(June 2021), 118933. https://doi.org/10.1016/j.atmosenv.2021.118933

American Meteorological Society. (n.d.). *African Easterly Wave*. https://glossary.ametsoc.org/wiki/African_Easterly_Wave#:~:text=A tropical easterly wave that,amplitude in the lower troposphere

Andreae, M. O., & Crutzen, P. J. (1997). Atmospheric aerosols: Biogeochemical sources and role in atmospheric chemistry. *Science*, *276*(5315), 1052–1058. https://doi.org/10.1126/science.276.5315.1052

Apituley, A., Pedergnana, M., Sneep, M., Veefkind, J. P., Loyola, D., & Stein Zweers, D. C. (2021). *Sentinel-5 Precursor / TROPOMI Level 2 Product User Manual UV Aerosol Index*.

Arnault, J., & Roux, F. (2011). Characteristics of African easterly waves associated with tropical cyclogenesis in the Cape Verde Islands region in July-August-September of 2004-2008. *Atmospheric Research*, *100*(1), 61–82. https://doi.org/10.1016/j.atmosres.2010.12.028

Aslanoğlu, S. Y., Proestakis, E., Gkikas, A., Güllü, G., & Amiridis, V. (2022). Dust Climatology of Turkey as a Part of the Eastern Mediterranean Basin via 9-Year CALIPSO-Derived Product. *Atmosphere*, *13*(5). https://doi.org/10.3390/atmos13050733

Barcelona Dust Regional Center. (n.d.). *Daily Dust Products*. https://dust.aemet.es/products/daily-dust-products

Becker, E. (2018). *October 2018 ENSO update*. National Oceanic and Atmospheric Administration. https://www.climate.gov/news-features/blogs/enso/october-2018-enso-update-trick-or-treat

Behera, M. D., Mudi, S., Shome, P., Das, P. K., Kumar, S., Joshi, A., Rathore, A., Deep, A., Kumar, A., Sanwariya, C., Kumar, N., Chandrakar, R., Seshadri, S., Mukherjee, S., Bhattaram, S. K., & Sirivella, Z. (2021). COVID-19 slowdown induced improvement in air quality in India: rapid assessment using Sentinel-5P TROPOMI data. *Geocarto International*, *0*(0), 1–21. https://doi.org/10.1080/10106049.2021.1993351

Behera, M. D., Mudi, S., Shome, P., Das, P. K., Kumar, S., Joshi, A., Rathore, A., Deep, A., Kumar, A., Sanwariya, C., Kumar, N., Chandrakar, R., Seshadri, S., Mukherjee, S., Bhattaram, S. K., & Sirivella, Z. (2022). COVID-19 slowdown induced improvement in air quality in India: rapid assessment using Sentinel-5P TROPOMI data. *Geocarto International*, *37*(25), 8127–8147. https://doi.org/10.1080/10106049.2021.1993351

Bilgiç, E., Tuna Tuygun, G., & Gündüz, O. (2023). Development of an emission estimation method with satellite observations for significant forest fires and comparison with global fire emission inventories: Application to catastrophic fires of summer 2021 over the Eastern Mediterranean. *Atmospheric Environment*, *308*(February), 119871. https://doi.org/10.1016/j.atmosenv.2023.119871

Bilgilioğlu, B. B., Erten, E., & Musaoğlu, N. (2021). Analysis of salt lake volume dynamics using sentinel-1 based SBAS measurements: A case study of lake Tuz, Turkey. *Remote Sensing*, *13*(14). https://doi.org/10.3390/rs13142701

Bo, Y., Cai, H., & Xie, S. D. (2008). Spatial and temporal variation of historical anthropogenic NMVOCs emission inventories in China. *Atmospheric Chemistry and Physics*, *8*(23), 7297–7316. https://doi.org/10.5194/acp-8-7297-2008

Brasseur, G. P., Prinn, R. G., & Pszenny, A. A. . (2003). Atmospheric Chemistry in a Changing World. In *Springer*.

Coakley, J. A. (2003). Reflectance and Albedo, Surface. *Encyclopedia of Atmospheric Sciences*, 1914–1923. https://doi.org/10.1016/b0-12-227090-8/00069-5

Copernicus Global Land Service. (n.d.). *Surface Albedo*.

https://land.copernicus.eu/global/products/sa

CREA. (2021). *2020 yılında Avrupa'da fosil yakıt kullanımı ve hava kirliliği ilişkisi*. https://www.temizhavahakki.org/wp-content/uploads/2021/03/2020HavaKirliligiAvrupa-CREA-1.pdf

CREA. (2023). *Russia–Ukraine war has not led to increased fossil fuel consumption in the EU*. https://energyandcleanair.org/russia-ukraine-war-has-not-led-to-increased-fossil-fuel-consumption-in-the-eu/).

DataCamp. (n.d.). *stl function - RDocumentation*. Retrieved April 4, 2023, from https://www.rdocumentation.org/packages/stats/versions/3.6.2/topics/stl

de Graaf, M., Stammes, P., Torres, O., & Koelemeijer, R. B. A. (2005a). Absorbing Aerosol Index: Sensitivity analysis, application to GOME and comparison with TOMS. *Journal of Geophysical Research D: Atmospheres*, *110*(1), 1–19. https://doi.org/10.1029/2004JD005178

de Graaf, M., Stammes, P., Torres, O., & Koelemeijer, R. B. A. (2005b). Absorbing Aerosol Index: Sensitivity analysis, application to GOME and comparison with TOMS. *Journal of Geophysical Research D: Atmospheres*, *110*(1), 1–19. https://doi.org/10.1029/2004JD005178

Douros, J., Eskes, H., Van Geffen, J., Folkert Boersma, K., Compernolle, S., Pinardi, G., Blechschmidt, A.-M., Peuch, V.-H., Colette, A., & Veefkind, P. (2022). *Comparing Sentinel-5P TROPOMI NO 2 column observations with the CAMS-regional air quality ensemble*. *2*, 509–534. https://doi.org/10.5194/egusphere-2022-365

Earth Engine Data Catalog. (n.d.). *Sentinel-5P OFFL AER AI: Offline UV Aerosol Index*. https://developers.google.com/earth-engine/datasets/catalog/COPERNICUS_S5P_OFFL_L3_AER_AI#description

Educba. (n.d.). *What is Time Series? Why we Need Time Series*. Retrieved April 10, 2023, from https://www.educba.com/what-is-time-series/

El Khoury, E., Ibrahim, E., & Ghanimeh, S. (2019). A look at the Relationship between Tropospheric Nitrogen Dioxide and Aerosol Optical Thickness over Lebanon using Spaceborne data of the Copernicus Programme. *2019 4th International Conference on Advances in Computational Tools for Engineering Applications, ACTEA 2019*, 1–6. https://doi.org/10.1109/ACTEA.2019.8851119

Engelstaedter, S., & Washington, R. (2007). Atmospheric controls on the annual cycle of North African dust. *Journal of Geophysical Research Atmospheres*, *112*(3). https://doi.org/10.1029/2006JD007195

ESA. (n.d.-a). *CALIPSO (Cloud-Aerosol Lidar and Infrared Pathfinder Satellite Observations)*. https://www.eoportal.org/satellite-missions/calipso#summary

ESA. (n.d.-b). *Data Products - Sentinel-5P Mission - Sentinel Online*. Retrieved February 9, 2023, from https://sentinel.esa.int/web/sentinel/missions/sentinel-5p/data-products

ESA. (n.d.-c). *Envisat SCIAMACHY Geo-located atmospheric spectra [SCI_NL__1P]*. https://earth.esa.int/eogateway/catalog/envisat-sciamachy-geo-located-atmospheric-spectra-sci_nl__1p-

ESA. (n.d.-d). *Geographical Coverage*. https://sentinels.copernicus.eu/web/sentinel/missions/sentinel-5p/geographical-coverage

ESA. (n.d.-e). *GOME*. https://earth.esa.int/eogateway/instruments/gome

ESA. (n.d.-f). *HARP*. Retrieved March 24, 2023, from https://atmospherictoolbox.org/harp/

ESA. (n.d.-g). *Level-2 Algorithms - Aerosol Index*. https://sentinels.copernicus.eu/web/sentinel/technical-guides/sentinel-5p/level-2/aerosol-index

ESA. (n.d.-h). *Mission Status Reports*. https://sentinels.copernicus.eu/web/sentinel/missions/sentinel-5p/mission-status

ESA. (n.d.-i). *Orbit*. https://sentinels.copernicus.eu/web/sentinel/missions/sentinel-5p/orbit

ESA. (n.d.-j). *Sentinel-5 Precursor - Pre-Operations Sample Data Set Description , processors version 2*. 1–18.

ESA. (n.d.-k). *Sentinel 5-P*. https://sentinel.esa.int/web/sentinel/missions/sentinel-5p

ESA. (n.d.-l). *Sentinel 5-P Heritage and Future*. https://sentinel.esa.int/web/sentinel/missions/sentinel-5p/heritage-and-future

ESA. (n.d.-m). *TOMS (Total Ozone Mapping Spectrometer)*.

https://www.eoportal.org/satellite-missions/toms#mission-status

ESA. (n.d.-n). *Usecase_2_S5P_AAI_Siberia_Smoke*. Retrieved March 24, 2023, from https://atmospherictoolbox.org/media/usecases/Usecase_2_S5P_AAI_Siberia_Smoke.html

ESA. (2019). *Mission Status Report 409 - 01-15-August-2019*.

EUMETSAT. (n.d.). *EUMETSAT Data Services*. European Organisation for the Exploitation of Meteorological Satellites (EUMETSAT). https://view.eumetsat.int/productviewer?v=default

Farahat, A. (2016). Air pollution in the Arabian Peninsula (Saudi Arabia, the United Arab Emirates, Kuwait, Qatar, Bahrain, and Oman): causes, effects, and aerosol categorization. *Arabian Journal of Geosciences*, *9*(3). https://doi.org/10.1007/s12517-015-2203-y

Fayad, L., Coeur, C., Houzel, N., Deboudt, K., Sécordel, X., Bouzidi, H., & Mouret, G. (2021). Formation of secondary organic aerosols from the reaction of γ-terpinene with ozone: yields and morphology. *Atmospheric Environment*, *262*(March). https://doi.org/10.1016/j.atmosenv.2021.118600

France, O. B., France, C. G., Germany, C. H., & Uk, A. J. (n.d.). *Ch 07 Clouds and Aerosols*.

Francis, D., Fonseca, R., Nelli, N., Bozkurt, D., Cuesta, J., & Bosc, E. (2023). On the Middle East's severe dust storms in spring 2022: Triggers and impacts. *Atmospheric Environment*, *296*(November 2022), 119539. https://doi.org/10.1016/j.atmosenv.2022.119539

Fuzzi, S., Andreae, M. O., Huebert, B. J., Kulmala, M., Bond, T. C., Boy, M., Doherty, S. J., Guenther, A., Kanakidou, M., Kawamura, K., Kerminen, V. M., Lohmann, U., Russell, L. M., & Pöschl, U. (2006). Critical assessment of the current state of scientific knowledge, terminology, and research needs concerning the role of organic aerosols in the atmosphere, climate, and global change. *Atmospheric Chemistry and Physics*, *6*(7), 2017–2038. https://doi.org/10.5194/acp-6-2017-2006

Gaál, N., & Ihász, I. (2014). Predictability of cold drops based on ECMWF's forecasts over Europe. *ECMWF Newsletter*, *140*(140), 32–36. https://doi.org/10.21957/tn09zec6

Ganbat, G., Lee, H., Karthe, D., Jo, H. W., & Jadamba, B. (2022). Assessment of COVID-19 Impacts on Air Quality in Ulaanbaatar, Mongolia, Based on Terrestrial and Sentinel-5P TROPOMI Data. *Aerosol and Air Quality Research*, *22*(10). https://doi.org/10.4209/aaqr.220196

Garane, K., Chan, K. L., Koukouli, M. E., Loyola, D., & Balis, D. (2023). TROPOMI/S5P Total Column Water Vapor validation against AERONET ground-based measurements. *Atmospheric Measurement Techniques*, *16*(1), 57–74. https://doi.org/10.5194/amt-16-57-2023

Georgoulias, A. K., Alexandri, G., Kourtidis, K. A., Lelieveld, J., Zanis, P., Pöschl, U., Levy, R., Amiridis, V., Marinou, E., & Tsikerdekis, A. (2016). Spatiotemporal variability and contribution of different aerosol types to the aerosol optical depth over the Eastern Mediterranean. *Atmospheric Chemistry and Physics*, *16*(21), 13853–13884. https://doi.org/10.5194/acp-16-13853-2016

Ghasempour, F., Sekertekin, A., & Kutoglu, S. H. (2021). Google Earth Engine based spatio-temporal analysis of air pollutants before and during the first wave COVID-19 outbreak over Turkey via remote sensing. *Journal of Cleaner Production*, *319*(August), 128599. https://doi.org/10.1016/j.jclepro.2021.128599

Gkikas, A., Hatzianastassiou, N., Mihalopoulos, N., & Torres, O. (2016). Characterization of aerosol episodes in the greater Mediterranean Sea area from satellite observations (2000-2007). *Atmospheric Environment*, *128*, 286–304. https://doi.org/10.1016/j.atmosenv.2015.11.056

Godłowska, J., Hajto, M. J., Lapeta, B., & Kaszowski, K. (2023). The attempt to estimate annual variability of NOx emission in Poland using Sentinel-5P/TROPOMI data. *Atmospheric Environment*, *294*(x). https://doi.org/10.1016/j.atmosenv.2022.119482

Halder, B., Ahmadianfar, I., Heddam, S., Mussa, Z. H., Goliatt, L., Tan, M. L., Sa'adi, Z., Al-Khafaji, Z., Al-Ansari, N., Jawad, A. H., & Yaseen, Z. M. (2023). Machine learning-based country-level annual air pollutants exploration using Sentinel-5P and Google Earth Engine. *Scientific Reports*, *13*(1), 1–19. https://doi.org/10.1038/s41598-023-34774-9

Hatzianastassiou, N., Gkikas, A., Mihalopoulos, N., Torres, O., & Katsoulis, B. D. (2009). *Natural versus anthropogenic aerosols in the eastern Mediterranean basin derived from multiyear TOMS and MODIS satellite data Natural versus* *anthropogenic aerosols in the eastern Mediterranean basin derived from multiyear TOMS and MODIS satellite data*. *December*. https://doi.org/10.1029/2009JD011982

Hecht, E. (2015). *Optics* (5th ed., pp. 96–104).

Helsel, D. R., Hirsch, R. M., Ryberg, K. R., Archfield, S. A., & Gilroy, E. J. (2020). Statistical methods in water resources. *U.S. Geological Survey Techniques and Methods*, *2020*(4-A3), 1–484. https://doi.org/10.3133/tm4a3

Huseyinca, M. Y., & Küpeli, S. (2021). Mineralogy and Geochemistry of Sediments from Lake Tuz. *Hittite Journal of Science and Engineering*, *8*(4), 329–338. https://doi.org/10.17350/hjse19030000246

Hyndman, R. J., & Athanasopoulos, G. (n.d.). Time series decomposition. In *Forecasting: Principles and Practice* (2nd ed.). Retrieved April 10, 2023, from https://otexts.com/fpp2/decomposition.html

Ialongo, I., Stepanova, N., Hakkarainen, J., Virta, H., & Gritsenko, D. (2021). Satellite-based estimates of nitrogen oxide and methane emissions from gas flaring and oil production activities in Sakha Republic, Russia. *Atmospheric Environment: X*, *11*(2), 100114. https://doi.org/10.1016/j.aeaoa.2021.100114

IPCC. (2007). *IPCC Fourth Assessment Report: Climate Change 2007*. https://archive.ipcc.ch/publications_and_data/ar4/wg1/en/faq-2-1.html#:~:text=Fossil fuel and biomass burning,increased dust in the atmosphere.

J, M. (n.d.). *Madden-Julian Oscillation (MJO)*. Australian Government. http://www.bom.gov.au/climate/mjo/#:~:text=The Madden-Julian Oscillation (MJO,every 30 to 60 days.

Jimenez, J. L., Canagaratna, M. R., Donahue, N. M., Prevot, A. S. H., Zhang, Q., Kroll, J. H., DeCarlo, P. F., Allan, J. D., Coe, H., Ng, N. L., Aiken, A. C., Docherty, K. S., Ulbrich, I. M., Grieshop, A. P., Robinson, A. L., Duplissy, J., Smith, J. D., Wilson, K. R., Lanz, V. A., … Worsnop, D. R. (2009). Evolution of organic aerosols in the atmosphere. *Science*, *326*(5959), 1525–1529. https://doi.org/10.1126/science.1180353

Judd, L. M., Al-Saadi, J. A., Szykman, J. J., Valin, L. C., Janz, S. J., Kowalewski, M. G., Eskes, H. J., Pepijn Veefkind, J., Cede, A., Mueller, M., Gebetsberger, M., Swap, R., Bradley Pierce, R., Nowlan, C. R., González Abad, G., Nehrir, A., & Williams, D. (2020). Evaluating Sentinel-5P TROPOMI tropospheric NO2 column densities with airborne and Pandora spectrometers near New York City and Long Island Sound. *Atmospheric Measurement Techniques*, *13*(11), 6113–6140. https://doi.org/10.5194/amt-13-6113-2020

Kanakidou, M., Seinfeld, J. H., Pandis, S. N., Barnes, I., Dentener, F. J., Facchini, M. C., Van Dingenen, R., Ervens, B., Nenes, A., Nielsen, C. J., Swietlicki, E., Putaud, J. P., Balkanski, Y., Fuzzi, S., Horth, J., Moortgat, G. K., Winterhalter, R., Myhre, C. E. L., Tsigaridis, K., … Wilson, J. (2005). Organic aerosol and global climate modelling: A review. *Atmospheric Chemistry and Physics*, *5*(4), 1053–1123. https://doi.org/10.5194/acp-5-1053-2005

Kaplan, G., & Avdan, Z. Y. (2020a). COVID-19: Spaceborne Nitrogen Dioxide Over Turkey. *Eskişehir Technical University Journal of Science and Technology A - Applied Sciences and Engineering*, *21*(2), 251–255. https://doi.org/10.18038/estubtda.724450

Kaplan, G., & Avdan, Z. Y. (2020b). Space-Borne Air Pollution Observation From Sentinel-5P Tropomi: Relationship Between Pollutants, Geographical and Demographic Data. *International Journal of Engineering and Geosciences*, *2*, 130–137. https://doi.org/10.26833/ijeg.644089

Kaplan, G., Avdan, Z. Y., & Avdan, U. (2019). Spaceborne Nitrogen Dioxide Observations from the Sentinel-5P TROPOMI over Turkey. *Proceedings*, *18*(1), 4. https://doi.org/10.3390/ecrs-3-06181

Karslıoğlu, S., Tezcan, E., Tuna, G., & Elbir, T. (2022). Türkiye’de Terra ve Aqua MODIS Uydularından Elde Edilen Aerosol Optik Derinliğinin Zamansal ve Mekansal Değişimi. *Deu Muhendislik Fakultesi Fen ve Muhendislik*, *24*(70), 303–316. https://doi.org/10.21205/deufmd.2022247027

Kavzoğlu, T., Çölkesen, İ., & Öztürk, M. Y. (2021). *Uzaktan Algılama ile Orman Yangınlarının Zamansal Analizi: 2021 Yılı Akdeniz Ve Ege Yangınları Temporal Analysis of Forest Fires With Remote Sensing Technologies: Mediterranean and Aegean Fires in 2021*.

Kilic, O., & Kilic, A. M. (2010). Salt crust mineralogy and geochemical evolution of the salt lake (Tuz Gölü), Turkey. *Scientific Research and Essays*, *5*(11), 1317–1324.

Kim, K. H., Kabir, E., & Kabir, S. (2015). A review on the human health impact of airborne particulate matter. *Environment International*, *74*, 136–143. https://doi.org/10.1016/j.envint.2014.10.005

Kooreman, M. L., Stammes, P., Trees, V., Sneep, M., Gijsbert Tilstra, L., De Graaf, M., Stein Zweers, D. C., Wang, P., Tuinder, O. N. E., & Pepijn, J. (n.d.). *Effects of clouds on the UV Absorbing Aerosol Index from TROPOMI*. https://doi.org/10.5194/amt-2020-112

Kroll, J. H., & Seinfeld, J. H. (2008). Chemistry of secondary organic aerosol: Formation and evolution of low-volatility organics in the atmosphere. *Atmospheric Environment*, *42*(16), 3593–3624. https://doi.org/10.1016/j.atmosenv.2008.01.003

Kubilay, N., & Koçak, M. (2009). *Doğu Akdeniz Bölgesindeki Aerosollerin İklimsel Önemi*.

Kumar, K. R., Attada, R., Dasari, H. P., Vellore, R. K., Langodan, S., Abualnaja, Y. O., & Hoteit, I. (2018). Aerosol Optical Depth variability over the Arabian Peninsula as inferred from satellite measurements. *Atmospheric Environment*, *187*, 346–357. https://doi.org/10.1016/j.atmosenv.2018.06.011

Kumari, S., Yadav, A. C., Saharia, M., & Dev, S. (2022). Spatio-temporal analysis of air quality and its relationship with COVID-19 lockdown over Dublin. *Remote Sensing Applications: Society and Environment*, *28*(August), 100835. https://doi.org/10.1016/j.rsase.2022.100835

Lelieveld, J., Berresheim, H., Borrmann, S., Crutzen, P. J., & Dentener, F. J. (2002). *Global Air Pollution Crossroads over the Mediterranean*. *November*. https://doi.org/10.1126/science.1075457

Lelieveld, J., Berresheim, H., Borrmann, S., Crutzen, P. J., Dentener, F. J., Fischer, H., Feichter, J., Flatau, P. J., Heland, J., Holzinger, R., Korrmann, R., Lawrence, M. G., Levin, Z., Markowicz, K. M., Mihalopoulos, N., Minikin, A., Ramanathan, V., De Reus, M., Roelofs, G. J., … Ziereis, H. (2002). Global air pollution crossroads over the Mediterranean. *Science*, *298*(5594), 794–799. https://doi.org/10.1126/science.1075457

Li, W., Thomas, R., El-Askary, H., Piechota, T., Struppa, D., & Abdel Ghaffar, K. A. (2020). Investigating the Significance of Aerosols in Determining the Coronavirus

Fatality Rate Among Three European Countries. *Earth Systems and Environment*, *4*(3), 513–522. https://doi.org/10.1007/s41748-020-00176-4

Liberto, T. Di. (2020). *December 2020 La Niña update: walking in a La Niña winter wonderland*. NOAA. https://www.climate.gov/news-features/blogs/enso/december-2020-la-niña-update-walking-la-niña-winter-wonderland

Lorente, A., Boersma, K. F., Eskes, H. J., Veefkind, J. P., van Geffen, J. H. G. M., de Zeeuw, M. B., Denier van der Gon, H. A. C., Beirle, S., & Krol, M. C. (2019). Quantification of nitrogen oxides emissions from build-up of pollution over Paris with TROPOMI. *Scientific Reports*, *9*(1), 1–10. https://doi.org/10.1038/s41598-019-56428-5

Madkour, K. M. (2022). Monitoring the impacts of COVID-19 pandemic on climate change and the environment on Egypt using Sentinel-5P Images, and the Carbon footprint methodology. *Egyptian Journal of Remote Sensing and Space Science*, *25*(1), 205–219. https://doi.org/10.1016/j.ejrs.2021.07.003

Maurya, N. K., Pandey, P. C., Sarkar, S., Kumar, R., & Srivastava, P. K. (2022). Spatio-Temporal Monitoring of Atmospheric Pollutants Using Earth Observation Sentinel 5P TROPOMI Data: Impact of Stubble Burning a Case Study. *ISPRS International Journal of Geo-Information*, *11*(5). https://doi.org/10.3390/ijgi11050301

Mazlan, N. A., Zaki, N. A. M., Narashid, R. H., Talib, N., Manokaran, J., Arshad, F. C., Fauzi, S. S. M., Dom, N. C., Valipour, M., Dambul, R., & Blenkinsop, S. (2023). COVID-19 Restriction Movement Control Order (MCO) Impacted Emissions of Peninsular Malaysia Using Sentinel-2a and Sentinel-5p Satellite. *Earth Systems and Environment*, *7*(1), 347–358. https://doi.org/10.1007/s41748-022-00329-7

Michailidis, K., Koukouli, M., Balis, D., Veefkind, J. P., Mona, L., Papagiannopoulos, N., Pappalardo, G., Tsikoudi, I., Marinou, E., Gialitaki, A., Mamouri, R., Nisantzi, A., Salgueiro, V., Papayannis, A., Mylonaki, M., Romano, S., Perrone, M. R., Baars, H., Bilt, D., … Unit, S. (2022). *Validation of the TROPOMI / S5P Aerosol Layer Height using EARLINET lidars*. *9*(July), 1–30.

Michailidis, K., Koukouli, M. E., Balis, D., Veefkind, J. P., De Graaf, M., Mona, L., Papagianopoulos, N., Pappalardo, G., Tsikoudi, I., Amiridis, V., Marinou, E., Gialitaki, A., Mamouri, R. E., Nisantzi, A., Bortoli, D., João Costa, M., Salgueiro, V., Papayannis, A., Mylonaki, M., … Baars, H. (2023). Validation of the

TROPOMI/S5P aerosol layer height using EARLINET lidars. *Atmospheric Chemistry and Physics*, *23*(3), 1919–1940. https://doi.org/10.5194/acp-23-1919-2023

Mohite, J., Sawant, S., Pandit, A., & Pappula, S. (2022). Impact of lockdown and crop stubble burning on air quality of India: a case study from wheat-growing region. *Environmental Monitoring and Assessment*, *194*(2). https://doi.org/10.1007/s10661-021-09723-6

Monahan, E. C., Fairall, C. W., Davidson, K. L., & Boyle, P. J. (1983). Observed interrelation between 10 m winds, ocean whitecaps and marine aerosols. *Quarterly Journal of the Royal Meteorological Society*, *109*(460), 379–392.

Morozova, A. E., Sizov, O. S., Elagin, P. O., Agzamov, N. A., Fedash, A. V., & Lobzhanidze, N. E. (2022). Integral Assessment of Atmospheric Air Quality in the Largest Cities of Russia Based on TROPOMI (Sentinel-5P) Data for 2019–2020. *Cosmic Research*, *60*(4), S57–S68. https://doi.org/10.1134/S0010952522700071

Myhre, C. L. (2013). *Aerosols and Their Relation to Global Climate and Climate Sensitivity*. *May*.

NASA. (n.d.-a). *Aura: Launch Event*. https://www.nasa.gov/mission_pages/aura/launch/index.html

NASA. (n.d.-b). *CALIPSO: Mission Overview*. https://www.nasa.gov/mission_pages/calipso/mission/

NASA. (n.d.-c). *Global Temperature Anomalies from 1880 to 2022*. Scientific Visualization Studio. https://svs.gsfc.nasa.gov/5060

NASA. (n.d.-d). *MODIS*. https://lpdaac.usgs.gov/data/get-started-data/collection-overview/missions/modis-overview/#:~:text=Its detectors measure 36 spectral,500 m%2C and 1%2C000 m.

NASA. (n.d.-e). *NASA Worldview*. https://worldview.earthdata.nasa.gov/?v=-49.716257293744995,-1.9500802393770513,116.30508414996379,75.98051037319718&l=Reference_Labels_15m,Reference_Features_15m,Coastlines_15m,BlueMarble_NextGeneration,VIIRS_SNPP_CorrectedReflectance_TrueColor,MODIS_Aqu

Nastos, P. T. (2012). Meteorological patterns associated with intense saharan dust outbreaks over greece in winter. *Advances in Meteorology*, *2012*, 12–14. https://doi.org/10.1155/2012/828301

National Centers for Environmental Information. (n.d.). *Meteorological Versus Astronomical Seasons*. https://www.ncei.noaa.gov/news/meteorological-versus-astronomical-seasons

National Institute of Water and Atmospheric Research. (n.d.). *What are El Niño and La Niña?* https://niwa.co.nz/climate/faq/what-are-el-niño-and-la-niña

National Intelligence Council. (2009). *North Africa: The Impact of Climate Change to 2030 (Selected Countries).*

National Oceanic and Atmospheric Administration. (n.d.). *What are atmospheric rivers?* https://www.noaa.gov/stories/what-are-atmospheric-rivers

National Snow and Ice Data Center. (n.d.). *What is netCDF? | National Snow and Ice Data Center*. Retrieved March 23, 2023, from https://nsidc.org/data/user-resources/help-center/what-netcdf

Nations, F. and A. O. of the U. (2000). North Africa. In *Global Forest Resources Assessment*. https://www.fao.org/3/Y1997E/y1997e0i.htm

Nguyen, H. M., He, J., & Wooster, M. J. (2023). Biomass burning CO, PM and fuel consumption per unit burned area estimates derived across Africa using geostationary SEVIRI fire radiative power and Sentinel-5P CO data. *Atmospheric Chemistry and Physics*, *23*(3), 2089–2118. https://doi.org/10.5194/acp-23-2089-2023

NOAA. (n.d.). *Climate Variability: Oceanic Niño Index*. https://www.climate.gov/news-features/understanding-climate/climate-variability-oceanic-nino-index#:~:text=The ONI is the rolling,or lower indicate La Niña.

Null, J. (2023). *El Niño and La Niña Years and Intensities*. https://ggweather.com/enso/oni.htm

Oğuz, K., & Pekin, M. A. (2019). *23-26 Nisan 2019 Tarihinde Türkiye'de Gerçekleşen Toz Taşınımı Olayının İncelenmesi*. *October*.

Omrani, B. (n.d.). *S5P-Analysis*. https://github.com/bilelomrani1/s5p-analysis

Ouerghi, E., Ehret, T., De Franchis, C., Facciolo, G., Lauvaux, T., Meinhardt, E., &

Morel, J. M. (2022). Automatic methane plumes detection in time series of sentinel-5p l1b images. *ISPRS Annals of the Photogrammetry, Remote Sensing and Spatial Information Sciences*, *5*(3), 147–154. https://doi.org/10.5194/isprs-Annals-V-3-2022-147-2022

Öztürk, F., Zarars, A., Dutkiewicz, V. A., Husain, L., Hopke, P. K., & Tuncel, G. (2012). *Temporal variations and sources of Eastern Mediterranean aerosols based on a 9-year observation*. *61*, 463–475. https://doi.org/10.1016/j.atmosenv.2012.07.051

Papachristopoulou, K., Fountoulakis, I., Gkikas, A., Kosmopoulos, P. G., Nastos, P. T., Hatzaki, M., & Kazadzis, S. (2022). 15-Year Analysis of Direct Effects of Total and Dust Aerosols in Solar Radiation/Energy over the Mediterranean Basin. *Remote Sensing*, *14*(7). https://doi.org/10.3390/rs14071535

Papadimas, C. D., Hatzianastassiou, N., Mihalopoulos, N., Querol, X., & Vardavas, I. (2008). Spatial and temporal variability in aerosol properties over the Mediterranean basin based on 6-year (2000-2006) MODIS data. *Journal of Geophysical Research Atmospheres*, *113*(11), 1–12. https://doi.org/10.1029/2007JD009189

Penner, J. E. (2022). *Scattering and absorbing aerosols in the climate system*. *3*(June). https://doi.org/10.1038/s43017-022-00296-7

Penning De Vries, M. J. M., Beirle, S., & Wagner, T. (2009). UV aerosol indices from SCIAMACHY: Introducing the SCattering Index (SCI). *Atmospheric Chemistry and Physics*, *9*(24), 9555–9567. https://doi.org/10.5194/acp-9-9555-2009

Peshev, Z., Deleva, A., Chaikovsky, A., Pescherenkov, V., Vulkova, L., & Dreischuh, T. (2022). Vertical and near-horizontal scanning lidar observations of aerosol loads over Sofia, Bulgaria, in the presence of Saharan dust. *Journal of Physics: Conference Series*, *2240*(1). https://doi.org/10.1088/1742-6596/2240/1/012032

Peshev, Zahari, Deleva, A., Vulkova, L., & Dreischuh, T. (2022). Large-Scale Saharan Dust Episode in April 2019: Study of Desert Aerosol Loads over Sofia, Bulgaria, Using Remote Sensing, In Situ, and Modeling Resources. *Atmosphere*, *13*(6). https://doi.org/10.3390/atmos13060981

Pitari, G., Ackerman, A., Adams, P., Austin, P., Boers, R., Boucher, O., Chin, M., Chuang, C., Collins, B., Cooke, W., Demott, P., Feng, Y., Fischer, H., Fung, I., Ghan, S., Ginoux, P., Gong, S., Guenther, A., Herzog, M., … Weele, M. Van.

(2001). Aerosols, their Direct and Indirect Effects. *Climate Change 2001: The Scientific Basis. Contribution of Working Group I to the Third Assessment Report of the Intergovernmental Panel on Climate Change*, *5*, 289–348. http://www.physics.harvard.edu/~wilson/energypmp/IPCC/Ch05_draft3.pdf

Prakash, S., Goswami, M., Khan, Y. D. I., & Nautiyal, S. (2021). Environmental impact of COVID-19 led lockdown: A satellite data-based assessment of air quality in Indian megacities. *Urban Climate*, *38*(June), 100900. https://doi.org/10.1016/j.uclim.2021.100900

Querol, X., Alastuey, A., Pey, J., & Cusack, M. (2009). *Variability in regional background aerosols within the Mediterranean*. 4575–4591.

Ramanathan, V., Diego, S., Crutzen, P. J., Kiehl, J. T., Cruz, S., & Rosenfeld, D. (2002). *Aerosols, Climate, and the Hydrological Cycle*. *June 2014*. https://doi.org/10.1126/science.1064034

Reimer, A., Landmann, G., & Kempe, S. (2009). Lake Van, Eastern Anatolia, hydrochemistry and history. *Aquatic Geochemistry*, *15*(1–2), 195–222. https://doi.org/10.1007/s10498-008-9049-9

Ritchie, H., Rosado, P., & Roser, M. (2022). *Fossil Fuels*. Our World in Data. https://ourworldindata.org/fossil-fuels

Robert B Cleveland, William S. Cleveland, Jean E. McRae, & Irma Terpenning. (1990). STL: A Seasonal-Trend decomposition Procedure Based on Loess. In *Journal of Official Statistics* (Vol. 6, Issue 1, pp. 3–73).

Rodríguez, E., Arqués, J. L., Rodríguez, R., Nuñez, M., Medina, M., Talarico, T. L., Casas, I. A., Chung, T. C., Dobrogosz, W. J., Axelsson, L., Lindgren, S. E., Dobrogosz, W. J., Kerkeni, L., Ruano, P., Delgado, L. L., Picco, S., Villegas, L., Tonelli, F., Merlo, M., … Masuelli, M. (1989). Air Pollution Determination Using Remote Sensing Technique. *Intech*, *32*(tourism), 137–144. https://www.intechopen.com/books/advanced-biometric-technologies/liveness-detection-in-biometrics

Roman-Gonzalez, A., & Vargas-Cuentas, N. I. (2020). Variation of aerosol pollution in Peru during the quarantine due to COVID-19. *International Journal of Advanced Computer Science and Applications*, *11*(4), 47–51.

https://doi.org/10.14569/IJACSA.2020.0110407

Royal Netherlands Meteorological Institute. (n.d.). *Ozone Monitoring Instrument (OMI)*. https://www.knmiprojects.nl/projects/ozone-monitoring-instrument#:~:text=OMI combines the advantages of,km) and daily global coverage.

Rozemeijer, N. C., & Van, R. C. (2015). *Algorithm theoretical basis document for the TROPOMI L01b Data Processor*.

Savenets, M. (2021). *Air pollution in Ukraine: A view from the Sentinel-5P satellite*. *June*. https://doi.org/10.28974/idojaras.2021.2.6

Schagerl, M. (2016). Soda lakes of East Africa. *Soda Lakes of East Africa*, *February*, 1–408. https://doi.org/10.1007/978-3-319-28622-8

Shikwambana, L. (2021). Emissions of toxic gases and aerosols in southern Africa observed during the 2019 JJASO period. *Air Quality, Atmosphere and Health*, *14*(4), 481–490. https://doi.org/10.1007/s11869-020-00952-1

Shikwambana, L., Kganyago, M., & Mhangara, P. (2021). Temporal analysis of changes in anthropogenic emissions and urban heat islands during covid-19 restrictions in Gauteng province, South Africa. *Aerosol and Air Quality Research*, *21*(9). https://doi.org/10.4209/aaqr.200437

Shikwambana, L., Mhangara, P., & Mbatha, N. (2020). *Trend analysis and first time observations of sulphur dioxide and nitrogen dioxide in South Africa using TROPOMI/Sentinel-5P data*. *91*(December 2019), 1–13.

Sokolik, I. N., & Toon, O. B. (1996). Direct radiative forcing by anthropogenic airborne mineral aerosols. *Nature*, *381*(6584), 681–683. https://doi.org/10.1038/381681a0

Statista. (n.d.). *Annual anomalies in global land surface temperature from 1880 to 2022, based on temperature departure*. Statista. https://www.statista.com/statistics/1048518/average-land-sea-temperature-anomaly-since-1850/

Stein Zweers, D. C. (2022). TROPOMI ATBD of the UV aerosol index document number - S5P-KNMI-L2-0008-RP. *The European Space Agency*, *2.1.0*, 30.

Tableau. (n.d.). *Time Series Analysis: Definition, Types & Techniques*. Retrieved April 10, 2023, from https://www.tableau.com/learn/articles/time-series-analysis

Taloor, A. K., Singh, A. K., Kumar, P., Kumar, A., Tripathi, J. N., Kumari, M., Kotlia, B. S., Kothyari, G. C., Tiwari, S. P., & Johnson, B. A. (2022). Geospatial Technology-Based Analysis of Air Quality in India during the COVID-19 Pandemic. *Remote Sensing*, *14*(18), 1–16. https://doi.org/10.3390/rs14184650

Tariq, S., ul-Haq, Z., Mariam, A., Mehmood, U., & Ahmed, W. (2023). Assessment of air quality during worst wildfires in Mugla and Antalya regions of Turkey. *Natural Hazards*, *115*(2), 1235–1254. https://doi.org/10.1007/s11069-022-05592-5

The Ministry of Environment Urbanization and Climate Change. (n.d.-a). *Number of Exceeding Air Quality Limit Values*. https://cevreselgostergeler.csb.gov.tr/hava-kalitesi-sinir-degerlerin-asim-sayilari-i-85777#_ednref1

The Ministry of Environment Urbanization and Climate Change. (n.d.-b). *SİM (Sürekli İzleme Merkezi)*. https://sim.csb.gov.tr/

The Ministry of Environment Urbanization and Climate Change. (n.d.-c). *Tuz Gölü*. https://tvk.csb.gov.tr/tuz-golu-i-400#:~:text=Tuz Gölü%3B sadece ülkemizin değil,tuz oranı %25 32.4'tür.

Torres, O., Tanskanen, A., Veihelmann, B., Ahn, C., Braak, R., Bhartia, P. K., Veefkind, P., & Levelt, P. (2007). Aerosols and surface UV products form Ozone Monitoring Instrument observations: An overview. *Journal of Geophysical Research Atmospheres*, *112*(24), 1–14. https://doi.org/10.1029/2007JD008809

Tutsak, E. (2018). *A 15-Year Clımatology Of Aerosol Optıcal And Physıcal Propertıes And Near-Real Tıme Measurements Of Water-Soluble Ions In PM2.5 And Theır Precursor Gases In The Atmosphere Over The Eastern Medıterranean*.

Tuygun, G. T., İşsever, G., & Elbir, T. (2023). *Türkiye ' de 2021 Yılında Yaşanan Büyük Orman Yangınlarında Yanan Orman Alanlarının ve Yangın Kaynaklı Atmosferik Aerosollerin Uydular ile İzlenmesi Satellite Monitoring of Burned Forest Areas and Atmospheric Aerosols Originated from Major Forest Fires in*. *25*(74), 351–369. https://doi.org/10.21205/deufmd.2023257408

United States Geological Survey. (n.d.-a). *MODIS*. https://asdc.larc.nasa.gov/project/MISR#:~:text=The Multi-angle Imaging SpectroRadiometer,the Earth%27s environment and climate.

United States Geological Survey. (n.d.-b). *What is remote sensing and what is it used for?*

https://www.usgs.gov/faqs/what-remote-sensing-and-what-it-used

Urdiales-Flores, D., Zittis, G., Hadjinicolaou, P., Osipov, S., Klingmüller, K., Mihalopoulos, N., Economou, T., & Lelieveld, J. (2023). Drivers of accelerated warming in Mediterranean climate-type regions. *Npj Climate and Atmospheric Science*, *in revision*. https://doi.org/10.1038/s41612-023-00423-1

Varga, G., Dagsson-Walhauserová, P., Gresina, F., & Helgadottir, A. (2021). Saharan dust and giant quartz particle transport towards Iceland. *Scientific Reports*, *11*(1), 1–12. https://doi.org/10.1038/s41598-021-91481-z

Verhoelst, T., Compernolle, S., Pinardi, G., Lambert, J. C., Eskes, H. J., Eichmann, K. U., Fjæraa, A. M., Granville, J., Niemeijer, S., Cede, A., Tiefengraber, M., Hendrick, F., Pazmiño, A., Bais, A., Bazureau, A., Folkert Boersma, K., Bognar, K., Dehn, A., Donner, S., … Zehner, C. (2021). Ground-based validation of the Copernicus Sentinel-5P TROPOMI NO2 measurements with the NDACC ZSL-DOAS, MAX-DOAS and Pandonia global networks. *Atmospheric Measurement Techniques*, *14*(1), 481–510. https://doi.org/10.5194/amt-14-481-2021

Vitousek, P. M., Mooney, H. A., Lubchenco, J., Melillo, J. M., Thomas, C. D., Cameron, A., Green, R. E., Bakkenes, M., Beaumont, L. J., Collingham, Y. C., Erasmus, B. F. N., De Siqueira, M. F., Grainger, A., Hannah, L., Hughes, L., Huntley, B., Van Jaarsveld, A. S., Midgley, G. F., Miles, L., … Andreae, M. O. (2004). Impacts of atmospheric aerosols and air pollution in Northern Eurasia and their dynamics. *Journal of Geophysical Research*, *4*(January), 1089. http://www.ipcc.ch/pdf/assessment-report/ar4/syr/ar4_syr.pdf

Wang, T., Huang, X., Wang, Z., Liu, Y., Zhou, D., Ding, K., Wang, H., Qi, X., & Ding, A. (2020). Secondary aerosol formation and its linkage with synoptic conditions during winter haze pollution over eastern China. *Science of the Total Environment*, *730*, 138888. https://doi.org/10.1016/j.scitotenv.2020.138888

Wang, Y., Yuan, Q., Li, T., Tan, S., & Zhang, L. (2021). Full-coverage spatiotemporal mapping of ambient PM2.5 and PM10 over China from Sentinel-5P and assimilated datasets: Considering the precursors and chemical compositions. *Science of the Total Environment*, *793*, 148535. https://doi.org/10.1016/j.scitotenv.2021.148535

Weather Spark. (n.d.-a). *Denizli Çardak Havalimanı Bölgesinde 2019 Tarihinde Hava Durumu Geçmişi*. https://tr.weatherspark.com/h/y/148620/2019/2019-yılı-için-at-

Denizli-Çardak-Havalimanı-Türkiye-Tarihi-Hava-Durumu#Figures-Temperature

Weather Spark. (n.d.-b). *Manavgat Bölgesinde 2021 Tarihinde Hava Durumu Geçmişi*. Weather Spark. https://tr.weatherspark.com/h/y/96964/2021/2021-yılı-için-Manavgat-Türkiye-Tarihi-Hava-Durumu#Figures-WindDirection

Whitby, K. T. (2007). The physical characteristics of sulfur aerosols. *Atmospheric Environment*, *41*(SUPPL.), 25–49. https://doi.org/10.1016/j.atmosenv.2007.10.057

Yilmaz, O. S., Acar, U., Sanli, F. B., Gulgen, F., & Ates, A. M. (2023a). Mapping burn severity and monitoring CO content in Türkiye's 2021 Wildfires, using Sentinel-2 and Sentinel-5P satellite data on the GEE platform. *Earth Science Informatics, 0123456789*. https://doi.org/10.1007/s12145-023-00933-9

Yilmaz, O. S., Acar, U., Sanli, F. B., Gulgen, F., & Ates, A. M. (2023b). Mapping burn severity and monitoring CO content in Türkiye's 2021 Wildfires, using Sentinel-2 and Sentinel-5P satellite data on the GEE platform. *Earth Science Informatics*, *16*(1), 221–240. https://doi.org/10.1007/s12145-023-00933-9

Yukhymchuk, Y., Milinevsky, G., Unga, F., National, I., & Pikridas, M. (2022). *Aerosol Mineral Dust Pollution o ver Nicosia , Cyprus , April*. *December*. https://doi.org/10.20944/preprints202210.0176.v1

Zhang, Q., Jimenez, J. L., Canagaratna, M. R., Allan, J. D., Coe, H., Ulbrich, I., Alfarra, M. R., Takami, A., Middlebrook, A. M., Sun, Y. L., Dzepina, K., Dunlea, E., Docherty, K., DeCarlo, P. F., Salcedo, D., Onasch, T., Jayne, J. T., Miyoshi, T., Shimono, A., … Worsnop, D. R. (2007). Ubiquity and dominance of oxygenated species in organic aerosols in anthropogenically-influenced Northern Hemisphere midlatitudes. *Geophysical Research Letters*, *34*(13), 1–6. https://doi.org/10.1029/2007GL029979

Zhao, F., Liu, C., Cai, Z., Liu, X., Bak, J., Kim, J., Hu, Q., Xia, C., Zhang, C., Sun, Y., Wang, W., & Liu, J. (2021). Ozone profile retrievals from TROPOMI: Implication for the variation of tropospheric ozone during the outbreak of COVID-19 in China. *Science of the Total Environment*, *764*. https://doi.org/10.1016/j.scitotenv.2020.142886

APPENDIX

APPENDIX 1 – Periodic Visualizations of the S5P Level-3 AAI Data

- **Data for the Eastern Mediterranean Basin**

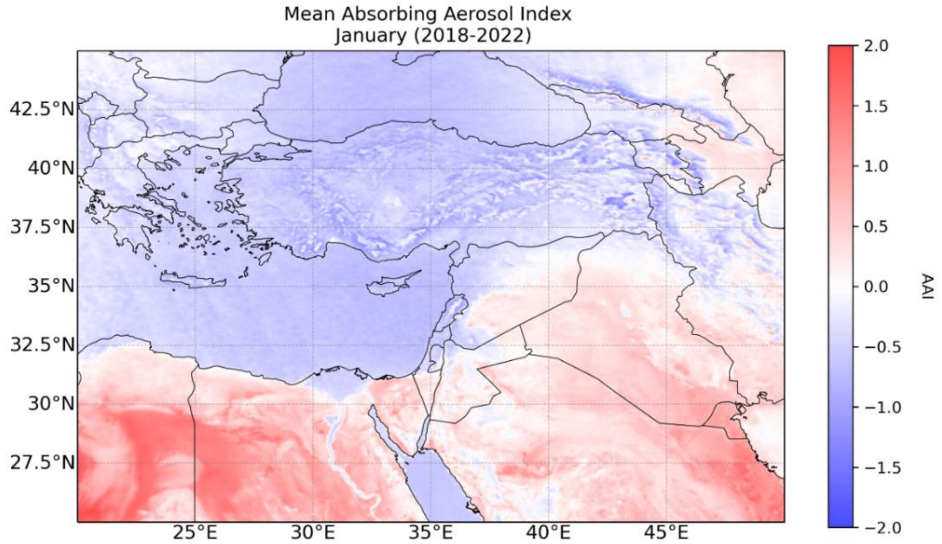

Figure 70. Visualization of AAI for January, EMB

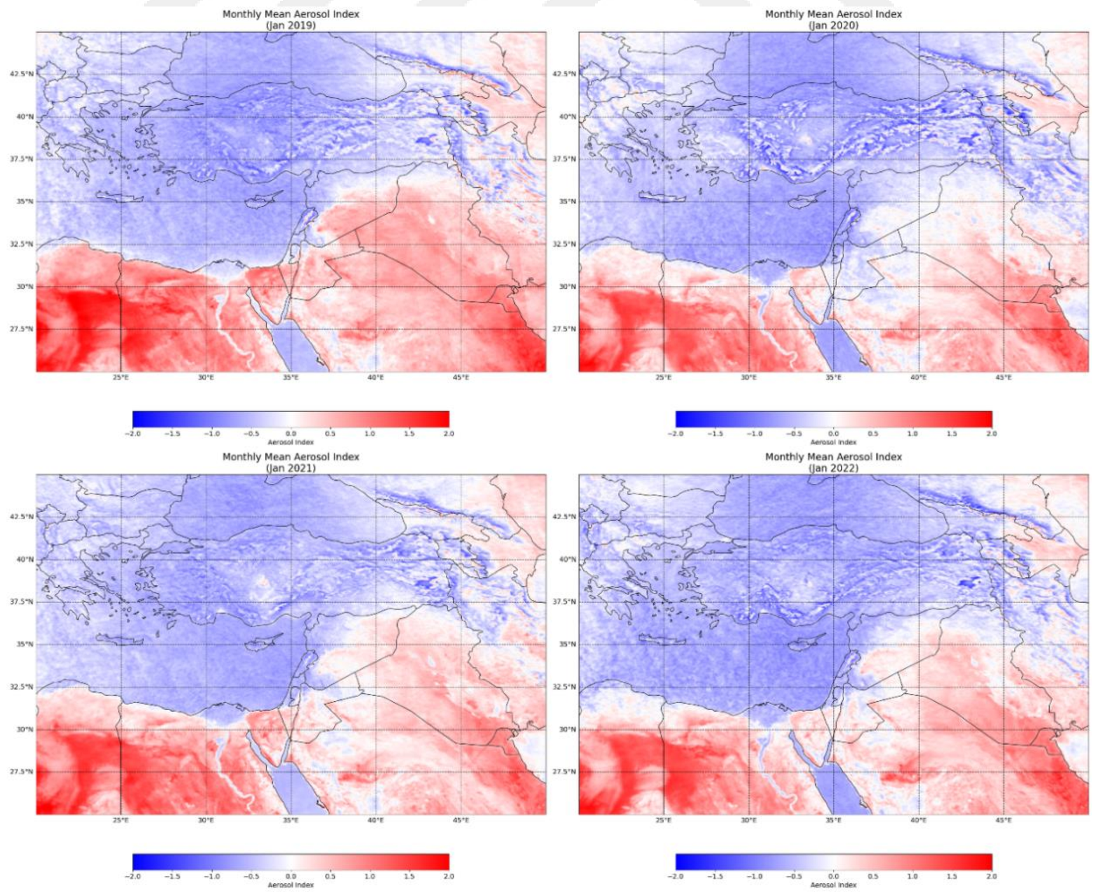

Figure 71. Monthly visualization of AAI for January, EMB (2019, 2020, 2021, 2022)

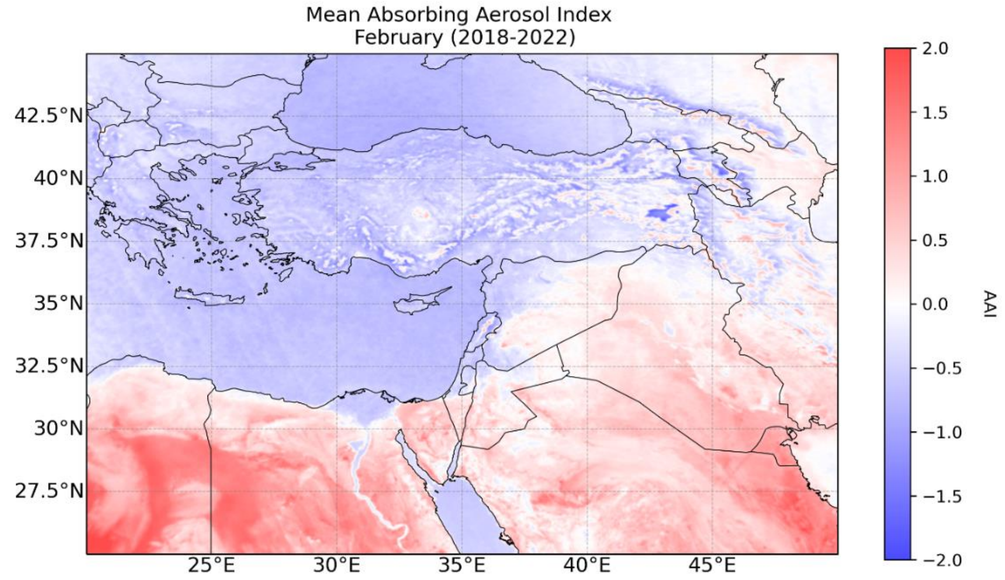

Figure 72. Visualization of AAI for February, EMB

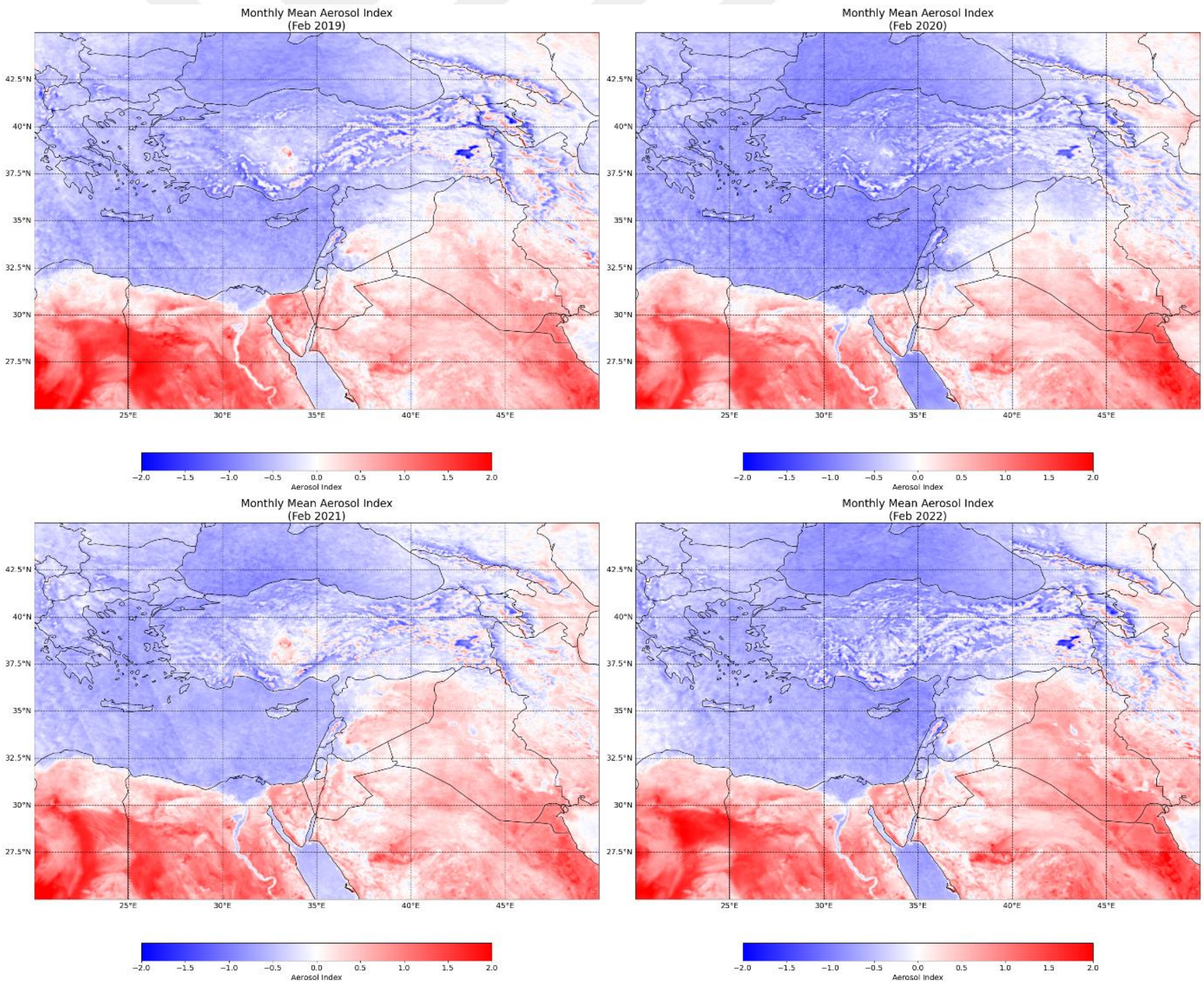

Figure 73. Monthly visualization of AAI for February, EMB (2019, 2020, 2021, 2022)

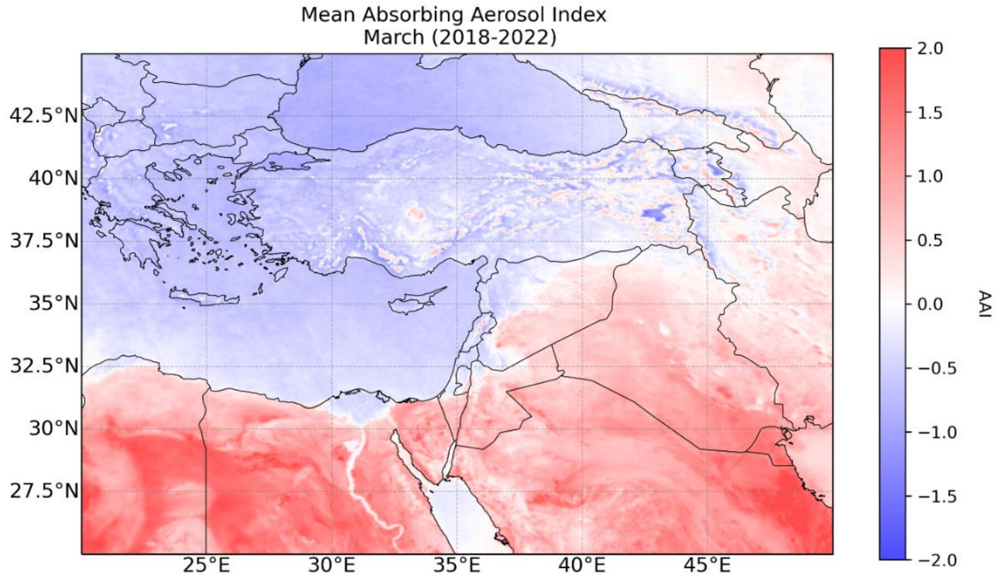

Figure 74. Visualization of AAI for March, EMB

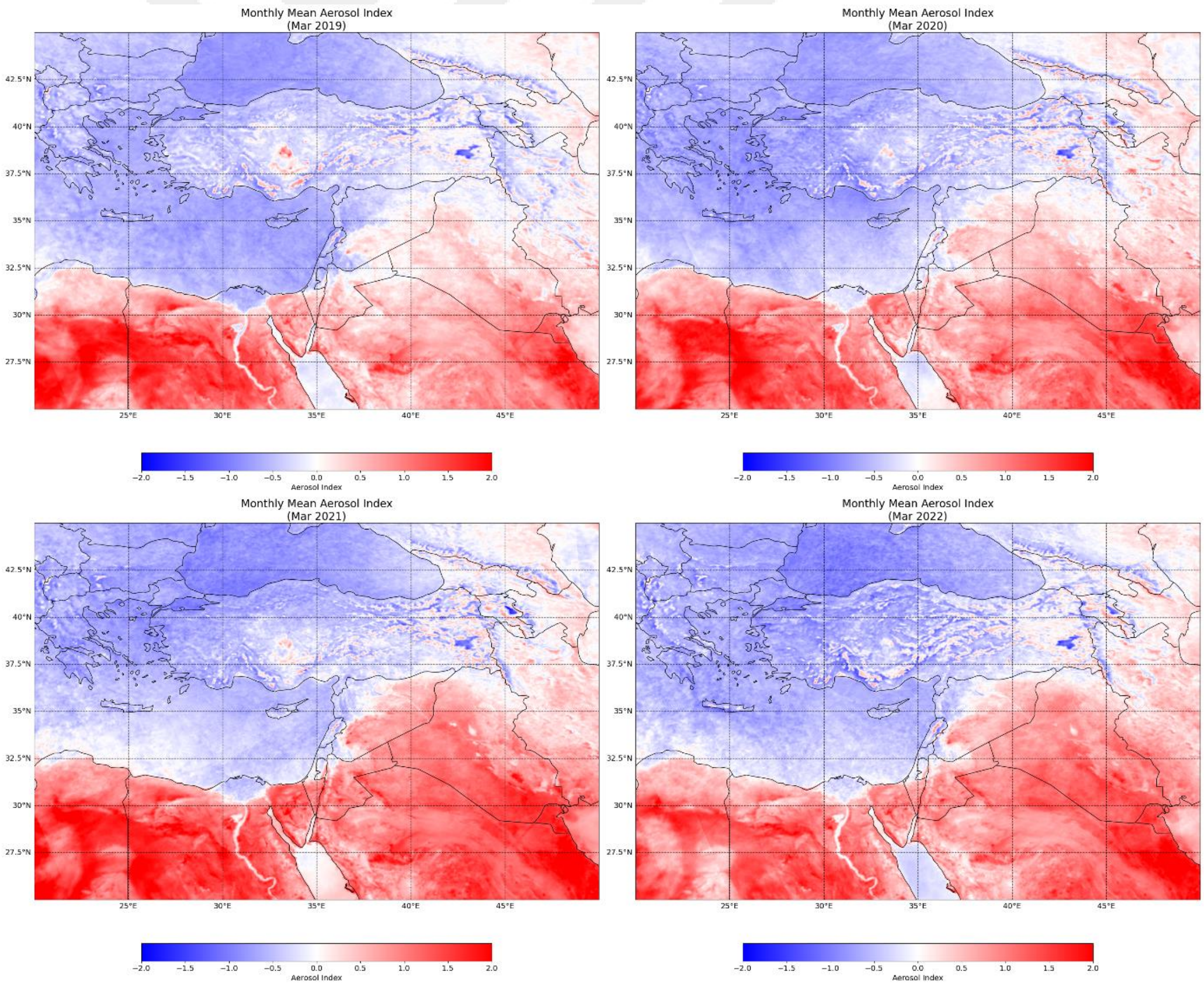

Figure 75. Monthly visualization of AAI for March, EMB (2019, 2020, 2021, 2022)

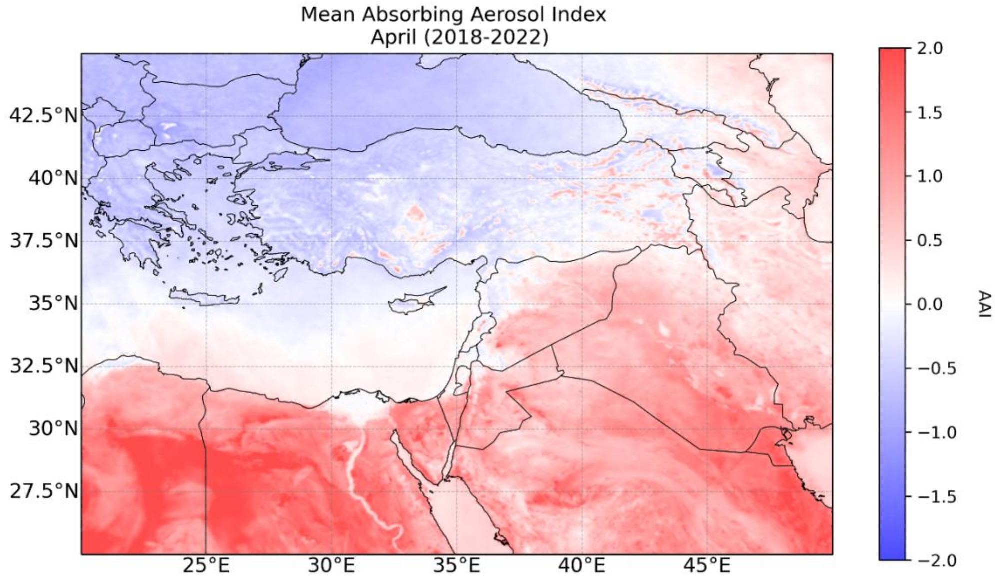

Figure 76. Visualization of AAI for March, EMB

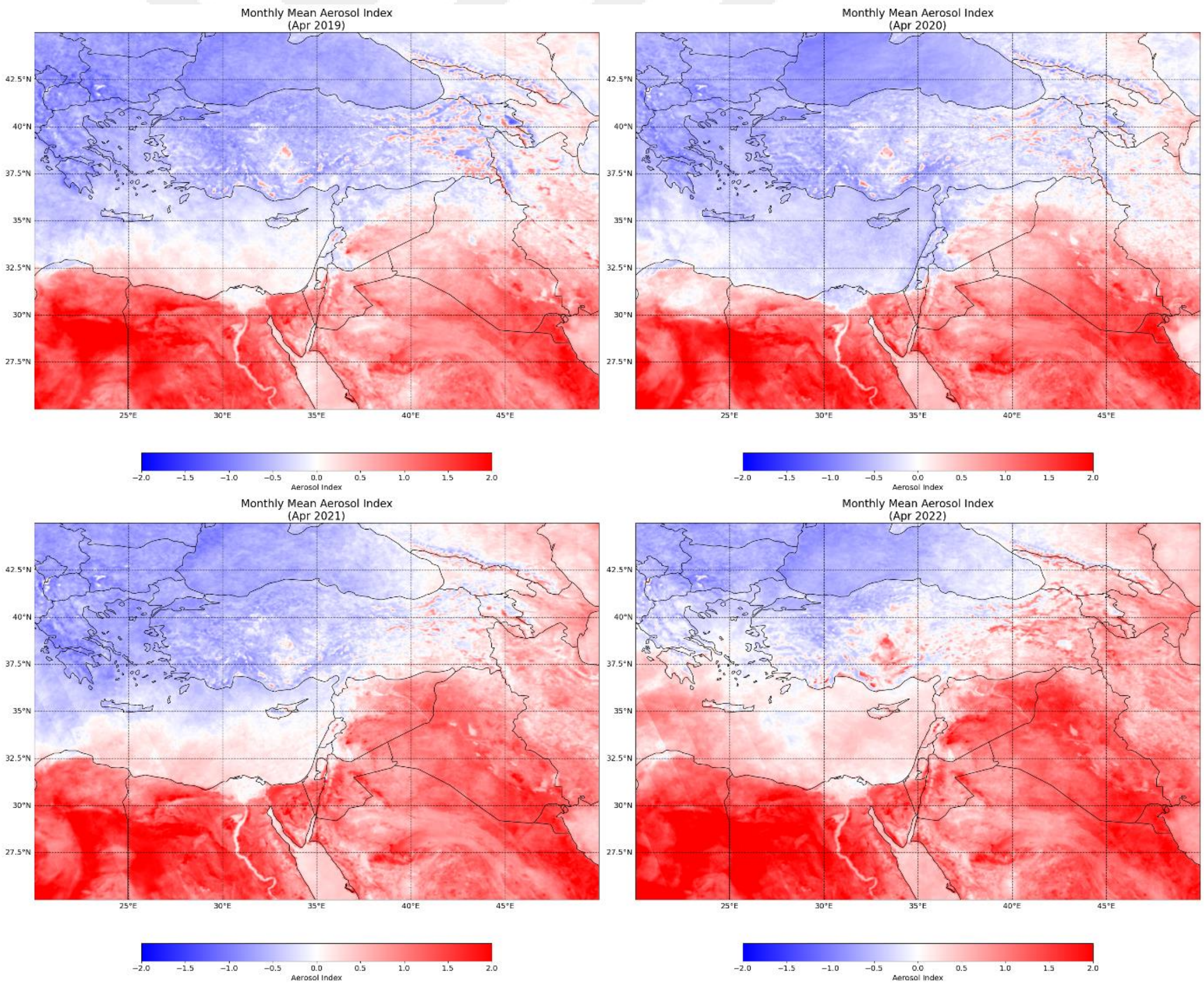

Figure 77. Monthly visualization of AAI for April, EMB (2019, 2020, 2021, 2022)

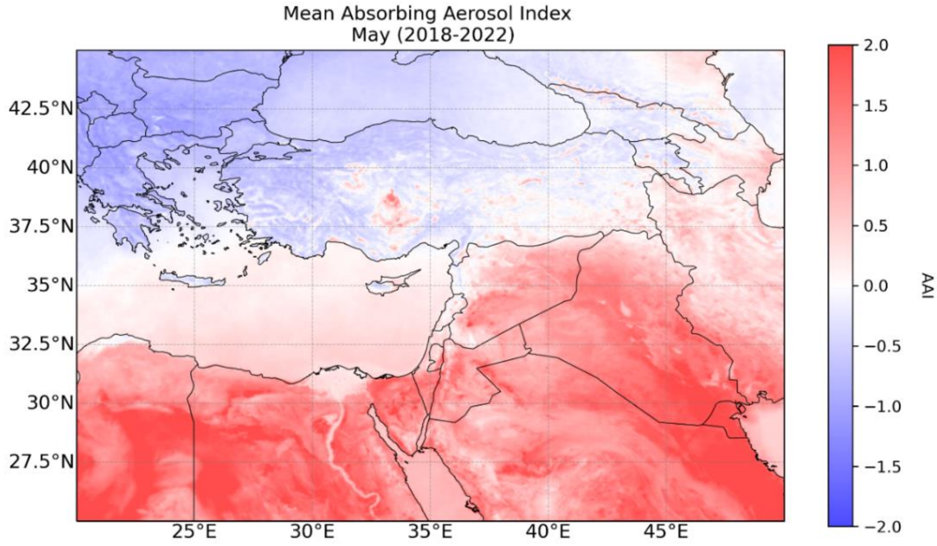

Figure 78. Visualization of AAI for May, EMB

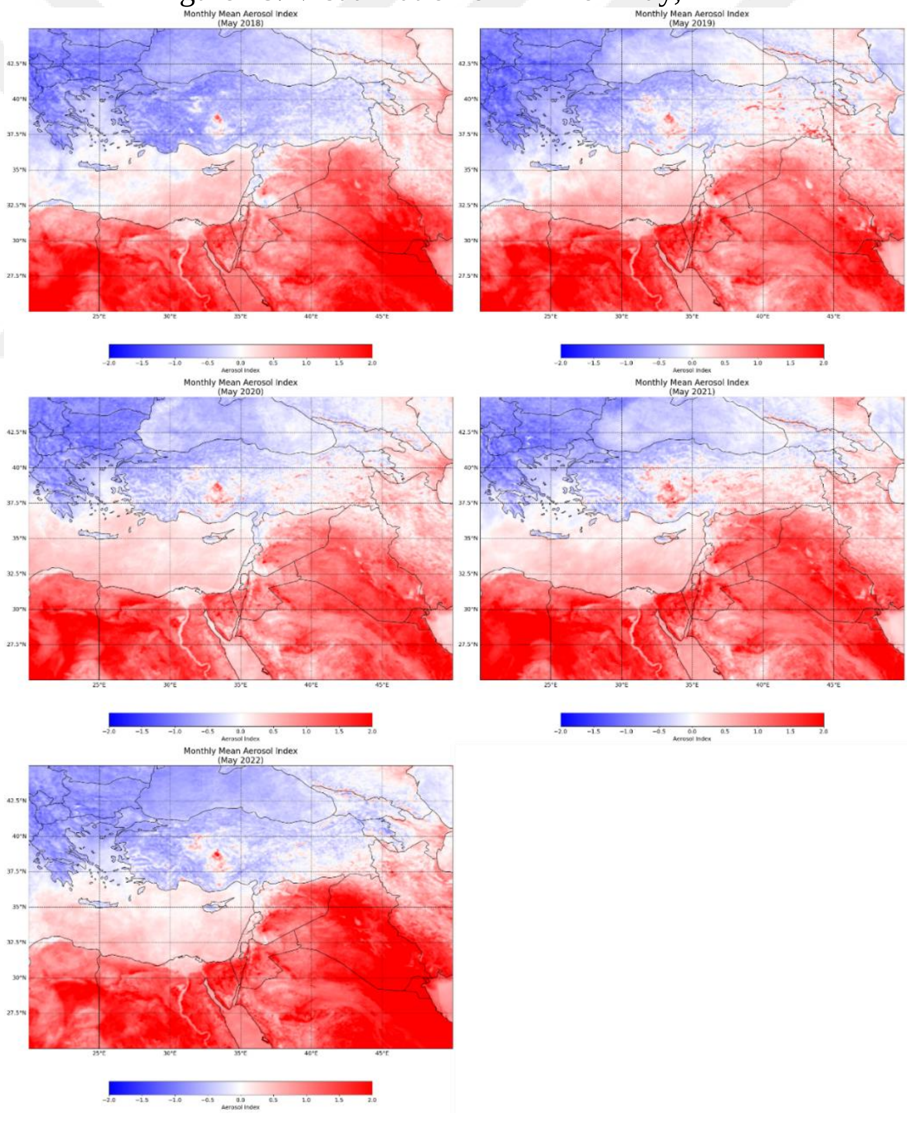

Figure 79. Monthly visualization of AAI for May, EMB (2018, 2019, 2020, 2021, 2022)

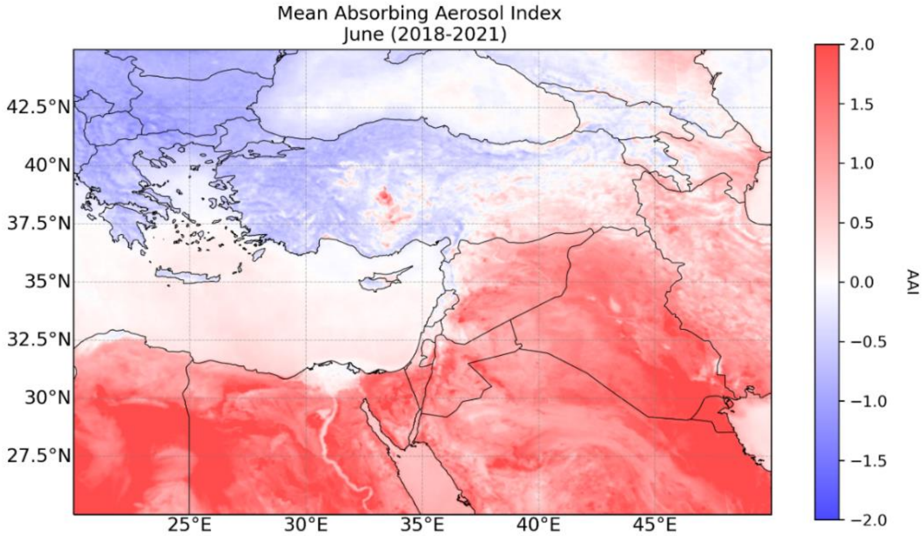

Figure 80. Visualization of AAI for June, EMB

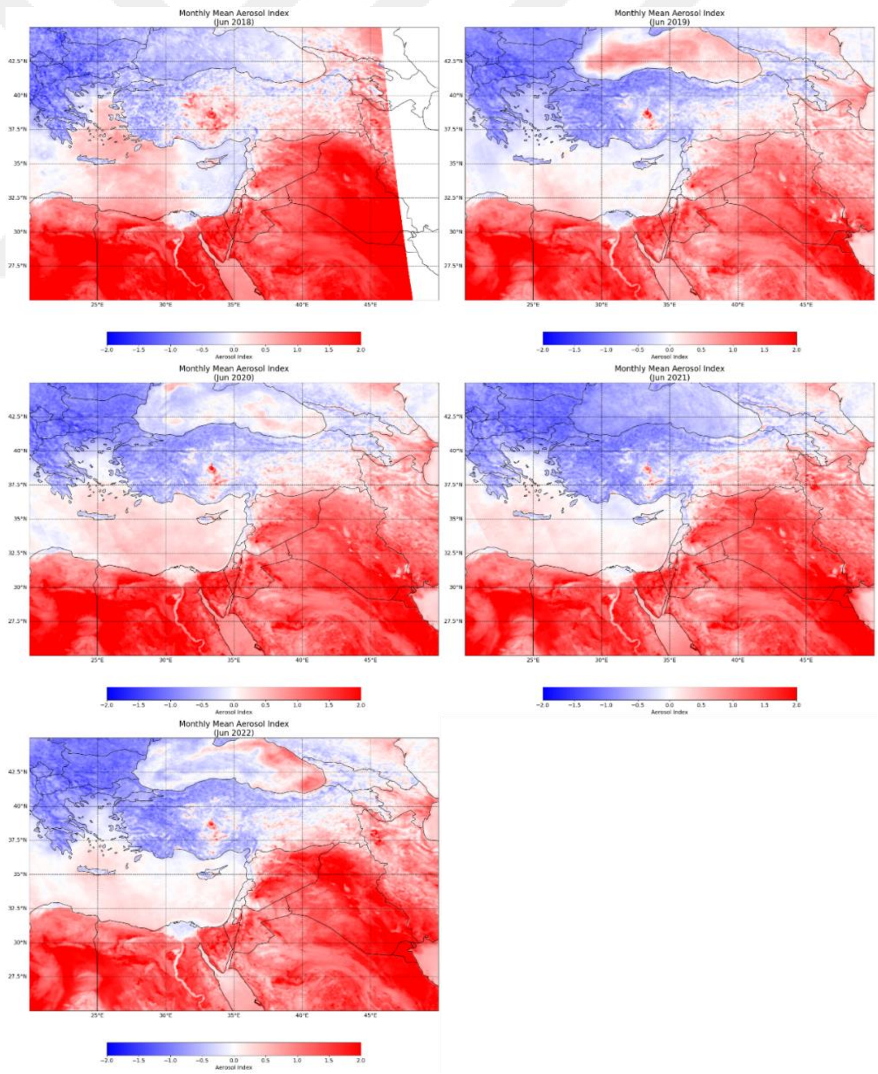

Figure 81. Monthly visualization of AAI for June, EMB (2018, 2019, 2020, 2021, 2022)

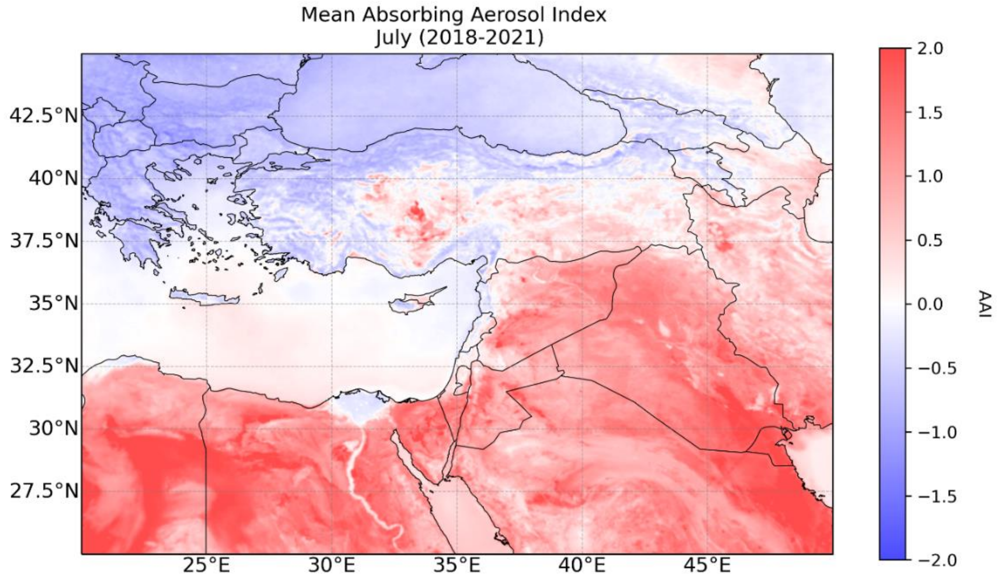

Figure 82. Visualization of AAI for July, EMB

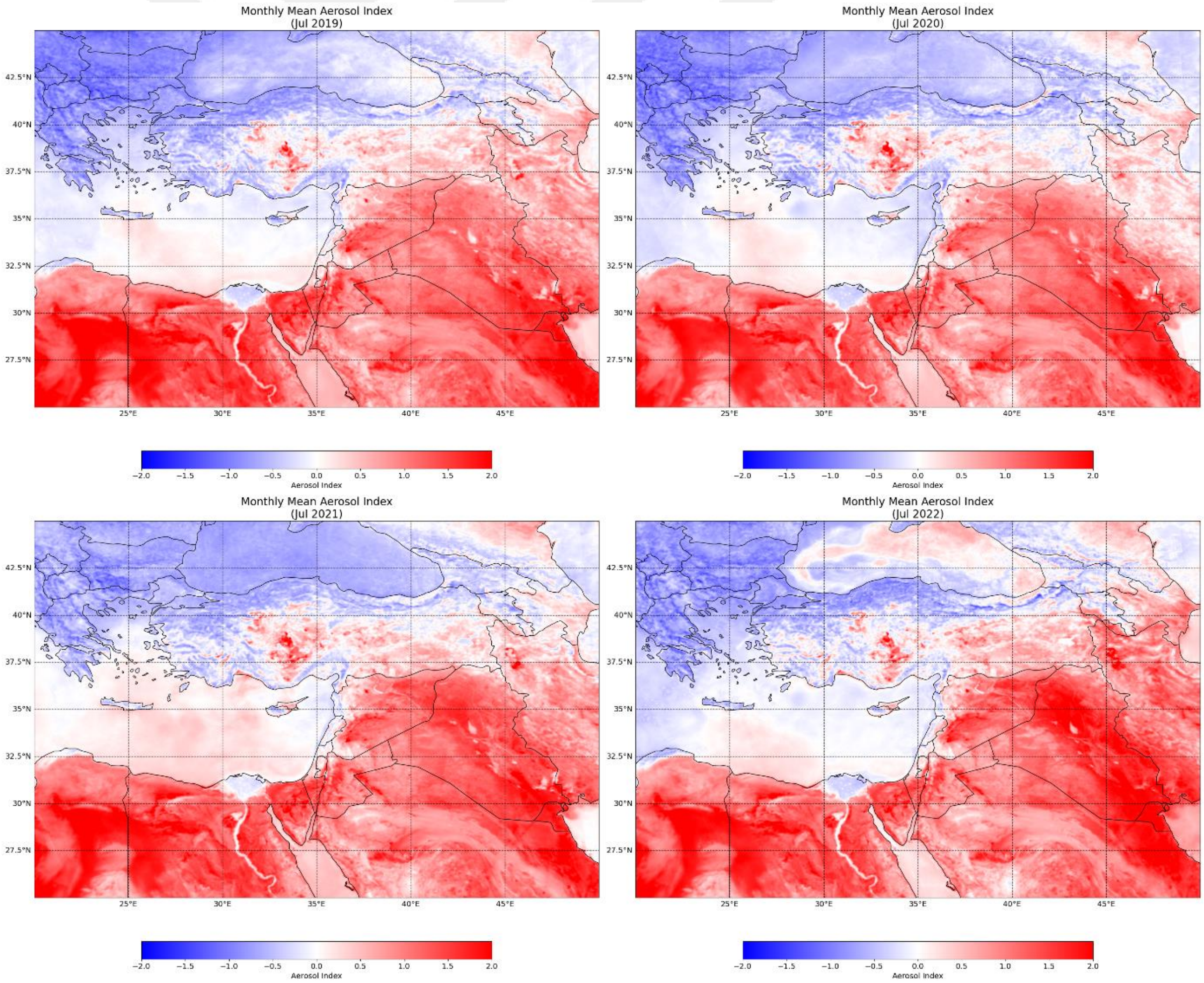

Figure 83. Monthly visualization of AAI for July, EMB (2018, 2019, 2020, 2021)

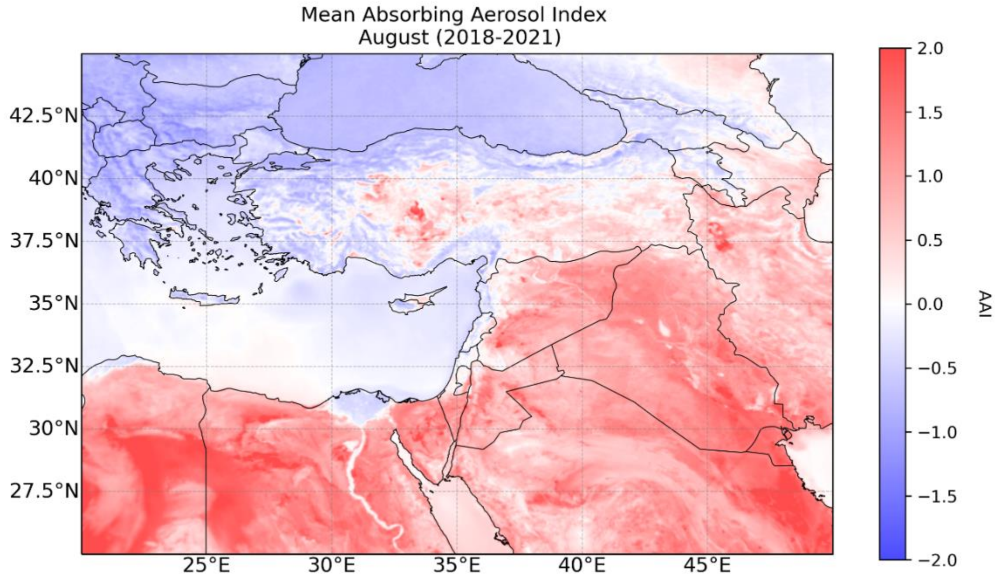

Figure 84. Visualization of AAI for August, EMB

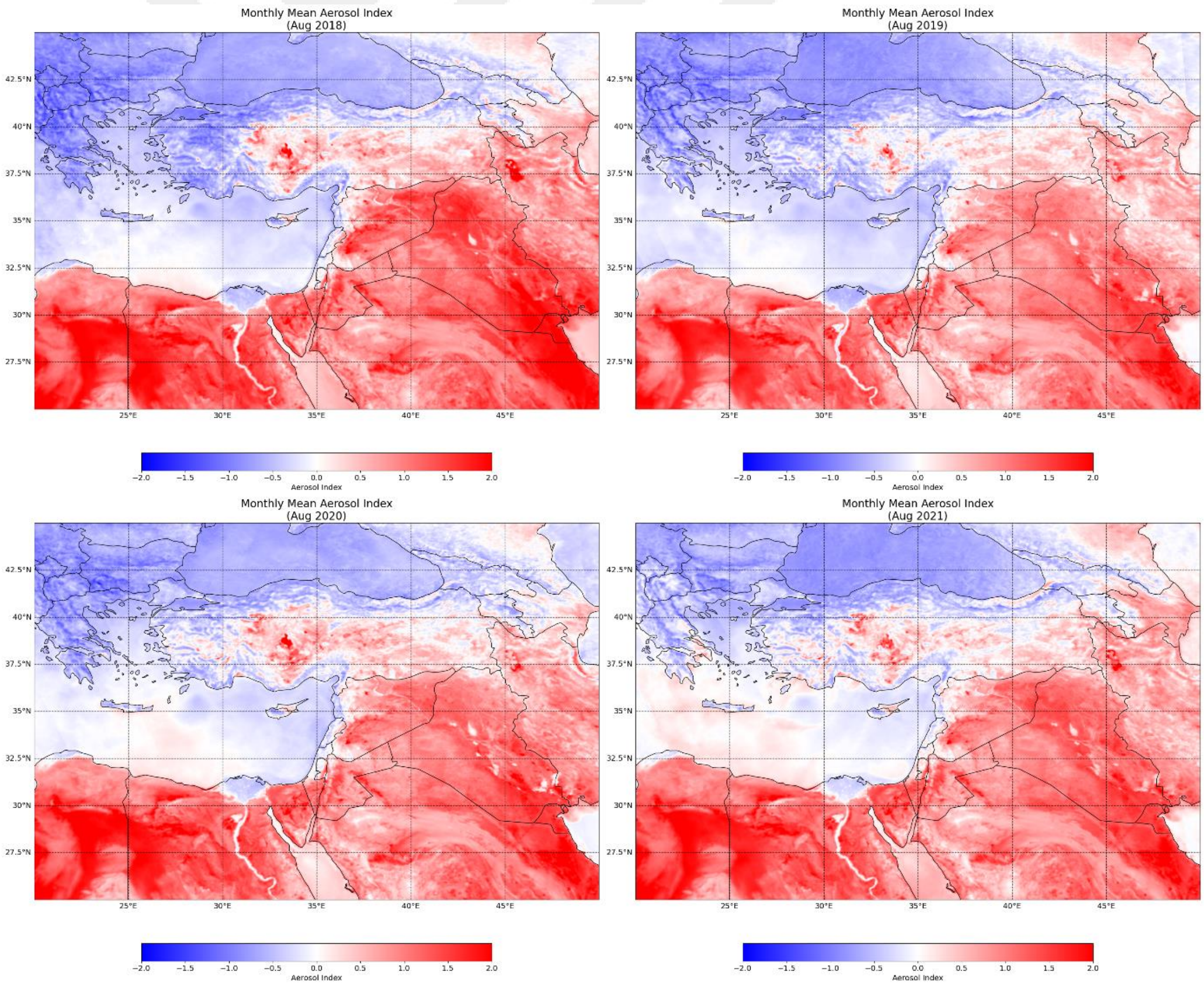

Figure 85. Monthly visualization of AAI for August, EMB (2018, 2019, 2020, 2021)

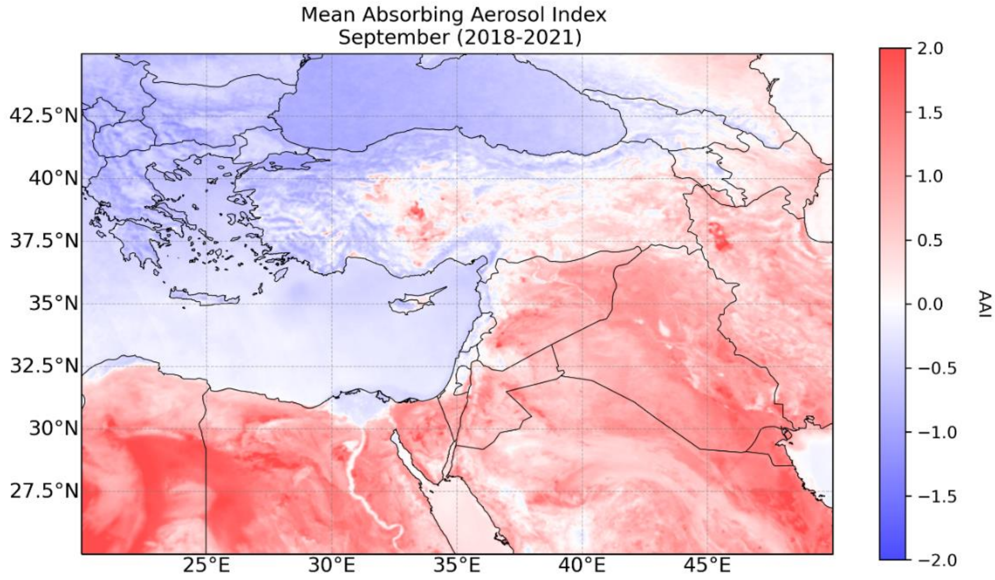

Figure 86. Visualization of AAI for September, EMB

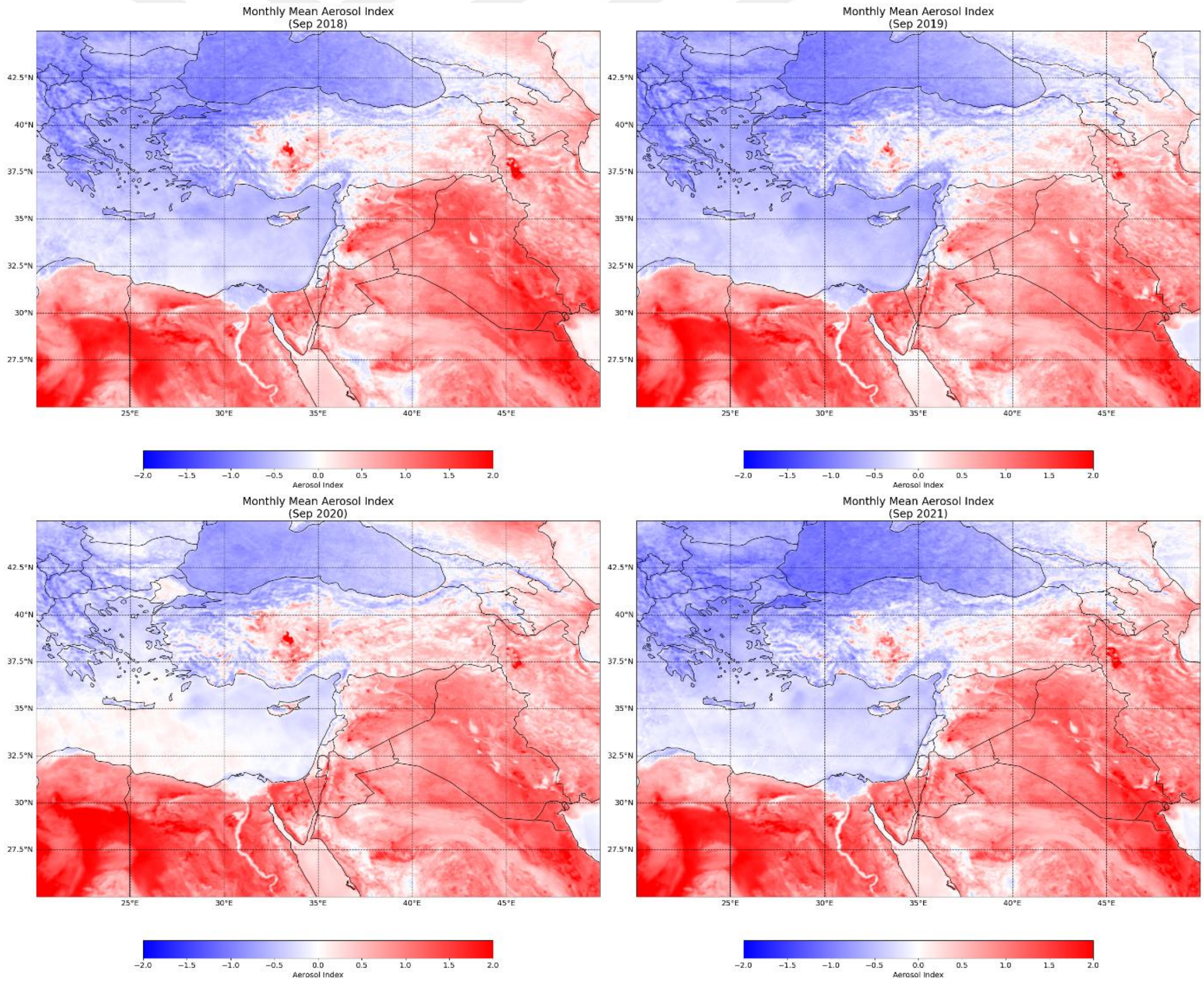

Figure 87. Monthly visualization of AAI for September, EMB (2018, 2019, 2020, 2021)

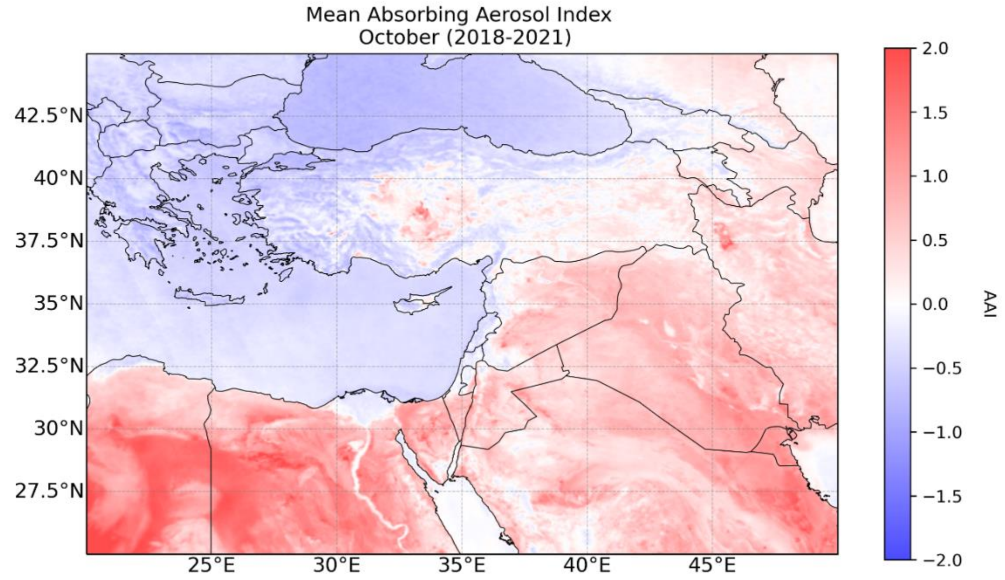

Figure 88. Visualization of AAI for October, EMB

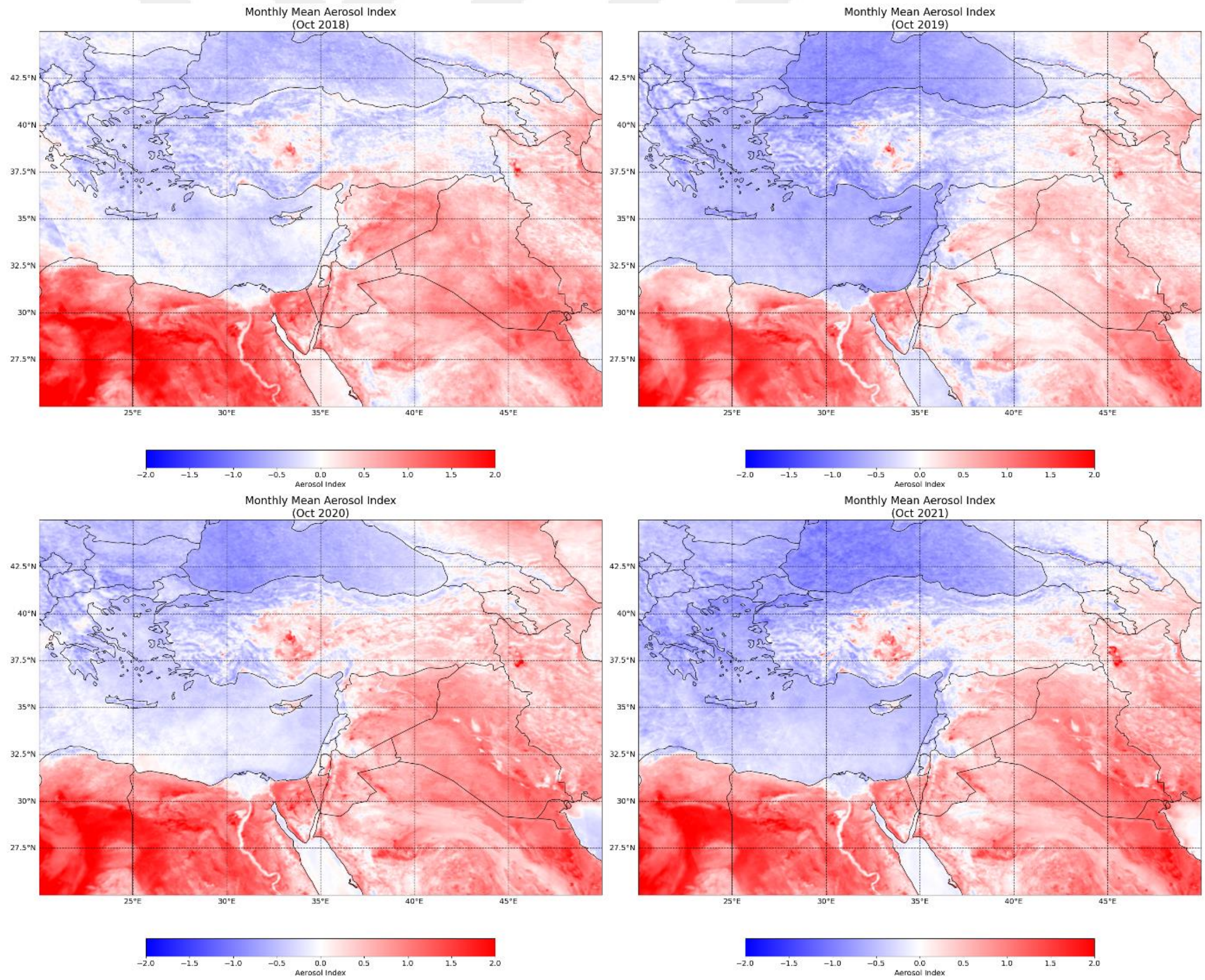

Figure 89. Monthly visualization of AAI for October, EMB (2018, 2019, 2020, 2021)

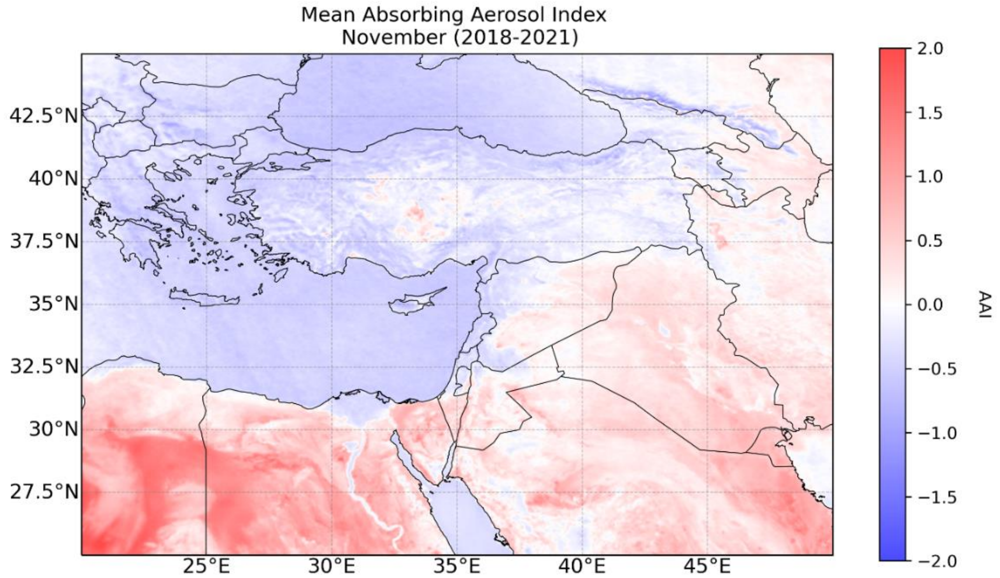

Figure 90. Visualization of AAI for November, EMB

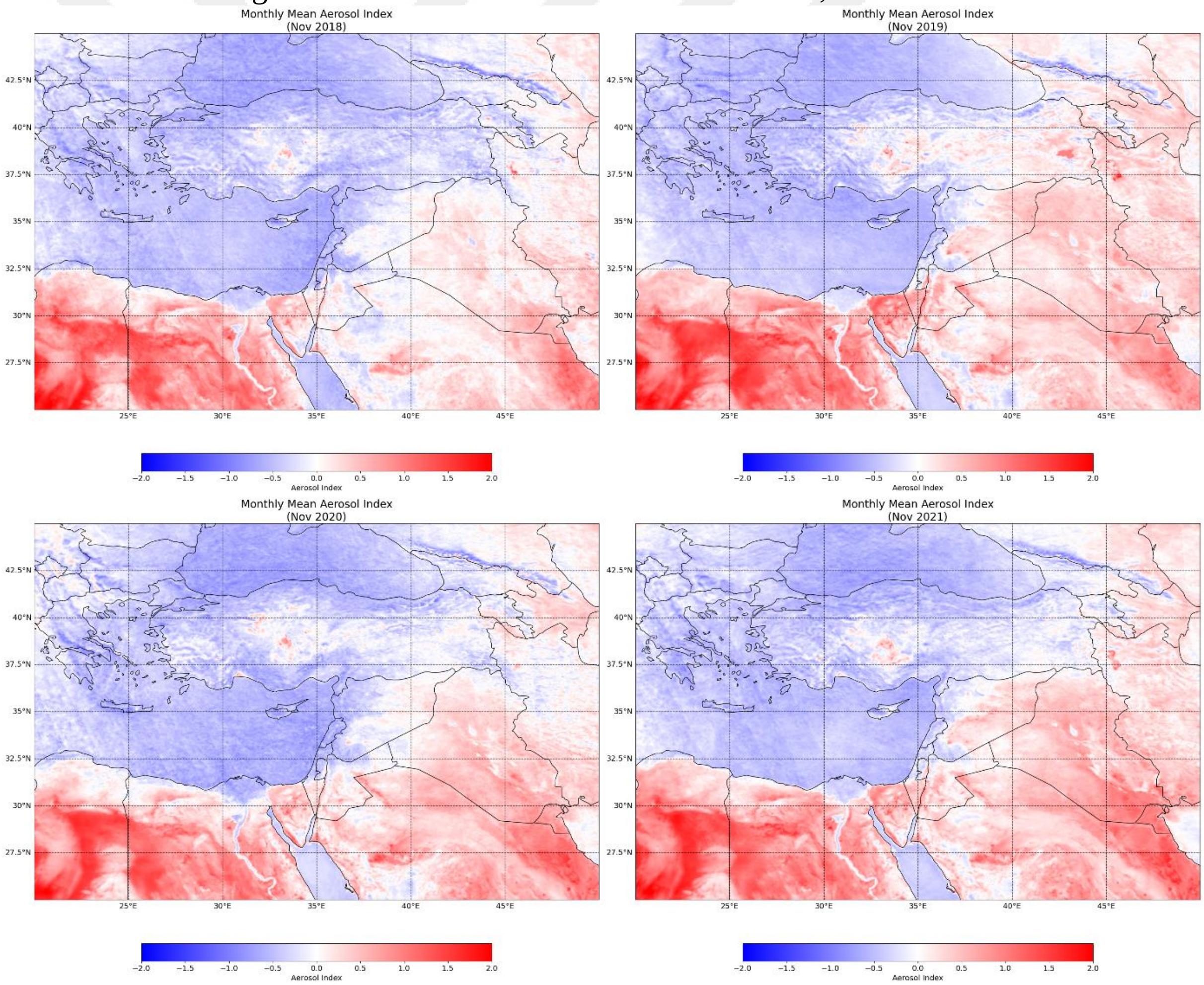

Figure 91. Monthly visualization of AAI for November, EMB (2018, 2019, 2020, 2021)

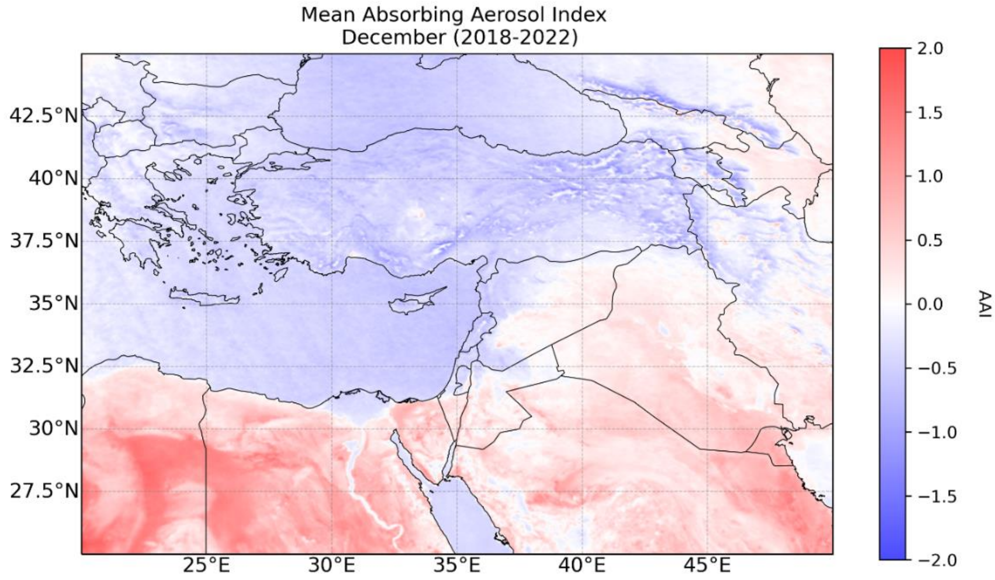

Figure 92. Visualization of AAI for December, EMB

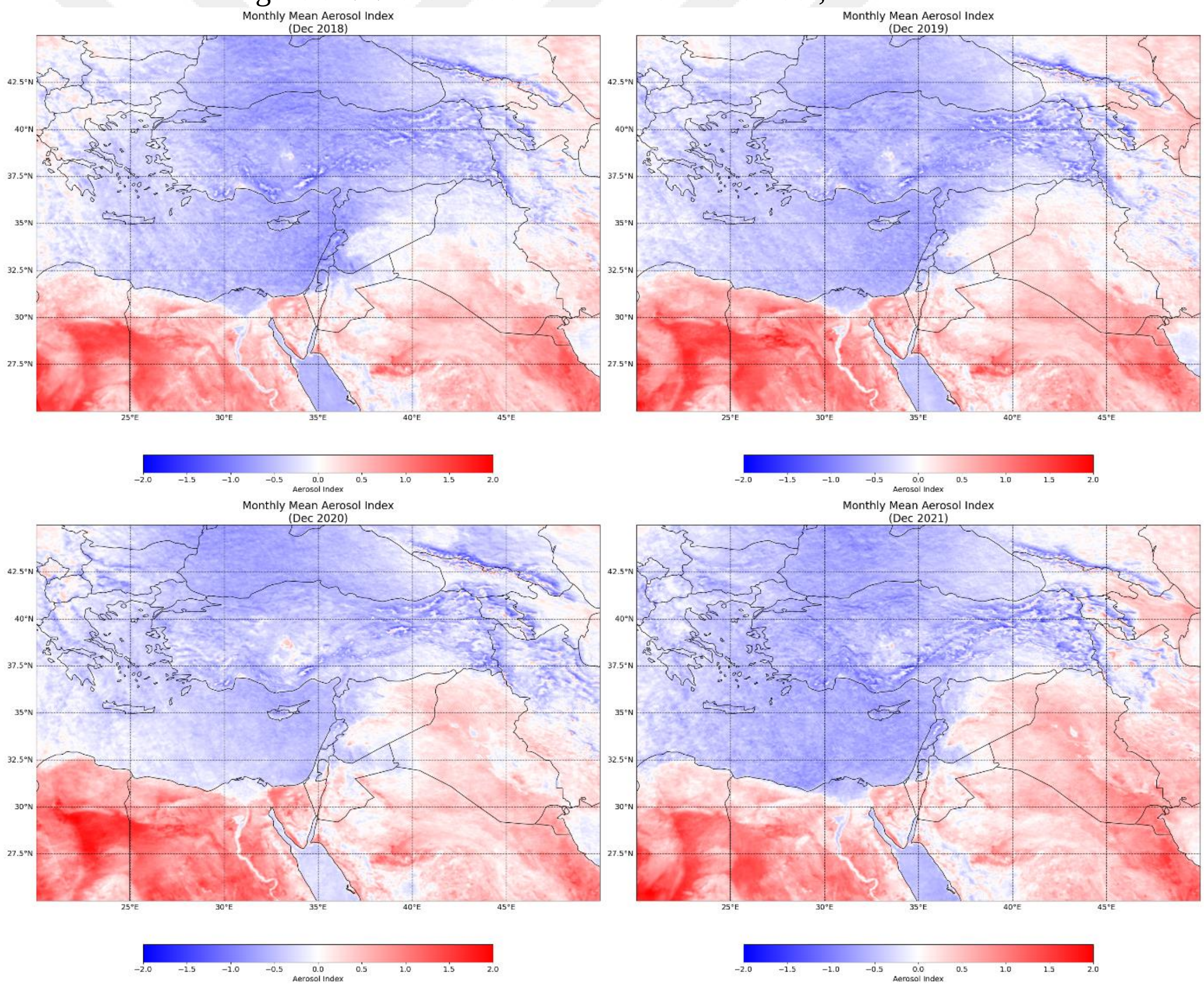

Figure 93. Monthly visualization of AAI for December, EMB (2018, 2019, 2020, 2021)

APPENDIX 2 – Trend statistics and time series graphs of AAI data for all domains

Table 17. Trend Statistics of AAI for All Domains for All Years

Time Series	First Year	Last Year	N	Test Z	Significance	Q	Lower Band Q	Upper Band Q
EMB	2018	2022	1554	0.15111	0.05	1.95996	0.15393	0.180291
Türkiye	2018	2022	1554	-0.23818	0.05	1.95996	-0.27433	-0.24088
NA	2018	2022	1554	0.24642	0.05	1.95996	0.24149	0.28313
NAP	2018	2022	1554	0.24459	0.05	1.95996	0.23859	0.28130

- **Time series graphs for the Eastern Mediterranean Basin**

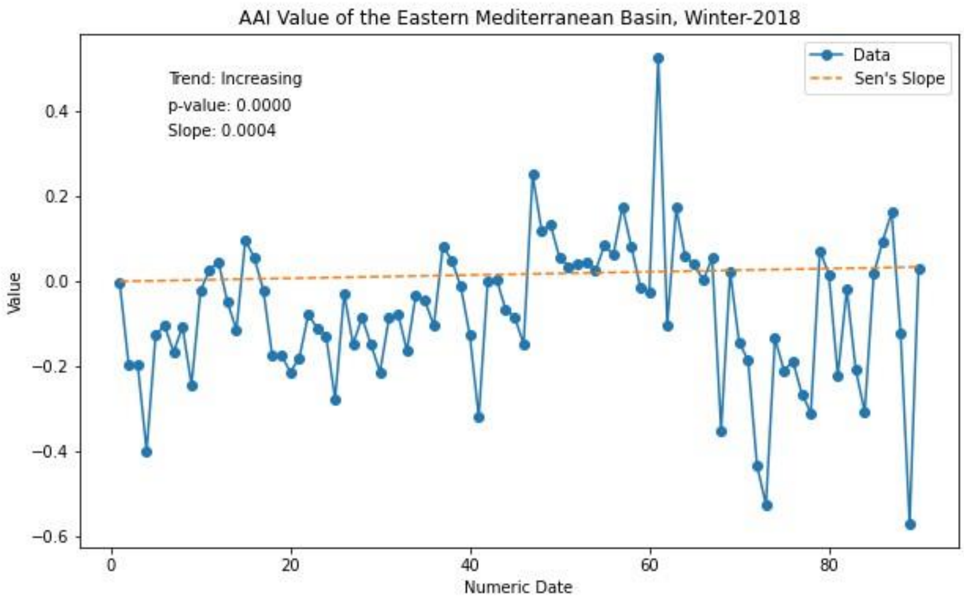

Figure 94. Seasonal trends of AAI in the EMB, Winter-2018

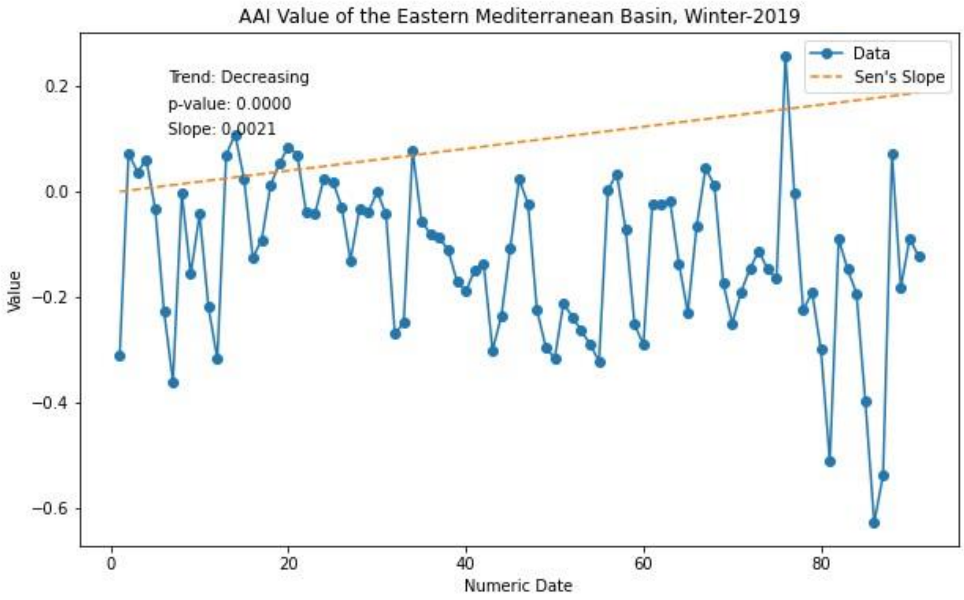

Figure 95. Seasonal trends of AAI in the EMB, Winter-2019

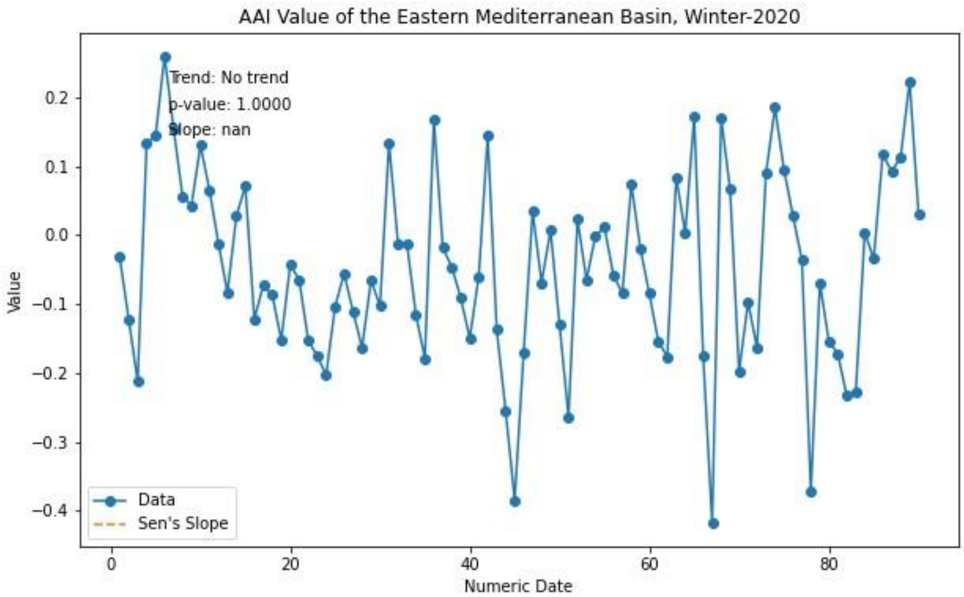

Figure 96. Seasonal trends of AAI in the EMB, Winter-2020

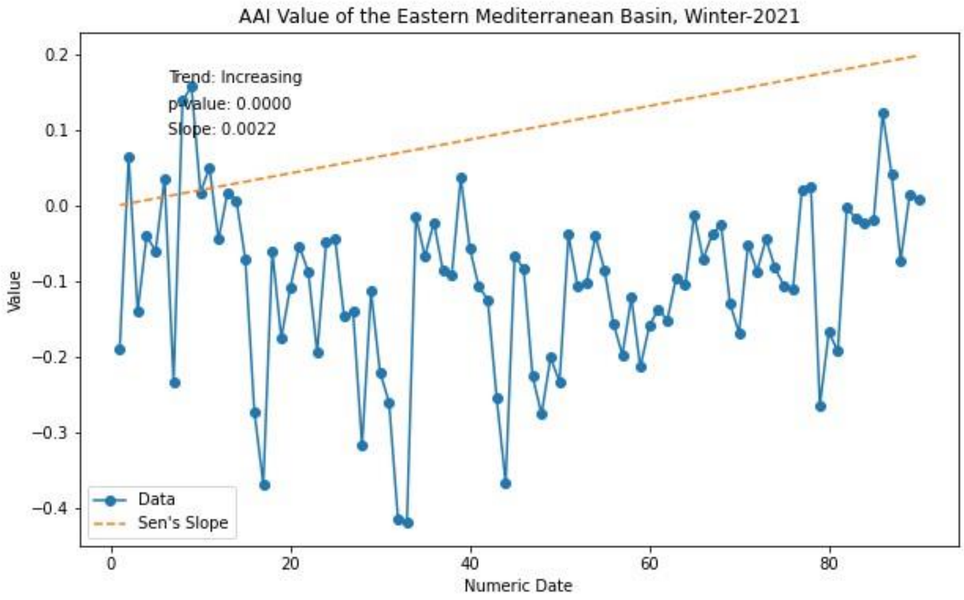

Figure 97. Seasonal trends of AAI in the EMB, Winter-2021

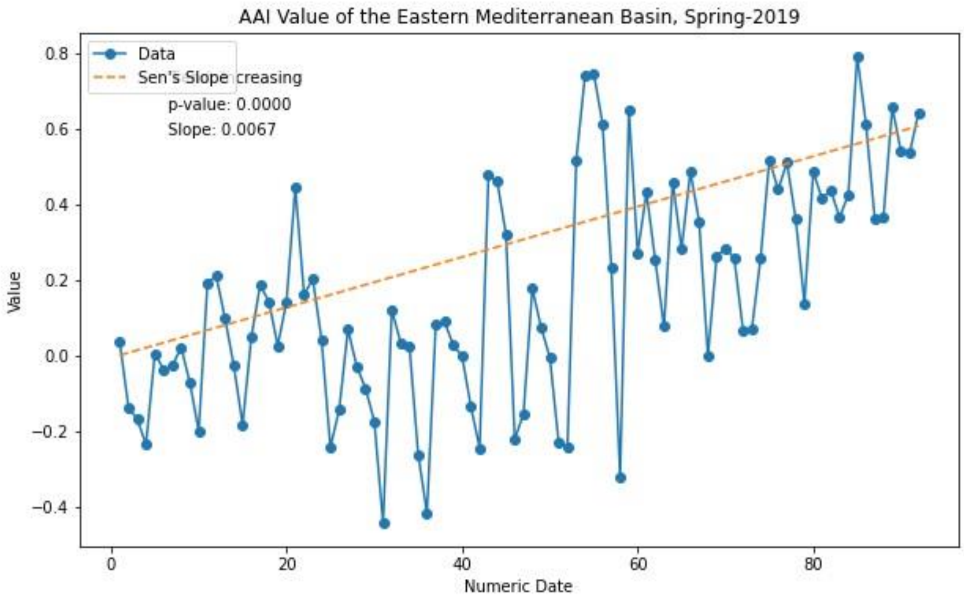

Figure 98. Seasonal trends of AAI in the EMB, Spring-2019

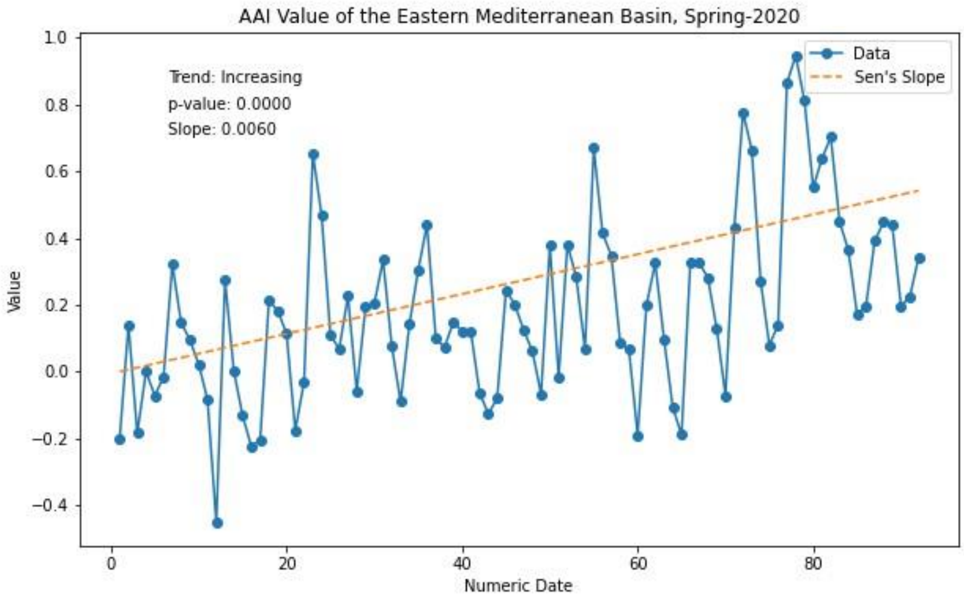

Figure 99. Seasonal trends of AAI in the EMB, Spring-2020

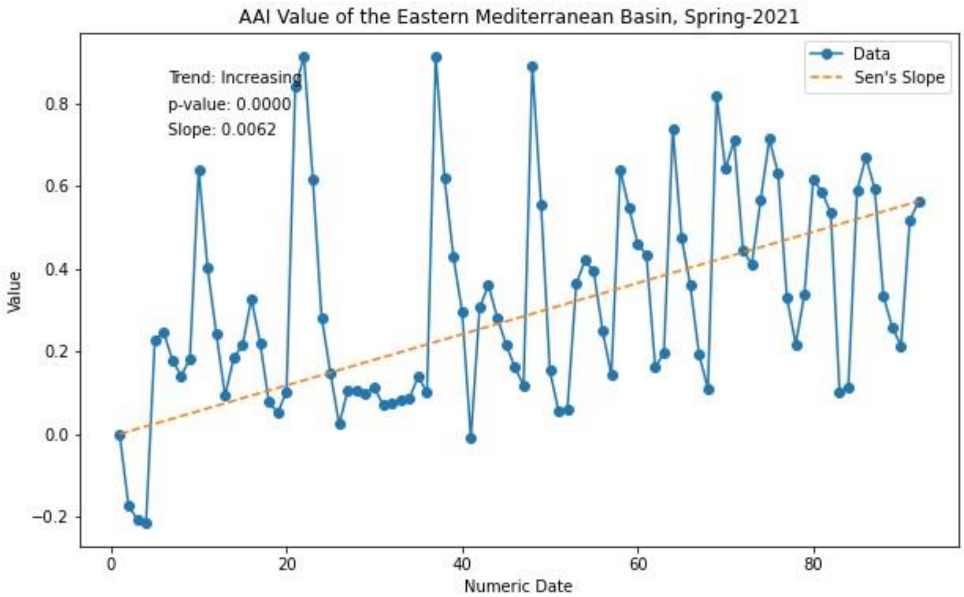

Figure 100. Seasonal trends of AAI in the EMB, Spring-2021

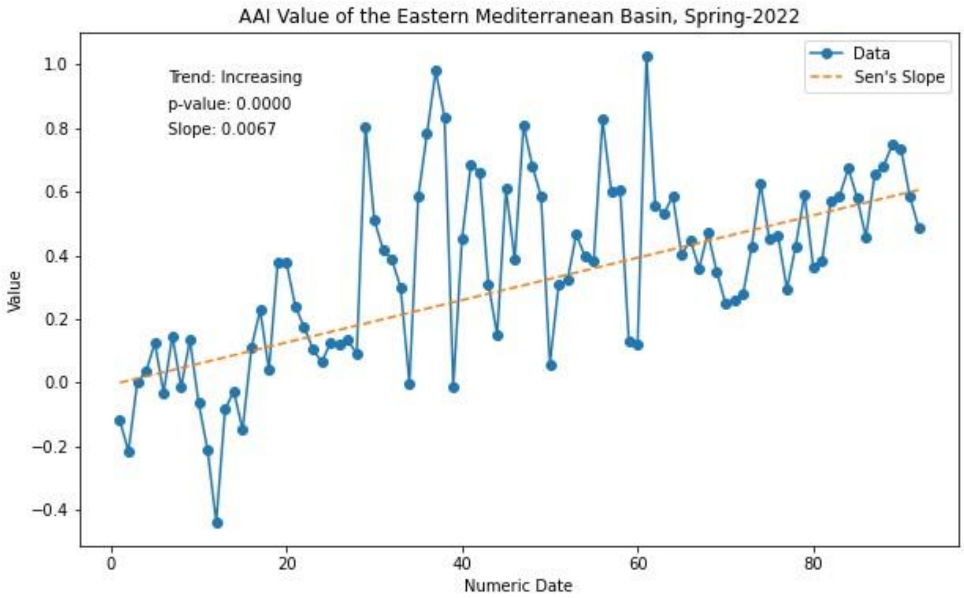

Figure 101. Seasonal trends of AAI in the EMB, Spring-2022

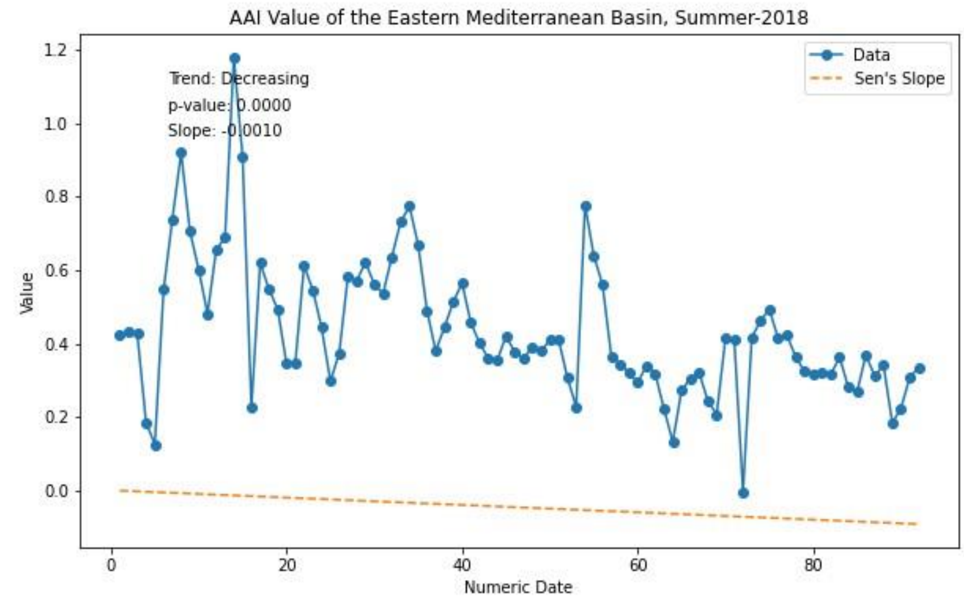

Figure 102. Seasonal trends of AAI in the EMB, Summer-2018

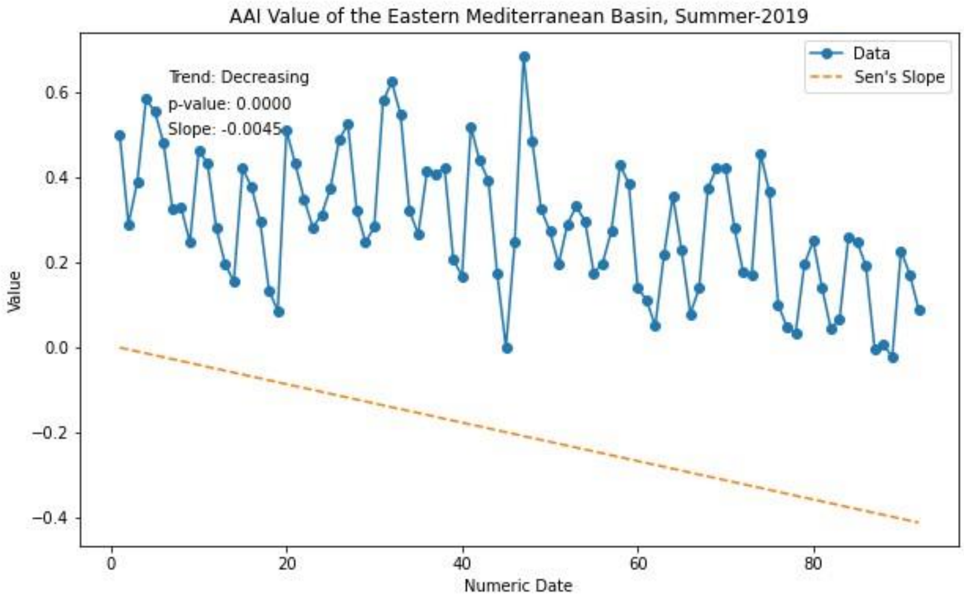

Figure 103. Seasonal trends of AAI in the EMB, Summer-2019

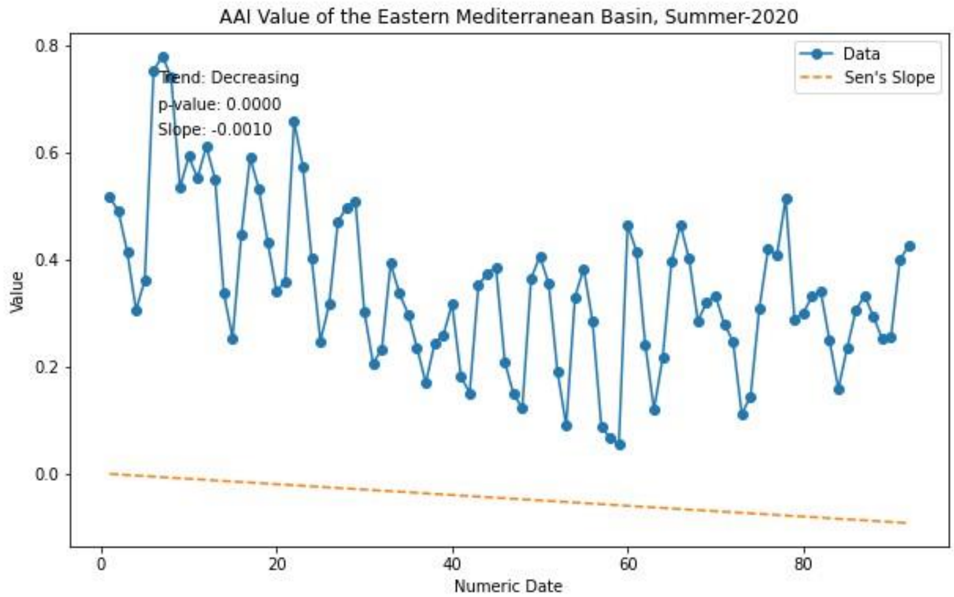

Figure 104. Seasonal trends of AAI in the EMB, Summer-2020

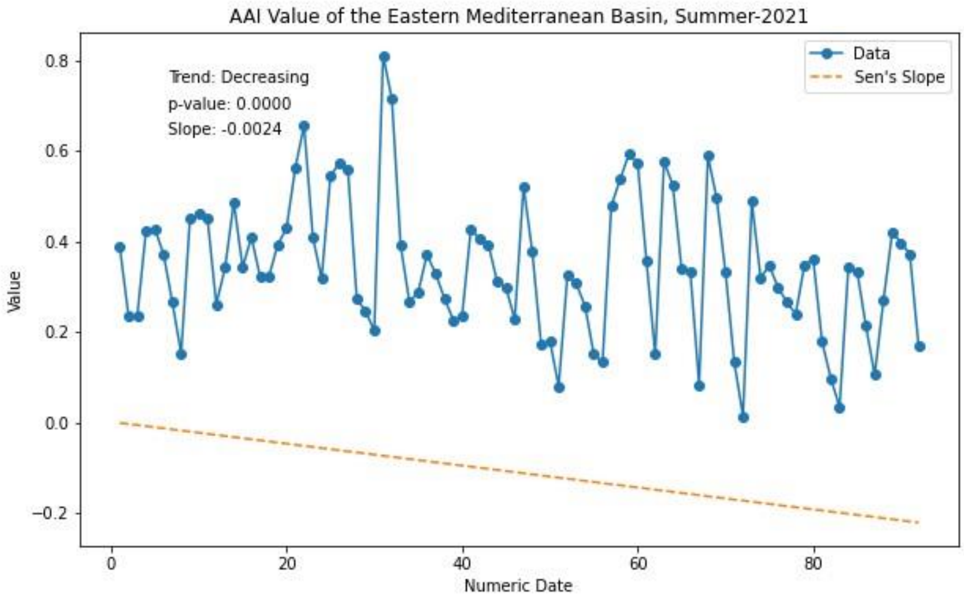

Figure 105. Seasonal trends of AAI in the EMB, Summer-2021

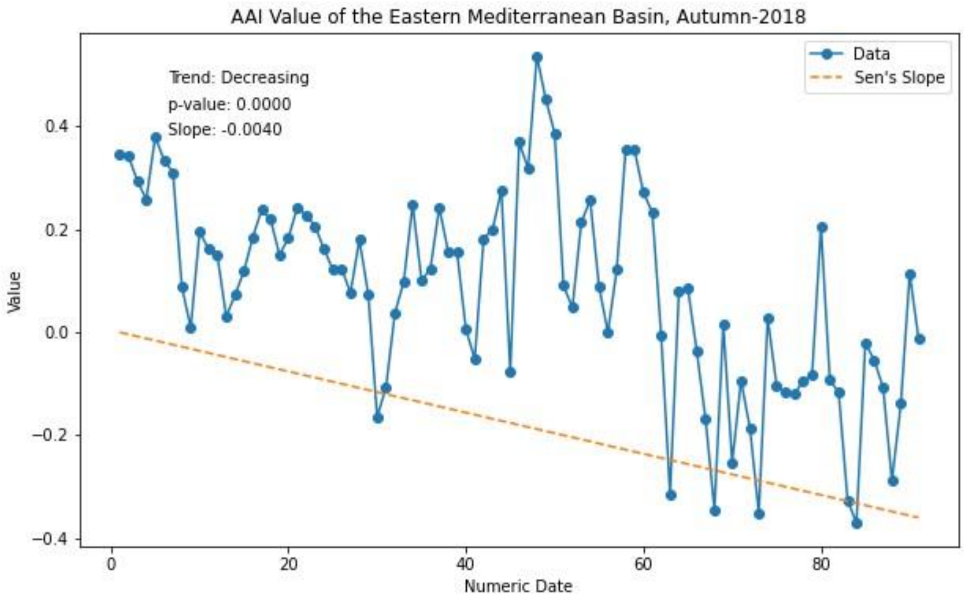

Figure 106. Seasonal trends of AAI in the EMB, Autumn-2018

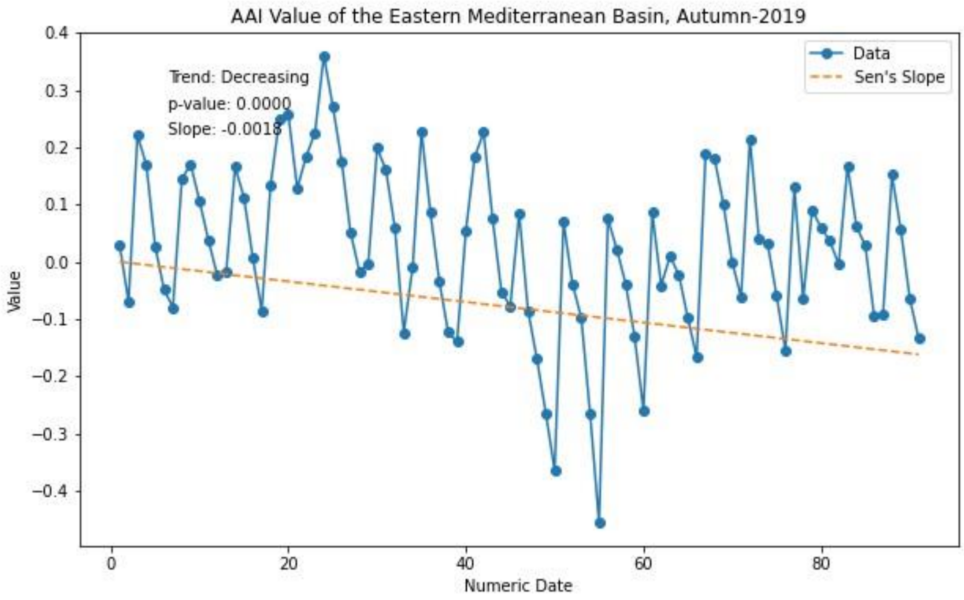

Figure 107. Seasonal trends of AAI in the EMB, Autumn-2019

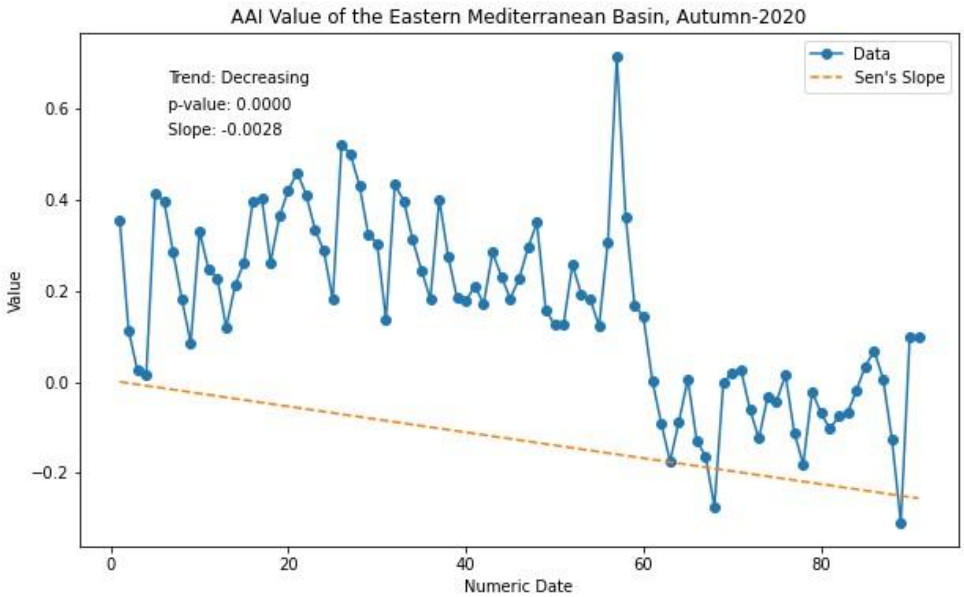

Figure 108. Seasonal trends of AAI in the EMB, Autumn-2020

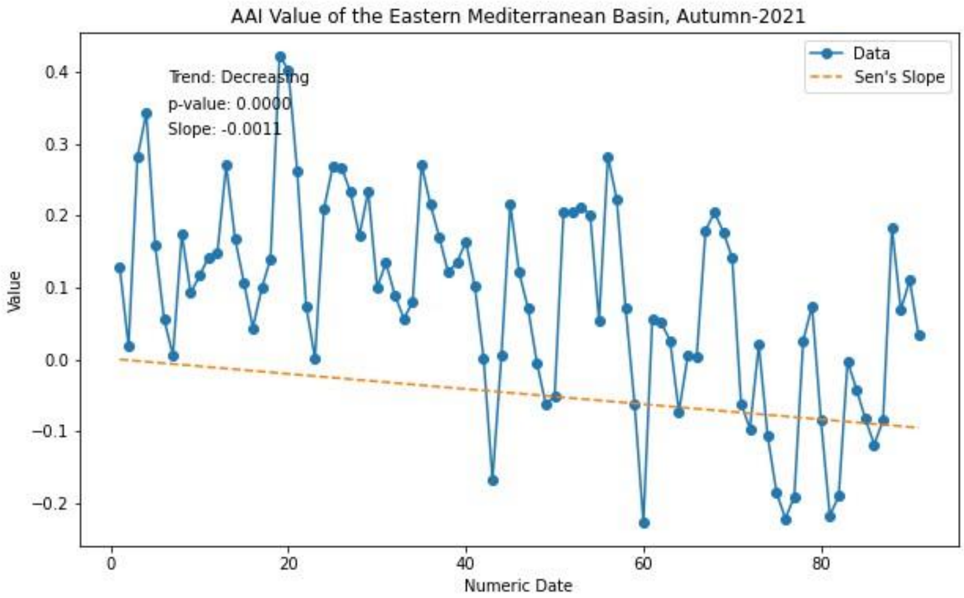

Figure 109. Seasonal trends of AAI in the EMB, Autumn-2021

- **Time series graphs for Türkiye**

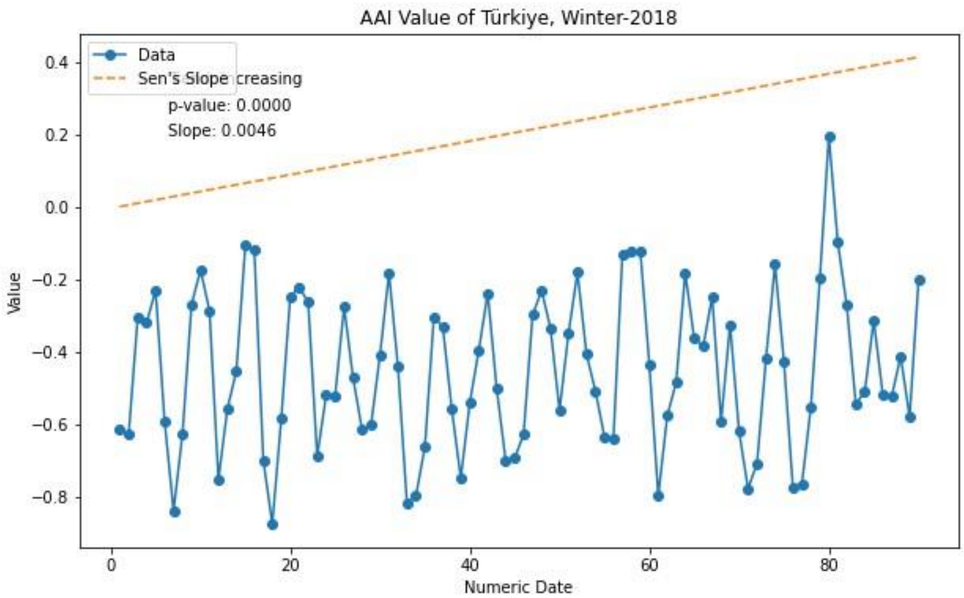

Figure 110. Seasonal trends of AAI in Türkiye, Winter-2018

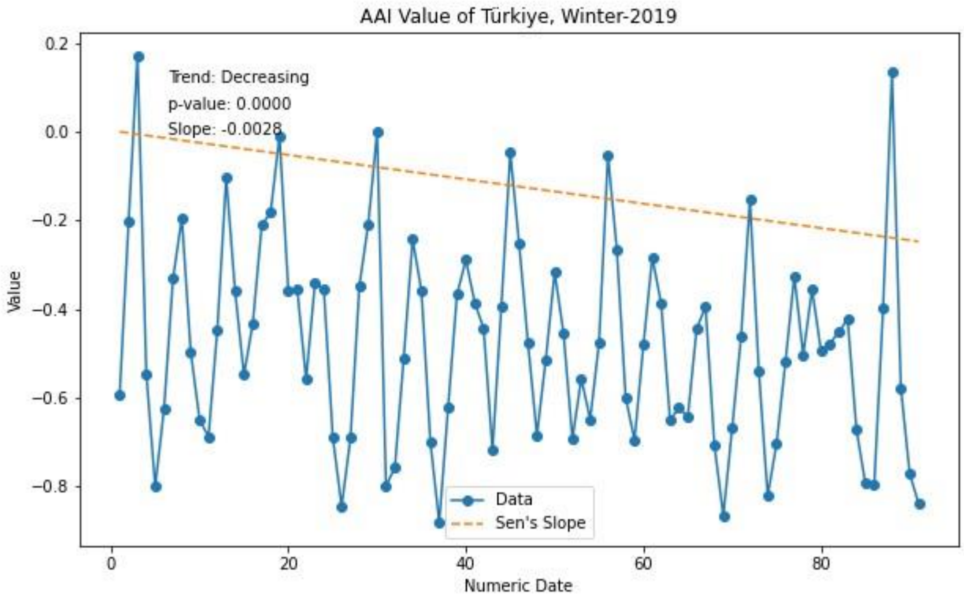

Figure 111. Seasonal trends of AAI in Türkiye, Winter-2019

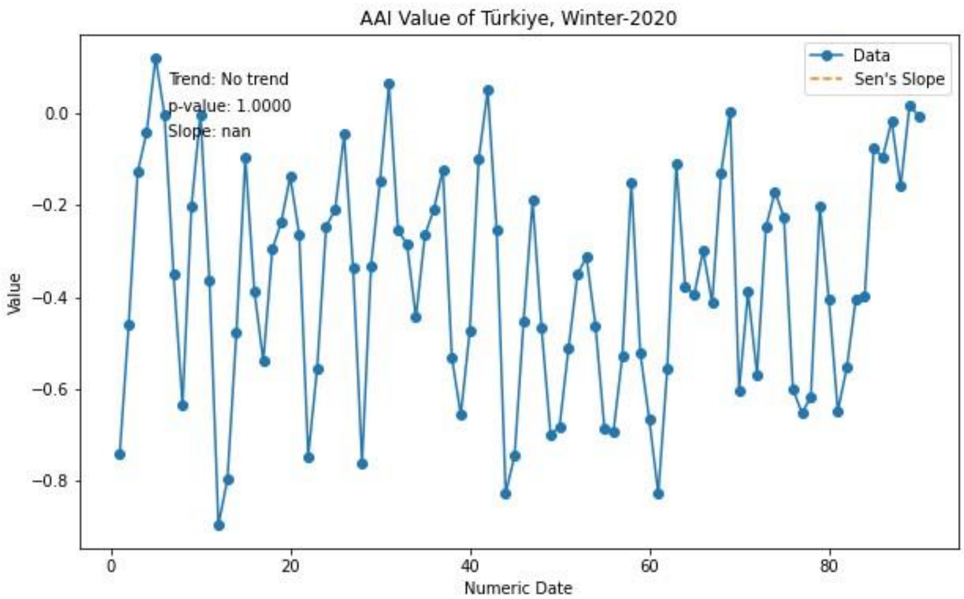

Figure 112. Seasonal trends of AAI in Türkiye, Winter-2020

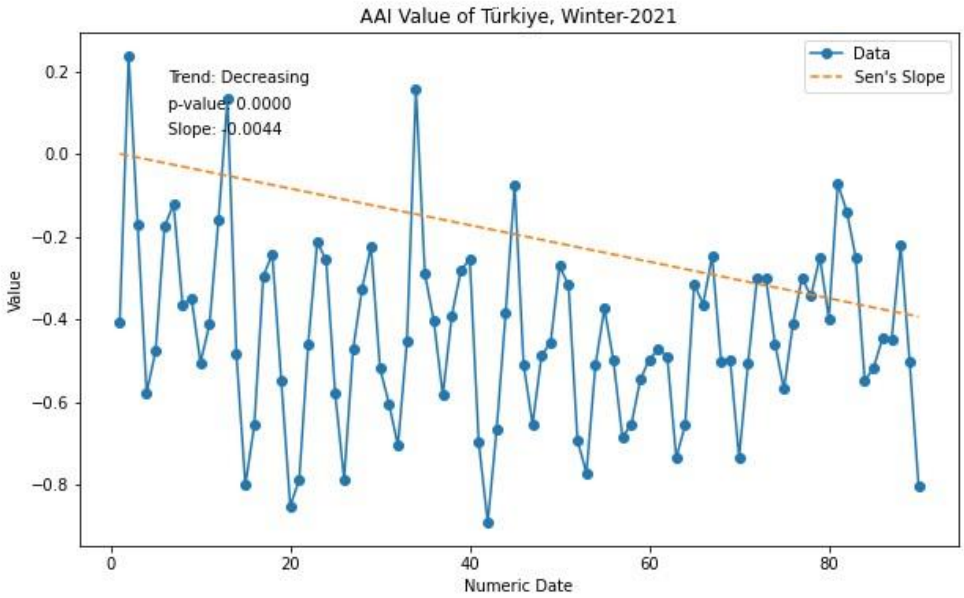

Figure 113. Seasonal trends of AAI in Türkiye, Winter-2021

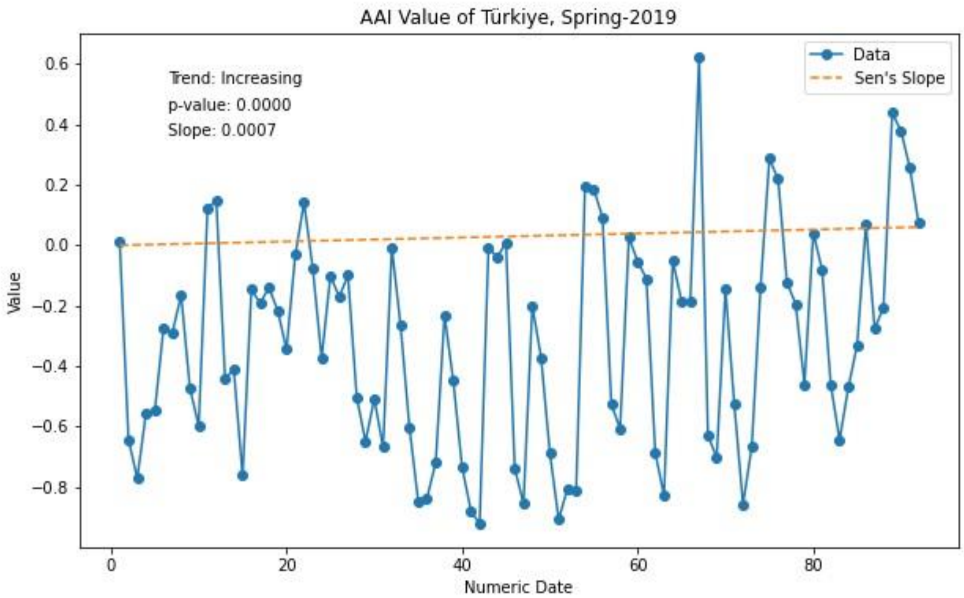

Figure 114. Seasonal trends of AAI in Türkiye, Spring-2019

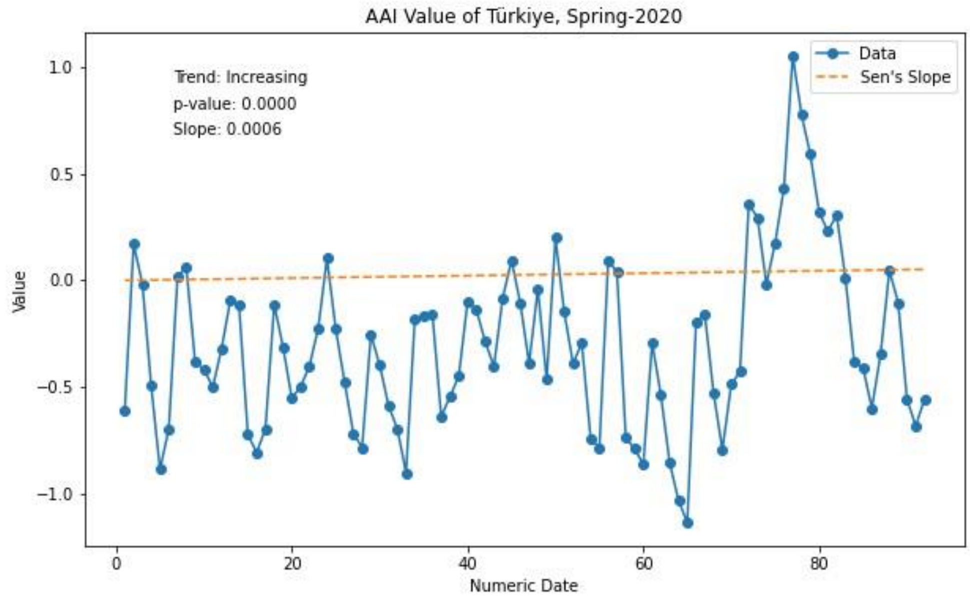

Figure 115. Seasonal trends of AAI in Türkiye, Spring-2020

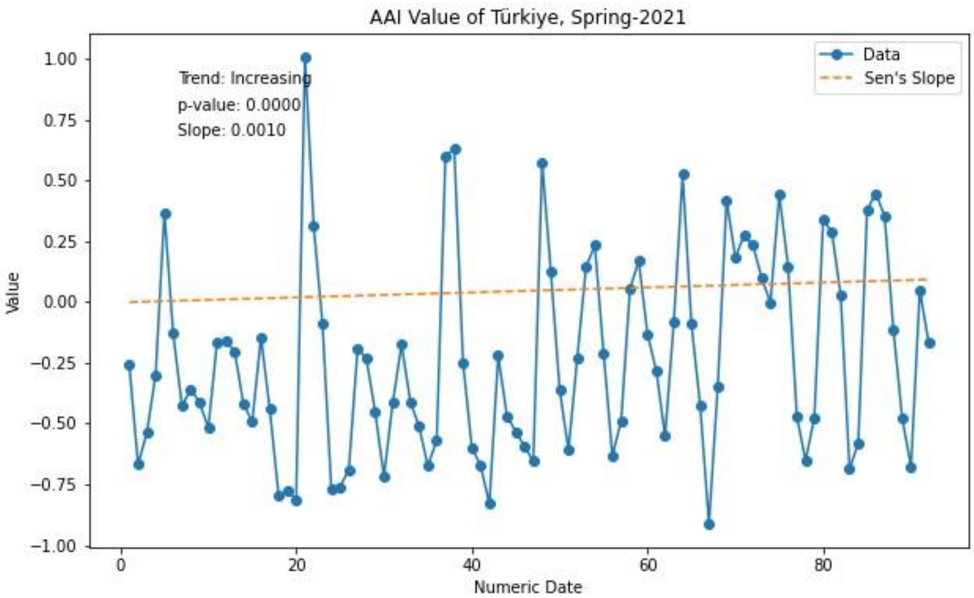

Figure 116. Seasonal trends of AAI in Türkiye, Spring-2021

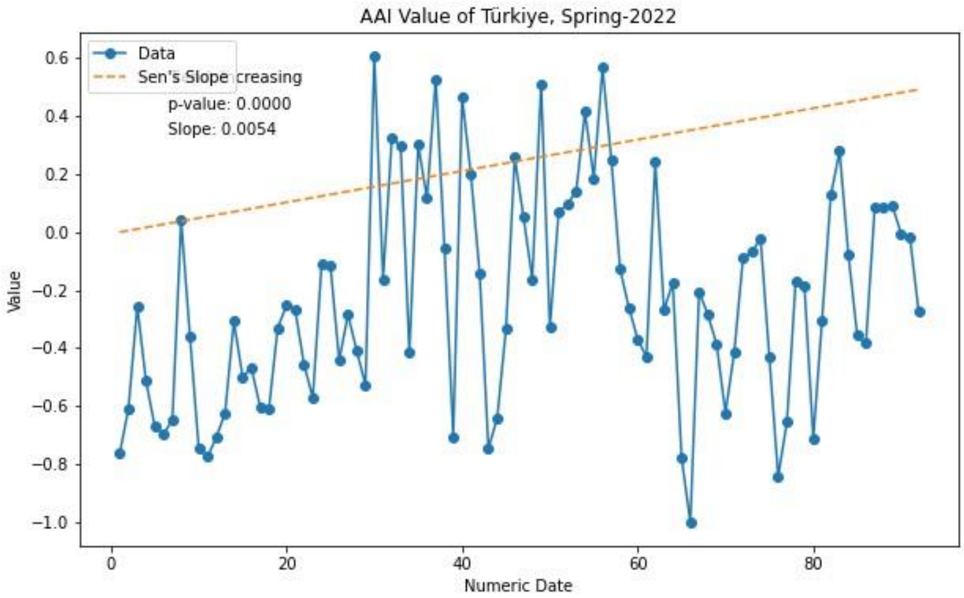

Figure 117. Seasonal trends of AAI in Türkiye, Spring-2022

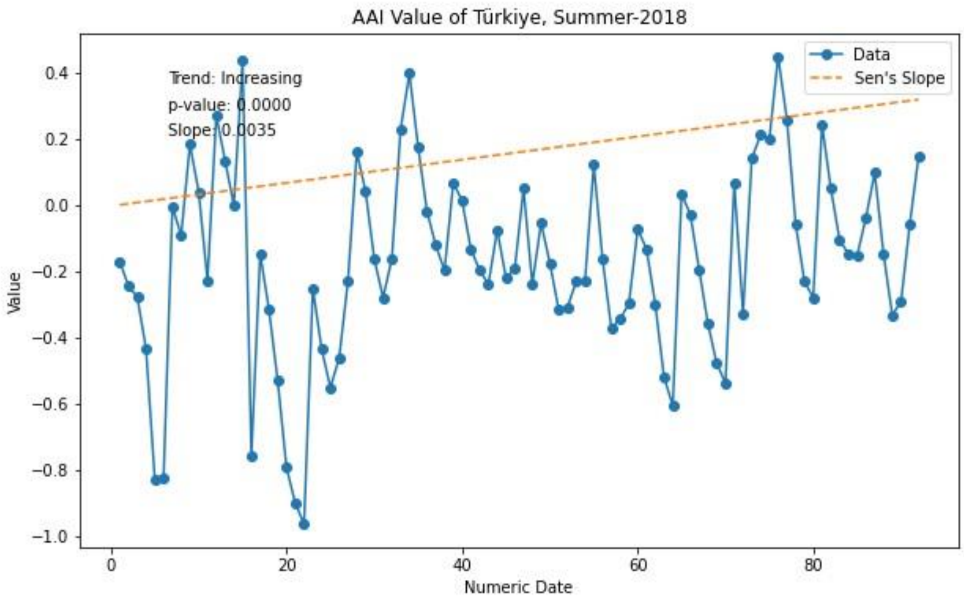

Figure 118. Seasonal trends of AAI in Türkiye, Summer-2018

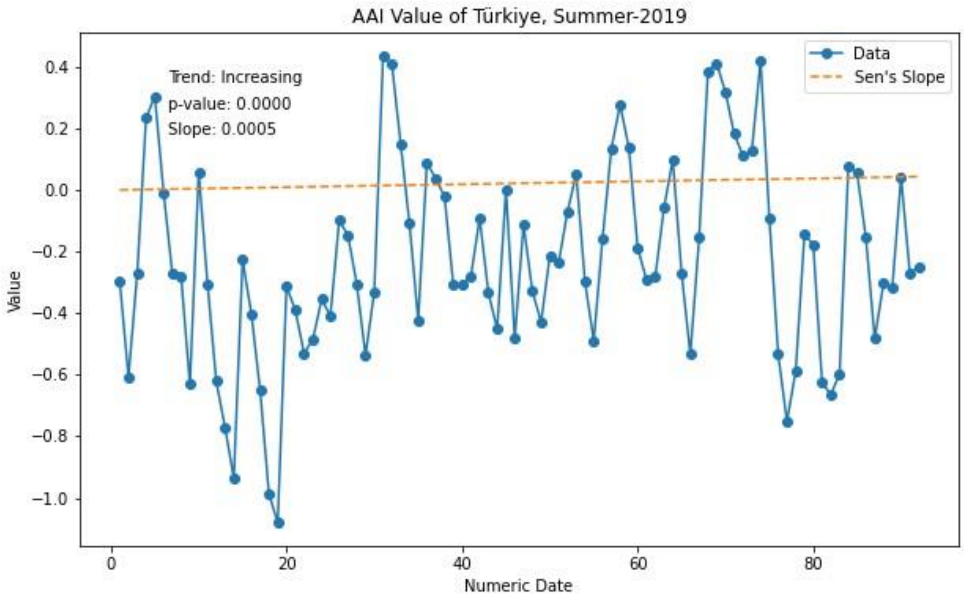

Figure 119. Seasonal trends of AAI in Türkiye, Summer-2019

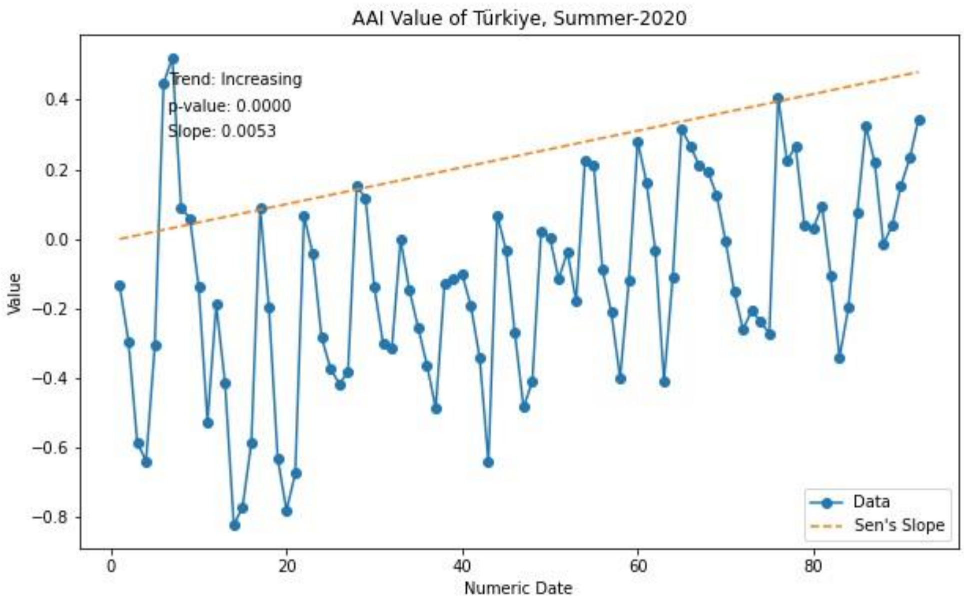

Figure 120. Seasonal trends of AAI in Türkiye, Summer-2020

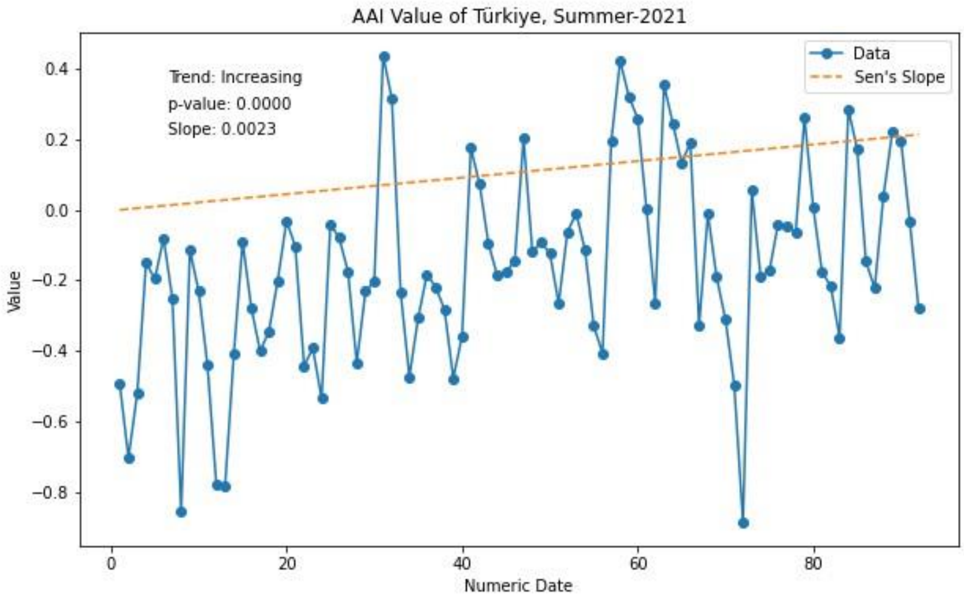

Figure 121. Seasonal trends of AAI in Türkiye, Summer-2021

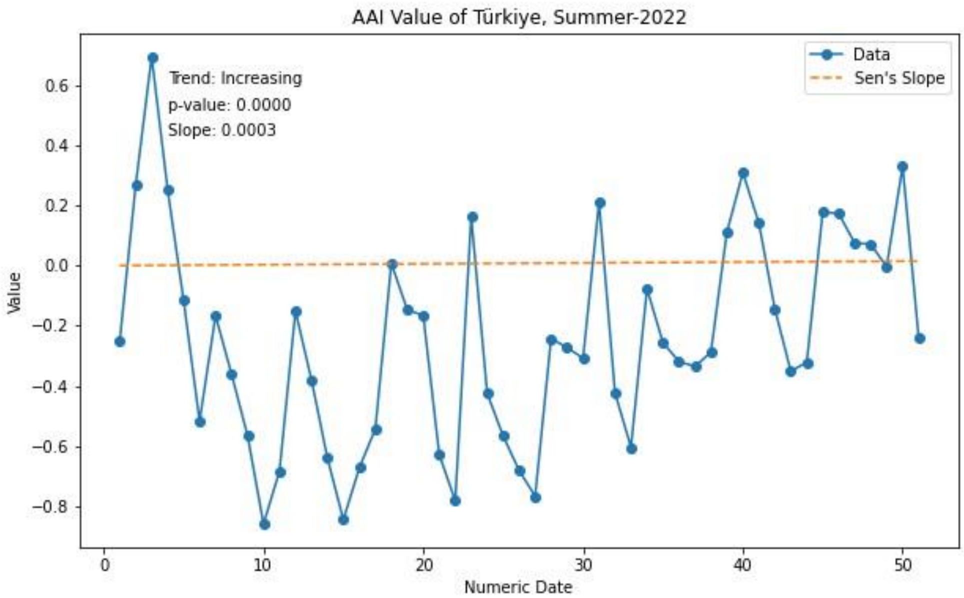

Figure 122. Seasonal trends of AAI in Türkiye, Summer-2022

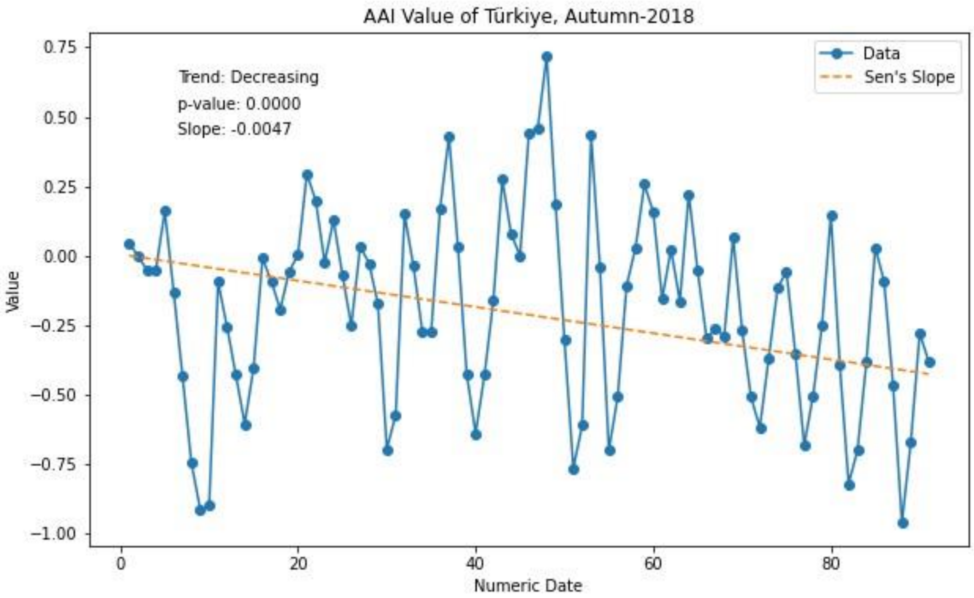

Figure 123. Seasonal trends of AAI in Türkiye, Autumn-2018

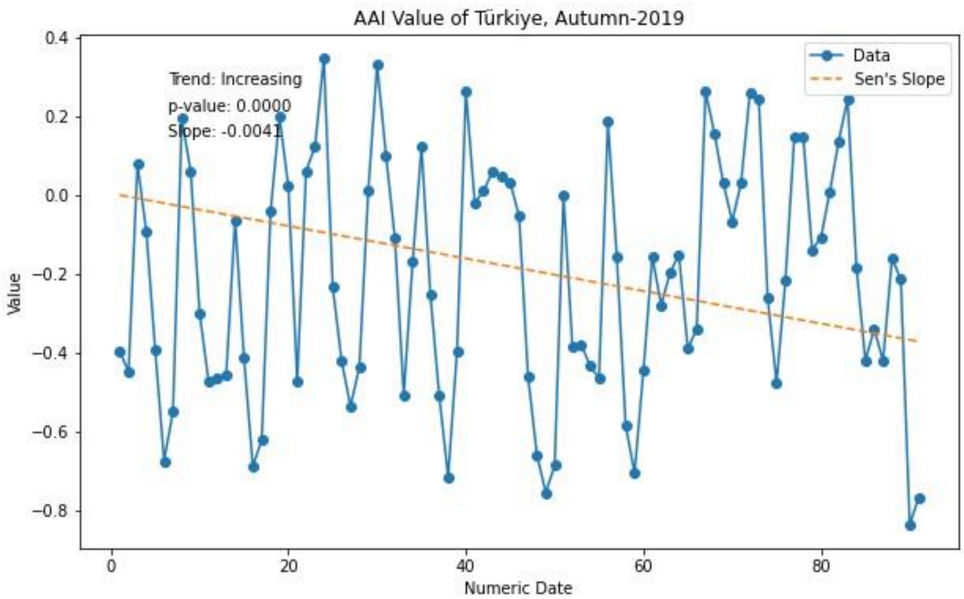

Figure 124. Seasonal trends of AAI in Türkiye, Autumn-2019

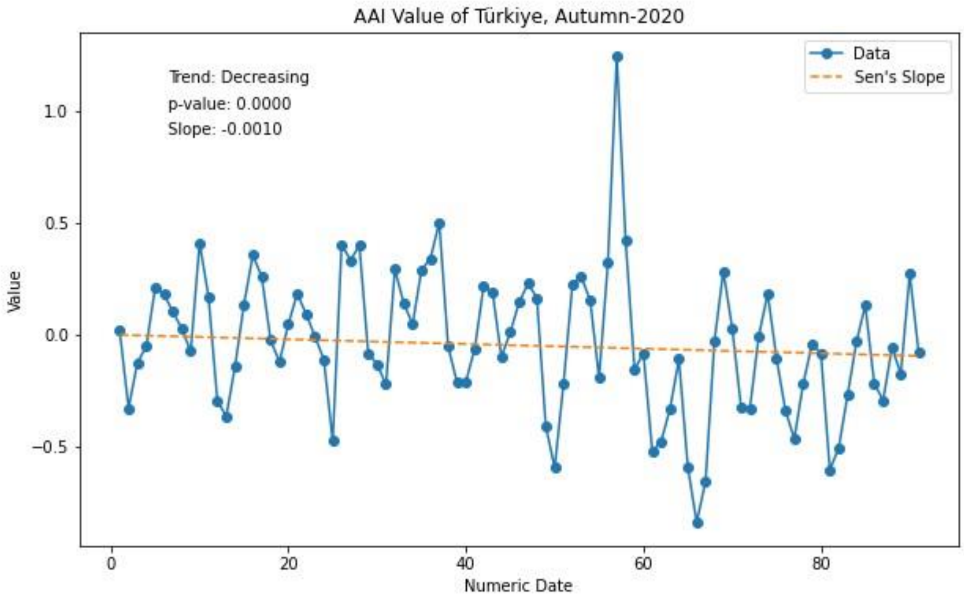

Figure 125. Seasonal trends of AAI in Türkiye, Autumn-2020

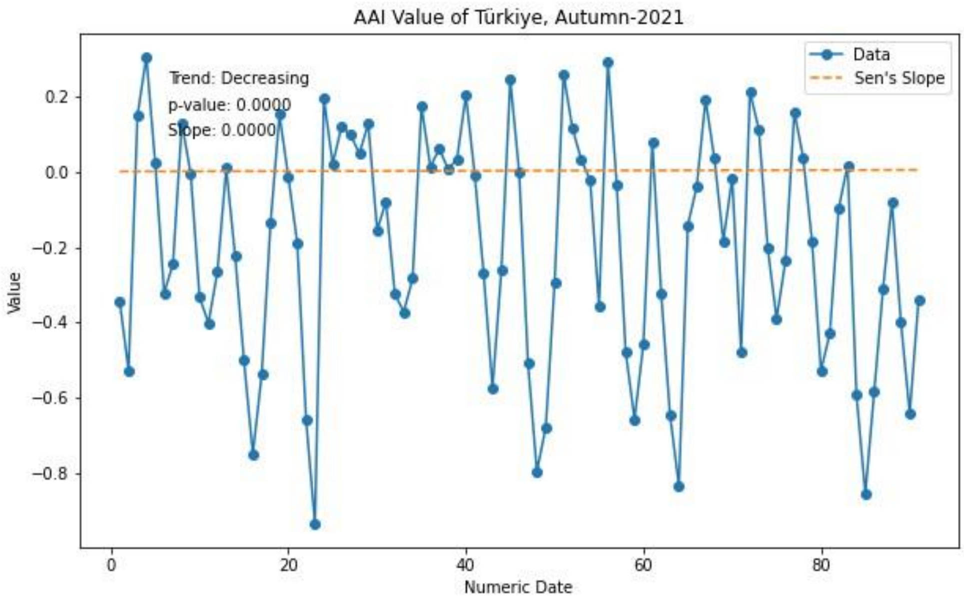

Figure 126. Seasonal trends of AAI in Türkiye, Autumn-2021

- **Time series graphs for the Northern Africa**

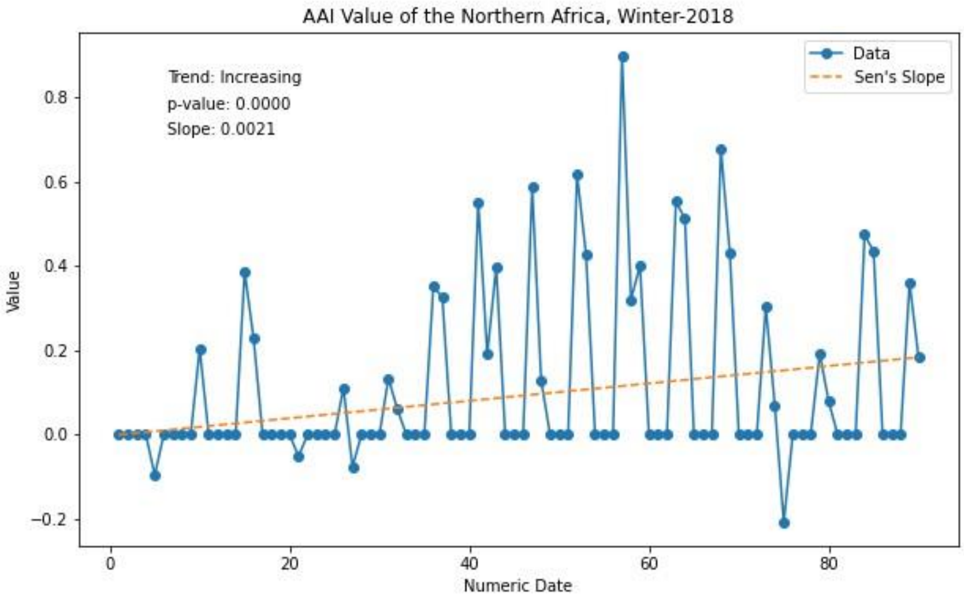

Figure 127. Seasonal trends of AAI in Northern Africa, Winter-2018

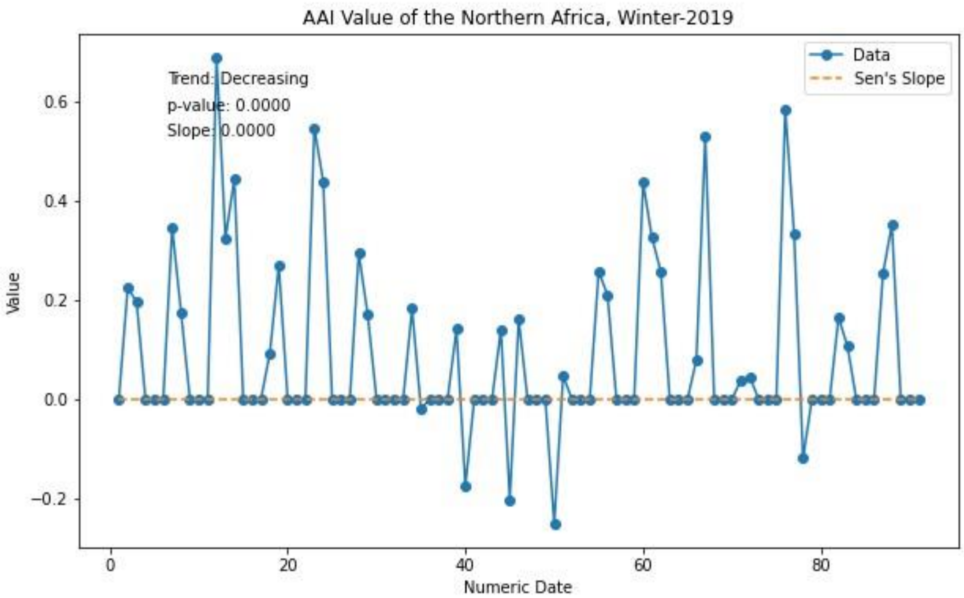

Figure 128. Seasonal trends of AAI in Northern Africa, Winter-2019

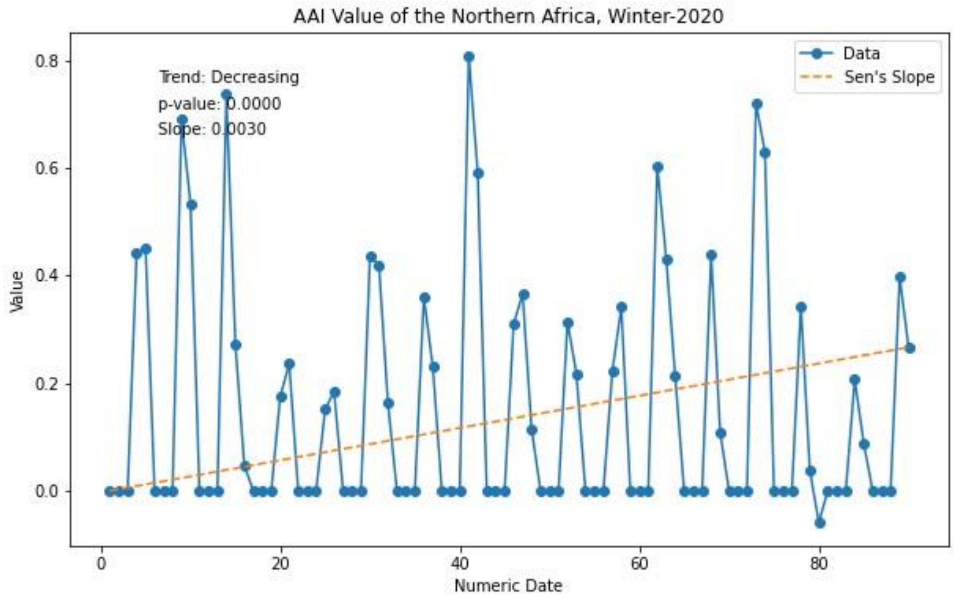

Figure 129. Seasonal trends of AAI in Northern Africa, Winter-2020

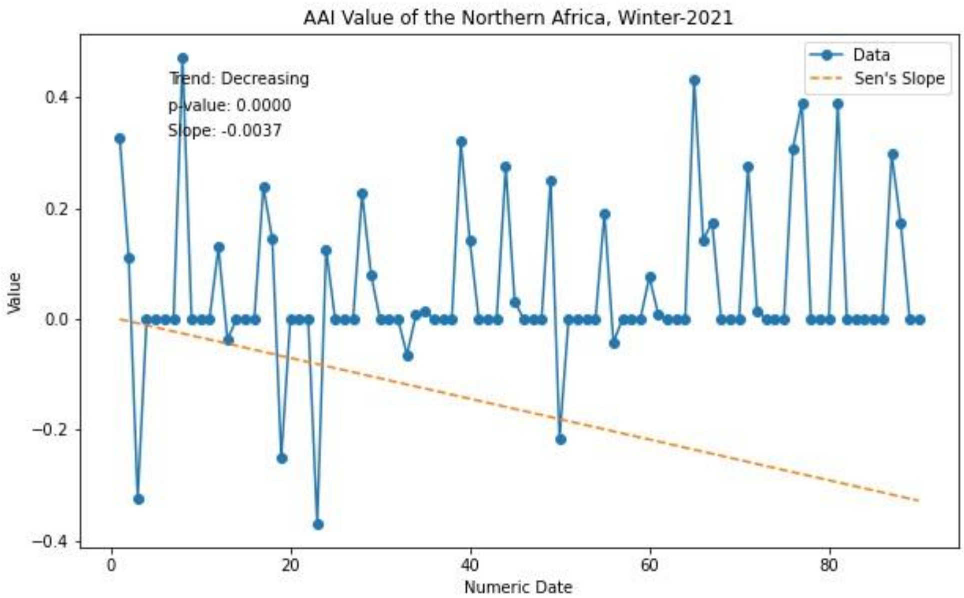

Figure 130. Seasonal trends of AAI in Northern Africa, Winter-2021

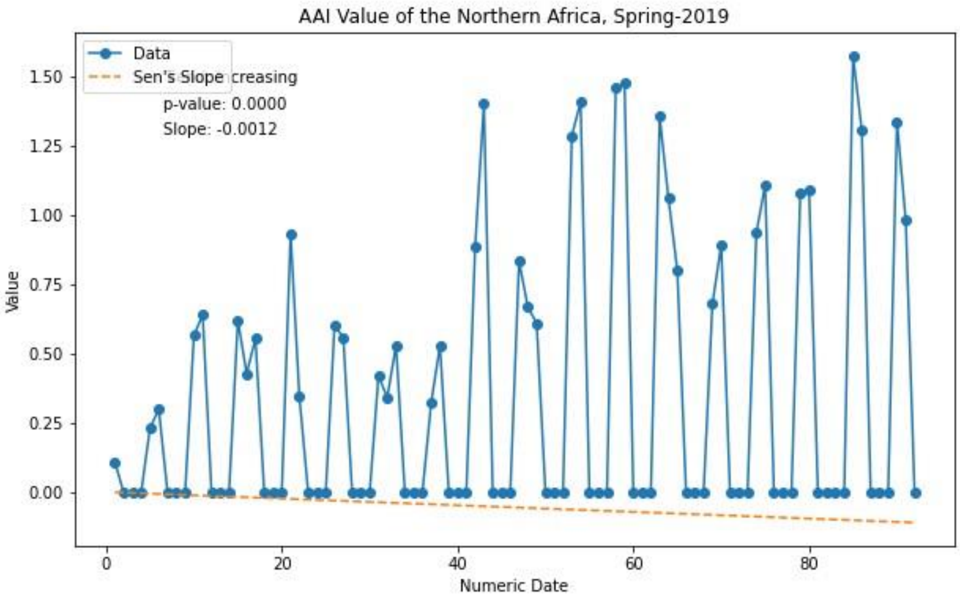

Figure 131. Seasonal trends of AAI in Northern Africa, Spring-2019

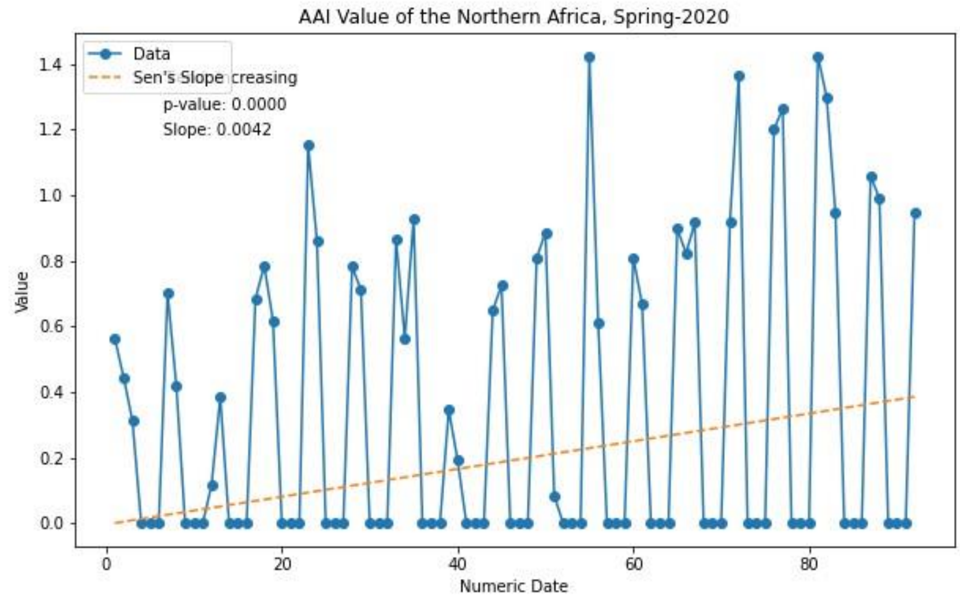

Figure 132. Seasonal trends of AAI in Northern Africa, Spring-2020

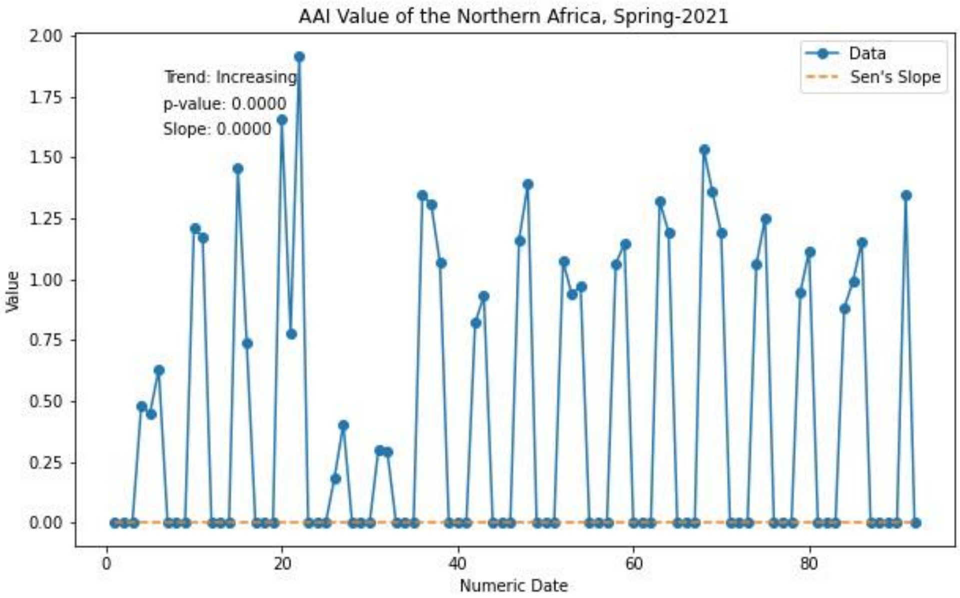

Figure 133. Seasonal trends of AAI in Northern Africa, Spring-2021

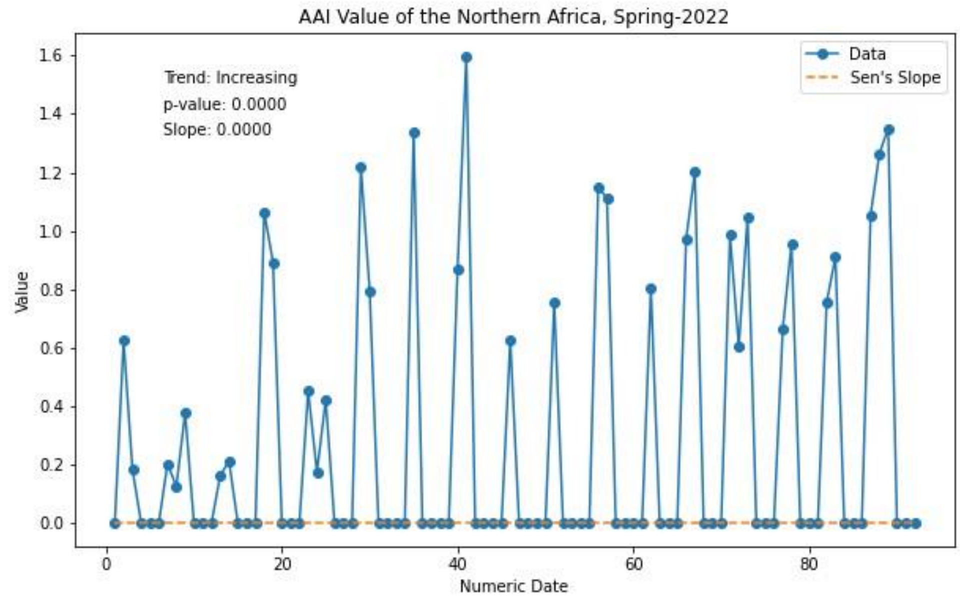

Figure 134. Seasonal trends of AAI in Northern Africa, Spring-2022

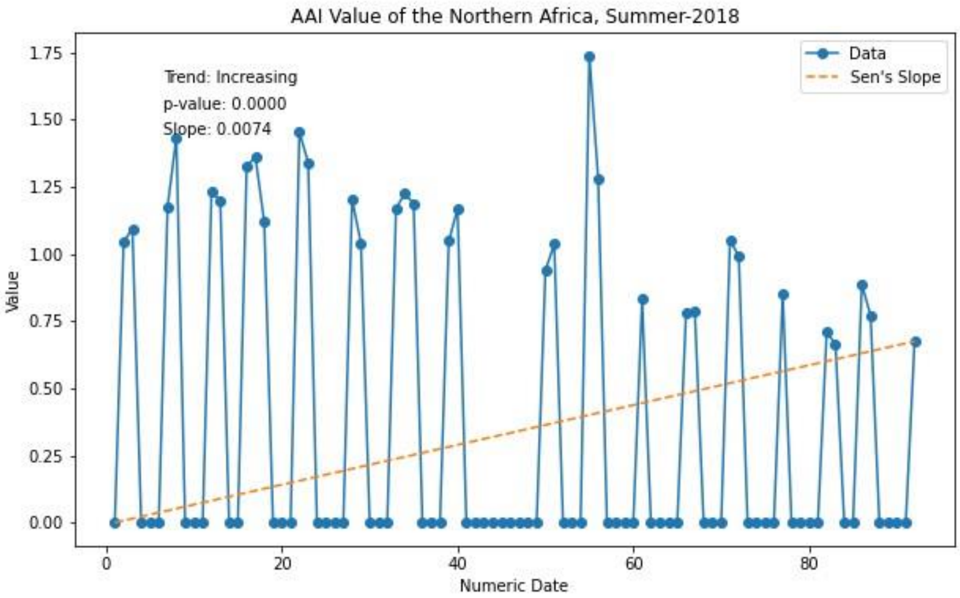

Figure 135. Seasonal trends of AAI in Northern Africa, Summer-2018

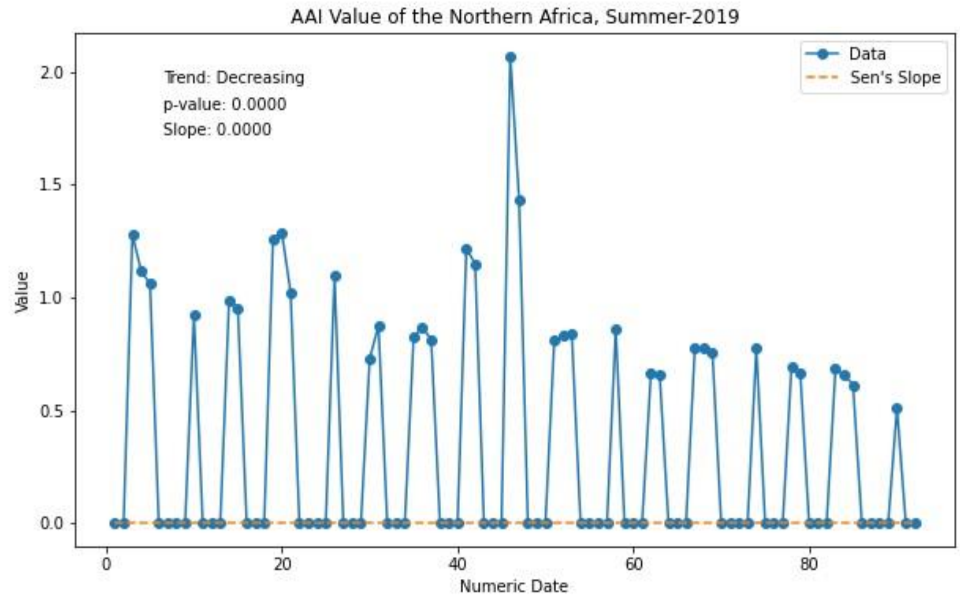

Figure 136. Seasonal trends of AAI in Northern Africa, Summer-2019

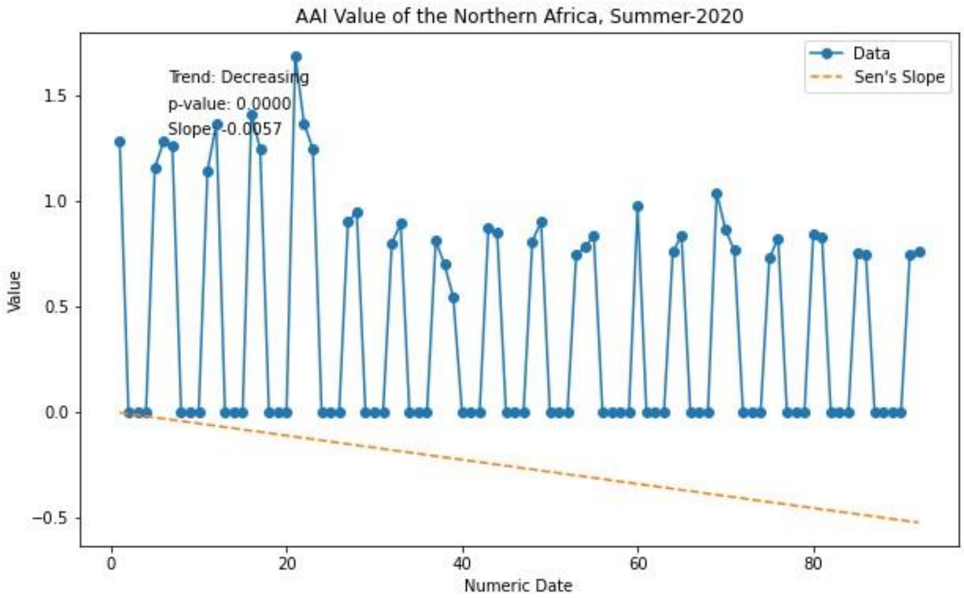

Figure 137. Seasonal trends of AAI in Northern Africa, Summer-2020

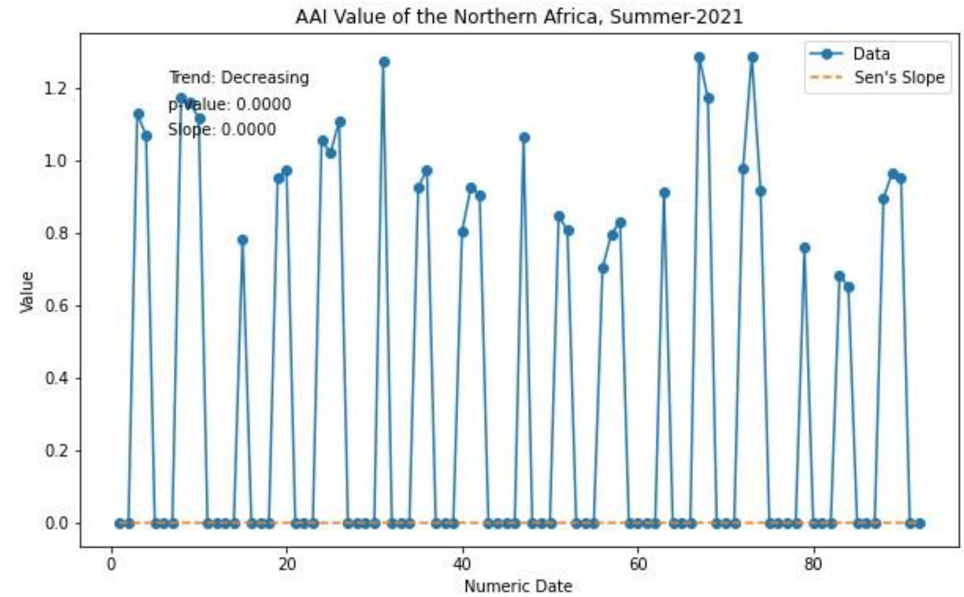

Figure 138. Seasonal trends of AAI in Northern Africa, Summer-2021

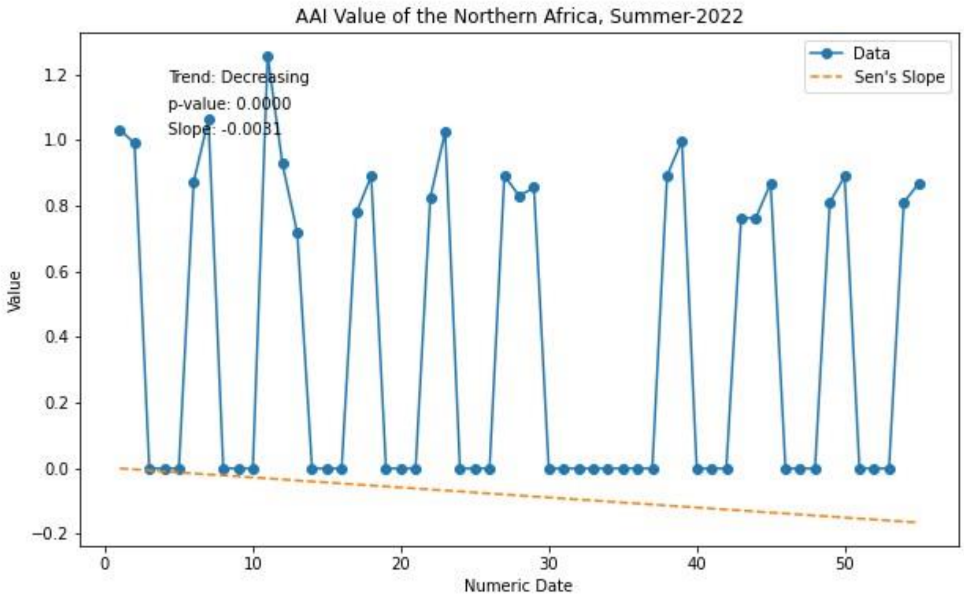

Figure 139. Seasonal trends of AAI in Northern Africa, Summer-2022

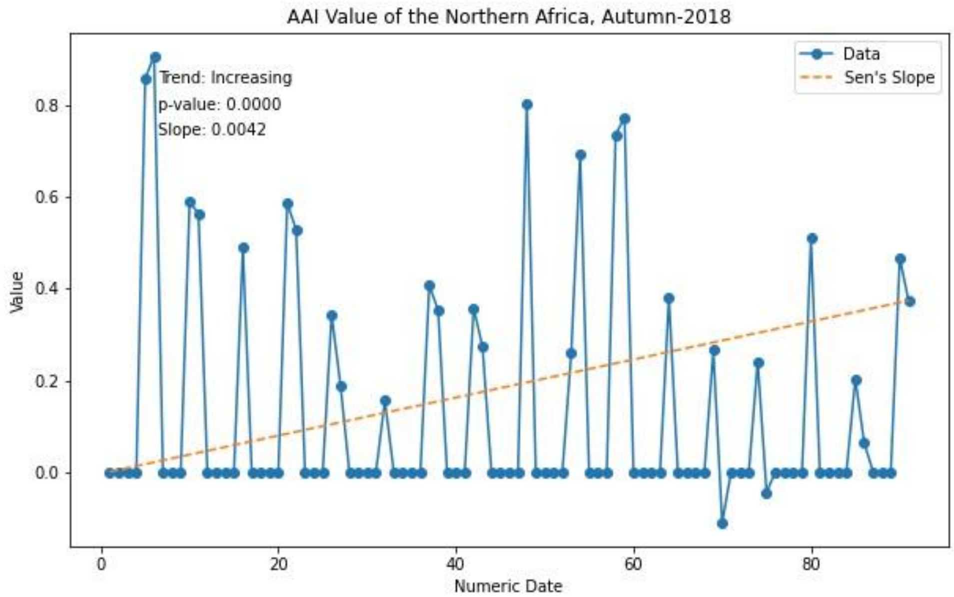

Figure 140. Seasonal trends of AAI in Northern Africa, Autumn-2018

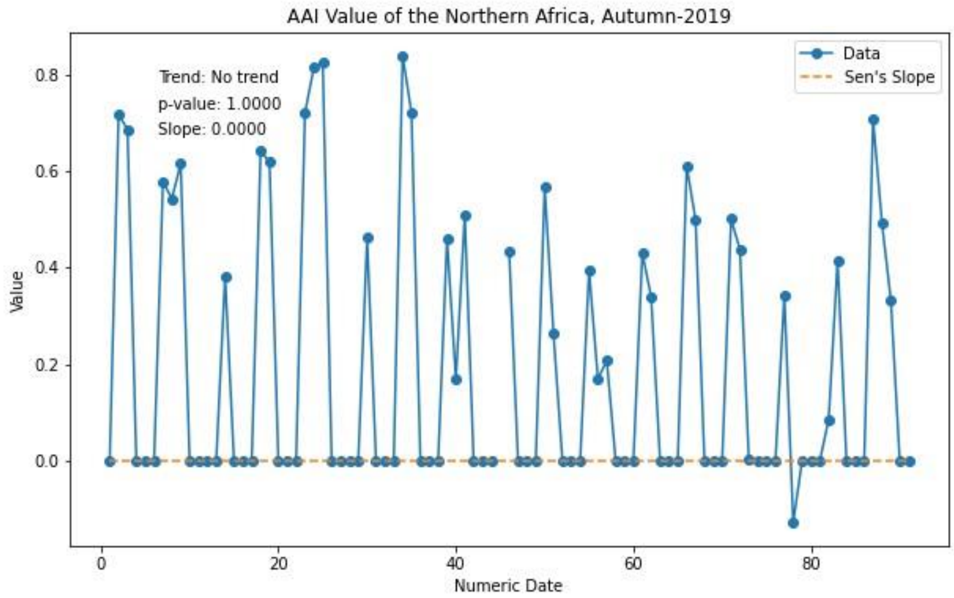

Figure 141. Seasonal trends of AAI in Northern Africa, Autumn-2019

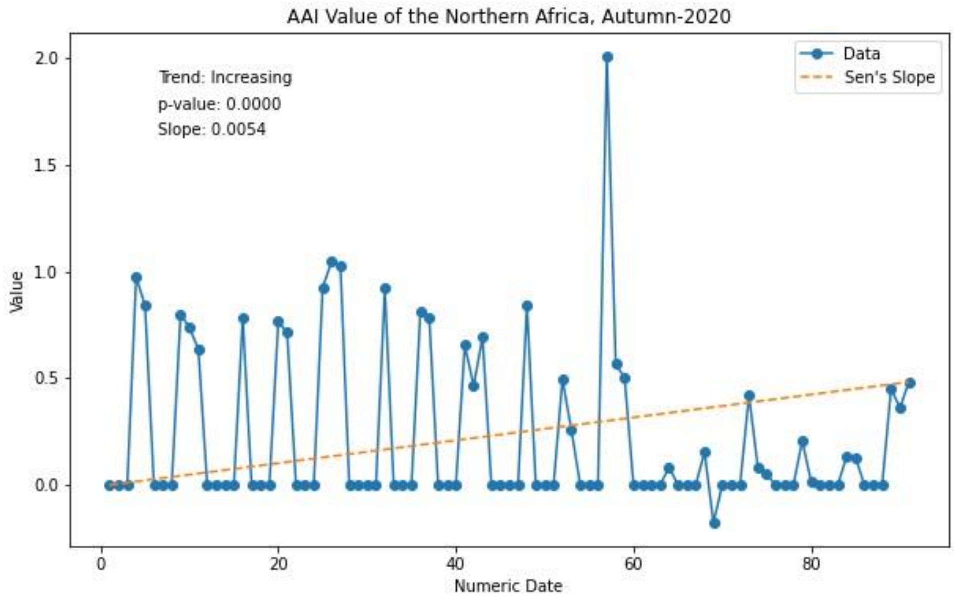

Figure 142. Seasonal trends of AAI in Northern Africa, Autumn-2020

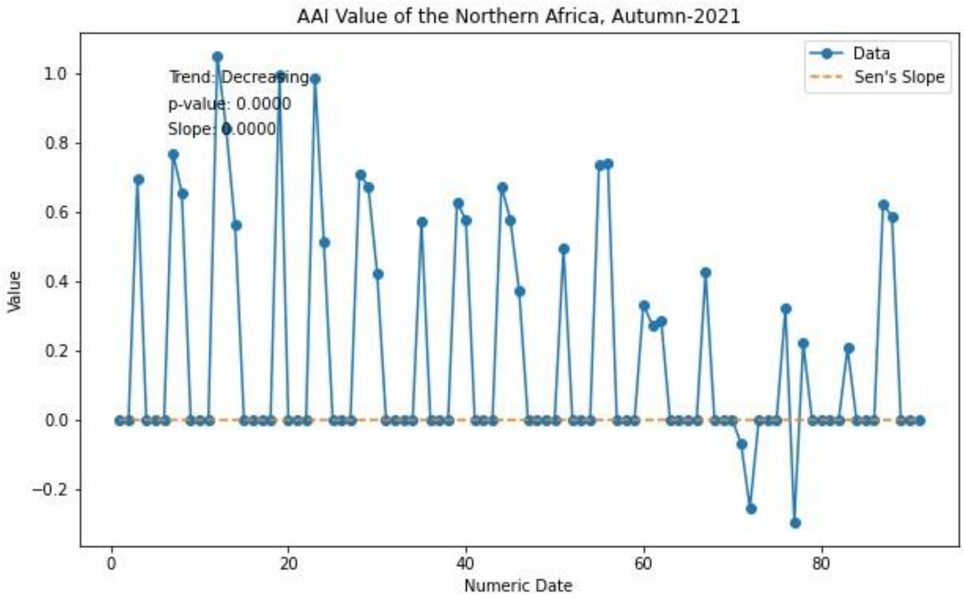

Figure 143. Seasonal trends of AAI in Northern Africa, Autumn-2021

- **Time series graphs for the Northern Arabian Peninsula**

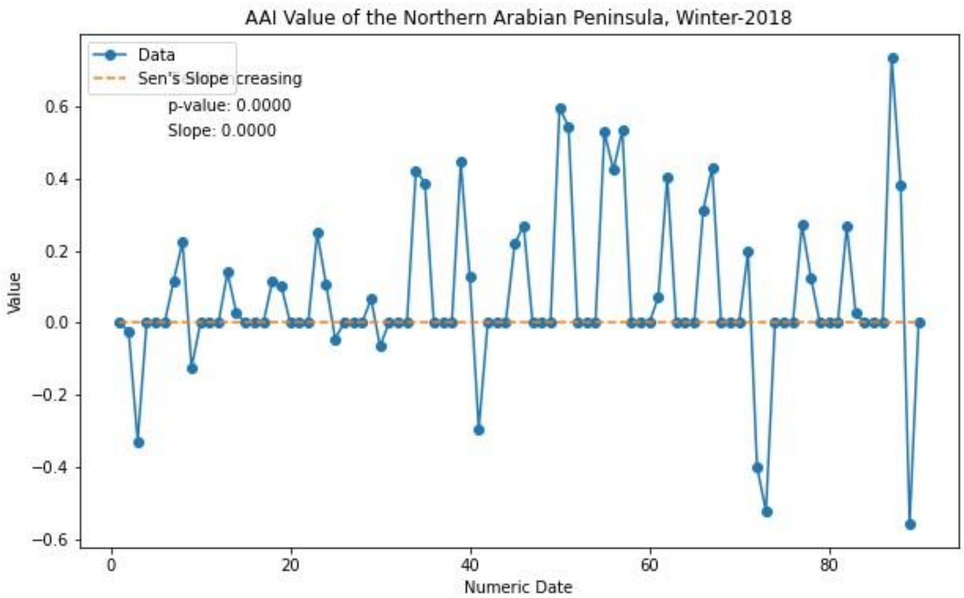

Figure 144. Seasonal trends of AAI in Northern Arabian Peninsula, Winter-2018

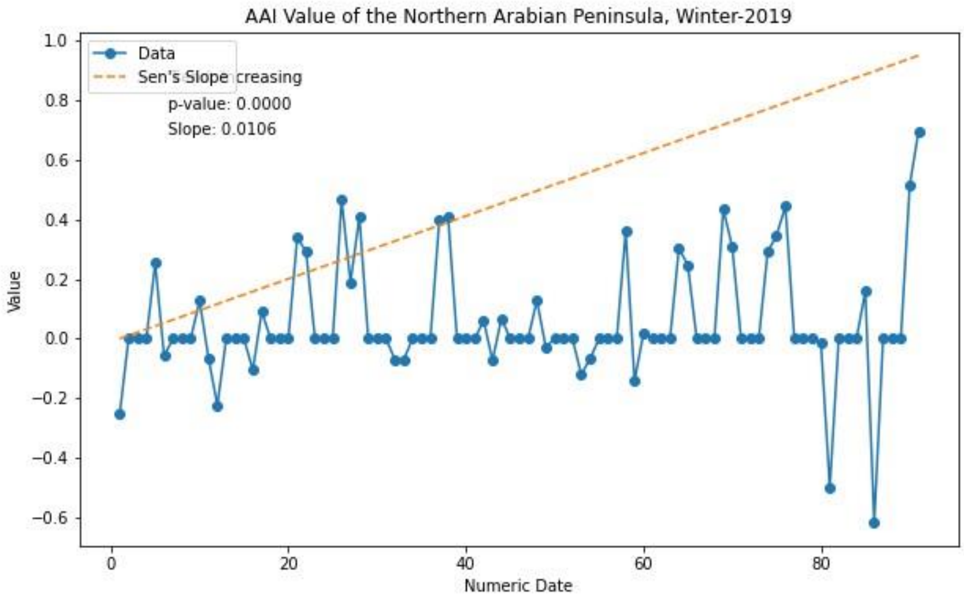

Figure 145. Seasonal trends of AAI in Northern Arabian Peninsula, Winter-2019

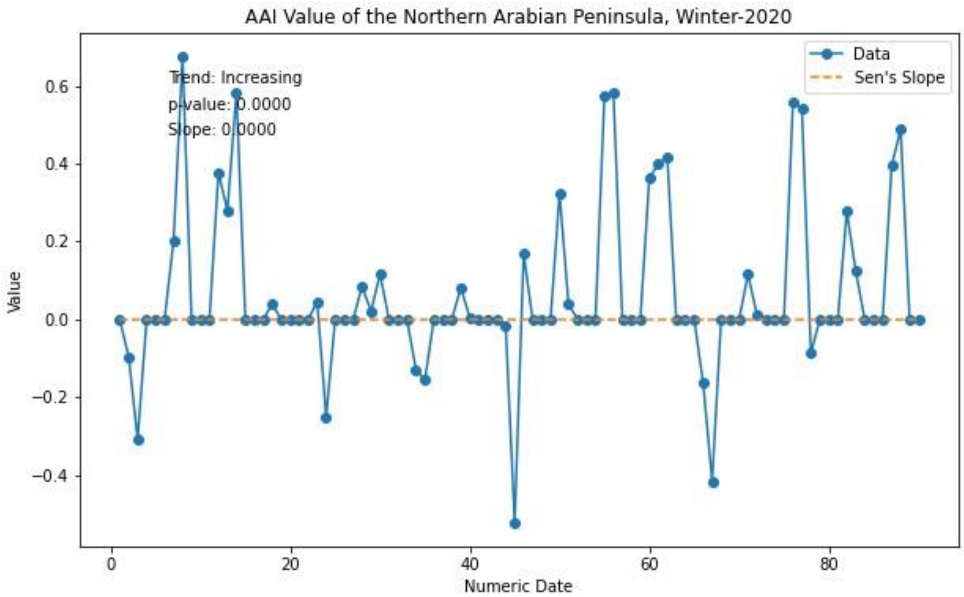

Figure 146. Seasonal trends of AAI in Northern Arabian Peninsula, Winter-2020

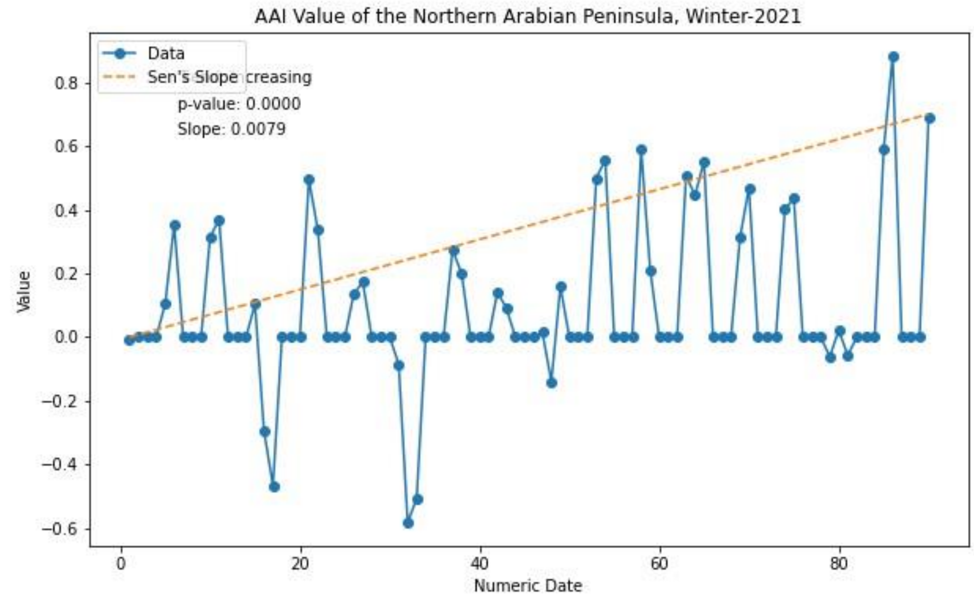

Figure 147. Seasonal trends of AAI in Northern Arabian Peninsula, Winter-2021

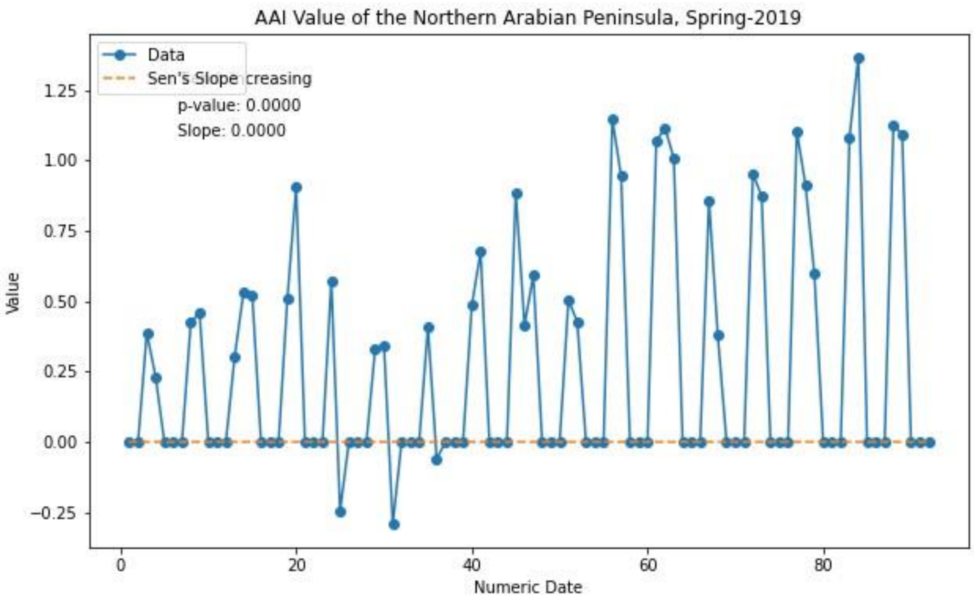

Figure 148. Seasonal trends of AAI in Northern Arabian Peninsula, Spring-2019

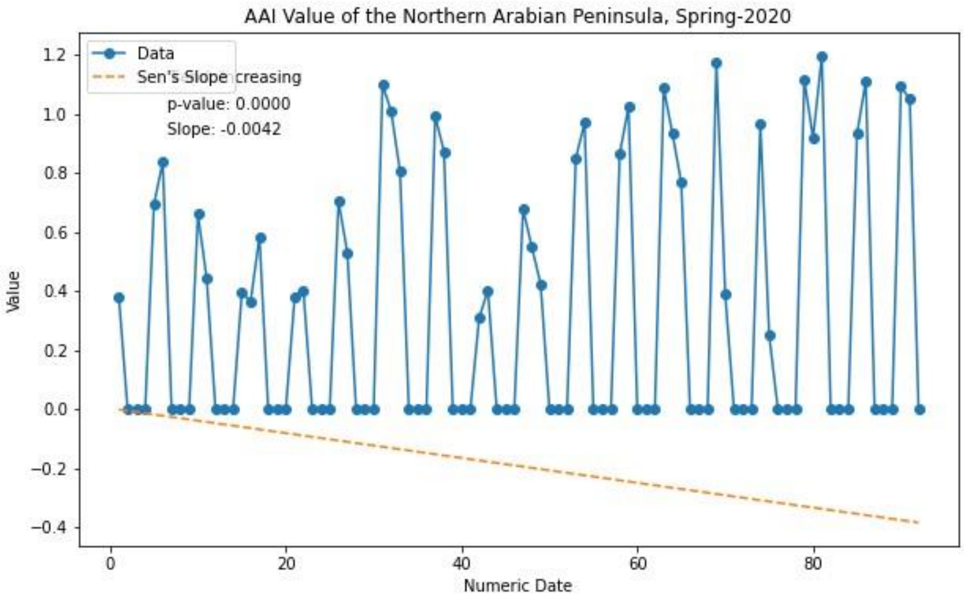

Figure 149. Seasonal trends of AAI in Northern Arabian Peninsula, Spring-2020

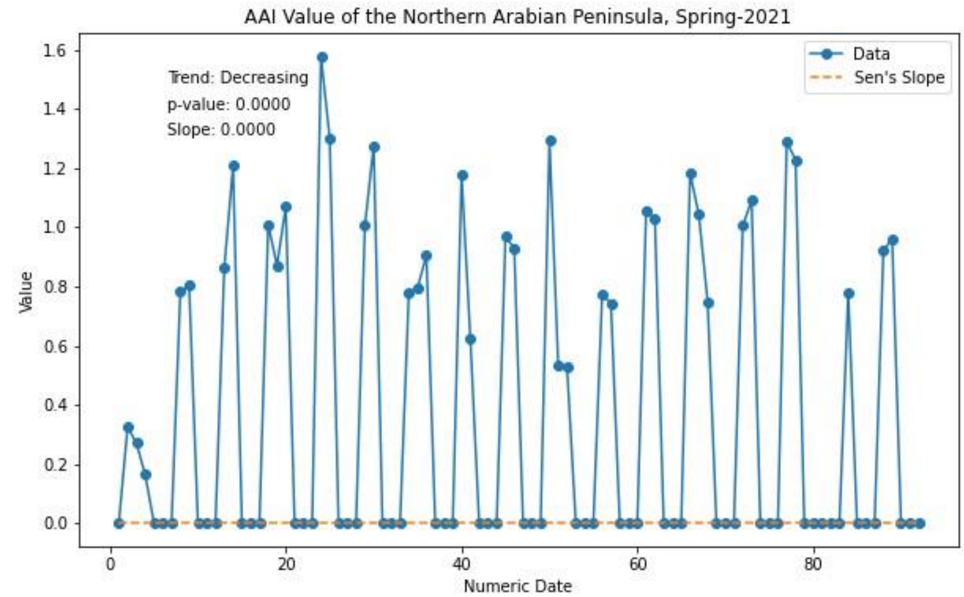

Figure 150. Seasonal trends of AAI in Northern Arabian Peninsula, Spring-2021

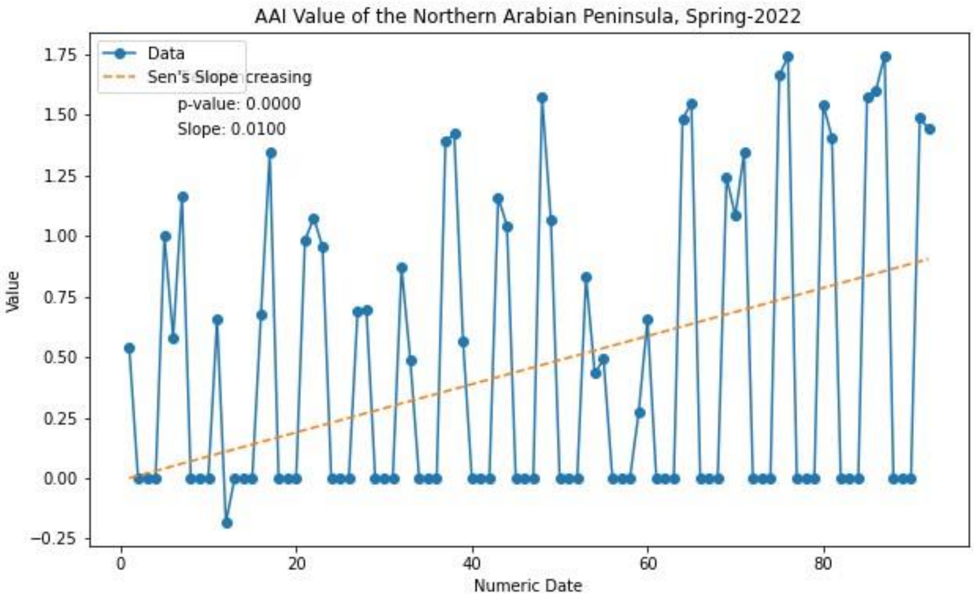

Figure 151. Seasonal trends of AAI in Northern Arabian Peninsula, Spring-2022

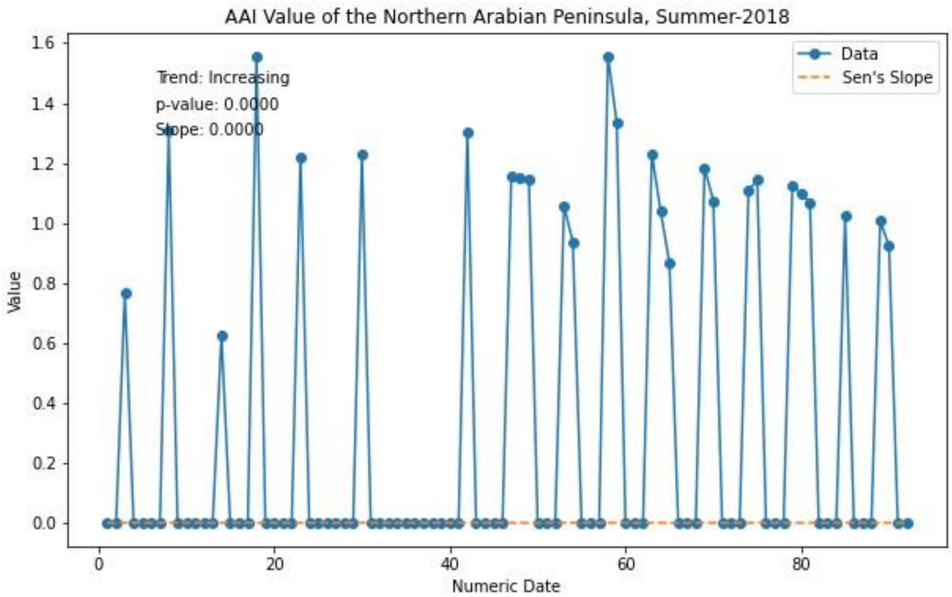

Figure 152. Seasonal trends of AAI in Northern Arabian Peninsula, Summer-2018

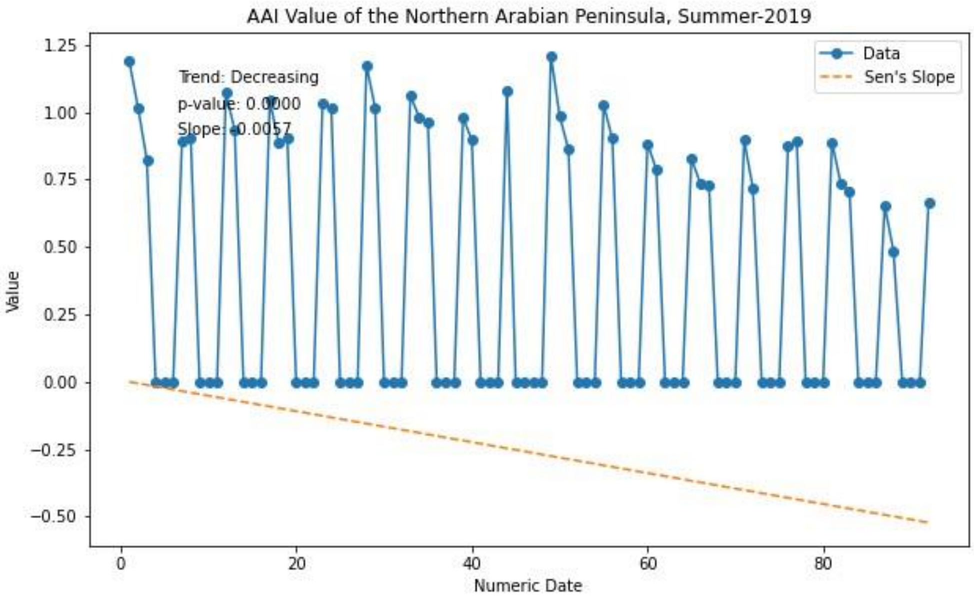

Figure 153. Seasonal trends of AAI in Northern Arabian Peninsula, Summer-2019

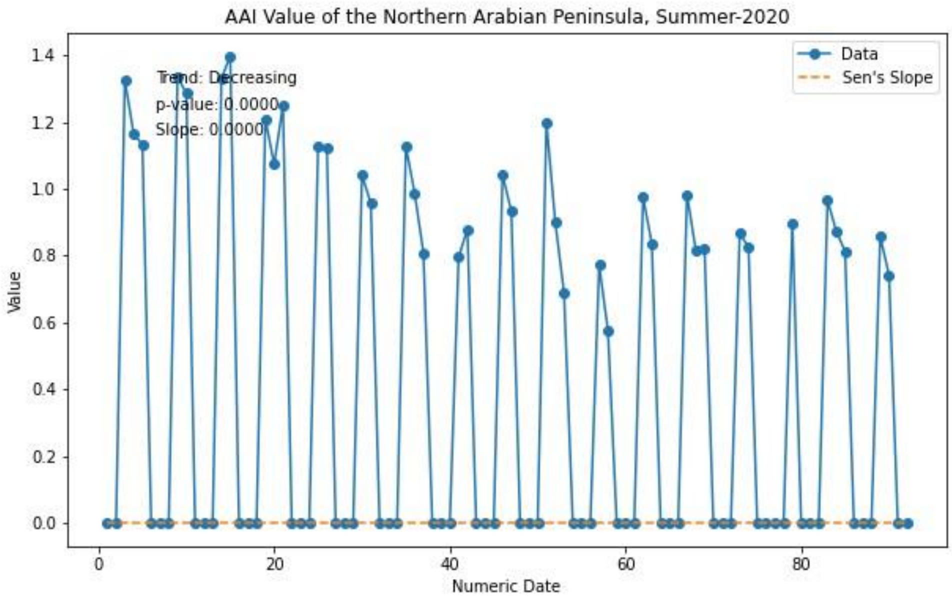

Figure 154. Seasonal trends of AAI in Northern Arabian Peninsula, Summer-2020

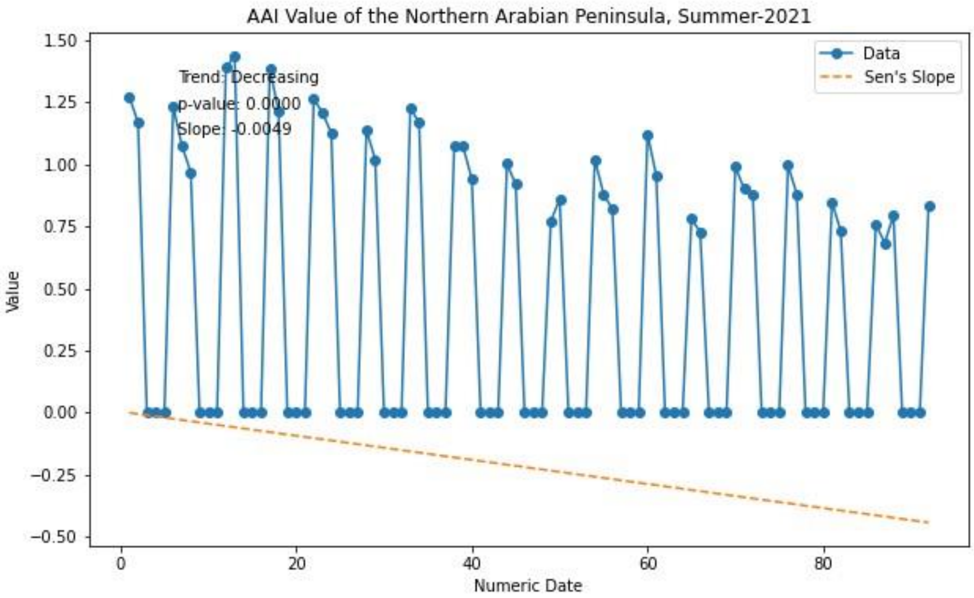

Figure 155. Seasonal trends of AAI in Northern Arabian Peninsula, Summer-2021

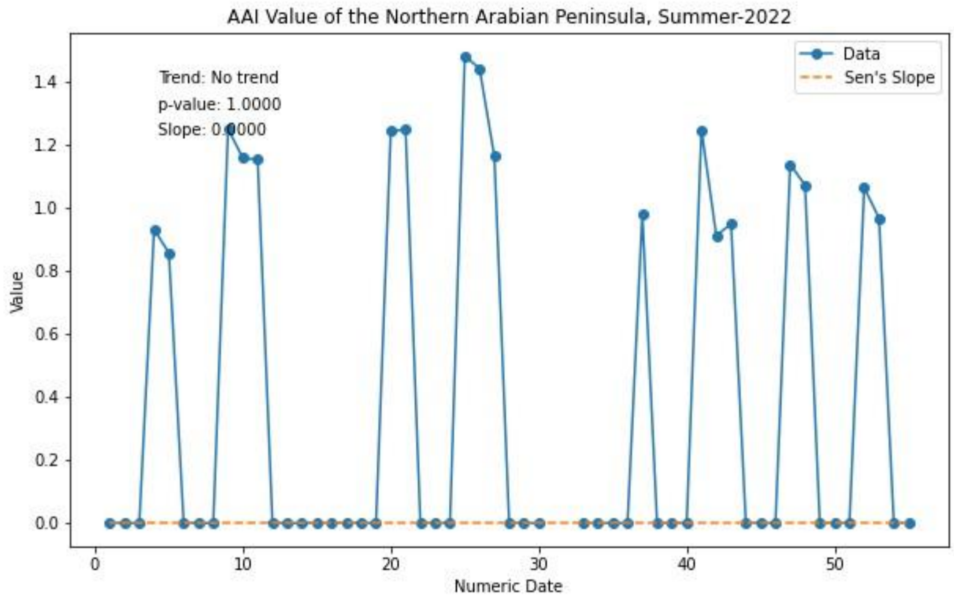

Figure 156. Seasonal trends of AAI in Northern Arabian Peninsula, Summer-2022

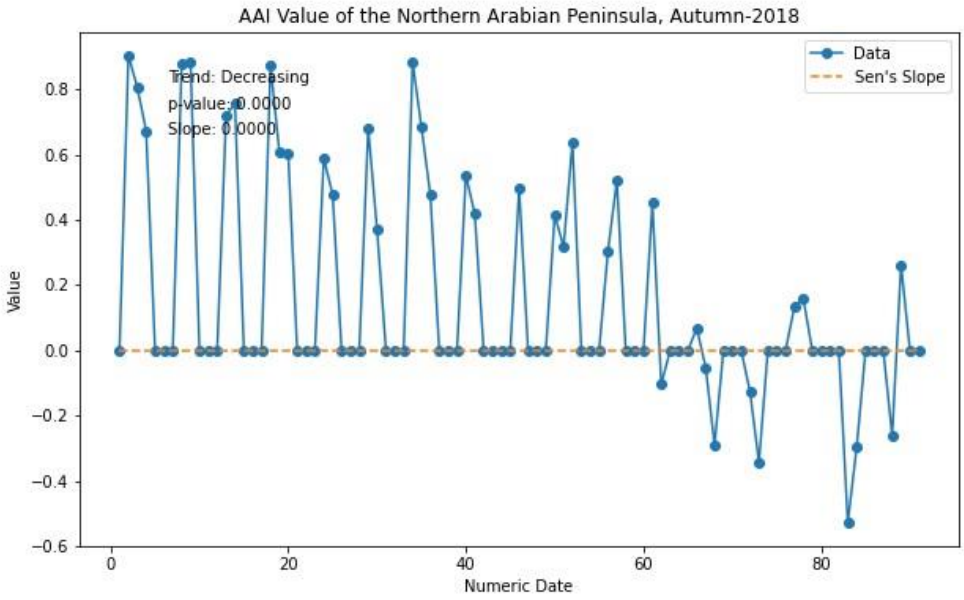

Figure 157. Seasonal trends of AAI in Northern Arabian Peninsula, Autumn-2018

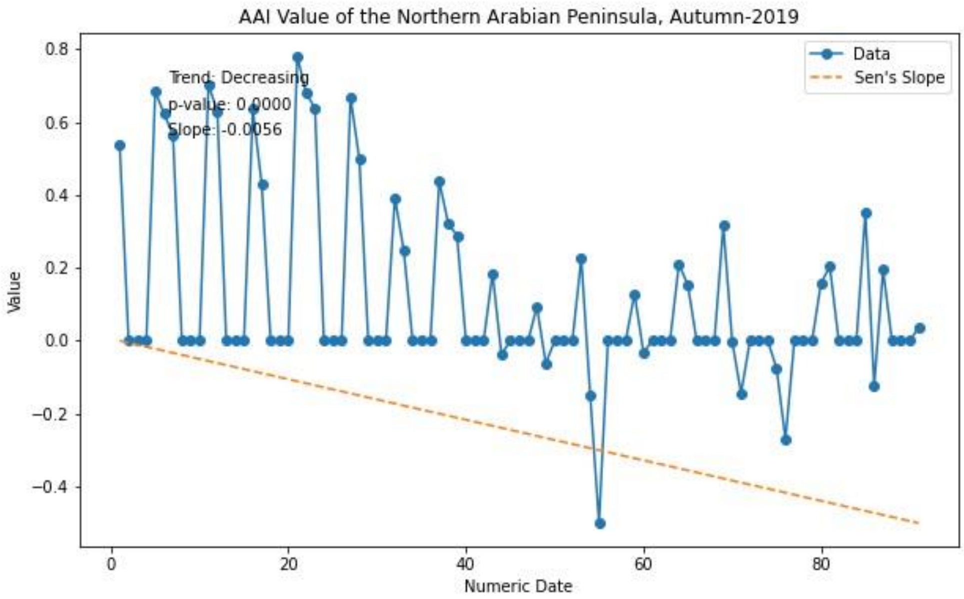

Figure 158. Seasonal trends of AAI in Northern Arabian Peninsula, Autumn-2019

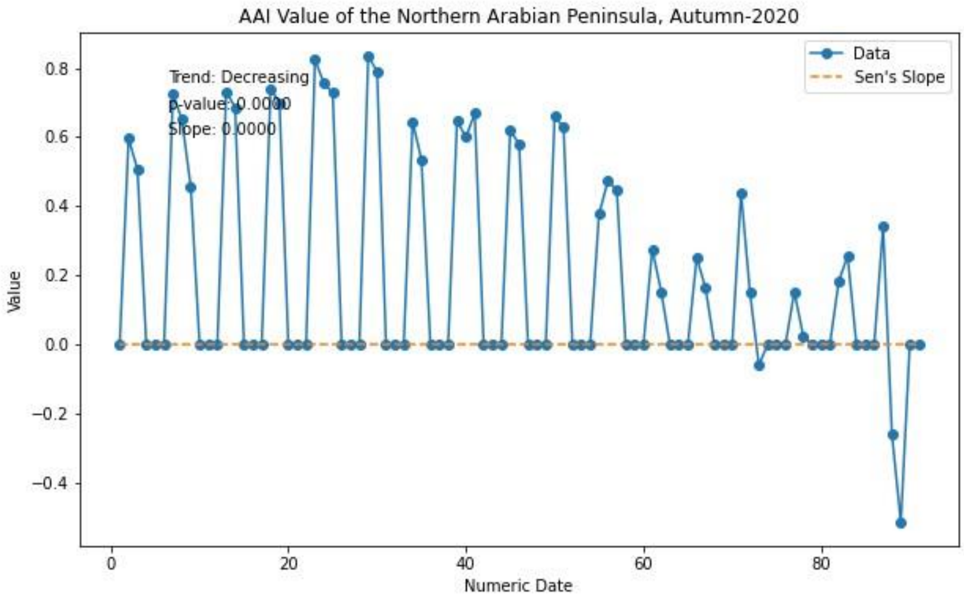

Figure 159. Seasonal trends of AAI in Northern Arabian Peninsula, Autumn-2020

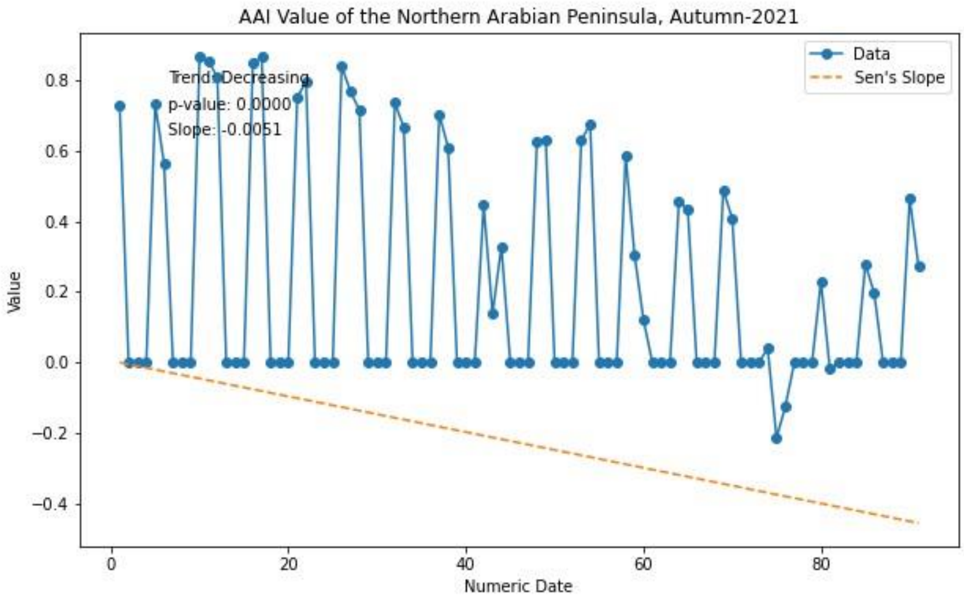

Figure 160. Seasonal trends of AAI in Northern Arabian Peninsula, Autumn-2021